Bulletin 57
(Part 2 of 4 Parts)

THE SHOCK AND VIBRATION BULLETIN

Part 2
Instrumentation, Shock Analysis,
and Shock Testing

JANUARY 1987

A Publication of
THE SHOCK AND VIBRATION
INFORMATION CENTER
Naval Research Laboratory, Washington, D.C.

Office of
The Under Secretary of Defense
for Research and Engineering

Bulletin 57
(Part 2 of 4 Parts)

THE SHOCK AND VIBRATION BULLETIN

JANUARY 1987

A Publication of
THE SHOCK AND VIBRATION
INFORMATION CENTER
Naval Research Laboratory, Washington, D.C.

The 57th Symposium on Shock and Vibration was held in New Orleans, Louisiana, October 14-16, 1986. The Defense Nuclear Agency, Washington, DC and the U.S. Army Engineer Waterways Experiment Station, Vicksburg, Mississippi were the hosts.

Office of
The Under Secretary of Defense
for Research and Engineering

CONTENTS

PAPERS APPEARING IN PART 2

PAPERS APPEARING IN PART 3

Isolation and Damping

Vibration Test Criteria

*This paper was presented in the Pyrotechnic Shock Workshop at the 57th Shock and Vibration Symposium

ZEROSHIFT OF PIEZOELECTRIC ACCELEROMETERS IN PYROSHOCK MEASUREMENTS*

A. Chu, Endevco Corporation, San Juan Capistrano, CA

SESSION CHAIRMEN AND COCHAIRMEN

Date	Session Title	Chairmen	CoChairmen
Tuesday 14 October, A.M.	Opening Session	Dr. Don A. Linger, Defense Nuclear Agency, Washington, DC	Dr. Sam Kiger, U.S. Army Engineer Waterways Experiment Station, Vicksburg, MS
Tuesday 14 October, P.M.	Instrumentation	Mr. Richard P. Joyce, IIT Research Institute, Chicago, IL	Mr. W. Scott Walton U.S. Army Combat Systems Test Activity, Aberdeen Proving Ground, MD
Tuesday 14 October, P.M.	Shock Analysis	Mr. James D. Cooper, Defense Nuclear Agency, Washington, DC	Mr. William J. Flathau, JAYCOR, Vicksburg, MS
Wednesday 15 October, A.M.	Plenary A	Rudolph H. Volin, P.E., Shock and Vibration Information Center, Naval Research Laboratory, Washington, DC	
Wednesday 15 October, A.M.	Nondevelopment Items Workshop, Session I, Methods	Mr. James W. Daniel, U.S. Army Missile Command, Redstone Arsenal, AL	Mr. Paul Hahn, Martin Marietta Orlando Aerospace, Orlando, FL
Wednesday 15 October, A.M.	Structural Dynamics I	Mr. Stanley Barrett, Martin Marietta Denver Aerospace, Denver, CO	Mr. W. Paul Dunn, The Aerospace Corporation, El Segundo, CA
Wednesday 15 October, A.M.	Isolation and Damping	Dr. Paul N. Sonnenburg, Physicon, Inc., Huntsville, AL	Matthew Kluesener, P.E., University of Dayton Research Institute, Dayton, OH
Wednesday 15 October, P.M.	Nondevelopment Items Workshop, Session II, Case Histories	Mr. Howard Camp, Jr., U.S. Army Communications- Electronics Command, Ft. Monmouth, NJ	Edgar K. Stewart, P.E., U.S. Army Armament Command, Dover NJ
Wednesday 15 October, P.M.	Structural Dynamics II	Dr. John L. Gubser, McDonnell Douglas Astronautics, St. Louis, MO	C. Allen Ross, Ph.D., P.E., Air Force Engineering Services Center, Tyndall Air Force Base, FL

Wednesday 15 October, P.M.	Shock Testing	Mr. David Coltharp, U.S. Army Engineer Waterways Experiment Station, Vicksburg, MS	Mr. Steve Tanner, Naval Weapons Center, China Lake, CA
Thursday 16 October, A.M.	Plenary B	Mr. Jerome Pearson, Air Force Wright Aeronautical Laboratories, Wright-Patterson Air Force Base, OH	
Thursday 16 October, A.M.	Vibration Test Criteria	Mr. Tommy Dobbon, 6585 Test Group, Holloman Air Force Base, NM	Mr. Edward Szymkowiak, Westinghouse Electric Corporation, Baltimore, MD
Thursday 16 October, A.M.	Modal Test and Analysis	Richard Stroud, Ph.D., P.E., Synergistic Technology, Cupertino, CA	Connor D. Johnson, Ph.D., P.E. CSA Engineering, Inc. Palo Alto, CA
Thursday 16 October, A.M.	Vibration Analysis and Test	Mr. Frederick Anderson, U.S. Army Missile Command, Redstone Arsenal, AL	Mr. David Bond, Northrop Advanced Systems Division, Pico Rivera, CA
Thursday 16 October, P.M.	Short Discussion Topics	Mr. William Wassmann, Naval Surface Weapons Center, Silver Spring, MD	

INSTRUMENTATION

AN INTEGRATION TEST FOR ACCELEROMETER EVALUATION

Eric C. Hansen
Underwater Explosions Research Division
David Taylor Naval Ship Research & Development Center
Portsmouth, Virginia

A simple means for quickly evaluating accelerometers for integrability is presented in detail. In this method the accelerometer is subjected to an unsymmetrical input and the resulting output is integrated and compared to a known result. Theoretical aspects of this test are discussed and a mechanical device coupled with an electronic integrator is described to illustrate a useful test system. Using this equipment, test results from selected accelerometers are shown to demonstrate the method.

INTRODUCTION

The most commonly used accelerometers at the Underwater Explosions Research Division (UERD) produce an electronic time history of the applied acceleration at the output using piezoresistive or piezoelectric sensitive elements. Both of these accelerometer types are generally comprised of a spring mass system with a natural frequency to be measured. In the case of the piezoresistive type, a small mass is suspended on a cantilever beam to which strain gages are attached at key stress points. Motion imposed on the assembly cause the beam to flex and this translates to a change in resistance in the strain gages proportional to the input acceleration. Most often the strain gages are intentionally connected in a wheatstone bridge fashion with an external excitation voltage applied at opposite nodes of the bridge. A voltage proportional to the acceleration is then created between the remaining nodes when the instrument is disturbed. Piezoelectric accelerometers are similar to the piezoresistive types except that piezoelectric crystals are used in lieu of strain gages as the sensitive elements. A charge proportional to the input acceleration is generated at the output and a charge amplifier in the first stage of the signal conditioning electronics converts this to a voltage.

It is easy to see that with both types, if an accurate output proportional to the input is to be expected, substantial design problems have to be overcome and the quality of the output of early accelerometers reflected this. Because of the appearance of improved features, such as the use of semiconductor strain gages and stops to limit internal motions, fewer problems remain with every new generation of accelerometers. In the early seventies, when accelerometers were first integrated for shock test purposes, relatively few accelerometer designs were available and functional problems were generally tolerated. Instrument evaluation was chiefly done by the intercomparison of records made during real test situations. New manufacturers and improved designs using advanced technology have enlarged the overall population of accelerometer types and broadened the hazards of selection. It is no longer feasible to try each available design in real test work as the sole means of evaluation. A method for discerning between those which will produce satisfactory velocity records when integrated, and those which will not, inclusive of all reasons was needed.

An expedient method to determine a group of accelerometers to be undamaged without an expensive recalibration was also needed. In shock test work, the events of interest occur so suddenly and irrepeatedly, measurement devices must be known to be properly working prior to a test, or the resulting data could be interpreted as questionable or lost completely. Reused accelerometers that may have been damaged during a previous test might not exhibit any obvious symptoms of their true condition. The test procedure presented here was developed to meet these needs; to aid in accelerometer design evaluation and assess individual accelerometers prior to their use in gathering data from a test.

THEORY

When an accelerometer is fastened to a solid spring loaded bar, (See Fig. 1) and is allowed to drop striking against a hard elastic surface, the assembly will bounce repeatedly with decreasing displacements as the kinetic energy is absorbed by the inherent frictions until it finally comes to rest. The output from a properly working accelerometer would look similar to Fig. 2a.

If this output is integrated, a velocity pattern shown in Fig. 2b will result with the

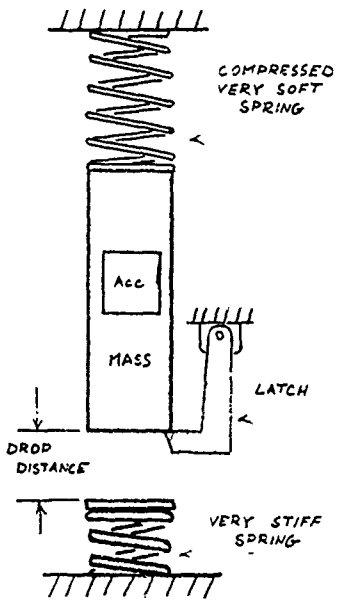

Fig. 1 - Conceptual Device for the Generation of Asymmetrical Acceleration

relative initial and final velocities equal to zero as they should be (assuming the laboratory has not undergone a significant velocity change during the test). Examining the physical input to the device, the actual acceleration history is composed of a series of high amplitude short duration accelerations separated by long periods of low amplitude accelerations in the opposite direction. This dissymmetry of the acceleration history presents an extreme test of the accelerometer's linearity. The areas which represent the velocities under the long negative low amplitude pulses must exactly cancel the areas of the sharp positive high amplitude pulses when these areas are summed after the unit comes to rest if the velocity of the bar assembly before and after the test is to be equal. Using this as a worst case input to the accelerometer, relative accuracy of these areas taken as the output from the accelerometer can be checked by adding them in an electronic integrator whose final value should be equal to and remain at its initial value.

Any relative errors or inconsistencies in the accelerometer output that alter these areas, will be summed and will appear as an offset at the output of the integrator. Hysteresis errors, which result in residual outputs from the accelerometer, when summed in the integrator will appear as an angular shifting of the output record and continued ramping of the integrator output base line after the accelerometer has come to rest.

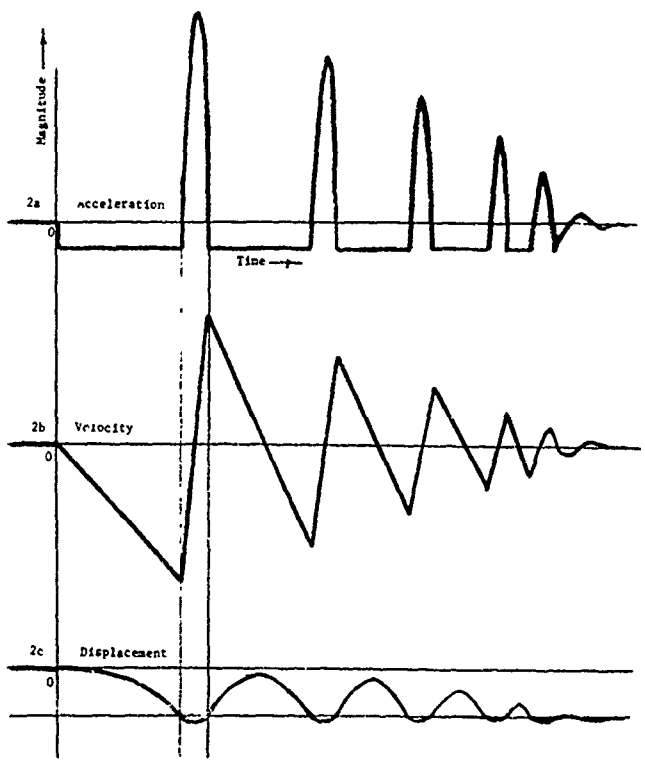

Fig. 2a, 2b, 2c - Acceleration, Velocity, and Displacement Characteristic Curves for the Acceleration Generator

TEST DEVICE

A detailed drawing and photo of our test device is shown in Figs. 3a, 3b, and 4. The base is a mild steel billet. The bar is also mild steel and has been machined at the top to properly accept the type of accelerometer under inspection. A slight spherical curvature is ground into the bottom of the bar such that the impacts will occur beneath the center of mass. To achieve results that are not misleading, care must be taken to insure that the motion of the bar and accelerometer assembly is truly along the vertical axis of interest and free from any significant horizontal or angular components. Four aluminum wires, seated in milled grooves and attached to support rods, constrain the bar to essentially vertical motion over the distance (less than 3/16 in.) that the bar assembly travels during the drop and subsequent bounces. A spring is hooked to a small clip welded on the bar loading it against the aluminum wires and against the billet surface.

The bar assembly is cocked by placing a small drill rod or rectangular metal stock between the bar and billet at the very edge of the bar separating them by a repeatable distance, equal to the thickness of the rod. This rod is quickly pulled back a small distance at the moment of test allowing the bar to drop. To insure a clean release, the bar has a flat filed into the spherical surface at the edge, and the rod or stock is slightly undercut.

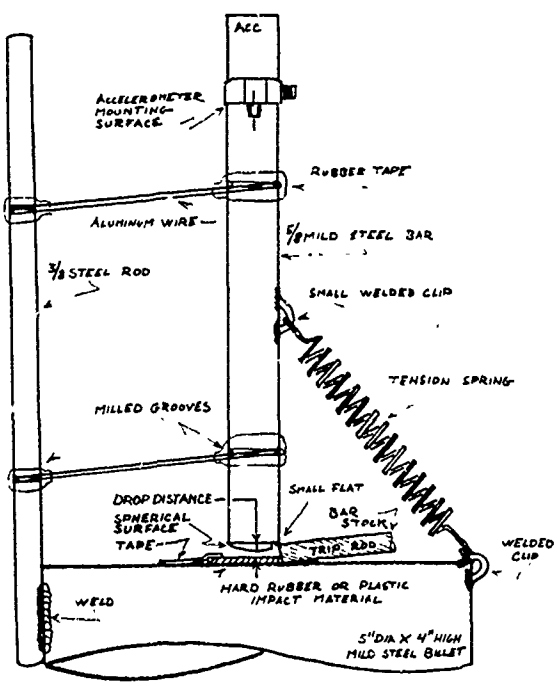

Figure 3a - Side View of Acceleration Generator

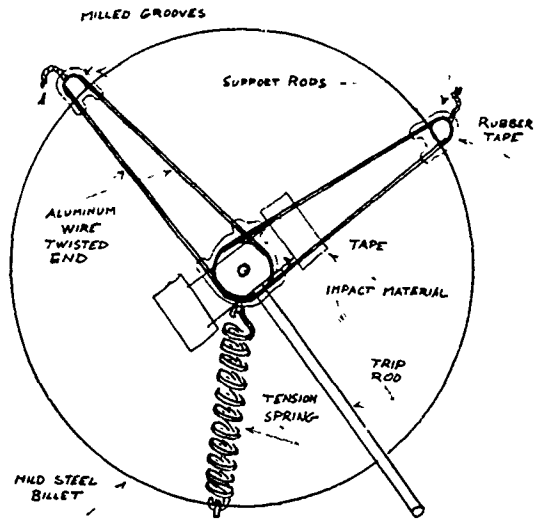

Figure 3b - Top View of Acceleration Generator

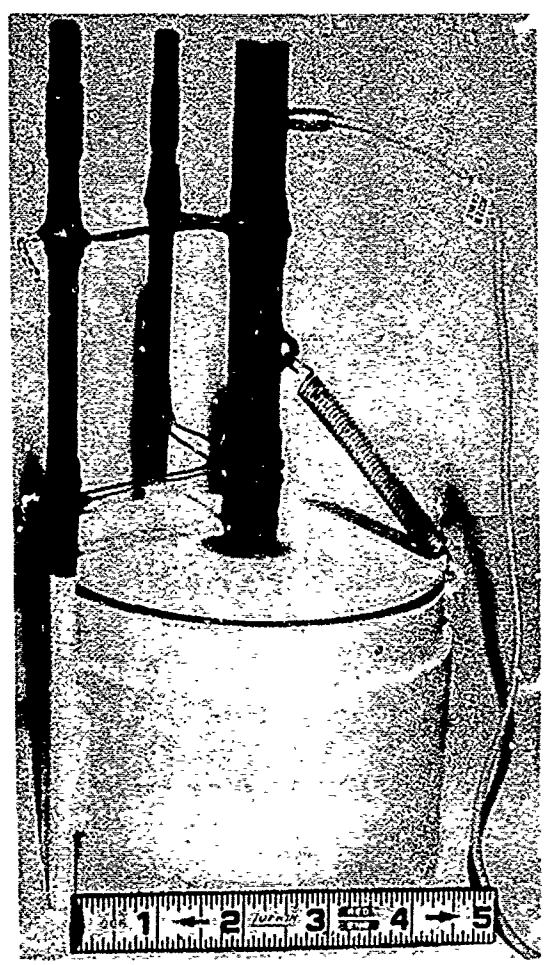

Figure 4 - Photograph of Acceleration Generator

With the accelerometer installed on the bar and connected to the appropriate signal conditioning electronics, the acceleration output is fed into a storage oscilloscope. Various elastic materials such as thin plastic or hard rubber are inserted between the bar and billet forming the impact surface. These are tried experimentally together with different rod thicknesses to achieve initial acceleration close to the upper range limit of the accelerometer, at least twelve or more significant bounces, and velocities as large as possible. This procedure must be done as part of the initial set-up for different accelerometers of the same designs. Once a good bounce pattern had been achieved, many accelerometers of the same design may be tested, observing the velocity record, with only occasional re-examination of the acceleration record.

Assuming a constant value for the initial acceleration to be sought, softer materials and large rods tend to yield high velocities but fewer bounces, while hard materials and small rods generally produce more bounces at the expense of velocity. Keep in mind the drop velocity must be large enough to be resolved from naturally occurring drifts within the integration systems used.

Using the mechanical device described, typical combinations of thin plastic or rubber impact materials and rod thicknesses between 1/8 and 3/16 in. will yield proper bounce patterns that return to zero velocity in 100 - 300 msec. An electronic integrator that will encompass this time plus sufficient final value observation time is presented here although other drop systems with longer bounce periods could demand longer integration times for satisfactory accelerometer evaluation.

A schematic for this integrator is given in Fig. 5.[1]*. Because the circuit inherently has a D.C. gain, accelerometers must be manually trimmed for less than 3 millivolts offset to avoid circuit saturation. With wheatstone bridge piezoresistive types, large fixed resistors placed in parallel across appropriate legs of the bridge will suffice. A circuit modification for the purpose of saving time using large fixed resistors and a multi-position switch has been tried with success. Any attempt by the author at placing a potentiometer type variable resistor anywhere ahead of the high gain input stage has resulted in intolerable output drift. The final balancing is accomplished using the first stage amplifier null adjustment.

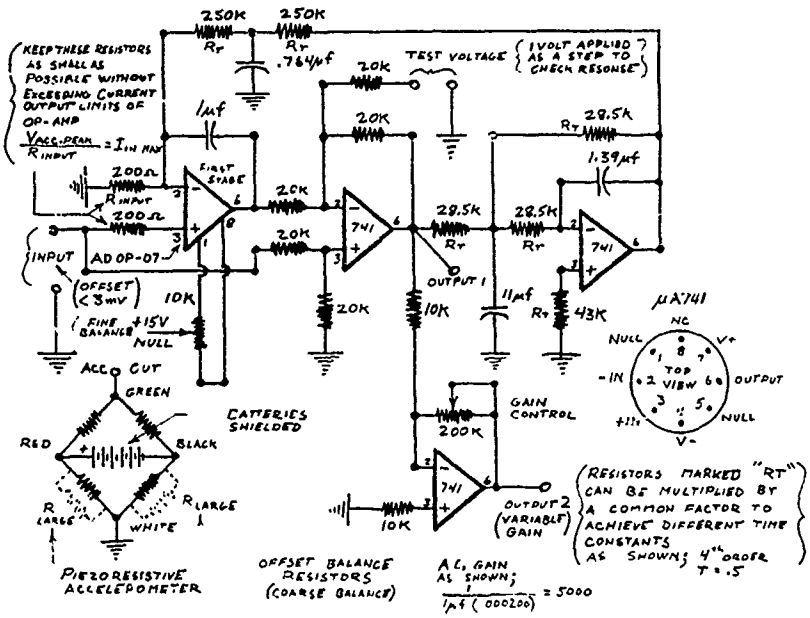

Figure 5 - Schematic for an Electronic Integrator with D.C. Gain

*List of references given on page 10.

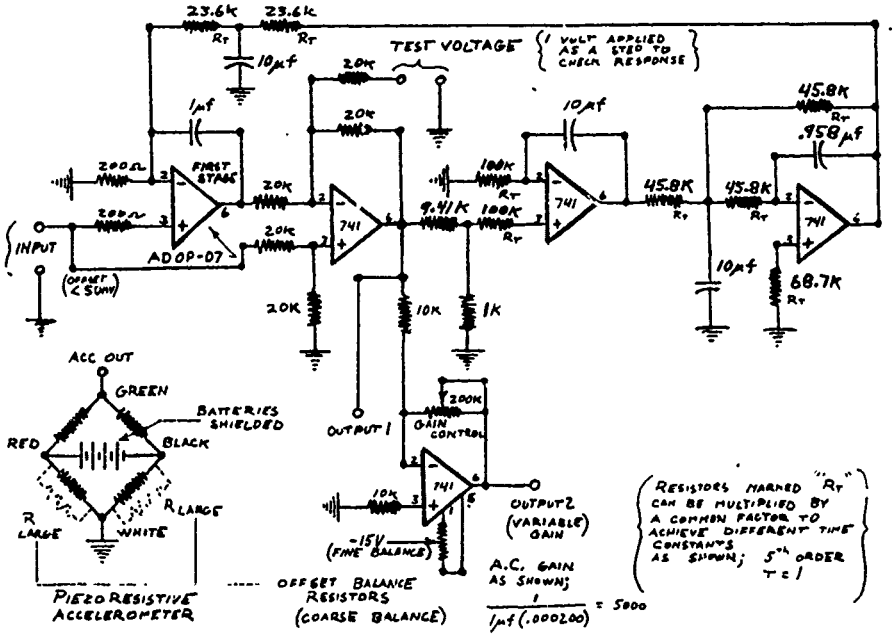

Figure 6 - Schematic for an Electronic Integrator with no D.C. Gain

An alternate circuit shown in Fig. 6 uses an additional feedback loop to eliminate the D. C. gain problem thereby allowing a much larger accelerometer zero offset. This circuit will self balance in several seconds which may save time when performing routine tests on many accelerometers of the same type. Looking at the frequency response curves in Fig. 7, one can readily see that the latter circuit is particularly sensitive to low frequency noise which will appear as a tendency for the output to drift around. Considering component value

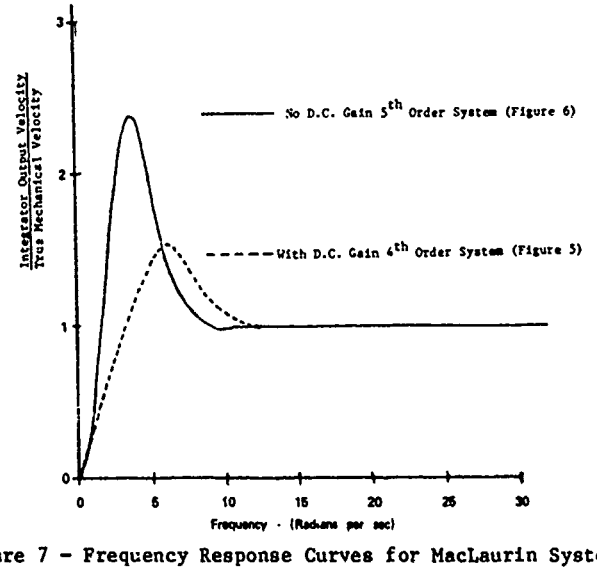

Figure 7 - Frequency Response Curves for MacLaurin System Integrators

changes due to temperature, electrical noise and operational amplifier driftiness, this circuit has only worked well using our test device when the actual sensitivity of the accelerometer was great enough to produce better than .2 volts output when operated near its maximum range. A test device capable of producing significantly larger velocities while maintaining a good acceleration pattern within the integrators time frame, would represent an improvement.

High quality low noise, low drift amplifiers and the use of quality fixed resistors are essential in the first stage of these integrators to make them sufficiently drift free to resolve good and poor city patterns with low sensitivity accelerometers. Shielding of the test apparatus may be necessary in some laboratory locations to reduce circuit drifts as will good connections between the electronics, base billet, accelerometer bar assembly, and release rod. Touching or loosing body contact with anything connected to the circuit, grounded or not, often introduce misleading drifts, and must be avoided in the release technique.

TEST PROCEDURE

It is prudent when initiating a test session to use a known good accelerometer first, checking the equipment. An acceleration record is generated and observed to verify the combination of rod thickness and impact material produce a pattern within a selected set of specifications (refer to Figs. 9, 10, and 15). A one volt step is applied at the integrators test point (refer to Figs. 5 and 6). The resulting output should resemble the corresponding impulse response as given in Fig. 8. The accelerometer is then connected to the integrator, and several drops are made as needed to reveal the repeatable character of the velocity pattern. When testing many accelerometers of the same design, they may be connected directly to the integrator once the system has been shown to be working. The integrators discussed are subject to occasional drifts, and it is a wise procedure to make several drops on each accelerometer avoiding the possibility of being misled by such a drift. Examples of typical velocity outputs generated by integrating good and poor accelerometers are given in Figs. 11 and 14.

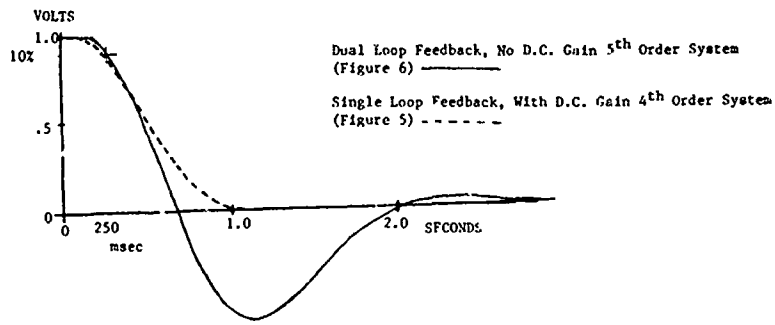

Figure 8 - Impulse Response Curves for MacLaurin System Integrators

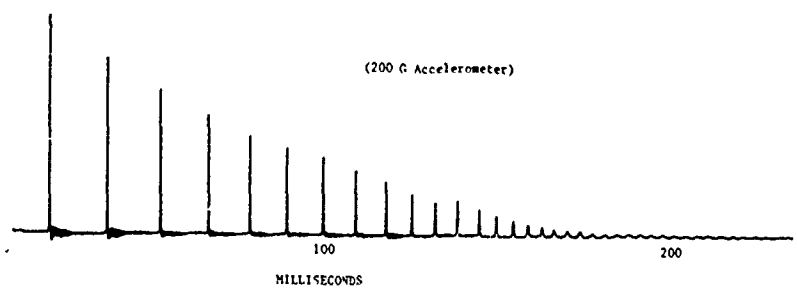

Figure 9 - Typical Acceleration Record Following Initial Set-Up

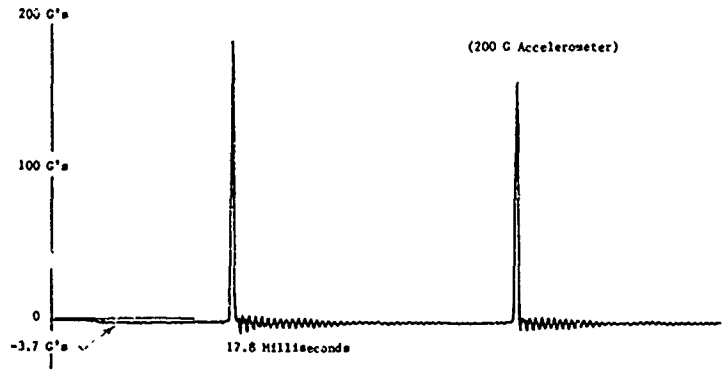

Figure 10 - Expanded View of Acceleration (Note the Initial Negative Acceleration)

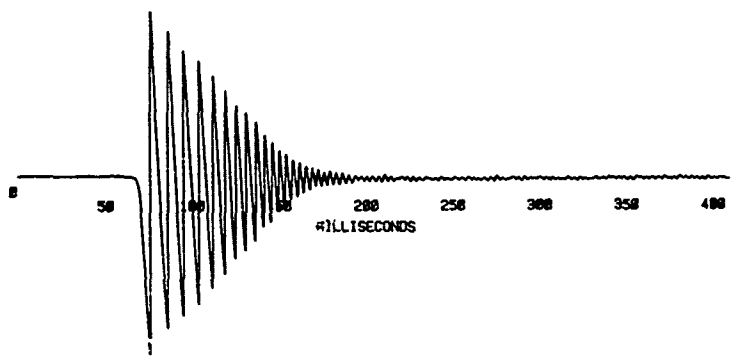

Figure 11 - Velocity Record Generated by Integrating a Properly Working Accelerometer (Note the Alignment of the Initial and Final Velocities)

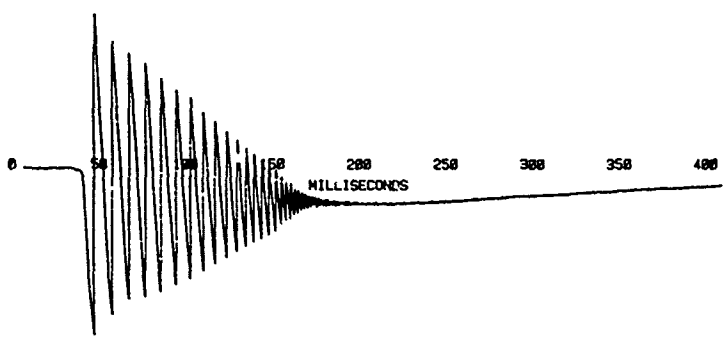

Figure 12 - Acceleration Integral with an Unacceptable Negative Offset (Note the Integrator Recovery Towards Zero)

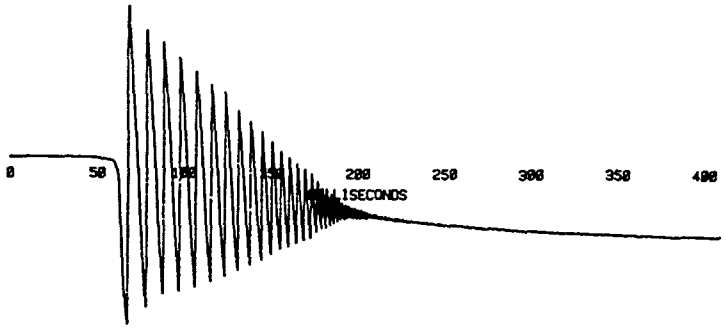

Fig. 13 - Acceleration Integral with an Unacceptable Negative Offset and Ramping

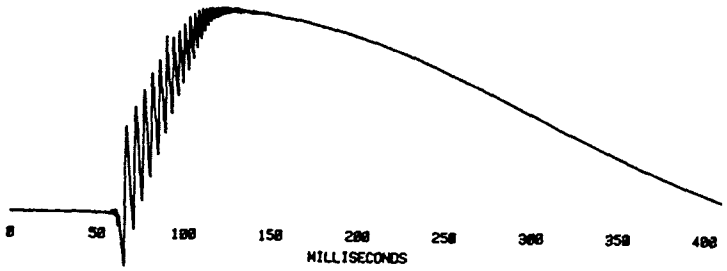

Fig. 14 - Acceleration Integral From a Damaged Accelerometer
(Note the Extreme Positive Offset)

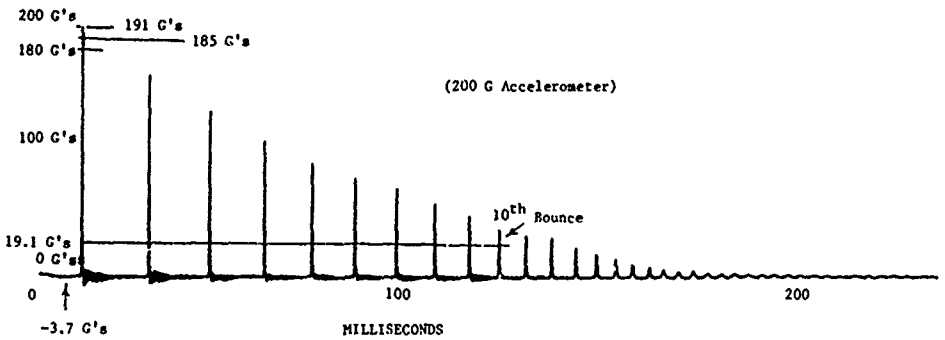

Fig. 15 - Specifications for the Input Acceleration

TEST SPECIFICATIONS

The need for an in-house, quantitative evaluation to support our own measurement standards has prompted the Instrumentation Group at Underwater Explosions Research Division of the David Taylor Naval Ship Research and Development Center (UERD/DTNSRDC) to develop certain specifications surrounding this test. The guidelines used in these specifications were adopted to keep the rigors of the test procedure to a minimum while resolving a standard we consider achievable at the present state of the art of accelerometer design. Presently, in our work, accelerometers with ranges smaller than 200 g are seldom used. These specifications apply to accelerometers with maximum inputs 200 greater.

PROCEDURE SPECIFICATIONS

1. The input to the accelerometer must be a series of large short duration accelerations separated by small long duration accelerations in the reverse direction with the largest acceleration having a magnitude at least 50 times greater than the small ones.

2. The first bounce must achieve an input acceleration between 90% and 100% of the upper range limit of the accelerometer being tested.

3. There must occur more than 10 bounces within 100 to 300 msec with the acceleration of the 10th bounce greater than 10% of the first bounce (refer to Fig. 15).

ACCELEROMETER SPECIFICATIONS

The accelerometer will be subjected to the inputs described, and the output will be accurately integrated into a velocity record. In the evaluation of the following, the largest peak to peak velocity transition, (generally the first) will represent 100%.

The final velocity must settle to within ± 2.5% of the pre-release velocity for at least 150 msec following the last peak to peak velocity transition less than 5% of the largest peak to peak velocity transition. Due to the residual bounces that are often present when measuring the final velocity, the mean value of the velocity transition at the point measured should be used. For more clarity, see Fig. 16.

ACCELEROMETER EVALUATION DISCUSSION

Often the differences between devices are obvious enough that qualitative decisions between which design is better or which one is not working can be easily made by a simple visual inspection of the velocity patterns. It has been the experience of the author that a batch of properly working accelerometers of one type will show no repeatable resolvable offset or ramping, whereas with another type, such as high temperature piezoelectric, every available accelerometer tested may exhibit similar problems such as a tendency to drift or to have an initial hysteresis. One particular device exhibited a horrendous offset and ramping on the first several tests, but it was noticed this condition improved with each drop. By the seventh or eighth test, the accelerometer had apparently "seasoned" and the errors were gone completely. All of the accelerometers of this design tested were found to behave this way, and whether shelf time would bring back the condition became a point of speculation.

At UERD different accelerometer designs are reviewed on a case to case basis with consideration towards the particular features offered and the job requirements. These observations must further be weighed against the ability of the design under scrutiny to meet our specifications accompanying this test. Generally we at UERD have found that records taken from accelerometers used in our type of work that do not come up to the specifications mentioned, when integrated, will result in velocity records with obvious flaws.

SUMMARY AND CONCLUSIONS

A method for quickly checking the integrability of accelerometers has been developed. The accelerometer under examination is mounted on a bar assembly which is allowed to fall and bounce repeatedly on a hard elastic surface until it comes to rest. Accelerations generated in this way are exceptionally unsymmetrical and present a worst case input to the accelerometer. An electronic integrator is used to convert the accelerometers output into a velocity history with a revealing characteristic pattern which should begin and end with zero velocity. Our experience with this test has found it to be sufficiently rigorous and inclusive to expose the existence of a majority of problems that might be inherent in a device, while remaining well adapted for checking large batches of accelerometers prior to installation. It can be expediently used to directly intercompare, and thereby evaluate different available accelerometer designs by the quality of their output. The mechanical apparatus, integrators, and specifications described herein present a working test system which will make possible the measurement of significant differences in integrability between accelerometer types. The specified equipment and techniques are provided for convenience to the reader, and are not intended to imply the exclusion of method refinements as needed to resolve a given standard achievable within the state of the art of accelerometer design.

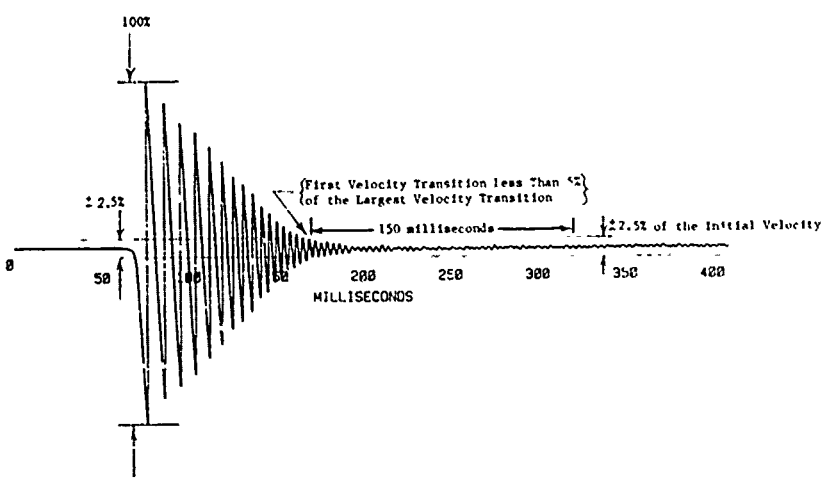

Figure 16 - Specifications for Accelerometer Integrability Test

REFERENCES

1. Gordon, John D., "Design of Stable Integration Systems for Motion Measurement," David Taylor Model Basin Report 3260 (Aug 1972)

SPECTRAL DENSITY ESTIMATES OF COARSELY QUANTIZED RANDOM VIBRATION DATA

Thomas J. Baca

Sandia National Laboratories
Albuquerque, New Mexico

The measurement of random vibration environments during flight testing of aerospace vehicles is usually accomplished by broadcasting analog signals via telemetery from the flight vehicle to a receiving station on the ground. At Sandia National Laboratories, digital telemetry systems are becoming attractive alternatives to traditional analog systems because they eliminate transmission noise and make more efficient use of telemetry bandwidth. A crucial decision must be made during the design of a digital telemetry system regarding the minimum number of bits in the word representing the digitized vibration signal. Utilizing fewer bits increases quantizing error but allows a greater number of measurement channels to be handled by the telemetry system. The objective of this paper is to assess the effect of low quantizing rates on auto-spectral density (ASD) estimates made on random vibration data. A 4-bit quantization scheme was evaluated by comparing the time histories and ASD estimates of the 4-bit data with those of the original data and an 8-bit version of the data. Three different types of random data were used for the comparison: 1) bandlimited white noise; 2) narrowband random; and 3) actual random vibration data obtained from an actual flight test utilizing a telemetry system. The study reveals that surprisingly accurate ASD estimates made using 4-bit data retain both the amplitude and frequency characteristics of the ASD of the original data. A simple reconstruction technique is introduced which makes the 4-bit quantized time history look more realistic.

INTRODUCTION

One major goal of a flight test program for an aerospace vehicle is to provide valid accelerometer data during flight. Flight test data are analyzed to characterize the random vibration environment experienced by the entire vehicle and its internal components. The prospect of gathering flight vibration data with digital telemetry (TM) systems has important implications for the final data analysis. This paper addresses one basic telemetry system design parameter, namely, the quantizing resolution which is required during conversion from an analog to a digital representation of the measured vibration data. A comparison of a coarse (4-bit) and a more refined (8-bit) quantization scheme is described which demonstrates the effect of the quantization process on the final spectral analysis of the data. The results of this study provide a good example of how a firm understanding of the ultimate use of telemetered flight test data is crucial to the most efficient design of the telemetry system itself.

* This work was sponsored by the U. S. Department of Energy under Contract No. DE-AC04-76-DP00789.

DIGITAL TELEMETRY SYSTEMS

Flight test instrumentation systems designed at Sandia National Laboratories typically utilize continuous analog telemetery data links (i.e., FM trasmitters and receivers using voltage controlled oscillators, VCO's) for passing accelerometer data measured in flight to recording stations on the ground. The engineer responsible for transforming the raw vibration data into an environmental definition converts the analog signals into a digital representation which has engineering units (e.g., g's for acceleration) and which can undergo additional computerized analysis. The digitization process may be repeated if different conversion parameters are desired. The ability to view the raw analog signal generated by the telemetry system and the flexibility of re-digitizing the data are two reasons why engineers responsible for analyzing flight vibration data are reluctant to depart from the use of VCO data.

The tradition of using VCO's to measure flight vibration data is now being challenged by TM designers who advocate the transmission of data in digital form. New telemetery system designs that include the capability to transmit digital data must provide an on-board analog-to-digital (A/D) conversion capability. Such a digital telemetry system is highly advantageous in three ways. First, in flight A/D conversion eliminates sources of noise contamination introduced by transmitting, receiving, and recording an analog VCO signal. Second, TM bandwidth can be used more efficiently with digital data than analog data to send the same amount of information. Finally, digital TM systems offer more flexibility than analog TM's in selecting the dynamic range of the measured data and in allowing for on-board data processing (e.g., peak detection, Fast Fourier Transform calculation, and root-mean-square estimation) because they can be programmed to handle configuration changes, while an analog system requires hardware modification to achieve the same effect.

One aspect of the digital TM design is so basic that it is not subject to change without hardware replacement. The A/D conversion process for the accelerometer output signals has to be defined early in the design of the telemetry system in terms of two parameters: sample rate and quantization resolution. The selection of a sampling rate is dictated by the maximum frequency content of the analog signal which must be preserved. Quantization defines the number of possible digital values which the analog signal can assume when it is sampled. Once a sampling rate is chosen, efficient use of the available transmission bandwidth of the digital telemetry system requires that the minimum number of quantization levels be used during A/D conversion. As far as the measurement capability of the entire TM system is concerned, this means that more measurements can be made on the flight test vehicle if the number of quantization levels is reduced significantly.

A reduction of the number of quantization levels, however, cannot be done arbitrarily. The data analyst responsible for specifying analysis techniques for flight random vibration data must assess the effects of such changes. Implementation of this assessment process motivated the work discussed in this paper. Specifically, a TM design decision had to be made at Sandia National Laboratories regarding the effects of coarse quantization on spectral density estimates of random vibration data. A coarse quantization scheme could only be deemed acceptable if it did not significantly alter the random vibration spectral density estimates used to characterize the flight environments of the flight test vehicle.

DIGITAL QUANTIZATION

Quantization involves assigning a numerical value to a sampled analog signal. Since the digital values are stored and transmitted in binary, the number of possible digital values are expressed in bits, where N bits implies 2**N different values. For example, a 4-bit system has 16 assignable values, while an 8-bit system has 256 available values. In the 4-bit system with a +/- 10 g operating range, the sequence 0000, 0001, 0010, ..., 1111, represents the values: -10 g, -8.75 g, -7.5 g, ..., 10 g. The 8-bit system has more resolution because it has more binary combinations to use in representing the digitized signal (e.g., 00000000, 00000001, 00000010, ... 11111111 represent -10 g, -9.92 g, -9.84 g, ..., 10 g). Normally, 10-bit or 12-bit quantizaton is used in a regular A/D conversion process. This high degree of resolution eliminates concern over the effects of quantization error during random vibration analysis. The reason the 4-bit quantization is referred to as being "coarse" is shown by a comparison of Figures 1 and 2. Figure 1 shows what might be a typical random vibraton time history. Figure 2 shows the effect of 4-bit quantization on the time history in Figure 1. It is not surprising that most engineers given the task of analyzing the data in Figure 2 would decline, arguing that the available data are hopelessly corrupted by coarse quantization. The nature of quantization error is discussed in the next section.

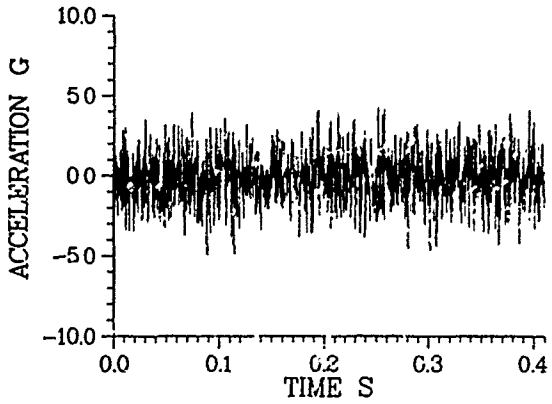

Figure 1 Original Random Vibration Time History.

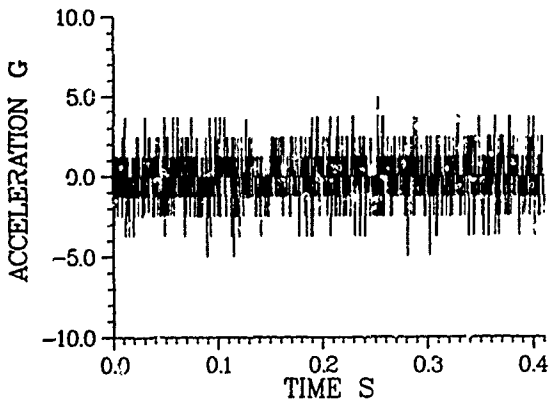

Figure 2 Coarsely Quantized Random Vibration Time History.

QUANTIZATION ERROR:

Both the time and frequency domain implications of quantization error need to be examined in the context of analyzing telemetered random vibration data. In the time domain, one valid concern with this 4-bit system centers on the relationship between the degree of quantization error and the size of the quantization intervals. The size of these intervals q is determined by dividing the full calibration range of the accelerometer by the number of quantization levels:

$$q = \frac{2 * CAL}{2 ** N} \qquad (1)$$

where CAL is the calibration level of the accelerometer channel (zero-to-peak) and N is the number of bits used in quantization. The symbols * and ** denote multiplication and exponentiation, respectively. Assuming that the quantization error e is uniformly distributed between -q/2 and q/2, it can be shown (Reference 1) that the root-mean-square quantizing error e-rms is given by:

$$e\text{-rms} = \frac{q}{\sqrt{12}} \qquad (2)$$

This relationship was used to construct Figure 3 which shows how the rms quantizing error varies as a function of bits for different calibration levels. The e-rms quantizing error of 0.361 g on a +/- 10 g channel with 4-bit quantization is only 3.6 percent of the calibration level of the channel. Assuming the measured signal is within the valid range of the channel, a relatively low amplitude error is generated in a typical flight vibration time history by coarse quantization.

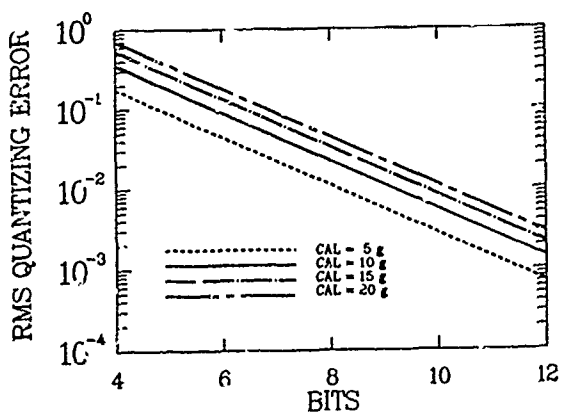

Figure 3 RMS Quantizing Error as a Function of the Number of Bits in the Quantizing Scheme for Different Channel Calibration Levels of +/- 5, 10, 15, 20 g.

Simulation studies of different levels of quantization resolution showed that the theoretical e-rms values given by Equation 2 and those generated during the simulations differed by only one percent or less. Still, it is important to note that the assumption of uniformly distributed quantization error becomes less valid if the number of quantization bits is reduced further. (See References 2 and 3.)

It must be recognized that a digitized time history is subject to the same potential errors as an analog channel if the measured signal is very small or very big relative to the calibration range of the channel. If the measured signal is too small, a poor signal to noise ratio exists in the analog system, and the signal may not exceed the first quantizing level in the digital system. Should the signal exceed the calibrated range of the channel, then both the analog and digital time histories are rendered useless by the clipping of the measured signal.

The frequency domain manifestations of quantization error can be seen by estimating the auto-spectral density (ASD) of the time history in Figures 1 and 2. The time history in Figure 1 is Gaussian distributed white noise which has a 10,000 samples per second sample rate and which has been lowpass filtered at 2 kHz. ASD estimates were made using Welch's method (Reference 4). The ASD estimate in Figure 4 shows a flat spectral characteristic of white noise. A normalized frequency axis is used to show the entire frequency content of the signal which can be represented for the specified sampling rate (i.e., 0.5 Hz-s corresponds to half of the sampling rate and is the Nyquist frequency of 5,000 Hz). The roll-off in the ASD at ~0.2 Hz-s reflects the lowpass filter applied to the data. The ASD estimate for the 4-bit quantized data in Figure 5 shows that spectrum in the 0-0.2 Hz-s range has not changed significantly, but there has been a uniform addition of spectral content over the remainder of the frequency range.

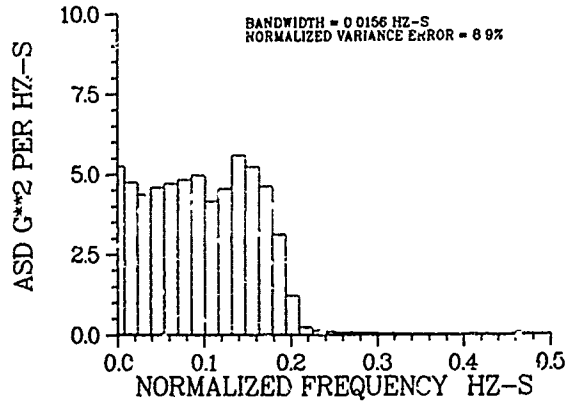

Figure 4 ASD Estimate of Original Random Vibration Time History in Figure 1.

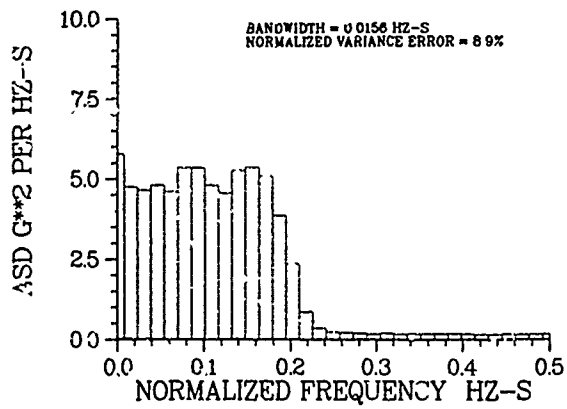

Figure 5 ASD Estimate of Coarsely Quantized Data in Figure 2.

The white noise character of the quantization error can also be seen by computing an ASD estimate for the quantization error e. Figure 6 shows the time history for quantization error between the bandlimited white noise in Figure 1 and the coarsely quantized version of the same data in Figure 2. Figure 7 reveals the white spectral content of the quantization error. Note that the magnitude of this quantization error ASD is governed by the overall e-rms value given in Equation 2 because the square root of the area under the ASD plot equals the e-rms of the time history being analyzed. In equation form:

$$\sqrt{\text{e-asd}_{W} * SR} = \frac{q}{\sqrt{12}} \qquad (3)$$

where e-asd$_W$ is the ASD spectral value for the white noise quantization error, SR is the sample rate of the data, and q is the quantization interval size given in Equation 1. Substituting Equation 1 in Equation 3 leads to the following expression:

$$\text{e-asd}_{W} = \frac{CAL^{**2}}{3*SR*2^{**(2N)}} \qquad (4)$$

where SR is equal to 1 in the normalized frequency plots in Figure 7. The average spectral value of 0.1307 g**2/Hz-s is observed in Figure 7. This agrees closely with the result predicted in Equation 4 which is 0.1302 g**2/Hz-s. Equation 4 suggests one way of reducing the error contribution to an ASD estimate in a digital telemetry system is to increase the sampling rate so that the spectral contribution of the quantization error spectrum is spread over a wider frequency range, resulting in a lower ASD level in the frequency range of interest.

Thus, quantization error in a 4-bit coarsely quantized time history has two predominant effects. First, the time history acquires a blocked appearance indicative of the quantizing levels. Second, the error is manifested in the frequency domain as the addition of white noise. Initial indications are that for the purpose of analyzing vibration data, the significance of the quantization error in terms of contribution to overall g-rms in the time domain and the ASD spectrum level in the frequency domain is relatively small for 4-bit quantized data.

TIME HISTORY RECONSTRUCTION

An improvement to the coarse 4-bit digital conversion process can be made by removing the higher frequency portions of the quantization

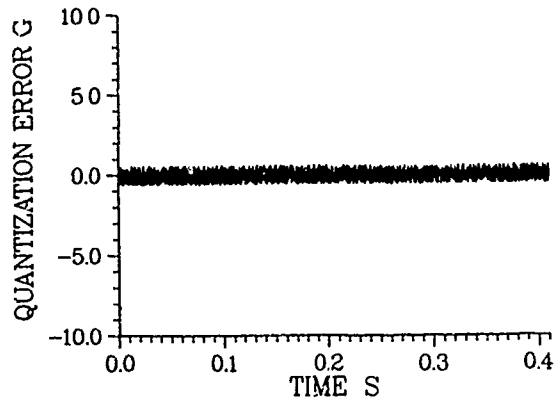

Figure 6 Quantization Error Time History for 4-bit Quantization in Figure 2, (i.e., Fig. 6 = Fig. 2 - Fig. 1).

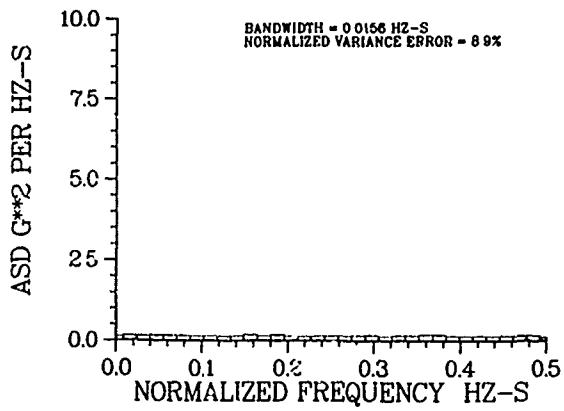

Figure 7 ASD Estimate of Quantization Error Time History in Figure 6.

error spectral density. Another zero phase shift lowpass filtering operation is carried out on the coarsely quantized data to achieve this effect. Figure 8 shows that this final filtering at ~2.4 kHz acts to reconstruct the time history so that it is very similar to the original data in Figure 1. (Note that final filtering was carried out at a higher cut-off frequency to minimize the effect of the second filtering operation on the data in the 0 to 2 kHz range.) The high frequency contribution of the quantization error has been eliminated as shown in Figure 9. Note the similarity between Figure 9 and Figure 4, indicating that the 4-bit quantized data can produce a spectral density estimate which is quite similar to that of the original data.

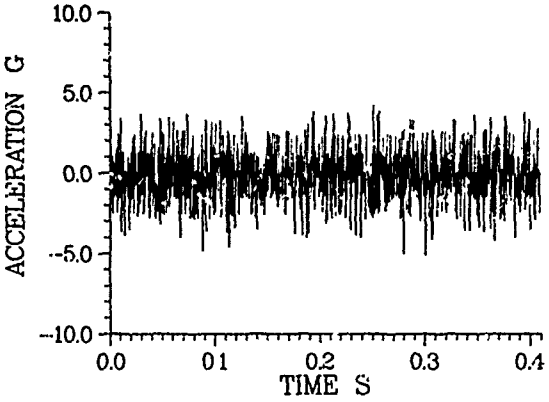

Figure 8 Result of Time History Reconstruction Technique Applied to the 4-bit Coarsely Quantized Data in Figure 2.

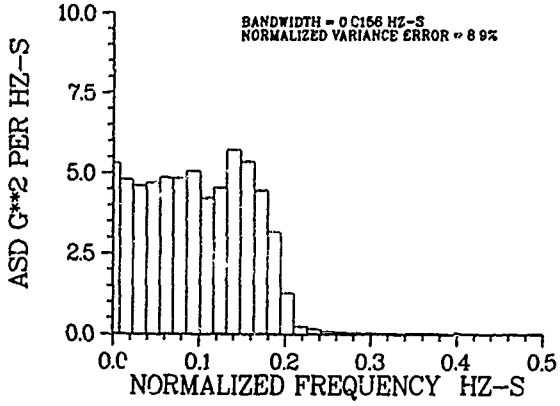

Figure 9 ASD Estimate for 4-bit Reconstructed Time History in Figure 8.

4-BIT VS 8-BIT COMPARISON

The coarse 4-bit quantization scheme was evaluated further by comparing the time histories and ASD estimates of the 4-bit reconstructed data with those of an 8-bit version of the data. The 8-bit quantization scheme was chosen because it was one possible design option suggested by TM designers at Sandia. Three different types of random data were used for the comparison: 1) bandlimited white noise; 2) narrowband random; and 3) actual random vibration data obtained form an actual VCO channel. The 4-bit and 8-bit data are juxtaposed in Figures 10-15. The comparisons are made between the 4-bit and 8-bit data in terms of: a) the time histories; b) the ASD estimate; and c) a plot of the difference between the ASD estimates of the quantized data and the original data.

BANDLIMITED WHITE NOISE: Generation of the Gaussian distributed white noise was discussed previously. Figures 10 and 11 show time and frequency domain agreement between the 4-bit reconstructed data and the 8-bit quantized data. The ASD difference plots in Figures 10c and 11c reveal that even though the error in the 4-bit ASD estimate is greater than the 8-bit data, it is still only 5 to 10 percent of the actual ASD level. This percentage is acceptable, particularly because first, it is evenly distributed over all frequencies, and second, because it is not much larger than the normalized variance error of 8.9 percent for the ASD estimate.

NARROWBAND RANDOM VIBRATION: The narrowband random vibration data were simulated on a 10 g channel by convolving the impulse response function of a viscously damped single-degree-of-freedom (SDOF) oscillator having a natural frequency of 0.1 Hz-s (1000 Hz for the sample rate of 10 kHz), with Gaussian distributed white noise. The resulting time history was then bandlimited to 2 kHz by zero phase shift lowpass filtering. Once again, the 4-bit reconstructed and 8-bit time histories (Figures 12a and 13a) are very similar in character. The ASD plots in Figures 12b and 13b appear indistinguishable because of the large dynamic range of the ASD estimates. Difference error plots in Figures 12c and 13c reveal that the error in the 4-bit data is greater than the error in the 8-bit data, but the error is less than 0.5 percent at the frequency range of peak response. The 4-bit reconstructed data does an excellent job of preserving the character of the ASD plot of the narowband random data.

ACTUAL VCO FLIGHT DATA: Figures 14 and 15 compare 4-bit reconstructed and 8-bit quantized data from acceleration measurements made with a telemetry system using a 4kHz VCO channel. The "original" form of the data was a 12-bit quantized time history sampled at 20 kHz. Once again the 4-bit reconstructed data provide an ASD estimate for the flight vibration environment which is accurate in terms of both magnitude and frequency content. Note that in order to be consistent with the analysis method used on actual flight data, the ASD estimates in Figures 14b and 15b express frequency in Hz, instead of normalized frequency units of Hz-s which were used previously.

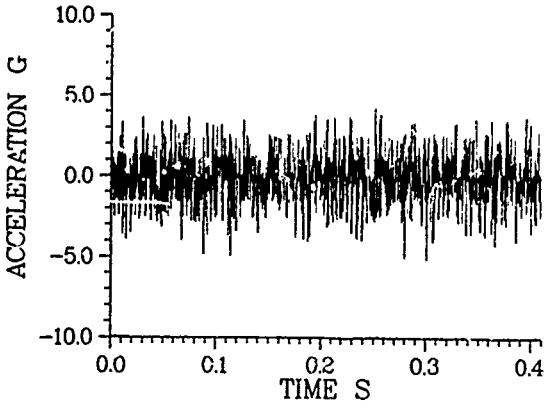

Figure 10a Reconstructed 4-Bit Time History of Bandlimited Gaussian White Noise.

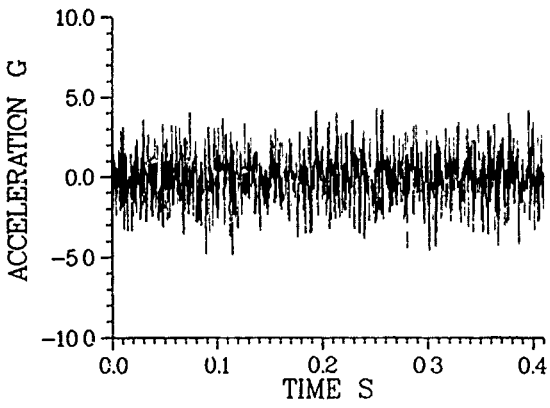

Figure 11a 8-Bit Quantized Time History of Bandlimited Gaussian White Noise.

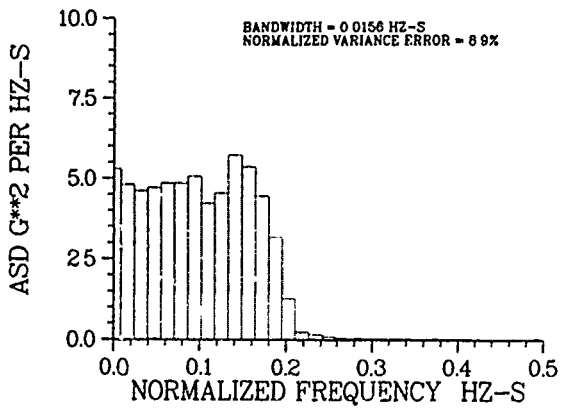

Figure 10b ASD Estimate for 4-Bit Reconstructed Bandlimited Gaussian White Noise.

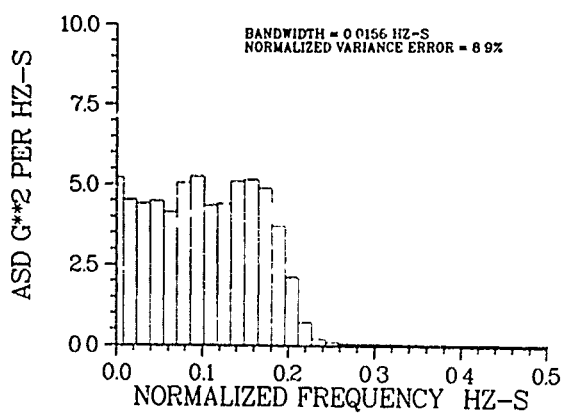

Figure 11b ASD Estimate for 8-Bit Quantized Bandlimited Gaussian White Noise.

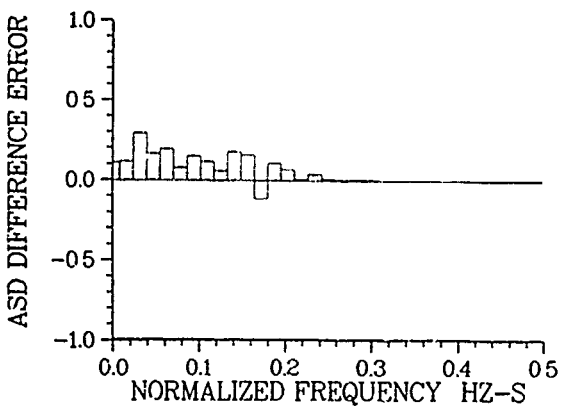

Figure 10c ASD Difference Error between 4-Bit Reconstructed and Original Bandlimited Gaussian White Noise.

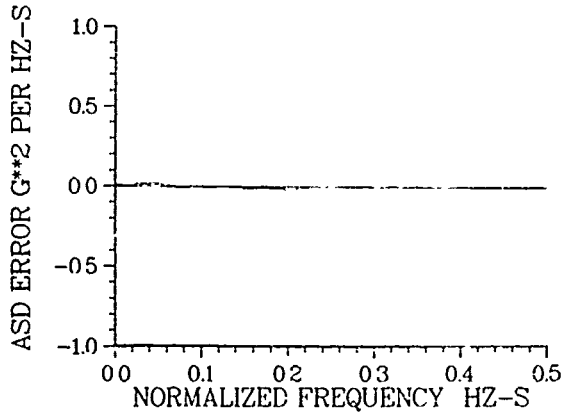

Figure 11c ASD Difference Error between 8-Bit Quantized and Original Bandlimited Gaussian White Noise.

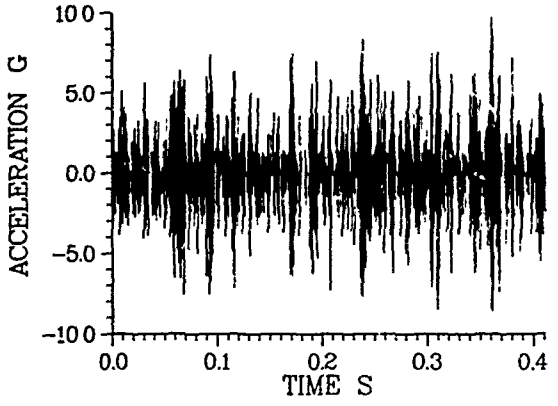

Figure 12a Reconstructed 4-Bit Time History of Simulated 1 KHz SDOF Data.

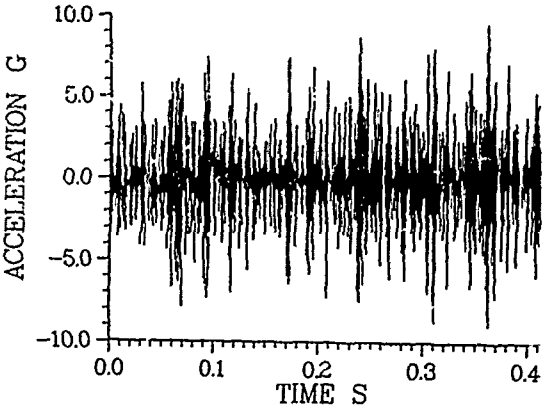

Figure 13a 8-Bit Quantized Time History of Simulated 1 KHz SDOF Data.

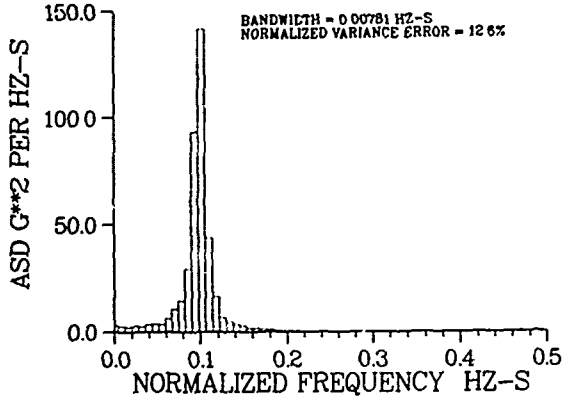

Figure 12b ASD Estimate for 4-Bit Reconstructed Simulated 1 KHz SDOF Data.

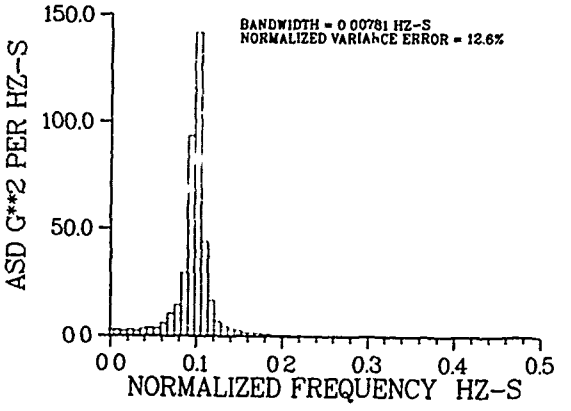

Figure 13b ASD Estimate for 8-Bit Quantized Simulated 1 KHz SDOF Data.

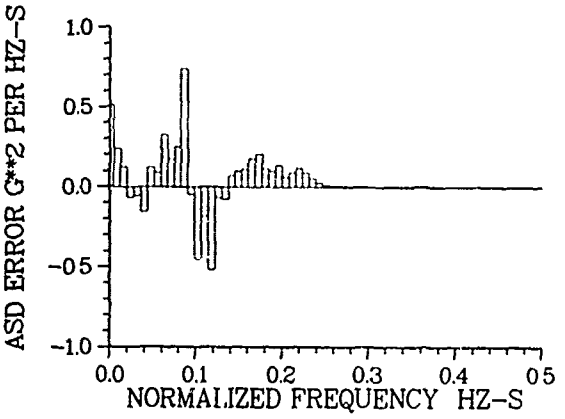

Figure 12c ASD Difference Error between 4-Bit Reconstructed and Original 1 KHz SDOF Data.

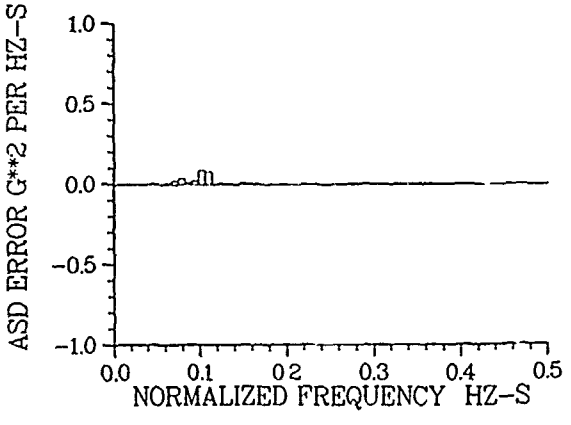

Figure 13c ASD Difference Error between 8-Bit Quantized and Original 1 KHz SDOF Data.

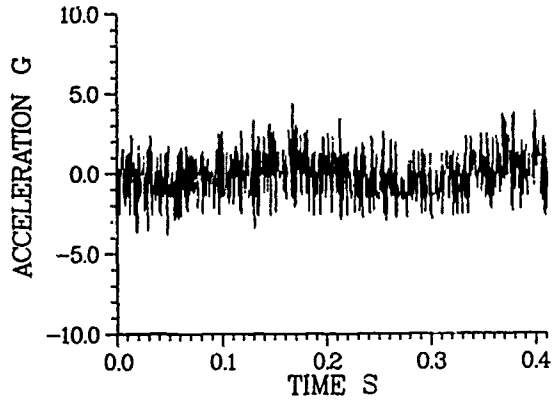

Figure 14a Reconstructed 4-Bit Time History of VCO Random Vibration Data.

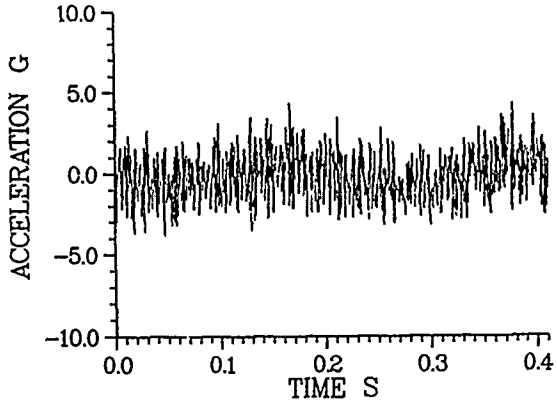

Figure 15a 8-Bit Quantized Time History of VCO Random Vibration Data.

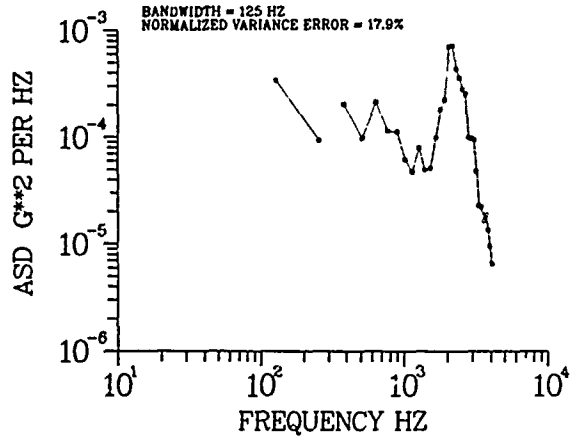

Figure 14b ASD Estimate for 4-Bit Reconstructed VCO Random Vibration Data.

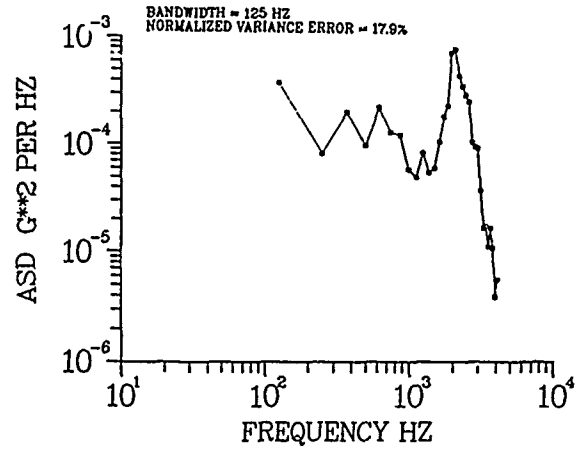

Figure 15b ASD Estimate for 8-Bit Quantized VCO Random Vibration Data.

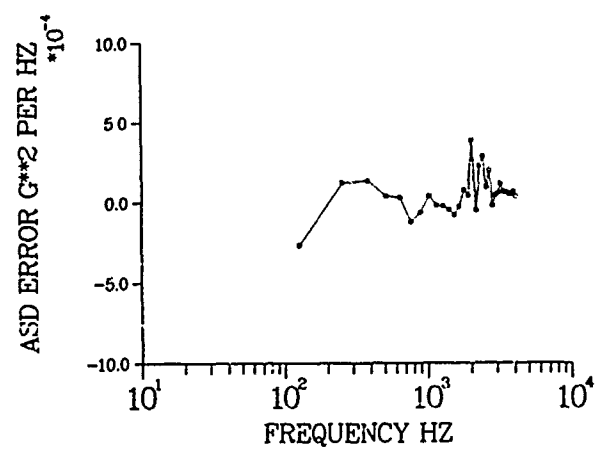

Figure 14c ASD Difference Error between 4-Bit Reconstructed and Original VCO Random Vibration Data.

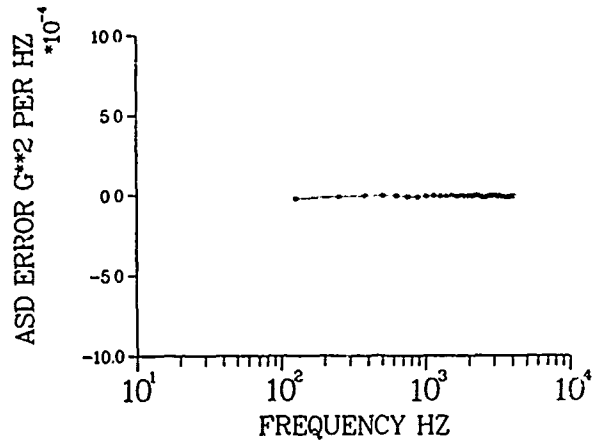

Figure 15c ASD Difference Error between 8-Bit Reconstructed and Original VCO Random Vibration Data.

CONCLUSIONS

ASD estimates of vibration data digitized using a 4-bit quantization scheme are acceptable for characterizing random vibration environments measured on digital flight test telemetry systems. A reconstructed time history which is very similar to the original data can be created using the method described in this paper. The overall effect of 4-bit quantizing on typical vibration signals is to add noise power uniformly over the entire frequency spectrum of the digitized data. This quantizing error power contribution has been shown to be small enough to be negligible for purposes of characterizing random vibration environments. Care must still be used with the ocarsely quantized data to make sure that data does not exceed the calibration range of the measurement channel. Practically, this means that a peak detector should be incorporated in the telemetery system design. The quantization error evaluation methods utilized in this study are significant because they demonstrate the ability of the coarcely quantized 4-bit data to provide nearly the same time histories and ASD estimates as finely quantized random vibration data.

In a more general sense, the error analysis study described in this paper demonstrates the importance of evaluating the impact of digital telemetry system design parameters on the analysis of random vibration data. Only by developing an understanding of the final use of the telemetered data can the TM designer and data analyst work together to develop a telemetery system which will provide data needed to define flight vibration environments in todays aerospace vehicles.

REFERENCES

1. Stearns, S. D., Digital Signal Analysis. Rochelle Park: Hayden, 1975.

2. Jayant, N. S., and P. Noll, Digital Coding of Waveforms: Principles and Applications to Speech and Video, Englewood Cliffs: Prentice-Hall, 1984.

3. Sripad, A. B., and D. L. Snyder, "A Necessary and Sufficient Condition for Quantization Errors to be Uniform and White," IEEE Transactions on Acoustics, Speech, and Signal Processing, Vol. ASSP-25, No. 5, October 1977, pp. 442-448.

4. Welch, P. D., "The Use of Fast Fourier Transform for the Estiration of Power Spectra: A Method Based on Time Averaging Over Short, Modified Periodograms," IEEE Transactions on Audio and Electroacoustics, Vol. AU-15, June 1967, pp. 70-73.

A QUANTITATIVE METHOD FOR EVALUATING SENSOR LAYOUTS

T. F. Chwastyk
Naval Sea Systems Command
Washington, D. C.

and

D. G. Rapp
Westinghouse Electric Corporation
Bettis Laboratory
West Mifflin, PA

The layout of sensors to measure shock response has traditionally been performed on an "engineering judgment" basis and typically has been done only with the intent of directly measuring local effects, e. g. stress intensity in a highly loaded area. Little appears to have been done to use data from widely distributed sensors to verify broad patterns of structural response predicted by analysis.

This paper gives a quantitative method for evaluating the use of sensors widely distributed over a structure to confirm and measure the amplitude of the dominant loading response patterns predicted by analysis. Application of this method to plausible traditional sensor layouts often shows surprisingly inefficient use of sensor channel capacity. Improved sensor layouts are readily achieved. The use of this method allows designing sensor layouts to guard against isolated errors either in sensor performance or in modeling. It also allows ready extrapolation of sensor results to uninstrumentable areas, with a quantitative estimate of the uncertainty in estimated values due to sensor noise or modeling inaccuracy.

INTRODUCTION

Both accelerometers and strain gages are used to measure the response of structures or components during shock tests. In the past, because only a limited amount of instrumentation was available, only a very few sensors were assigned to any given component. For more recent tests, data acquisition systems have been improved significantly so that several hundred sensor signals can be recorded for each test shot. As a result, it is now reasonable to assign enough sensors to high interest components to resolve superimposed shock response characteristics not directly measurable by any single sensor. In some cases, it is warranted to include more sensors than there are response characteristics to be resolved, and thereby incorporate some measurement replication to verify the consistency of the data. The problem is to select the best sensor layout for measuring the shock response characteristics of interest.

This paper describes a general, quantitative method that has been developed to evaluate sensor layouts for which the shock response characteristics are linearly related to the sensor readings. With this method, different sensor layouts can be evaluated (a) to verify that all response characteristics of interest are resolvable, (b) to determine the extent of "aliasing" or interference from response characteristics not of interest, (c) to determine how much consistency checking is provided for each sensor, and (d) to see how much normal sensor noise shows up in the resolved response characteristics. Examples are included to show how this general method was used to evaluate three different types of sensor layouts. In the first type of layout to be evaluated, strain gages are used to measure forces and moments in thin-walled cylindrical components. The second type of layout to be evaluated involves the use of accelerometers to determine the linear and angular accelerations at the Center of Gravity (CG) of a

rigid body. The last type of sensor layout to be evaluated utilizes accelerometers to measure the shock response of a flexible body in terms of its normal modes of vibration.

FUNDAMENTAL CONCEPTS

Improvements in computer and instrumentation technology have led to larger and more detailed analytical models and increased numbers of sensors. However, sensors have typically been assigned to measure local responses in areas where analysis predicts cause for concern, and prediction vs. measurement comparison has typically centered on local peak values only. Such peak level comparisons are quite sensitive to the influence of localized modes affecting the sensor location, as well as to phasing errors in modal combination rules, and do not try to confirm or take advantage of modeshape information fundamental to many analyses. On the other hand, most of the response energy tends to remain concentrated in a few global modes affecting broad areas throughout the component or structure. This is true even when modeling detail is increased permitting large numbers of modes. Thus, this paper is based on work intended to confirm the accuracy of the basic modeshape and modal amplitude predictions of the model for the dominant global modes. Resolution of such global modes permits extrapolation of global effects to uninstrumentable areas, and is useful in isolating and providing a better picture of the effects of localized modes that cause concern in isolated high response areas of the component. Although the method was developed primarily to resolve traditional vibration modal information, it has been found equally applicable to nonvibration work as well, to resolve the effects of superposed distinct loading cases.

Modal Description versus Point-by-Point Description: A system response to external inputs can often be analyzed by identifying characteristic patterns or "modes" of response of the system. The analyst can calculate the extent to which each mode will respond to a given input, and then superpose the individual modal responses of the system to obtain an overall system response. The advantage of the modal approach over the brute-force approach of treating all point parameters in the system individually is that for repetitive treatment of many different inputs, redundant information is minimized; the number of modes necessary for reasonably accurate system response calculations in the areas of greatest interest is typically far smaller than the number of system point parameters that would have to be treated individually.

NOTE: The "modes" used to describe the system response need not necessarily be modes of vibration; all that is necessary is that each mode have associated with it a constant "modeshape" describing the relative response of each system point parameter, so that the modal response of a large number of point parameters can be described by a single variable (the modal amplitude). Thus, a nondynamic model of a beam might be described by six modes of response - one axial mode, two transverse shear modes, two transverse bending modes, and one torsional mode.

Sensors Give Point Parameter Measurements: A basic problem in applying modal techniques to test data is that sensors generally do not measure quantities attributable to a single mode; rather, each sensor measures the effect on a given point parameter of all modes superposed. The particular point parameter measured depends on the type of sensor (e. g., strain gage, accelerometer, hydrophone), its location in the system, and typically on its orientation. Orientation is significant if the measured parameter is part of a vector or tensor field, e. g., acceleration or strain, and can be neglected only when the parameter field is scalar (e. g., temperature, pressure, voltage). In general, the parameters of interest are sensitive to sensor orientation. A brute-force point-by-point approach to measure system response would require sufficient sensors at every point to measure all parameters of interest at each point. This is obviously impractical because of the large number of sensors required and is inefficient as well; from a modal standpoint, much of the sensor data could be shown to be redundant. In addition, systems frequently contain points which, while essential to analysis, are inaccessible or otherwise impractical to instrument.

Sensor Layouts Sample the System Response: While fully instrumenting every system point parameter is not practical, it is usually possible to find a small representative subset of the system point parameters which are both accessible for measurement and sufficiently diverse that the amplitudes of the desired modes can be resolved unambiguously when the system response is sampled only for these representative point parameters. The sensor layout determines what portions of the system response are actually sampled, both for the total response measured by the sensors and for the desired modal responses making up the total. For a given sensor layout, each mode of response will have associated with it a "sensor modeshape" indicating the response of each sensor to

the presence of a unit modal amplitude response in that mode.

Sampling Quality Determines Confidence in Inferred Response at Uninstrumented Points: For a given sensor layout and a consequent set of sensor modeshapes, a matrix can be generated which transforms any set of actual sensor readings into least-squares estimates of the corresponding modal amplitudes. Using these modal amplitude estimates, the response at uninstrumented points in the system can be calculated. The confidence associated with these inferred uninstrumented responses depends on two sets of factors: first, the confidence level of the system model from which the significant modes were selected and the sensor modeshapes were extracted; and second, the confidence level in the validity of the sensor data, coupled with (a) the numerical characteristics of the transformation matrix and (b) the signal-to-noise characteristics of a normally functioning sensor. Because the transformation matrix varies only with the sensor layout and does not depend on the actual sensor data, the quality of the estimated quantities depends only on the sensor layout (for a fixed model of the system), and it depends on the layout to a surprising degree. The quality associated with a layout can be assessed to a certain extent in advance, before any sensor data is obtained.

Redundant Sensors Allow Checks for Modeling and Sensor Deficiencies: When the number of sensors exactly equals the number of modal amplitudes being estimated, the least-squares fit provided by the transformation matrix will always be exact and the residuals between actual sensor readings and best-fit sensor readings will be zero. If additional sensors are provided - generally distinct from the original sensors, but in some cases almost exact replicates - then each sensor will have associated with it a known extent of residual error checking to help detect malfunctions of an individual sensor or overall modeling deficiencies.

Use of Residual Time-History Data: In the typical dynamic case, where sensor data is available in time-history form rather than as static responses to different static input cases, the time-history behavior of residuals can provide useful information. Residual time histories for one or more sensors which strongly resemble one of the modal amplitude time histories suggest an error in the sensor modeshape used to resolve that mode. Residual time histories with large amplitudes only in a narrow time interval, particularly if evident only for sensors in a localized area, suggest a temporary localized unmodeled event such as an impact between system parts modeled as non-contacting. Finally, residuals with strong nonlinear features such as sudden apparent zero shifts, presentation only of peaks which appear clipped in the original sensor data, or step rises and truncated exponential decays, may provide clues to signal conditioning electronics problems.

Aliasing Checks: Frequently, it is not intended to resolve all modal responses of a system, but only those significant for evaluating certain system point parameters of interest. In this case, the modes intended to be neglected must be evaluated to ensure that their sensor modeshapes and expected peak modal amplitudes do not seriously affect the estimated modal amplitudes for desired modes. A quantitative measure of aliasing effects is provided by using the sensor-to-modal transformation matrix on sensor readings corresponding to neglected modes at their peak level.

METHOD OF EVALUATION

The general steps used in evaluating sensor layouts are as follows:

1. Identify which system response modes are to be measured. These could be (a) forces and moments in a support skirt or section of piping, (b) rigid body linear and angular accelerations about the CG, or (c) mode shape multipliers which establish the magnitude of shock response in the normal modes being considered.

2. Select a tentative sensor layout.

3. Set up an equation that gives the sensor readings as linear combinations of the amplitudes of the desired modes, i. e.

$$\{S\} = [R]\{C\}.$$

In the above equation, $\{S\}$ is a vector of sensor readings, $[R]$ is a response matrix whose elements R_{ik} are the response of the i-th sensor to a unit value of the k-th system mode and $\{C\}$ is a vector of the system modal amplitudes.

If an accelerometer layout were being evaluated to see if it could measure the response of a flexible body in terms of its normal modes of vibration, then the normal mode shape components corresponding to each sensor location and orientation could be used for the columns of $[R]$. The corresponding elements in $\{C\}$ are the multipliers which establish the magnitude of shock response in each mode. The columns of $[R]$, in any case,

are the "sensor mode shapes" that are being measured in response to the presence of a unit modal amplitude of the corresponding mode.

Note that each element R_{ik} intrinsically has associated with it units of (units for sensor i)(units for modal amplitude k)$^{-1}$, or the sensor scale associated with each row divided by the modal scale associated with each column. As shown in Appendix A, the choice of modal scale is arbitrary and has no effect on the nature of the least squares fit; it simply changes the interpretation of a given modal amplitude level. The sensor (row) scale factor does, however, affect the nature of the fit by influencing the way residuals are distributed among the sensors. This is also discussed further in Appendix A. The units associated with the elements of the matrix [P], defined below, are the inverse of those for [R], i. e., P_{ik} has units (units for mode i)(units for sensor k)$^{-1}$.

4. Calculate the pseudo inverse matrix [P] as follows:

$$[P] = [R^T R]^{-1}[R^T].$$

When the pseudo inverse matrix is multiplied times a set of sensor readings, the desired modal amplitudes are obtained, i. e.

$$[P]\{S\} = [P][R]\{C\}$$

$$= [R^T R]^{-1}[R^T][R]\{C\} = \{C\}.$$

Whenever the number of sensors is equal to the number of modes being resolved, the above procedure is equivalent to finding the inverse of the [R] matrix. For this case, the [R] matrix is square and the equation for the [P] matrix simplifies to

$$[P] = [R^T R]^{-1}[R^T]$$

$$= [R]^{-1}[R^T]^{-1}[R^T] = [R]^{-1}.$$

If the number of sensors is larger than the number of modes being resolved, the above procedure gives the best estimate (in the least squares sense) of the modal amplitudes that correspond to the sensor readings.

If the number of sensors is smaller than the number of modes being resolved or if there are linearly dependent sensor modeshape columns, then the $[R^T R]$ matrix will be singular and the inverse will not exist. (This is equivalent to trying to find a number of unknowns that is larger than the number of independent equations available.) A nonsingular $[R^T R]$ matrix can be obtained either by revising the sensor layout being considered (to change one or more sensor modeshape columns to eliminate linear dependence between columns) or by reducing the number of sensor modes being resolved (a corresponding column is deleted from the [R] matrix for each mode that is eliminated). If a mode is deleted from the response matrix, it is essential to check later for aliasing of the neglected mode into the retained modes (see step 8).

5. Calculate the least squares filtering matrix [U] as follows:

$$[U] = [R][P].$$

The utility of the [U] matrix can be seen best if it is assumed that a set of sensor readings {S} is available. The best fit modal amplitudes {C} corresponding to these sensor readings are given in Step 4 above as

$$\{C\} = [P]\{S\}.$$

Then, using the equation from Step 3, the sensor readings $\{\bar{S}\}$ that correspond to the best-fit modal amplitudes are given by

$$\{\bar{S}\} = [R]\{C\} = [R][P]\{S\}$$

$$\{\bar{S}\} = [U]\{S\}.$$

Thus, it can be seen that the [U] matrix filters or transforms a set of sensor readings such that they correspond to the sensor values predicted by the model [R] for the best-fit values of the modal amplitudes. Another way of viewing this is to set up a residual vector $\{\Psi\} = \{S\} - \{\bar{S}\}$. It can be shown that if $\{\Psi\} \neq 0$, then $\{\Psi\}$ cannot be expressed by any combination of the columns of [R]. This residual $\{\Psi\}$ is the "unmodeled component" of {S} and is stripped off by [U] to leave the "modeled component", $\{\bar{S}\}$.

6. Examine the diagonal of the [U] matrix to determine the amount of consistency checking for each gage. If a diagonal element U_{ii} equals one, the other entries in that row and column will be zero and the best fit sensor value $\bar{S}_i$ is directly equal to the corresponding sensor reading S_i. In this case, there is no consistency checking between sensor i and the other sensors.

   However, when a diagonal term U_{ii} is less than one, and an instrument error occurs on sensor i but not for any other sensors with non-zero coefficients in row i of [U], then the fraction $(1 - U_{ii})$ of the instrument error will show up in the residual Ψ_i and the same fraction $(1 - U_{ii})$ of the squared instrument error will show up in the residual squares, i. e., in

$$\{\Psi\}^T\{\Psi\} = \Sigma_i(S_i - \bar{S}_i)^2.$$

   (Although the contribution of a given error ΔS acting on sensor i to the squared residual for sensor i is only $(1-U_{ii})^2\,\Delta S^2$, the error will also produce apparent residuals $U_{ij}\Delta S$ for other sensors $j \neq i$. It can be shown that the total contribution to the sum of squared residuals,

$$\Delta S^2\left((1-U_{ii})^2 + \sum_{j\neq i} U_{ij}^2\right),$$

   is equal to $\Delta S^2(1-U_{ii})$, which is larger than $\Delta S^2(1-U_{ii})^2$.)

   Having U_{ii} values less than one provides consistency checking among the sensors in row i of [U] that have non-zero coefficients; i. e., as long as U_{ii} is less than one, a single sensor malfunction involving sensor i is guaranteed to show up in the residual for sensor i and in the total squared residuals summed over all sensors, to the extent shown by $(1 - U_{ii})$.

   The consistency of a set of sensor readings can be checked by calculating the ratio of (sum of residuals squared) to (sum of raw data squared) where the sums are taken over all sensors. The smaller this ratio, the better the data fits the model. A perfect fit would have zero residuals and a ratio of zero. In practice, for dynamic time history data one could calculate this ratio for each time sample of sensor data to determine an average value of the ratio over a transient. One would then investigate more closely the individual sensor readings and sensor residuals for time intervals in which the ratio becomes much worse than the average, i. e., at times when the data becomes less consistent with the model.

   The matrix [U] is a square matrix having as many rows and columns as there are sensors being used. Also, the sum of its diagonal terms U_{ii} is equal to the number of modes being resolved. Therefore, the optimum condition for getting the maximum amount of consistency checking for each sensor is to have the diagonal terms in the [U] matrix equal to the number of modes being resolved divided by the number of sensors being used. Also, it appears desirable to have as many off-diagonal terms in the [U] matrix be non-zero as possible since this spreads the consistency checking over the largest number of sensors.

   Finally, it should be apparent that if U_{ii} is very low (e. g., less than 35 percent of the maximum U_{jj}), sensor i is being used inefficiently. A sensor with such low U_{ii} uses most of its own data simply to check itself for errors; its reading can be predicted with good confidence from the readings of other sensors and is not very useful in helping resolve modal amplitudes or in checking the consistency of other gages. Low U_{ii} values typically arise when sensor i duplicates or nearly duplicates the reading of another sensor (or set of sensors) at a lower scale, e. g., a Poisson effect strain gage where the model includes no independent loading in the direction of the Poisson gage. Unless there is a desire to test the specific feature of the system model that leads to such a low scaled and redundant sensor prediction, the offending sensor should be reoriented or moved to get more reasonable U_{ii} and better values for the other U_{jj}. Even if checking a model feature is considered desirable, alternate layouts will frequently show a better distributed sensitivity to model inaccuracies (see step 9) and provide a better check than that provided by the residual of a sensor with very low U_{ii}.

7. Calculate the variance for each of the resolved modes ($\sigma^2(C_i)$) as a function of the variance in the sensor readings ($\sigma^2(S_k)$). Here variance in the sensor readings is taken to mean the square of the sensor RMS "noise floor" or "grass level".

   From the second equation in Step 5, it can be seen that the modal amplitudes are linear combinations of the sensor readings. If the noise contributions to the sensor readings are uncorrelated between sensors, the variance for mode (i) is equal to

$$\sigma^2(C_i) = \sum_k P_{ik} \sigma^2(S_k).$$

   Then, if all sensors are assumed to have the same variance $\sigma^2(S)$ this reduces to

$$\sigma^2(C_i) = \sigma^2(S) \sum_k P_{ik}^2.$$

   Thus, when all sensors are assumed to have the same variance, the row sums of squares of the pseudo inverse matrix [P] provide indexes or measures of the variances for the corresponding modes.

   The variances of the modes are an indication of the sensor noise that will be superimposed on the modal amplitude signal. The smaller the variances the better.

   While the variances are based strictly on sensor noise, a sensor layout with variances that are high (compared to other layouts) will be more sensitive to small errors in model accuracy, in sensor placement, and in sensor linearity.

   Comparison of modal variances is generally sufficient to evaluate the relative merits of one sensor layout compared to another. However, modal variances are somewhat abstract and hard to relate to easily comprehended system point parameter values. The second part of Appendix A shows how to express layout performance in system terms vice modal terms, using realistic (not necessarily all equal) sensor noise floor levels.

8. If there are any predicted modes of system response which are not included in the modes to be resolved, determine the sensor responses associated with the peak level expected for the neglected modes. Apply the [P] matrix to these sensor response vectors to determine the extent to which the neglected modes will be resolved as false indications of the desired modes, and compare the aliasing level apparent for each undesired mode to the expected level for the desired mode.

   The extent of aliasing acceptable will depend upon the application. If the aliasing is unacceptable, change the sensor layout (either add a sensor or move/reorient some existing sensor(s)) and reevaluate from step 3. If aliasing is still unacceptable (e. g., greater than 10 or 15 percent) after several iterations of the sensor layout, it is generally best to include the offending, neglected mode into the [R] matrix. This will drive up the variances of the desired modes previously suffering aliasing, but it is often easier to resolve the variance deficiencies than an aliasing deficiency.

   In cases where the modes to be resolved are vibration modes with known associated frequencies, it may be acceptable to allow substantially more aliasing if the desired and interfering modes are widely enough separated in frequency to permit use of bandpass or band-reject filters to reduce aliasing. This approach must be used with caution, however. Filter effects on timing and phasing of the filtered modal amplitude must be considered before using the filtered modal time history with any differently filtered or unfiltered modal time histories.

9. If there is uncertainty about the accuracy of the sensor mode shapes, the effect of modeling inaccuracy can be determined by perturbing the model with changes of a size appropriate to the uncertainty in the model parameters. Generate a perturbed model sensor response matrix [R'] and then examine [P][R'] for differences from the identity matrix. Such differences indicate the interpretation errors that would result from using the assumed original model to reduce data from a system actually reflecting the perturbed model.

EVALUATION OF SENSOR LAYOUTS

In the following three sections, examples are given to show how different types of sensor layouts can be evaluated using the method described above. For maximum effectiveness, the procedure should be automated as much as possible so that attention can be focused on selecting and comparing sensor layouts rather than the mathematical calculations. Three short (~40 lines) APL (A Programming Language) functions were used

for the calculations in the following sections. APL was a particularly convenient programming language for this application because of its ability to handle arrays of different sizes automatically.

Evaluation of Strain Gage Layouts

In this section, different strain gage layouts are evaluated based on their ability to measure the forces and moments in a thin-walled cylinder. The coordinate system, force definitions, and response formulas used in the evaluations are shown in Figure 1. In developing the strain gage response modeshapes shown in Figure 1, the units for all sensors were taken as microstrain or 10^{-6}, and the following values of force or moment were adopted as corresponding to a unit modal amplitude; the result of these conventions is that +1 is the maximum element possible in any sensor modeshape:

Mode	Load for Unit Modal Amplitude
X-Shear ($R_{i,1}$)	$AG/10^6$
Y-Shear ($R_{i,2}$)	$AG/10^6$
Z-Tension ($R_{i,3}$)	$AE/10^6$
X-Bending ($R_{i,4}$)	$IE/(10^6\ R_o)$
Y-Bending ($R_{i,5}$)	$IE/(10^6\ R_o)$
Z-Torsion ($R_{i,6}$)	$2JG/(10^6\ R_o)$

where: A = Area of cross-section
E = Material modulus of elasticity
G = Shear modulus of elasticity = $E/2(1+\nu)$
ν = Poisson's ratio = 0.3
R_o = Outside radius
I = Moment of inertia of cross-section
J = Polar moment of inertia of cross-section

The first strain gage layout to be evaluated consists of nine strain gages arranged in rosettes at T_i = 0°, 90°, and 180°. Within each rosette, one gage is circumferential (A_i = 0°), one gage is axial (A_i = 90°), and the third gage is centered between the other two gages at A_i = 45°. This layout along with the results of the quantitative evaluation is shown in Figure 2. The low diagonal values (0.083) in the [U] matrix for the first, fourth, and seventh gages indicates that these circumferential gages are not being utilized effectively. Their best estimate value is seen to be little more than "minus Poisson's ratio times the axial gage readings." If pressure surges were included in the load set, the circumferential gages would be more effective because circumferential strain is the major response to pressure surges. However, since pressure surges were not included in the specified set of loadings, it is concluded that a better strain gage layout can be found.

The second strain gage layout to be evaluated was selected to show how significant improvements can be obtained by minor changes in a sensor layout. For this layout, the strain gage rosettes in the first layout were rotated 45° so that the center gage is aligned with the axis of the cylinder, i. e., "crow-foot" rosettes. This layout along with the results of the quantitative evaluation is shown in Figure 3. Inspection of the [U] matrix shows significant improvements in the amount of consistency checking for all gages. Significant reductions in the modal (load) variance indexes were also obtained.

The third strain gage layout to be evaluated was selected to show why it is important to consider the variances for the modal amplitudes. This layout consists of nine strain gages arranged in three crow-foot rosettes just like the second case. However, in this case the rosettes are located at T_i = 0°, 45°, and 90° and hence are closer together, covering only one quarter of the circumference. This layout is shown in Figure 4 with the corresponding evaluation results. It is interesting to note that the [U] matrix obtained for this layout is identical to the one obtained for the second layout. Thus, the two layouts provide the same amount of consistency checking between gage readings. But, as one might expect intuitively, the third layout is less desirable for resolving forces and moments. This is evidenced by the overall large increases in the variance indexes and hence uncertainties in the loads being measured. In general, it has been found that the variances for the forces and moments are minimized by equally spacing the rosettes. (The second part of Appendix A notes that the Figure 4 layout does give performance marginally superior to the Figure 3 layout for inferring the response of points in and near the heavily instrumented quadrant. However, it does so only by imposing gross penalties on the accuracy of responses for points even a short distance outside the quadrant, to the extent that its use would normally be unacceptable.)

The fourth strain gage layout considered shows how an arrangement of eight gages can be optimized for measuring the three forces and three moments at a plane along the axis of a thin-walled cylinder. This layout has two gages at each of the transverse coordinate axes, i.e., at T_i = 0°, 90°, 180° and 270°. At each location, one of the gages is oriented halfway between the circumferential and the axial directions (A_i =

45°) and the other gage is oriented in the axial direction (A_i = 90°). Figure 5 shows the layout and the corresponding evaluation results. This layout is considered to be an optimum layout because all of the diagonal terms in the [U] matrix are equal. In this case each diagonal term equals 0.75 because six modes are being resolved with eight strain gages and 6/8 = 0.75. When all diagonal terms in the [U] matrix are equal, an equal amount of consistency checking is provided for each gage reading. The load variance indexes shown in Figure 5 are generally less and better balanced than those shown in Figure 3. Thus by optimizing the layout, fewer gages can be used to measure the same response characteristics with better accuracy. The Figure 5 strain gage layout also has an additional advantage in that all forces and moments could be resolved even though both of the gages at one measuring station were lost. This would not be possible with the Figure 3 strain gage layout.

Evaluation of Accelerometer Layouts Used to Measure the Shock Response of Rigid Bodies

In this section two different accelerometer layouts are evaluated to show different approaches that can be used to determine the CG accelerations of rigid bodies. The coordinate system, CG acceleration definitions, and response formulas used in the evaluations are shown in Figure 6. The sensor signals are assumed to be in "g's". The unit modal amplitudes then correspond to "g's" for translational modes and "g's per length unit" for rotational modes. In writing the response formulas it has been assumed that centrifugal ($r\omega^2$) accelerations are negligible when compared to tangential ($r\alpha$) and translational accelerations. This assumption has been found to be valid in evaluating the shock response of components in a large number of cases. When made, this assumption reduces the responses of accelerometers on a rigid body to linear combinations of the CG accelerations.

NOTE: It is possible to account for centrifugal accelerations due to high rigid body angular velocities for cases such as systems in flight or freefall which have enough spin or tumbling to impose nonnegligible centrifugal sensor response. However, an additional response mode is required for each orthogonal axis through the CG about which centrifugal effects are to be resolved. This cuts down on the amount of consistency checking available from a given number of sensors. Also, since oscillations in angular velocity are generally slower than oscillations in angular acceleration, the centrifugal modes will have a low frequency dominated spectrum - 0 Hz, in fact, for steady state spin - and resolution will be difficult unless accelerometer frequency response extends to DC. This would dictate use of strain gages and piezoresistive rather than piezoelectric accelerometers. Third, because centrifugal modes respond to the square of the angular velocity rather than the first power, (a) accuracy will be poor at low angular velocities, e. g., 1 percent response for 10 percent of full scale angular velocity, and (b) the sign or sense of the velocity will be ambiguous. The net effect of these considerations is that CG centrifugal modes should be accounted for only where vehicle or system centrifugal effects about the CG are directly of interest.

For illustrative purposes, a cylindrical rigid body is assumed which has a radius of 25 length units and a height of 100 length units. Two different approaches are shown in Figures 7 and 8 for measuring the CG accelerations for this component. In Figure 7, six accelerometers are shown for measuring the six CG accelerations. In this case there is no redundancy and hence no consistency checking among the accelerometer readings. This is evidenced by the 1.0 values on the diagonal of the [U] matrix. The variances calculated for the CG translational accelerations are seen to be of the same order of magnitude as the variances for the accelerometer readings. The variance for the CG acceleration in the y-direction is noted to be better (lower) than the variances for the CG accelerations in the x and z-directions. Thus this type of layout might be used when all of the CG accelerations were to be measured and the one in the y-direction was considered to be the most significant.

For many components the shock response is such that the CG angular acceleration about the z-axis is negligible. For these cases, an accelerometer layout similar to the one shown in Figure 8 is more appropriate. In this layout, six accelerometers are used to measure five of the CG accelerations, i.e., the angular acceleration about the z-axis is not evaluated. The accelerometers have been deliberately arranged to have no sensitivity to rotation about the z-axis by locating their sensitive axis always in a radial-vertical plane. This makes the z-rotation sensor mode shape all zeros, as shown by the last column of the "FULL RESPONSE MATRIX"

in Figure 8, and prevents aliasing. In this case some consistency checking is provided for the accelerometers that sense acceleration in the vertical direction. Attention is also called to the fact that by inclining two of the accelerometers with respect to the coordinate axes, approximately equal variances were obtained for the translational CG accelerations.

Evaluation of Accelerometer Layouts Used to Measure Mode Shape Multipliers for Flexible Bodies

In this section different accelerometer layouts are evaluated based on their ability to measure the normal modes of vibration in a flexible body. If the deformation of a flexible body can be described by a linear, elastic model, then its shock response can be described in terms of its normal modes of vibration. Furthermore, the response of an accelerometer located at some point on the body can be represented as a linear combination of mode shape multipliers, i.e.,

$$\{S\} = [R]\{C\}.$$

In the above equation entries in the {S} column vector are accelerometer readings, columns in the [R] matrix are the mode shape values at the accelerometer locations, and entries in the {C} column vector are modal amplitudes, i.e. the levels of excitation in each mode.

Care must be used to maintain consistent interpretation for the level of excitation corresponding to unit modal amplitude. One convention used for shock analyses normalizes the system mode shapes to have a value of 1.0 at the maximum responding system degree of freedom. In this case, the normalized system mode shapes are consistent with modal amplitudes whose units are "g's at the peak responding system degree of freedom." We normally extract flexible-body sensor mode shapes from such unit-normalized analysis results by just using the mode shape value for the degree of freedom corresponding to the sensor location and orientation; therefore, we use sensor units of "g's" and have modal amplitudes interpretable as "g's at the peak responding system degree of freedom." Two things are important to note here: first, sensor mode shapes are not normalized to a largest component of 1.0, and 1.0 might not appear in a given column of [R] unless we happen to assign a sensor to the peak responding system degree of freedom; and second, the sensor mode shape may contain values larger than 1.0 if we orient an accelerometer partway between two system degrees of freedom both of which have large responses. Thus, in a sensor modeshape derived on this basis, neither the absence of 1.0 nor the presence of values bigger than 1.0 (for sensors oriented between system degrees of freedom) indicates an error. When rotational effects at a node are neglected, the maximum value that can appear in [R] for a sensor oriented between two 0.999... response system degrees of freedom is 1.414... and between three such system degrees of freedom is 1.732... ($2^{1/2}$ and $3^{1/2}$ respectively).

For illustrative purposes a simply supported beam that is 12 units long was selected as the flexible body. The shape for the n-th mode is thus equal to $\sin(n\pi x/12)$, assuming shear and rotational effects are neglected and assuming the accelerometer masses have negligible influence on the beam mode shapes. Figure 9 shows the results obtained from an evaluation of a layout where five equally spaced accelerometers are used to measure multipliers for the first three modes. The consistency checking among the gage readings is fairly good as are the variance indexes for the mode shape multipliers.

In general, the level of excitation will be low in the even modes if both end supports see similar inputs; therefore it may be desirable to concentrate on measuring the response for odd modes. Figure 10 shows the results obtained when using five equally spaced accelerometers to measure the multipliers for modes 1, 3 and 5. In this case there is no consistency checking for the center accelerometer, but the variance indexes are the same as those obtained in the Figure 9 case.

The available degrees of freedom in the Figure 10 accelerometer layout cannot be used to measure multipliers for additional odd modes. If this is attempted, the response matrix becomes singular. The reason for this lies in the symmetric sensor placement about the center; in any odd mode, the sensor at position x shows the same response as a sensor at position L-x. For purposes of resolving odd modes, the arrangement shown on Figure 10 might as well be an arrangement where the sensors on the right half of the beam have been relocated on top of the corresponding sensors at the left half, so data is effectively sampled at only three points (two of which have replicated sensors). Note that the Figure 10 layout would be perfectly capable of resolving additional even modes, such as 2 and 4, since the even mode response is not identical for symmetric sensors (magnitudes are the same but signs change). This was not pursued because of lack of interest in the even modes.

To avoid effectively replicating sensors for odd modes by symmetry, a layout was next attempted with the five accelerometers equally spaced over the left side of the beam as shown in Figure 11. By locating all accelerometers on one side of the beam the multipliers for odd modes 1 through 9 can be measured. In this case there is no consistency checking between gages since five modes are being resolved with five accelerometers. The variance indexes for the modal amplitudes are only slightly higher than those obtained when measuring three mode shape multipliers with the Figure 10 layout.

Although satisfactory from a variance standpoint, the Figure 11 layout proved very poor with respect to aliasing, as shown by the results in Table 1. Each row of this table is computed by generating sin(nπx/12) at the sensor locations as the sensor mode shape for the n-th mode shown in the row labels, and applying the pseudo-inverse matrix [P] from Figure 11 to obtain the apparent modal amplitude for the desired modes shown in the column headings. Zero responses are shown as blanks for greater clarity. The following items shown in Table 1 are of interest.

a. Desired modes 1, 3, 5, 7, and 9 show up properly, with unit amplitude in the true mode and no aliasing into other desired modes.

b. The even modes alias badly into the desired modes, and do so in a way that makes filtering on a frequency basis difficult, i. e., the worst aliasing from even modes is seen in the immediately adjacent odd modes. Mode 1 suffers most from mode 2, mode 3 suffers from both modes 2 and 4, mode 5 has substantial aliasing from 4 and 6, etc.

c. Worse yet mode 9 looks exactly like mode 11 with the sign reversed; similarly, mode 7 looks like an inverted mode 13, etc., down to mode 1 which equals inverted mode 19 or uninverted mode 21. A filter sharp enough to significantly diminish a response at mode 11 frequency may severely distort the mode 9 time history. The situation gets better for lower modes which are more widely separated in frequency from their aliases.

d. The table is carried very high (mode 50) to illustrate that it repeats in blocks (b) of 20 modes, i. e., row i is identical with row (20b+i) and identical with a sign-reversed row (20b-i). However, the high mode number examined is not unrealistic with respect to raw, unfiltered shock accelerometer data. For impulsive shock, the velocity spectrum tends to remain constant and acceleration levels, therefore, tend to increase linearly with frequency (provided modal mass is small enough to avoid causing a spectral dip). The basic periodicity of the table is caused by the uniform L/10 spacing of the accelerometers.

e. Note that modes 10, 20, ...10n cause no aliasing because they have nodes (zero response points) at all the sensor locations.

In order to resolve both the high level of even-mode aliasing (although even-mode amplitude is expected to be small, minimizing the concern) and the mode 9/mode 11 problem, two changes were made in the layout shown on Figure 11. First, all sensors were located at nodes of mode 11 (i. e., at multiples of L/11) so that the closest unresolved odd mode which could alias into mode 9 would be mode 13. Second, to take advantage of the change in sign of even modes compared to adjacent odd modes over the length of the beam, sensors were placed at locations 2, 4, 6, 8, and 10 times L/11 to sample both halves of the even mode cycles. As shown in Figure 12, variances are essentially unchanged from Figure 11. The aliasing characteristics are greatly improved, however, as shown by the results in Table 2. Note the following:

a. Even modes alias solely into a single desired mode vice into several. While the aliasing amplitude is higher, the difficult frequency separations are far better except for modes 5 and 6. Even for mode 5, the Figure 13 aliasing of 100% mode 6 is probably better than the probable combined effect of 62% mode 4 plus 62% mode 6 (root sum of squares = 87% combined) because it occurs at only a single frequency rather than in balanced sidebands.

b. The block periodic structure now repeats at multiples of 11 modes vice 20. However, even though modes 1 and 3 now have large aliasing from modes 10 and 8 vice 19 and 17 previously, the frequency separation is great enough to permit filtering out effects smoothly. Note that modes 11, 22, 33... produce no aliasing, as intended.

Finally, to investigate sensitivity of aliasing to errors in sensor placement, the aliasing checks of Tables 3 through 5 were run with the basic fraction of L for each sensor position rounded to the nearest .001L, .01L, and .05L, respectively. Notice that for .01L precision (Table 4), the change in aliasing does not exceed 10 percent until mode 11 or higher. Notice also

that changes in aliasing become more prominent with increasing mode order, so that the pristine regularity of Table 2 sinks gradually into more and more noise. Finally, observe in Table 5 that by placing all sensors on exact multiples of L/20, we have imposed a zero aliasing for modes 20 and 40; however, the table does not repeat in blocks of 20. This is a consequence of the irregular spacing of the sensors at 4, 7, 11, 15, and 18 times L/20. By not using uniform sampling intervals, a larger periodicity results, in this case folding about mode 40 (because of the symmetric 3-4-4-3 L/20 spacing between sensors).

The aliasing checks in Tables 1 through 5 are less informative than usual because unit amplitudes of all modes were used, rather than realistic expected peak or RMS values. In usual practice, representative modal amplitudes would be assigned to both the aliasing modes and the desired modes, and the aliasing effect would be expressed as percent of expected true value for the desired mode. This makes a larger or smaller basic aliasing effect acceptable as appropriate.

The lesson intended by these aliasing tables is that while good variance performance is necessary, it is not a complete description of sensor layout performance. Failure to thoroughly evaluate aliasing - not covering high frequency modes, for example - can lead to embarrassing surprises when test data are obtained.

CONCLUSIONS

The overall lesson intended by this paper is that a systematic approach to sensor layout evaluation in advance of testing can yield great benefits in the quality of the data. Very small changes in a sensor layout such as rotating some rosettes, aligning accelerometers to avoid a rotational effect, or changing inter-accelerometer spacings on a beam by only 9 percent can make a great difference in the quality, consistency, and utility of the data.

An important corollary found in developing this method is that it is extremely important to minimize the user's effort needed to evaluate a sensor layout or changes to a previous layout. If the user has to calculate the [R] matrix entries by hand, there will be few layouts evaluated and considerable chance for error; but if the user just has to edit some easily understandable information on sensor type/location/orientation and then can let the computer calculate the [R] matrix, there is much more likelihood of finding a near-optimum gage layout. Experiments with randomly placed sensors have convinced us that most random layouts are terrible compared to layouts selected by "engineering judgment". However, experience with plausible "engineering judgment" layouts has also convinced us that many such layouts contain hidden pitfalls and inefficiencies that can be eliminated or drastically improved by minor "fine tuning." Most layouts can be optimized with only a few alternative evaluations; a few cases have required twenty or thirty alternatives to be evaluated before arriving at a decidedly superior layout. Ease of user input is crucial in finding such good layouts when project constraints make good layouts relatively rare.

The method described herein was developed by the authors in support of a specific test, but is considered to be quite general in applicability and has been communicated to the Naval Research Laboratory for use in other projects. Questions and observations about use of the method should be directed to Mr. R. L. Bort at NRL, Code 5837, Washington, D. C. 20375.

APPENDIX A

I. Sensor Units, Modal Units, and Interpretation of Variance

It was stated in the text that each entry of the response matrix [R] has associated with it a combination of sensor units and modal units, and similarly for the [P] matrix (except that the units of P_{ki} are the reciprocal of those for R_{ik}). This statement is slightly stronger than necessary, and at the same time somewhat incomplete and imprecise. The discussion that follows attempts to clarify the significance of modal and sensor units.

Modal Amplitude Units

Each mode has associated with it (1) a constant system modeshape which defines the relative magnitude of the modal response at all system points and (2) a modal amplitude which varies to describe the magnitude of the modal response. The elements in the system modeshape can be thought of as having only the engineering units appropriate to their system point parameter; in this case, the modal amplitude is a dimensionless multiplier that tells how much each lement of the system modeshape must be scaled up or down to give the size of the modal effect. However, by definition, all elements of the system modeshape give the system point parameter responses when the modal amplitude has the numerical value 1.0; hence, it seems clearer to assign "modal amplitude units" to the modal amplitude parameter and think of the system modeshape components as having

units of "engineering units of system response per unit of modal amplitude".

Further, the modal amplitude unit can be made more concrete and visualizable by finding a single meaningful system parameter to associate it with; this system parameter may or may not be observable at any single system point. In the case of static beam loading, for example, one might choose for the axial loading mode "one modal amplitude unit (axial mode) equals one kilonewton (2,204.6 pounds-force) axial tension". In this case, an axial modal amplitude of 5.36 [modal amplitude units] is equivalent to 5,360 Newtons (11,817 lbf) axial tension. Similarly, a unit modal amplitude of shear, bending, or torsion could be attributed to an appropriate size force or moment load. For vibration modes, one frequently used convention is to normalize each system mode-shape so that its highest responding system point parameter has the numerical value 1. If the highest responding point parameter is at location number 39, and point parameter 39 is the acceleration of a particular mass point in a particular direction, then use of a system modeshape normalized to a unit response for point parameter 39 implies "one modal amplitude unit = 9.8 m/sec^2 (32.2 ft./sec^2) or one g contribution from this mode to point parameter 39". Note that this definition must be used consistently regardless of whether or not a sensor is assigned to measure point parameter 39.

As it turns out, the choice of level for a unit modal amplitude does not affect the results of a sensor layout evaluation in terms of system units as long as some choice is made and used consistently. The rows of matrix [P] and the entries of the modal amplitude vector {C} have associated with them the corresponding modal amplitude units; the columns of [R] have associated with them inverse modal amplitude units, or are values "per modal amplitude unit"; and variance results are given in modal amplitude units squared. If a new layout analysis were performed using a unit modal amplitude for mode i corresponding to a system response twice as big as previously used, then (all other things being equal) the effects would be: (1) column i of [R'] would be twice the magnitude of column i of [R]; (2) row i of [P'] would be half the size of row i of [P], so $\{C_i'\}$ would be half the size of $\{C_i\}$ for a given set of sensor readings; and (3) the apparent variance of mode i would be one fourth as large in new modal amplitude units squared as in old modal amplitude units squared. When converted to system units, corresponding quantities would be numerically equal regardless of the choice of unit modal amplitude.

At times it has been helpful to explicitly maintain a vector {μ} of "system equivalent interpretations of unit modal amplitude", typically thought of as a vector of labels for the columns of [R], the rows of [P], or the elements of {C}. There are no calculations involving this vector for sensor layout analysis; however, the discipline of writing it down helps fix the interpretation of the modal amplitudes in one's mind, and it can be a handy reference for later system calculations. The designation "mu (μ)" is intended to be mnemonic with "modal amplitude unit system equivalent". Keeping track of {μ} becomes essential if one wishes to compare layout analyses which use different definitions of the system mode shapes or unit modal amplitudes.

Sensor Units

Sensor units are the units needed to interpret the elements of {S}, the rows of [R], and the rows of [U]; inverse sensor units apply to the columns of [P] and [U]. Similar to {μ} above, it is often helpful to write a vector {γ} ("gamma" for "gage unit level") such that "$s_i = z$" means "sensor i reads $(z\gamma_i)$", where both the numerical value and the units associated with γ_i are included.

When all sensors are the same type (e. g., all accelerometers or all strain gages) and particularly when there are no redundant sensors, {γ} is not of much use; the numerical values in {γ'} can be different from those in {γ}, but [R'], [P'], and [U'] will produce results which (in system units) are exactly equivalent. In this case, one might as well simply set all elements of {γ} to the same appropriate value, e. g., 1 μstrain or 1 g, and not worry about {γ} further.

When sensors are of different types (e. g., strain gages mixed with accelerometers), or when there is some degree of sensor consistency checking, then {γ} becomes quite significant, as shown below.

A. Redundant Mixed Sensors: Consider the case of a lumped mass on a cantilever beam foundation where an accelerometer is measuring mass motion transverse to the beam and a strain gage is measuring the beam bending corresponding to the transverse motion. Assume that there i only one significant mode and that this mode produces a peak bending strain of 350 μstrain for a 1 g peak transverse acceleration of the mass.

If $\{\gamma\}^T$ is taken as {1 g, 1 μstrain} and the RMS sensor noise levels are assumed to be 0.05 g and 5 μstrain, then the layout evaluation would be:

{μ} = {1 g transverse acceleration of mass}

$$\begin{Bmatrix} S_1 \\ S_2 \end{Bmatrix} = \begin{bmatrix} 1 \\ 350 \end{bmatrix} \{C_1\}$$

$$[R] = \begin{bmatrix} 1 \\ 350 \end{bmatrix}$$

$$[P] = ([R]^T[R])^{-1}[R^T]$$

$$= \frac{1}{(1)^2 + (350)^2} [1 \ 350]$$

$$= [8.163E\text{-}6 \quad 2.857E\text{-}3]$$

$$[U] = \begin{bmatrix} 8.163E\text{-}6 & 2.857E\text{-}3 \\ 2.857E\text{-}3 & 0.9999918 \end{bmatrix}$$

Variance:

$$\sigma^2 \cong (8.163E\text{-}6)^2(.05)^2 + (2.857E\text{-}3)^2(5)^2$$

$$= 1.6659E\text{-}13 + 2.0406E\text{-}4$$

$$\cong 2.0406E\text{-}4 \text{ (modal amplitude units)}^2$$

RMS noise:

σ = 0.0143 modal amplitude units or g's at the accelerometer mass

One can see from the relatively small U_{11} value that the least squares estimate for the accelerometer, $\bar{S}_1$, is formed almost entirely from the strain gage; the accelerometer is used almost entirely to estimate its own residual. The modal amplitude time history will be almost exactly that of the strain gage and, because the strain gage signal does not show the high ω^2 scaling of an accelerometer signal, the modal time history will show much less high frequency content than would be the case if the accelerometer made a large contribution. To some extent, this is desirable; but if the evaluation stopped here, one would be throwing away the accelerometer results for purposes of estimating the modal amplitude. Note that with this {γ}, the variance or RMS noise level is just that of the strain gage.

Consider the opposite extreme that results when $\{\gamma\}^T$ is replaced by $\{\gamma'\}^T$ = {1 g, 1.0 strain}. In this case, 350 microstrain will appear as 350E-6 in {S}. Then the analysis would change, for the same {μ}, to:

$$[R'] = \begin{bmatrix} 1 \\ .00035 \end{bmatrix}$$

$$[P'] = \frac{1}{(1)^2 + (3.5E\text{-}4)^2} [1 \ 3.5E\text{-}4]$$

$$= [0.999999877 \ 3.5E\text{-}4] \cong [1 \ 0.00035]$$

$$[U'] = \begin{bmatrix} 1 & 0.00035 \\ 0.00035 & 1.225E\text{-}7 \end{bmatrix}$$

In terms of the new sensor units, the strain gage RMS sensor noise level is (5E-6) strain. The variance and RMS noise level for the modal amplitude are then

$$(\sigma')^2 = (1)^2(.05)^2 + (3.5E\text{-}4)^2(5E\text{-}6)^2$$

$$= 2.5E\text{-}3 + 3.0625E\text{-}18$$

$$= 2.5E\text{-}3 \text{ (modal amplitude units)}^2$$

σ' = 0.05 modal amplitude units or g's at the accelerometer mass

Note that now the strain gage best fit is estimated almost completely from the accelerometer, and the RMS noise level of the mode is due solely to the accelerometer. If we stopped here, we would be throwing away the strain gage results.

A reasonable happy medium is achieved when sensors of equal credibility contribute equally to each others' consistency checking. In this case, that would happen when $U''_{11} = U''_{22} = 0.5$. If we keep $\gamma''_1 = 1$ g, we can set $\gamma''_2 = 350$ μstrain and see that

$$[R''] = \begin{bmatrix} 1 \\ 1 \end{bmatrix}$$

$$[P''] = \frac{1}{(1)^2 + (1)^2} [1 \ 1]$$

$$= [.5 \quad .5]$$

$$[U''] = \begin{bmatrix} .5 & .5 \\ .5 & .5 \end{bmatrix}$$

The strain gage RMS noise level now becomes (5/350) in sensor units of 350 μstrain. The variance and RMS noise level for the modal amplitude are then

$$(\sigma'')^2 = (.5)^2(.05)^2 + (.5)^2(5/350)^2$$

$$= 6.25E\text{-}4 + 5.102E\text{-}5$$

$= 6.7602E\text{-}4$ (modal amplitude units)^2

(σ'') = 0.026 modal amplitude units or g's at the accelerometer mass

Note that while this choice of $\{\gamma''\}$ achieved equal consistency checking for both sensors, it did not minimize variance or standard error (RMS modal noise due to sensor noise). This case is simple enough that one could analytically calculate the $\{\gamma'''\}$ that yields minimum σ'''; in general, however, it proves faster for most cases (and was faster even for a simple case such as this) to simply vary $\{\gamma'''\}$ and use an automated routine to calculate σ''' until one finds the minimum or at least its neighborhood. Such a procedure showed that the minimum σ''' was obtained with $\{\gamma'''\}^T$ = {1 g, 100 μstrain} giving an analysis of:

$$[R'''] = \begin{bmatrix} 1 \\ 3.5 \end{bmatrix}$$

$$[P'''] = \frac{1}{(1)^2 + (3.5)^2} [1 \quad 3.5]$$

$$= [0.07547 \quad 0.26415]$$

$$[U'''] = \begin{bmatrix} 0.07547 & 0.26415 \\ 0.26415 & 0.92453 \end{bmatrix}$$

$$(\sigma''')^2 = (0.07547)^2(0.05)^2 + (0.26415)^2(5/100)^2$$

$$= 0.000188679 \text{ (modal amplitude units)}^2$$

σ''' = 0.013736 modal amplitude units or g's at the accelerometer mass

Note that σ''' is only 4 percent lower than σ (which essentially used the strain gage alone) but is 47 percent lower than σ'' where the strain gage and accelerometer checked each other equally. Note also that minimum variance was achieved when the apparent RMS noise level of each sensor, scaled by γ''', gave values of 0.05 for each sensor. This result holds in general; minimum variance for a mode is achieved when the sensor scaling is such that all sensors yield the same apparent noise level.

Finally, one more example is presented to show that only the ratios of the γ_i to one another, and not their absolute size, affect the least squares fit and variance. To demonstrate this point, let us reanalyze [R"] using $\{\gamma^{IV}\}^T$ = {0.1 g, 35 μstrain} so that

$$\frac{\gamma_2^{IV}}{\gamma_1^{IV}} = \frac{\gamma_2''}{\gamma_1''} = 350 \text{ μstrain/g:}$$

$$[R^{IV}] = \begin{bmatrix} 10 \\ 10 \end{bmatrix} \text{ (for } \mu = 1 \text{ g mass response)}$$

$$[P^{IV}] = \frac{1}{10^2 + 10^2} [10 \quad 10]$$

$$= [0.05 \quad 0.05]$$

$$[U^{IV}] = \begin{bmatrix} 10 \\ 10 \end{bmatrix} [0.05 \quad 0.05]$$

$$= \begin{bmatrix} 0.5 & 0.5 \\ 0.5 & 0.5 \end{bmatrix} \cdot [U'']$$

In this case, the accelerometer RMS noise level becomes (0.05/0.1) in sensor units of 0.1 g's. Similarly, the strain gage RMS noise level becomes (5/35) in sensor units of 35 μstrain. The variances and RMS noise level for the modal amplitude are then

$$(\sigma^{IV})^2 = (0.05)^2(0.05/0.1)^2 + (0.05)^2(5/35)^2$$

$$= 6.25E\text{-}4 + 5.102E\text{-}5$$

$$= 6.7602E\text{-}4 \text{ (modal amplitude units)}^2$$

σ^{IV} = 0.026 modal amplitude units or g's at the accelerometer mass

$= \sigma''$

Thus, for a constant ratio of γ_1/γ_2, a change in the scale of $\{\gamma\}$ affects only [R] and [P] but not [U], σ^2, or σ.

B. Nonredundant Mixed Sensors: When there are as many modes to be resolved as there are sensors, i. e., when the [R] matrix is square, then the choice of $\{\gamma\}$ has no influence on modal variance $\{\sigma^2\}$. The only effect is to cause consistent changes in [R] and [P] ([U] always equals [I] for this case). To illustrate this, we continue with the previous cantilever foundation but add a second mode of response to be resolved. The second mode is assumed to be such that with $\mu_1 = \mu_2$ = 1 g translational

response at the mass supporting the accelerometer and $\{\gamma\}^T = \{1\ g,\ 1\ \mu strain\}$, our two-mode [R] matrix is:

$$[R] = \begin{bmatrix} 1 & 1 \\ 350 & 3850 \end{bmatrix}$$

For convenience, let us redefine γ_2 as being equal to (350 μstrain/x). This will let us rewrite [R] as

$$[R] = \begin{bmatrix} 1 & 1 \\ x & 11x \end{bmatrix}$$

Then:

$$[P] = [R]^{-1} = \frac{1}{10x}\begin{bmatrix} 11x & -1 \\ -x & 1 \end{bmatrix}.$$

We check that

$$[P][R] = [I] = \frac{1}{10x}\begin{bmatrix} 11x & -1 \\ -x & 1 \end{bmatrix}\begin{bmatrix} 1 & 1 \\ x & 11x \end{bmatrix}$$

$$= \frac{1}{10x}\begin{bmatrix} 11x-x & 11x-11x \\ -x+x & -x+11x \end{bmatrix}$$

$$= \begin{bmatrix} 1 & 0 \\ 0 & 1 \end{bmatrix}.$$

Now since [R] is square, [P] is both a left inverse and a right inverse for [R]. Thus, [U] = [R][P] = [I], consistent with the fact that there is no sensor consistency checking (since there are no redundant sensors). The strain gage RMS noise level becomes (5x/350) in sensor units of (350 μstrain/x). The variances and the RMS noise levels for the two modal amplitudes are then calculated by the usual method as follows:

$$\sigma_1^2 = \left(\frac{11x}{10x}\right)^2(0.05)^2 + \left(\frac{-1}{10x}\right)^2\left(\frac{5x}{350}\right)^2$$

$$\sigma_1^2 = 0.003025\ \frac{x^2}{x^2} + 0.000002041\ \frac{x^2}{x^2}$$

$$\sigma_1^2 = 0.003027041\ (\text{modal amplitude units})^2$$

RMS noise, mode 1:

$$\sigma_1 \cong 0.055 \text{ modal amplitude units or g's at the accelerometer mass}$$

$$\sigma_2^2 = \left(\frac{-x}{10x}\right)^2(0.05)^2 + \left(\frac{1}{10x}\right)^2\left(\frac{5x}{350}\right)^2$$

$$\sigma_2^2 = 2.5\text{E-}5\ \frac{x^2}{x^2} + 2.041\text{E-}6\ \frac{x^2}{x^2}$$

$$\sigma_2^2 \cong 2.704\text{E-}5\ (\text{modal amplitude units})^2$$

RMS noise, mode 2:

$$\sigma_2 \cong 0.0052 \text{ modal amplitude units or g's at the accelerometer mass.}$$

Note that although γ_2 was effectively made variable,

$$\gamma_2 = 350\ \mu strain/x,$$

the modal variances and noise levels are independent of x and γ_2. Unlike the examples in topic A. above, the same variances are obtained for mode 1 and mode 2 regardless of the ratio γ_1/γ_2. This is always the case where there are no redundant sensors.

C. Weighting: When redundant sensors - of mixed types or of uniform type - are available, it has been shown in topic A. above that changing the values of the γ_i/γ_j ratios changes the nature of the least squares fit by changing [R], [P], [U], and σ^2, σ. One might ask whether there would be occasions to use nonuniform γ_i with sensors all of the same type, e. g., all accelerometers. The answer is "probably yes". For example, if one accelerometer measured transverse motion on an end closure plate or tubesheet that was very stiff in the direction of motion, while another accelerometer measured radial motion of a section of a shell which was lumped into a rigid mass thereby ignoring possible shell (out-of-round) modes, then it could be argued that the residual of the shell mounted sensor should not "count" as heavily as the residual of the tubesheet mounted sensor in minimizing residual squares. Similarly, if one sensor must be set for 1000 g full scale and has a noise floor of 1.8 g (because the recording channel has a signal-to-noise ratio of 55dB), while another has a full scale range of only 100 g and a noise floor of 0.18 g, then a (somewhat weaker) argument could be made that a 2 g residual for the quieter sensor should "count" more than a 2 g residual barely above the noise floor of the noisier sensor.

Finally, a reasonable case can be made that the residual of a sensor with little consistency checking (say $U_{ii} \cong 0.95$) is less reliable, because it is

less subject to confirmation, than the same size residual from a sensor with considerably more consistency checking (say $U_{jj} = 0.70$), and that, therefore, greater weight should be placed on minimizing residuals for the better-checked sensors.

There is a drawback in adjusting the γ_i to achieve this effect: namely, the sensor data {S} and the response matrix [R] must be scaled whenever {γ} is changed, in addition to recalculating [P], [U], and {σ}.

It has been found convenient to achieve weighted least squares fits not by adjusting {γ}, but rather by using an explicit diagonal matrix [W] of weighting factors W_{ii}. In effect, least residual squares are obtained not for the data {S} relative to model [R], but rather for weighted data [W]{S} relative to the weighted model [W][R]. This can be done leaving the original model [R] and data {S} unaltered, by calculating a modified pseudoinverse matrix $[P_W]$ and least squares filtering matrix $[U_W]$ that operate directly on the unscaled data {S}, as follows:

1. Call the equally weighted pseudoinverse we have used up to now $[P_I^R]$ where the superscript indicates the sensor response matrix and the subscript indicates the diagonal weighting matrix. (An I subscript denotes the identity matrix and thus equal weighting of all sensors or an "unweighted fit".) Then $[P_I^{WR}]$ would be the pseudoinverse matrix appropriate for fitting weighted data [W]{S} to weighted model [W][R].

2. $[P_I^{WR}] = ([R]^T[W]^T[W][R])^{-1}[R]^T[W]^T$. Since [W] is diagonal, $[W]^T = [W]$ and $([W][W])_{ii} = W_{ii}^2$. Then

$$[P_I^{WR}] = ([R]^T[W^2][R])^{-1}[R]^T[W].$$

3. $[P_I^{WR}]$ operates on weighted data [W]{S} to obtain the best fit modal amplitudes $\{C_W\}$ as shown in

$$\{C_W\} = [P_I^{WR}][W]\{S\}.$$

We designate the weighted fit modal amplitudes by $\{C_W\}$ because in general they do not equal the unweighted fit modal amplitudes {C} if the residuals ({S} - {$\bar{S}$}) are not all zero. The modal amplitudes $\{C_W\}$ and {C} will be identical if all residuals are zero; otherwise they will differ such that {S} - [R]$\{C_W\}$ = {S} - {$\bar{S}_W$}} has smaller residuals for higher weighted sensors than the unweighted fit residuals {S} - {$\bar{S}$}.

4. However, we can define a weighted pseudoinverse $[P_W^R]$ equal to $[P_I^{WR}][W]$; then $[P_W^R]$, operating on unweighted data {S}, produces the same $\{C_W\}$ as $[P_I^{WR}]$ operating on weighted data [W]{S}. We can write the full definition

$$[P_W^R] = ([R]^T[W^2][R])^{-1}[R^T][W^2]$$

from which it follows that

$[P_W^R][R] = [I]$ as required.

5. Note that associated with the $[P_I^{WR}]$ matrix there is the least squares filtering matrix $[U_I^{WR}] = ([W][R])[P_I^{WR}]$ which transforms [W]{S} into its weighted estimate [W]{$\bar{S}_W$}. This unweighted [U] matrix, like those we have been dealing with so far, is symmetric. However, it operates consistently only with weighted inputs and outputs.

6. The $[P_W^R]$ matrix takes unweighted data {S} to modal amplitudes $\{C_W\}$; the matrix [R] takes $\{C_W\}$ back to $\{S_W\}$. Thus, we can define the weighted least squares filtering matrix $[U_W^R]$ as

$$[U_W^R] = [R][P_W^R].$$

By expanding both $[U_W^R]$ and $[U_I^{WR}]$, it can be shown that

$$[U_W^R] = [W]^{-1}[U_I^{WR}][W]$$

This means that $[U_W^R]$ performs exactly the same type of least squares fitting operation that $[U_I^{WR}]$ does, but it operates to and from the unweighted original form of the data.

7. Because of the premultiplication by $[W]^{-1}$ and postmultiplication by $[W]$, only the diagonal elements of $[U_W^R]$ and $[U_I^{WR}]$ are equal. Other elements of the two matrices are unequal; in fact, since $[U_I^{WR}]$ is symmetric, one can show

$$[U_W^R]_{ij} = \frac{W_j}{W_i}[U_I^{WR}]_{ij} \text{ and}$$

$$[U_W^R]_{ji} = \frac{W_i}{W_j}[U_I^{WR}]_{ij}, \text{ so}$$

$$[U_W^R]_{ji} = \frac{W_i^2}{W_j^2}[U_W^R]_{ij}$$

which if $W_i^2 \neq W_j^2$ makes $[U_W^R]$ nonsymmetric. This is useful because

   a. A nonsymmetric [U] matrix is clear evidence that a weighted fit is being performed, and

   b. The ratios of W_i to W_j can be recovered from $[U_W^R]$ without much difficulty, if there is any doubt. To do so, set $W_1 = 1$, $i = 1$, and calculate $W_j = ([U_W^R]_{ij}/[U_W^R]_{ji})^{1/2}$ for all $[U_W^R]_{ij} \neq 0$. Some zero entries can be defined using other values for i and the now-defined values of W_i; this procedure recovers all the W_i ratios within a related group of sensors, i. e., those which interacted (directly or through a chain of other sensors) in $[U_W^R]$. Note that sometimes sensors interact only within distinct groups, e. g., there is an axial gage group and a shear gage group, each with four of the eight sensors, in the unweighted [U] matrix for the Figure 5 layout. When this happens, one sensor of each successive group can be assigned $W_i = 1$ to get the ratios for that group. Since sensors and residuals do not interact between groups, there is no significance to ratios outside the group. Sensor grouping may differ for analyses with different weighting.

8. A reasonable question to ask is in what way the weighted and unweighted least squares fits differ; the answer lies in the residual vectors $\{\Psi\}$ and $\{\Psi_W\}$ where $\{\Psi\} = \{S\} - \{\overline{S}\}$ and $\{\Psi_W\} = \{S\} - \{\overline{S}_W\}$. The following graphic example and analytical discussion may help develop a feel for the significance of weighting functions, and point out some of the advantages and disadvantages of their use.

   a. Consider the case originally labeled [R"] in Section I.A. above, where (dropping the double primes) we had

$$[R] = \begin{bmatrix}1\\1\end{bmatrix},\ \{\gamma\} = \{1\text{ g, }350\ \mu\text{strain}\},$$

$$[W] = \begin{bmatrix}1 & 0\\0 & 1\end{bmatrix} \text{ (unweighted fit)},$$

$$[P] = [.5 \quad .5], \text{ and}$$

$$[U] = \begin{bmatrix}.5 & .5\\.5 & .5\end{bmatrix}.$$

Then assuming data point $\{S\}^T = \{4,2\}$, which represents actual sensor readings of $\{4\gamma_1, 2\gamma_2\}$ or {4 g, 700 μstrain}, we calculate

$$\{C\} = [P]\{S\} = 3.0$$

and

$$\{\bar{S}\} = [U]\{S\} = \begin{Bmatrix} 3.0 \\ 3.0 \end{Bmatrix} .$$

This "best-fit" solution is shown graphically in Figure A.1.

b. Also shown on Figure A.1 is a dashed line labeled "Amplitude, mode 1" and a dotted line at right angles labeled "Amplitude, residual mode". These lines are labeled in multiples of the column vectors of $[R^+]$, which is the [R] matrix extended by adding on a unit "residual mode" column to make it square. If there are n_s sensors and n_m modes, there will be $n_\Delta = n_s - n_m$ columns added, or only one added column in this case. For consistency, the {C} vector must also be extended to $\{C^+\}$ to include amplitudes for the residual modes. The columns to be added to the [R] matrix can be designated $\Delta_1, \Delta_2, \ldots \Delta_{n_\Delta}$ and thought of as the columns of a unitary n_s by n_Δ matrix [Δ] satisfying the conditions

$$[\Delta]^T[R] = [0]_{(n_\Delta,\ n_m)}$$

$$[\Delta]^T[\Delta] = [I]_{(n_\Delta,\ n_\Delta)}$$

c. An effective way of finding the columns of [Δ] can be derived from the above equations. From the first equation, it follows that $[R]^T[\Delta] = [0]_{(n_m,\ n_\Delta)}$. Also,

$$[P][\Delta] = ([R]^T[R])^{-1}[R]^T[\Delta]$$

$$= ([R]^T[R])^{-1}[0]_{(n_m,n_\Delta)}$$

$$= [0]_{(n_m,n_\Delta)}$$

Then defining

$$[R^+] = [R|\Delta]$$

and

$$[P^+] = \left[\frac{P}{\Delta^T}\right]$$

it follows that

$$[P^+][R^+] = \left[\frac{P}{\Delta^T}\right][R|\Delta]$$

$$= \left[\begin{array}{c|c} PR & P\Delta \\ \hline \Delta^T R & \Delta^T\Delta \end{array}\right]$$

$$= \left[\begin{array}{c|c} [I]_{(n_m,n_m)} & [0]_{(n_m,n_\Delta)} \\ \hline [0]_{(n_\Delta,n_m)} & [I]_{(n_\Delta,n_\Delta)} \end{array}\right]$$

$$= [I]_{(n_s,n_s)}.$$

Thus $[P^+] = [R^+]^{-1}$.

Therefore, we can write

$$[R^+][P^+] = [I]_{(n_s,n_s)}$$

$$= [R][P]+[\Delta][\Delta]^T$$

which gives

$$[I] - [U] = [\Delta][\Delta]^T.$$

The columns of [Δ] can now be found as follows:

(1) Set [Q] = [I]-[U]. Set j to 0 and [Δ] to an empty n_s by j matrix;

(2) Find the magnitude of the columns in the [Q] matrix, i.e., the column norms $\|Q_i\| = q_i$, $i = 1 \ldots n_s$.

(3) If all q_i are less than some small tolerance, quit with the finished [Δ].

(4) Otherwise, find an i for which q_i has maximum value, set j to j+1, and set $[\Delta]_j$ to $\frac{1}{q_i}[Q]_i$.

(5) Set $[Q]$ to $[Q]-[\Delta]_j[\Delta]_j^T$ and return to step (2).

d. Now consider the minimum variance case labeled $[R"']$ in I.A. above, where $\{\gamma"'\}^T$ = {1 g, 100 μstrain} and $[R"'] = \begin{bmatrix}1\\3.5\end{bmatrix}$. We can obtain this case in a weighted analysis using $[R] = \begin{bmatrix}1\\1\end{bmatrix}$, with $\{\gamma\}^T$ = {1 g, 350 μstrain} - both the same as before - but with $[W'] = \begin{bmatrix}1 & 0\\0 & 3.5\end{bmatrix}$. Then

$$[P^R_{W'}] = ([1\ 1]\begin{bmatrix}1 & 0\\0 & 12.25\end{bmatrix}\begin{bmatrix}1\\1\end{bmatrix})^{-1}[1\ 1]\begin{bmatrix}1 & 0\\0 & 12.25\end{bmatrix}$$

$$= \frac{1}{13.25}[1\ 12.25] \text{ and}$$

$$[U^R_{W'}] = \begin{bmatrix}1\\1\end{bmatrix}\frac{1}{13.25}[1\ \ 12.25]$$

$$= \frac{1}{13.25}\begin{bmatrix}1 & 12.25\\1 & 12.25\end{bmatrix}$$

(which is asymmetric, as expected).

The weighted fit of data point $\{S\}^T$ = {4,2} is then

$$\{\bar{S}_{W'}\} = [U^R_{W'}]\{S\}$$

$$= \frac{1}{13.25}\begin{bmatrix}1 & 12.25\\1 & 12.25\end{bmatrix}\begin{bmatrix}4\\2\end{bmatrix}$$

$$\cong \begin{bmatrix}2.15094\\2.15094\end{bmatrix}.$$

e. A graphical representation is shown on Figure A.2. Note that the orientation of the residual vector

$$\{\Psi_{W'}\} = \{S\} - \{\bar{S}_{W'}\}$$

$$= [\Delta_{W'}]\{C^+\}_2$$

has changed such that it is no longer perpendicular to the dashed line denoting mode 1 amplitudes. The effect has been to diminish the $\{\Psi_{W'}\}_2$ component of the residual at the expense of increasing the $\{\Psi_{W'}\}_1$ component compared to $\{\Psi\}_2$ and $\{\Psi\}_1$ from the unweighted fit. Also, the total length $\|\Psi_{W'}\|$ is greater than $\|\Psi\|$ from Figure A.1. The reason for this is that the least squares fit <u>is actually effected using the weighted model and weighted sensor data</u>; this is shown on Figure A.3. Figure A.2 looks odd because the values actually used on the fit have been scaled down by $[W']^{-1}$, i. e., the S_2 axis values have been shrunk to (1/3.5) of the values at which the fit was made.

f. For completeness, we can write, for consistency with previous definitions,

$$[\Delta^R_W] = [W]^{-1}[\Delta^{WR}_I],$$

$$[R^+_W] = [R|\Delta^R_W],$$

$$[(P^+)^R_W] = \left[\frac{P^R_W}{[\Delta^{WR}_I]^T[W]}\right]$$

$$= [R^+_W]^{-1}, \text{ and}$$

$$[U^R_W] = [I]-[W]^{-1}[\Delta^{WR}_I][\Delta^{WR}_I]^T[W].$$

However, the $[\Delta^R_W]$ are of less utility in the weighted fit case than $[\Delta]$ for the unweighted case. The chief features of interest for the $[\Delta^R_W]$ may be the weighted residual aliasing effects, evident as

$$[\alpha^R_W] = [P][\Delta^R_W]$$

which show the extent to which certain combinations of modal amplitudes that would be resolved in an <u>unweighted</u> least squares fit will disappear (i.e., be attributed completely to residual unmodeled effects) in a <u>weighted</u> least squares analysis.

Note that $[\Delta^R_W]$ is no longer unitary, since the $[W]^{-1}$ premultiplication means the columns may have euclidean norms greater

or less than one. Also, the columns will generally not be orthogonal. It is possible, of course, if $n_\Delta \geq 2$, to find an orthonormal set of n_Δ vectors $\{\delta\}$ such that

$$[U_W^R][\delta] = [0] \text{ and}$$

$$[\delta]^T[\delta] = [I]_{(n_\Delta, n_\Delta)},$$

but, because $[U_W^R]$ is asymmetric

$$[U_W^R] \neq [I] - [\delta][\delta]^T$$

and $[\frac{P_W^R}{\delta^T}] \neq [R|\delta]^{-1}$ because

$$[\frac{P_W^R}{\delta^T}][R|\delta] = [\frac{I_{(n_m,n_m)} \mid [0]_{n_m,n_\Delta}}{[\delta]^T[R] \mid I_{(n_\Delta,n_\Delta)}}]$$

where $[\delta]^T[R] \neq [0]_{(n_\Delta,n_m)}$.

9. Equalization of Consistency Checking Through Weighted Fits:

One application of weighting which may be useful is to equalize the extent of consistency checking among sensors, i. e., to make the diagonal of $[U_W^R]$ relatively uniform near n_m/n_s. To accomplish this, one takes a sensor response matrix [R] for which [U] shows at least some consistency checking for all sensors, (i. e., no $U_{ii} = 1$) and forms a trial [W] matrix whose elements $W_{ii} = (1-U_{ii})^{1/2}$.

The resulting weighted least squares filtering matrix $[U_W^R]$ will have much less diverse diagonal elements. If desired, the process can be continued

with $W'_{ii} = W_{ii}(1-[U_W^R]_{ii})^{1/2}$,

$W''_{ii} = W'_{ii}(1-[U_{W'}^R]_{ii})^{1/2}$, etc.,

where the diagonal elements become uniform quite rapidly.

Since only the ratios of the i^{th} and j^{th} elements on the [W] matrix diagonal are significant, it helps put the matrix in perspective to apply some normalization by scaling all the W_{ii} by the same factor, such that either the average or the harmonic mean W_{ii} will be 1.0, rather than letting all the $W_{ii}^{(n)}$ become smaller and smaller as would otherwise occur with the formulas above.

It is important that the variances and aliasing associated with the weighted $[P_W^R(n)]$ matrix be considered carefully before deciding to use it solely to obtain improved consistency checking, and even then pains should be taken to avoid use of a weighting matrix with elements larger than about 2 or smaller than about 1/2. Sensors with high weighting had too much consistency checking originally (relatively low U_{ii} values). Sensors with low weighting had too little consistency checking originally (U_{ii} values near 1.0). It appears preferable to alter the location or orientation of sensors with low U_{ii} values, or to replicate sensors with U_{ii} values near 1.0, instead of relying on a weighted fit to make major changes in the extent of consistency checking for different sensors.

II. ESTIMATING EFFECTS AND VARIANCES AT UNINSTRUMENTED AREAS

Effects at uninstrumented areas of interest can be calculated quite simply as follows:

A. Form a sensor response matrix $[R_d]$ as though there were sensors to be installed measuring the specific system point parameters of interest, $\{S_d\}$. The modal amplitude unit equivalents $\{\mu\}$ for $[R_d]$ must be consistent with those for the actual sensor matrix $[R]$; however, the "sensor" unit vector $\{\gamma_d\}$ can have any units convenient and consistent with the desired $\{S_d\}$ as long as $\{\gamma_d\}$ is used consistently in formulating $[R_d]$.

B. Form the matrix $[U_d]$ which translates $\{S\}$ directly into the desired system parameter estimates $\{\bar{S}_d\}$,

$$[U_d] = [R_d][P],$$

$$\{\bar{S}_d\} = [U_d]\{S\} = [U_d]\{\bar{S}\},$$

where $[P]$ is the usual pseudoinverse associated with the actual sensor matrix $[R]$.

C. The variance $\sigma^2(\{S_d\}_i)$ of the i^{th} desired system characteristic is given by

$$\sigma^2(\{S_d\}_i) = \Sigma_k [U_d]^2_{ik}\ \sigma^2(\{S\}_k)$$

and its units are the square of those implied by $\{\gamma_d\}$. The RMS noise level $\sigma(\{S_d\}_i)$ is just the corresponding square root, with units implied by $\{\gamma_d\}$.

D. Note carefully that it is generally not correct to assume that equality holds in

$$\sigma^2(\{S_d\}_i) \stackrel{?}{=} \Sigma_k [R_d]^2_{ik}\sigma^2(C_k)$$

using the known modal variances $\sigma^2(C_k)$. The reason for this is that C_k and $C_{k'}$ are not, in general, independent uncorrelated quantities. A change ΔS_i in the data from sensor i which produces a change $P_{ki}\Delta S_i$ in the value of C_k is always accompanied by a corresponding change $P_{k'i}\Delta S_i$ in the value of $C_{k'}$. The relationship between C_k and $C_{k'}$ cannot be expressed solely by $\sigma^2(C_k)$ and $\sigma^2(C_{k'})$, as for independent uncorrelated variates; rather, the covariance $\sigma^2_{kk'}(C)$ must also be known. The general estimator for the covariance of a zero-mean, time varying vector $\{X\}$ is

$$[\sigma^2\{X\}]_{ij} \simeq \frac{1}{n}\sum_{t=1}^{n} X_i(t)X_j(t)$$

or, if $X_i(t)$ is regarded as a matrix element X_{it},

$$[\sigma^2[X]] \simeq \frac{1}{n}[X][X]^T$$

It can be seen that if $[Y] = [A][X]$, then

$$[\sigma^2[Y]] \simeq \frac{1}{n}[A][X][X]^T[A]^T \text{ or}$$

$$[\sigma^2[A][X]] = [A][\sigma^2[X]][A]^T. \text{ Thus}$$

$$[\sigma^2[R_d][C]] = [R_d][\sigma^2[C]][R_d]^T$$

$$= [R_d][P][\sigma^2[S]][P]^T[R_d]^T$$

$$= [U_d][\sigma^2[S]][U_d]^T$$

Since sensor noise is assumed to be uncorrelated, $[\sigma^2[S]]$ is a diagonal matrix $[\text{diag}\{\sigma^2(S_i)\}]$ and the last expression above reduces, for diagonal elements $[\sigma^2[R_d][C]]_{ii}$, to

$$\Sigma_k [U_d]_{ik}[\sigma^2[S]]_{kk}[U_d]_{ik} =$$

$$\Sigma_k [U_d]^2_{ik}\sigma^2(S_k) = \sigma^2(\{S_d\}_i).$$

For sensor noise effects, only the $\sigma^2(\{S_d\}_i)$ variances are generally of interest. The covariances $[\sigma^2(S_d)]_{ij}$, while generally not zero, are of little interest unless further transformations of the $\{S_d\}$ are undertaken, in which case they should be accounted for.

It might be expected intuitively that clustered (rather than widely dispersed) sensor arrays tend to produce better $\{S_d\}$ variances if the $\{S_d\}$ are limited to the local areas where sensors are clustered. Figure A.4 shows the RMS noise level ratios expected for axial and shear strain (A = 90° and 45°, respectively) as a function of circumferential location angle T, for several gage layouts, including those mentioned previously in the paper. A uniform individual RMS strain gage noise level of 10 μstrain was assumed for all individual gages, and the RMS noise levels of the $\{S_d\}$ were divided by this uniform 10 μstrain assumed level. Noise level ratios less than 1.0 are, therefore, better than could be obtained by measuring $\{S_d\}$ directly with a single gage. The relevant strain gage layouts are sketched in along the T-axis. The data for Figure A.4 and the numerical noise ratios cited below are based on computing $\{S_d\}$ for axial and shear gages at 10 degree intervals around the circumference; the exact values of the noise ratios at in-between locations may vary slightly from those presented.

Several features shown by Figure A.4 are of interest:

1. For all layouts that show varying performance around the cylinder circumference, the best performance (i. e., lowest RMS noise ratio) occurs not at the gage stations themselves but rather at points in-between the most closely spaced gage stations.

2. The noise ratio for layouts using complete rosettes is better with shear-axial-shear rosettes than with hoop-shear-axial rosettes in all cases.

3. Uniform performance all around the circumference is provided when the gage stations are uniformly spaced (three full rosettes at 120 degree intervals or four two-gage stations at 90 degree intervals).

4. Comparing the one-quadrant rosette layout (T = 0, 45, 90) with the more typical two-quadrant layout (T = 0, 90, 180):

   a. There is a minor gain in optimum performance for the more clustered layout (best RMS noise ratios 0.731 vs. 0.776 axial and 0.631 vs. 0.670 shear).

   b. There is a major loss in the worst performing regions for the more clustered layout (worst RMS noise ratios 6.769 vs. 1.552 axial and 5.843 vs. 1.340 shear).

5. The eight-gage, four station layout provides equal RMS noise ratios (0.866) for both axial and shear strain. This performance is better than the nine-gage, equally spaced hoop-shear-axial rosette noise ratios for both axial strain (0.958) and shear strain (1.000). The eight gage layout does slightly better than the nine-gage, equally spaced shear-axial-shear rosette noise ratio for axial strain (0.896), but does not quite match the latter's noise ratio for shear strain (0.774).

If both gages at one of the [illegible] tions in the eight gage l[illegible] performance of the remai[illegible] is almost as good as the n[illegible] 90-180 layout with hoop rose[illegible] not much worse than the 0-90-180 layout with shear rosettes. This comparison and others are tabulated in Table A.1 using the RMS noise ratio, $\sigma(S_d(T,A))/\sigma_{gage}$ and assuming identical noise levels in all gages. They illustrate the advantages of (1) equally spaced stations, (2) shear-axial-shear "crowfoot" rosettes vice hoop-shear-axial rosettes when there are no hoop loads in the model, and (3) use of redundant stations with less than full rosettes, to allow for failure of all gages at a station. Note that only the eight-gage array can stand failure of a station. Failure of a station in any of the nine-gage arrays listed would also leave six gages, but only two stations; the [R] matrix resulting from two stations is always singular because there will be modes not sensed at either station or there will be nonzero combinations of modes whose effects add to zero at all six remaining gages (i. e., linearly dependent six-gage mode shapes). Failure of all gages at a station is conceivable considering dropped tool damage to station wiring,

failure of the glue bond for a rosette substrate, or failure of rosette moisture proofing.

Comparisons using model inaccuracies, gage factor inaccuracies, and gage placement and orientation errors show similar effects but are too extensive to include here. In general, clustering sensors to concentrate on local high interest areas produces minor improvements for heavily instrumented areas only at the expense of major, probably unacceptable errors and noise in areas away from the gage clustering. The rapidity with which this occurs can be appreciated by thinking of the diametral 0-90-180 three station layouts as slightly clustered versions of the equispaced 0-120-240 three station layouts. The 1:2 best-to-worst noise ratio is caused by only a 30° shift in two 120° station spacings.

Table 1. Results of Aliasing Study for Simply Supported Beam with Left Side Accelerometer Layout

Mode Being Checked	Modal Amplitude Percentage of Mode Being Checked That is Aliased into Modes Being Measured				
	Mode 1	Mode 3	Mode 5	Mode 7	Mode 9
1	100				
2	83	53	-15	8	-7
3		100			
4	-30	68	62	-21	15
5			100		
6	15	-21	62	68	-30
7				100	
8	-7	8	-15	53	83
9					100
10					
11					-100
12	7	-8	15	-53	-83
13				-100	
14	-15	21	-62	-68	30
15			-100		
16	30	-68	-62	21	-15
17		-100			
18	-83	-53	15	-8	7
19	-100				
20					
21	100				
22	83	53	-15	8	-7
23		100			
24	-30	68	62	-21	15
25			100		
26	15	-21	62	68	-30
27				100	
28	-7	8	-15	53	83
29					100
30					
31					-100
32	7	-8	15	-53	-83
33				-100	
34	-15	21	-62	-68	30
35			-100		
36	30	-68	-62	21	-15
37		-100			
38	-83	-53	15	-8	7
39	-100				
40					
41	100				
42	83	53	-15	8	-7
43		100			
44	-30	68	62	-21	15
45			100		
46	15	-21	62	68	-30
47				100	
48	-7	8	-15	53	83
49					100
50					

Table 2. Results of Aliasing Study for Simply Supported Beam with Accelerometers Located Exactly at Multiples of 2L/11

Mode Being Checked	Modal Amplitude Percentage of Mode Being Checked That is Aliased into Modes Being Measured				
	Mode 1	Mode 3	Mode 5	Mode 7	Mode 9
1	100				
2					-100
3		100			
4				-100	
5			100		
6			-100		
7				100	
8		-100			
9					100
10	-100				
11					
12	100				
13					-100
14		100			
15				-100	
16			100		
17			-100		
18				100	
19		-100			
20					100
21	-100				
22					
23	100				
24					-100
25		100			
26				-100	
27			100		
28			-100		
29				100	
30		-100			
31					100
32	-100				
33					
34	100				
35					-100
36		100			
37				-100	
38			100		
39			-100		
40				100	
41		-100			
42					100
43	-100				
44					
45	100				
46					-100
47		100			
48				-100	
49			100		
50			-100		

Table 3. Results of Aliasing Study for Simply Supported Beam With Accelerometers Located at Multiples of 2L/11 Rounded to Nearest L/1000

Mode Being Checked	Modal Amplitude Percentage of Mode Being Checked That is Aliased into Modes Being Measured				
	Mode 1	Mode 3	Mode 5	Mode 7	Mode 9
1	100				
2				-1	-100
3		100			
4			-1	-100	
5			100		
6		-1	-100		
7				100	
8	-1	-100			
9					100
10	-99				
11				1	-1
12	101				
13	1	-1	1	-2	-99
14	-1	100			
15	-1	1	-1	-100	1
16		-1	100		
17	1	-1	-100	1	
18			-1	100	
19	-2	-100	1		
20				-1	100
21	-99	1			
22	-1	1	-1	1	-2
23	101	1			
24	1	-1	1	-2	-99
25	-2	100	1		
26	-1	1	-2	-99	1
27	1	-1	100	1	
28	1	-2	-99	1	
29	-1	1	-1	100	1
30	3	-99	1		
31	1	-1	1	-2	101
32	-98	1			
33	-1	1	-1	2	-3
34	102	1			
35	1	-1	2	-3	-99
36	-3	101	1		
37	-2	2	-3	-99	1
38	1	-2	100	1	
39	2	-3	-99	2	
40	-1	1	-2	100	1
41	-3	-99	1	-1	
42	1	-1	1	-2	101
43	-98	1			
44	-1	1	-2	2	-4
45	102	1			
46	2	-2	2	-4	-98
47	-3	101	2	-1	
48	-2	2	-4	-99	2
49	2	-3	101	2	
50	3	-4	-99	2	-1

Table 4. Results of Aliasing Study for Simply Supported Beam With Accelerometers Located at Multiples of 2L/11 Rounded to Nearest L/100

Mode Being Checked	Modal Amplitude Percentage of Mode Being Checked That is Aliased into Modes Being Measured				
	Mode 1	Mode 3	Mode 5	Mode 7	Mode 9
1	100				
2	-4	4	-5	8	-103
3		100			
4	4	-5	7	-101	-4
5			100		
6	-5	7	-101	-4	1
7				100	
8	8	-102	-4	1	
9					100
10	-105	-3	1		
11	4	-4	5	-6	11
12	94	-2	1		
13	-8	8	-10	15	-105
14	9	97	-3	1	
15	8	-9	14	-102	-8
16	-5	8	98	-4	1
17	-10	14	-101	-9	2
18	4	-5	8	98	-3
19	16	-102	-9	3	-1
20	-4	4	-5	8	96
21	-108	-7	2	-1	
22	8	-8	10	-13	22
23	86	-4	1	-1	
24	-11	12	-15	22	-106
25	19	94	-6	2	-1
26	11	-13	19	-101	-12
27	-11	16	95	-7	2
28	-14	19	-101	-14	4
29	8	-10	16	94	-6
30	22	-102	-14	4	-1
31	-8	8	-10	17	92
32	-110	-11	3	-1	
33	11	-12	14	-19	33
34	76	-5	2	-1	
35	-14	16	-19	28	-107
36	29	89	-9	3	-1
37	15	-17	24	-100	-17
38	-16	25	91	-9	3
39	-16	24	-99	-20	5
40	12	-14	25	90	-8
41	27	-100	-20	6	-2
42	-11	12	-15	26	86
43	-109	-17	5	-2	1
44	14	-15	18	-24	44
45	66	-5	2	-1	
46	-17	19	-22	33	-106
47	39	84	-10	4	-1
48	17	-20	28	-97	-23
49	-21	34	86	-11	3
50	-21	28	-96	-26	6

Table 5. Results of Aliasing Study for Simply Supported Beam With Accelerometers Located at Even Multiples of 2L/11 Rounded to Nearest L/20

Mode Being Checked	Modal Amplitude Percentage of Mode Being Checked That is Aliased into Modes Being Measured				
	Mode 1	Mode 3	Mode 5	Mode 7	Mode 9
1	100				
2	2	1	-11		-157
3		100			
4	-16	-32	15	-88	-25
5			100		
6	-21	-6	-106	3	65
7				100	
8	37	-85	-24	14	38
9					100
10	-98	24	31	-8	-45
11	9	15	-9	-51	16
12	81	12	44	-5	-54
13	7	3	-38	-1	-149
14	23	94	-19	26	32
15	-27	-68	24	-59	-41
16	-8	-3	73	1	85
17	-51	-12	-85	5	83
18	-10	-17	10	88	-17
19	74	-56	-38	15	59
20					
21	-74	56	38	-15	-59
22	10	17	-10	-88	17
23	51	12	85	-5	-83
24	8	3	-73	-1	-85
25	27	68	-24	59	41
26	-23	-94	19	-26	-32
27	-7	-3	38	1	149
28	-81	-12	-44	5	54
29	-9	-15	9	51	-16
30	98	-24	-31	8	45
31					-100
32	-37	85	24	-14	-38
33				-100	
34	21	6	106	-3	-65
35			-100		
36	16	32	-15	88	25
37		-100			
38	-2	-1	11		157
39	-100				
40					
41	100				
42	2	1	-11		-157
43		100			
44	-16	-32	15	-88	-25
45			100		
46	-21	-6	-106	3	65
47				100	
48	37	-85	-24	14	38
49					100
50	-98	24	31	-8	-45

Table A.1. Results from a Noise Ratio Performance Study for Several Strain Gage Layouts

Number of Gages	Station Locations (T)	Rosette Angles (A)	RMS Noise Ratio Performance		Remarks
			Axial Best/Worst (ratio)	Shear Best/Worst (ratio)	
9	0-90-180	0-45-90	0.830/1.659 (1:2)	0.866/1.732 (1:2)	Traditional-diametral stations, "hoop" rosette
9	0-90-180	45-90-135	0.776/1.552 (1:2)	0.670/1.340 (1:2)	Diametral stations, "crowfoot" rosette
9	0-45-90	45-90-135	0.731/6.769 (1:9.26)	0.631/5.843 (1:9.26)	Crowded stations.
8	0-90-180-270	45-90	0.866 uniform	0.866 uniform	Eight gage optimum, equispaced stations.
6	0-90-180	45-90	0.866/1.732 (1:2)	0.866/1.732 (1:2)	Eight gage with one station's gages failed.
9	0-120-240	0-45-90	0.958 uniform	1.000 uniform	Equispaced "hoop" rosettes.
9	0-120-240	45-90-135	0.896 uniform	0.774 uniform	Equispaced "crowfoot" rosettes.

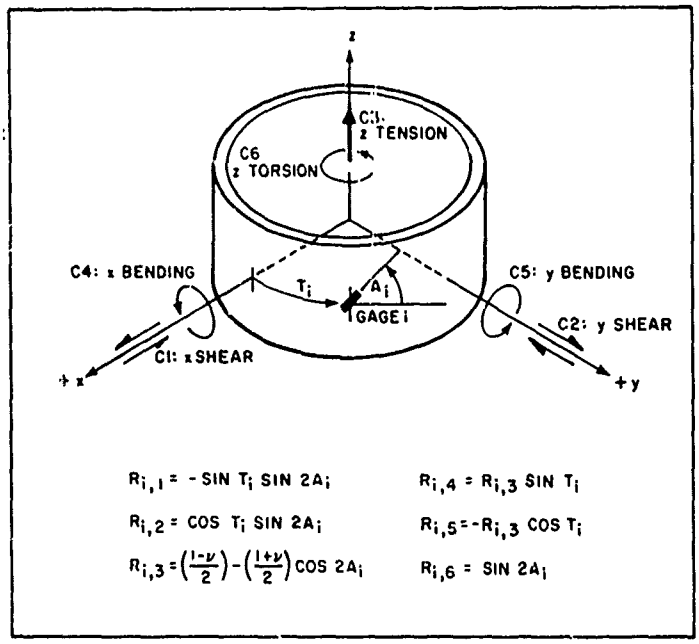

Figure 1. Coordinate System, Force Definition and Response Formulas Used in Evaluating Strain Gage Layouts

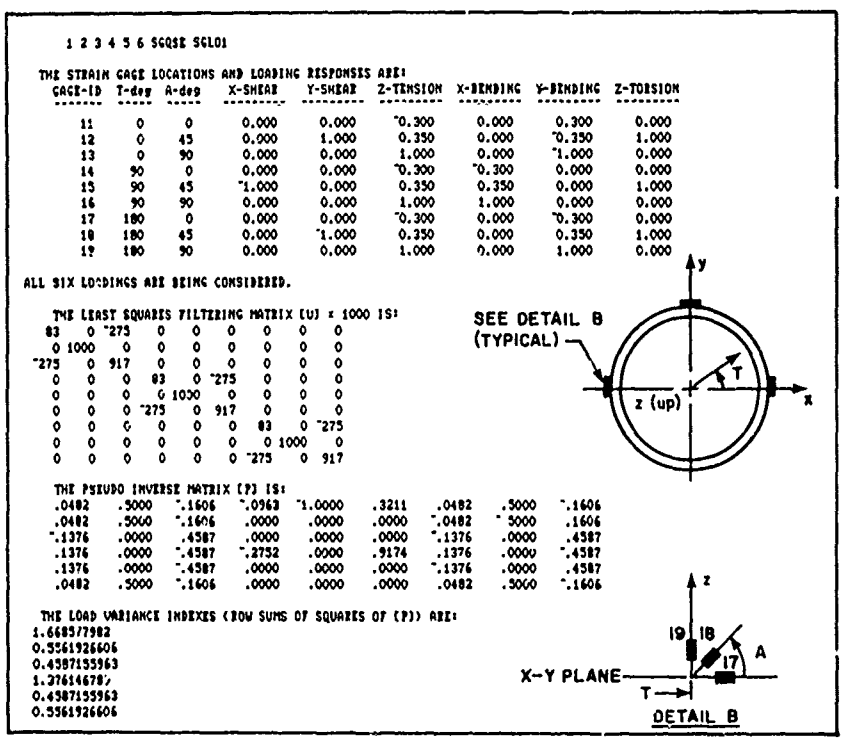

```
 1 2 3 4 5 6 SGQSE SGLOI

THE STRAIN GAGE LOCATIONS AND LOADING RESPONSES ARE:
 GAGE-ID  T-deg  A-deg   X-SHEAR   Y-SHEAR   Z-TENSION  X-BENDING  Y-BENDING  Z-TORSION
    11      0      0      0.000     0.000     -0.300      0.000      0.300      0.000
    12      0     45      0.000     1.000      0.350      0.000     -0.350      1.000
    13      0     90      0.000     0.000      1.000      0.000     -1.000      0.000
    14     90      0      0.000     0.000     -0.300     -0.300      0.000      0.000
    15     90     45     -1.000     0.000      0.350      0.350      0.000      1.000
    16     90     90      0.000     0.000      1.000      1.000      0.000      0.000
    17    180      0      0.000     0.000     -0.300      0.000     -0.300      0.000
    18    180     45      0.000    -1.000      0.350      0.000      0.350      1.000
    19    180     90      0.000     0.000      1.000      0.000      1.000      0.000

ALL SIX LOADINGS ARE BEING CONSIDERED.

   THE LEAST SQUARES FILTERING MATRIX (U) x 1000 IS:
  83    0 -275    0    0    0    0    0    0
   0 1000    0    0    0    0    0    0    0
-275    0  917    0    0    0    0    0    0
   0    0    0   83    0 -275    0    0    0
   0    0    0    0 1000    0    0    0    0
   0    0    0 -275    0  917    0    0    0
   0    0    0    0    0    0   83    0 -275
   0    0    0    0    0    0    0 1000    0
   0    0    0    0    0 -275    0  917

   THE PSEUDO INVERSE MATRIX (P) IS:
   .0482    .5000   -.1606   -.0963   -1.0000    .3211    .0482    .5000   -.1606
   .0482    .5000   -.1606    .0000    .0000    .0000   -.0482    .5000    .1606
  -.1376    .0000    .4587    .0000    .0000    .0000   -.1376    .0000    .4587
   .1376    .0000   -.4587   -.2752    .0000    .9174    .1376    .0000   -.4587
   .1376    .0000   -.4587    .0000    .0000    .0000   -.1376    .0000    .4587
   .0482    .5000   -.1606    .0000    .0000    .0000    .0482    .5000   -.1606

 THE LOAD VARIANCE INDEXES (ROW SUMS OF SQUARES OF (P)) ARE:
1.6685779B2
0.5561926606
0.4587155963
1.276146787
0.4587155963
0.5561926606
```


Figure 2. Sketch of and Quantitative Evaluation Results for First Strain Gage Layout on a Thin-Walled Cylinder

1 2 3 4 5 6 SGQSE SGL02

THE STRAIN GAGE LOCATIONS AND LOADING RESPONSES ARE:

GAGE-ID	T-deg	A-deg	X-SHEAR	Y-SHEAR	Z-TENSION	X-BENDING	Y-BENDING	Z-TORSION
21	0	45	0.000	1.000	0.350	0.000	-0.350	1.000
22	0	90	0.000	0.000	1.000	0.000	-1.000	0.000
23	0	135	0.000	-1.000	0.350	0.000	-0.350	-1.000
24	90	45	-1.000	0.000	0.350	0.350	0.000	1.000
25	90	90	0.000	0.000	1.000	1.000	0.000	0.000
26	90	135	1.000	0.000	0.350	0.350	0.000	-1.000
27	180	45	0.000	-1.000	0.350	0.000	0.350	1.000
28	180	90	0.000	0.000	1.000	0.000	1.000	0.000
29	180	135	0.000	1.000	0.350	0.000	0.350	-1.000

ALL SIX LOADINGS ARE BEING CONSIDERED.

THE LEAST SQUARES FILTERING MATRIX [U] x 1000 IS:

598	281	-402	0	0	0	0	0	0
281	803	281	0	0	0	0	0	0
-402	281	598	0	0	0	0	0	0
0	0	0	598	281	-402	0	0	0
0	0	0	281	803	281	0	0	0
0	0	0	-402	281	598	0	0	0
0	0	0	0	0	0	598	281	-402
0	0	0	0	0	0	281	803	281
0	0	0	0	0	0	-402	281	598

THE PSEUDO INVERSE MATRIX [P] IS:

.2500	.0000	-.2500	-.5000	.0000	.5000	.2500	.0000	-.2500
.2500	.0000	-.2500	.0000	.0000	.0000	-.2500	.0000	.2500
.1406	.4016	.1406	.0000	.0000	.0000	.1406	.4016	.1406
-.1406	-.4016	-.1406	.2811	.8032	.2811	-.1406	-.4016	-.1406
-.1406	-.4016	-.1406	.0000	.0000	.0000	.1406	.4016	.1406
.2500	.0000	-.2500	.0000	.0000	.0000	.2500	.0000	-.2500

THE LOAD VARIANCE INDEXES (ROW SUMS OF SQUARES OF [P]) ARE:

0.75
0.25
0.4016064257
1.204819277
0.4016064257
0.25

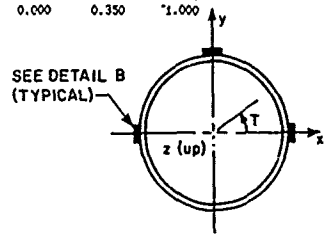

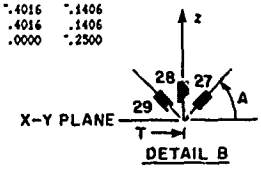

Figure 3. Sketch of and Quantitative Evaluation Results for Second Strain Gage Layout on a Thin-Walled Cylinder

1 2 3 4 5 6 SGQSE SGL03

THE STRAIN GAGE LOCATIONS AND LOADING RESPONSES ARE:

GAGE-ID	T-deg	A-deg	X-SHEAR	Y-SHEAR	Z-TENSION	X-BENDING	Y-BENDING	Z-TORSION
31	0	45	0.000	1.000	0.350	0.000	-0.350	1.000
32	0	90	0.000	0.000	1.000	0.000	-1.000	0.000
33	0	135	0.000	-1.000	0.350	0.000	-0.350	-1.000
34	45	45	-0.707	0.707	0.350	0.247	-0.247	1.000
35	45	90	0.000	0.000	1.000	0.707	-0.707	0.000
36	45	135	0.707	-0.707	0.350	0.247	-0.247	-1.000
37	90	45	-1.000	0.000	0.350	0.350	0.000	1.000
38	90	90	0.000	0.000	1.000	1.000	0.000	0.000
39	90	135	1.000	0.000	0.350	0.350	0.000	-1.000

ALL SIX LOADINGS ARE BEING CONSIDERED.

THE LEAST SQUARES FILTERING MATRIX [U] x 1000 IS:

598	281	-402	0	0	0	0	0	0
281	803	281	0	0	0	0	0	0
-402	281	598	0	0	0	0	0	0
0	0	0	598	281	-402	0	0	0
0	0	0	281	803	281	0	0	0
0	0	0	-402	281	598	0	0	0
0	0	0	0	0	0	598	281	-402
0	0	0	0	0	0	281	803	281
0	0	0	0	0	0	-402	281	598

THE PSEUDO INVERSE MATRIX [P] IS:

.8536	.0000	-.8536	-1.2071	.0000	1.2071	.3536	.0000	-.3536
-.3536	.0000	.3536	1.2071	.0000	-1.2071	-.8536	.0000	.8536
.4799	1.3712	.4799	-.6787	-1.9391	-.6787	.4799	1.3712	.4799
-.4799	-1.3712	-.4799	.6787	1.9391	.6787	-.1988	-.5680	-.1988
.1988	.5680	.1988	-.6787	-1.9391	-.6787	.4799	1.3712	.4799
.8536	.0000	-.8536	-1.2071	.0000	1.2071	.8536	.0000	-.8536

THE LOAD VARIANCE INDEXES (ROW SUMS OF SQUARES OF [P]) ARE:

4.621320344
4.621320344
9.36293514
7.423807781
7.423807781
5.828427125

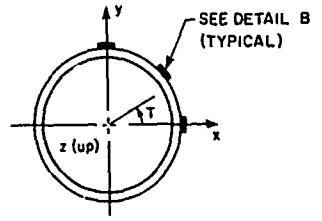

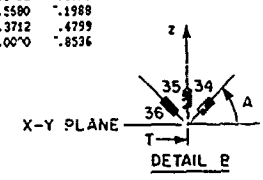

Figure 4. Sketch of and Quantitative Evaluation Results for Third Strain Gage Layout on a Thin-Walled Cylinder

1 2 3 4 5 6 SCQSE SGL04

THE STRAIN GAGE LOCATIONS AND LOADING RESPONSES ARE:

GAGE-ID	T-deg	A-deg	X-SHEAR	Y-SHEAR	Z-TENSION	X-BENDING	Y-BENDING	Z-TORSION
41	0	45	0.000	1.000	0.350	0.000	-0.350	1.000
42	0	90	0.000	0.000	1.000	0.000	-1.000	0.000
43	90	45	-1.000	0.000	0.350	0.350	0.000	1.000
44	90	90	0.000	0.000	1.000	1.000	0.000	0.000
45	180	45	0.000	-1.000	0.350	0.000	0.350	1.000
46	180	90	0.000	0.000	1.000	0.000	1.000	0.000
47	270	45	1.000	0.000	0.350	-0.350	0.000	1.000
48	270	90	0.000	0.000	1.000	-1.000	0.000	0.000

ALL SIX LOADINGS ARE BEING CONSIDERED.

THE LEAST SQUARES FILTERING MATRIX [U] x 1000 IS:

750	0	250	0	-250	0	250	0
0	750	0	250	0	-250	0	250
250	0	750	0	250	0	-250	0
0	250	0	750	0	250	0	-250
-250	0	250	0	750	0	250	0
0	-250	0	250	0	750	0	250
250	0	-250	0	250	0	750	0
0	250	0	-250	0	250	0	750

THE PSEUDO INVERSE MATRIX [P] IS:

.0000	.0000	-.5000	.1750	.0000	.0000	.5000	-.1750
.5000	-.1750	.0000	.0000	-.5000	.1750	.0000	.0000
.0000	.2500	.0000	.2500	.0000	.2500	.0000	.2500
.0000	.0000	.0000	.5000	.0000	.0000	.0000	-.5000
.0000	-.5000	.0000	.0000	.0000	.5000	.0000	.0000
.2500	-.0875	.2500	-.0875	.2500	-.0875	.2500	-.0875

THE LOAD VARIANCE INDEXES (ROW SUMS OF SQUARES OF [P]) ARE:

0.56125
0.56125
0.25
0.5
0.5
0.280625

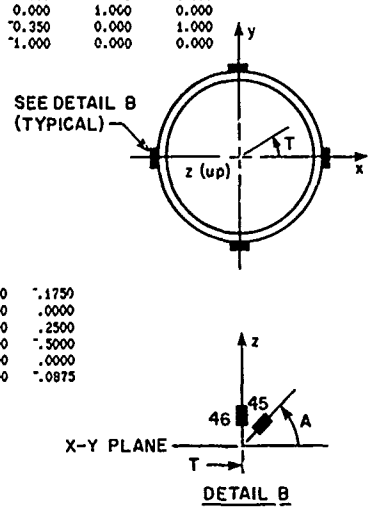

Figure 5. Sketch of and Quantitative Evaluation Results for Fourth Strain Gage Layout on a Thin-Walled Cylinder

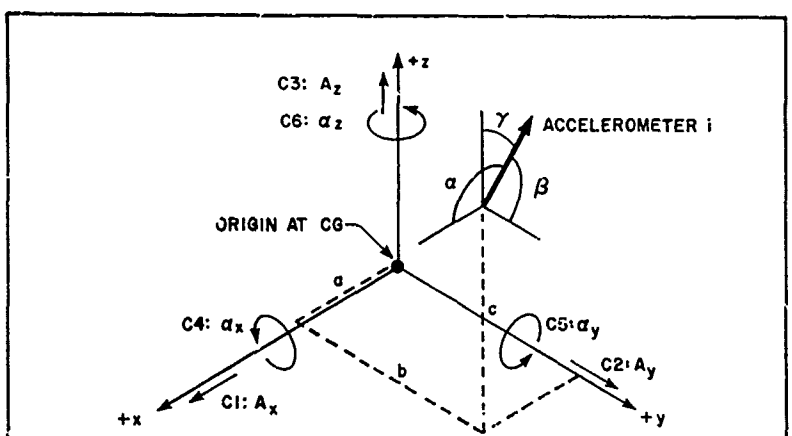

$R_{i,1} = \cos\alpha$ $\qquad$ $R_{i,4} = (b\cos\gamma - c\cos\beta)$

$R_{i,2} = \cos\beta$ $\qquad$ $R_{i,5} = (c\cos\alpha - a\cos\gamma)$

$R_{i,3} = \cos\gamma$ $\qquad$ $R_{i,6} = (a\cos\beta - b\cos\alpha)$

Figure 6 Coordinate System, CG Acceleration Definition and Response Formulas Used for Calculating Rigid Body CG Accelerations

```
      1 2 3 4 5 6 MEASURE BODY1

 THE ACCELEROMETER LOCATIONS AND DIRECTION COSINES ARE:
  GAGE-ID     X        Y        Z       COS-X    COS-Y    COS-Z
  -------   -----    -----    -----     -----    -----    -----
     11     25.00     0.00    50.00     0.000    1.000    0.000
     12      0.00    25.00    50.00     1.000    0.000    0.000
     13      0.00    25.00    50.00     0.000    0.000    1.000
     14     25.00     0.00   -50.00     0.000    1.000    0.000
     15      0.00    25.00   -50.00     1.000    0.000    0.000
     16    -25.00     0.00   -50.00     0.000    1.000    0.000

   THE FULL RESPONSE MATRIX IS:
      0.000   1.000   0.000  -50.00     0.00    25.00
      1.000   0.000   0.000    0.00    50.00   -25.00
      0.000   0.000   1.000   25.00     0.00     0.00
      0.000   1.000   0.000   50.00     0.00    25.00
      1.000   0.000   0.000    0.00   -50.00   -25.00
      0.000   1.000   0.000   50.00     0.00   -25.00

 ALL SIX CG ACCELERATIONS ARE BEING RETAINED.

    THE LEAST SQUARES FILTERING MATRIX [U] x 1000 IS:
 1000    0    0    0    0    0
    0 1000    0    0    0    0
    0    0 1000    0    0    0
    0    0    0 1000    0    0
    0    0    0    0 1000    0
    0    0    0    0    0 1000

    THE PSEUDO INVERSE MATRIX [P] IS:
     .0000    .5000    .0000    .5000    .5000   -.5000
     .5000    .0000    .0000    .0000    .0000    .5000
     .2500    .0000   1.0000   -.2500    .0000    .0000
    -.0100    .0000    .0000    .0100    .0000    .0000
     .0000    .0100    .0000    .0000   -.0100    .0000
     .0000    .0000    .0000    .0200    .0000   -.0200

    (VARIANCE OF CG ACCELERATIONS)/(VARIANCE OF ACCELEROMETER READINGS)
 1
 0.5
 1.125
 2E-6
 2E-6
 8E-6
```

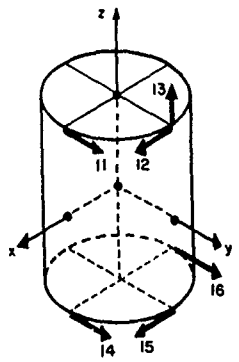

Figure 7. Sketch of and Quantitative Evaluation Results for First Accelerometer Layout on a Rigid Body

```
      1 2 3 4 5 0 MEASURE BODY2

 THE ACCELEROMETER LOCATIONS AND DIRECTION COSINES ARE:
  GAGE-ID     X        Y        Z       COS-X    COS-Y    COS-Z
  -------   -----    -----    -----     -----    -----    -----
     21     25.00     0.00    50.00     1.000    0.000    0.000
     22      0.00    25.00    50.00     0.000    1.000    0.000
     23      0.00     0.00    50.00     0.000    0.000    1.000
     24     25.00     0.00   -50.00     1.000    0.000    0.000
     25      0.00    25.00   -50.00     0.000    0.707    0.707
     26      0.00   -25.00   -50.00     0.000   -0.707    0.707

   THE FULL RESPONSE MATRIX IS:
      1.000   0.000   0.000    0.00    50.00     0.00
      0.000   1.000   0.000  -50.00     0.00     0.00
      0.000   0.000   1.000    0.00     0.00     0.00
      1.000   0.000   0.000    0.00   -50.00     0.00
      0.000   0.707   0.707   53.03     0.00     0.00
      0.000  -0.707   0.707  -53.03     0.00     0.00

  CG ACC. BEING RETAINED ARE: X-ACC  Y-ACC  Z-ACC  ALPH-X ALPH-Y

   THE REDUCED RESPONSE MATRIX IS:
 1       0       0       0      50
 0       1       0     -50       0
 0       0       1       0       0
 1       0       0       0     -50
 0       0.707   0.707  53.025   0
 0      -0.707   0.707 -53.025   0

                          THE LEAST SQUARES FILTERING MATRIX [U] x 1000 IS:
                       1000    0    0    0    0    0
                          0 1000    0    0    0    0
                          0    0  500    0  354  354
                          0    0    0 1000    0    0
                          0    0  354    0  750 -250
                          0    0  354    0 -250  750

    THE PSEUDO INVERSE MATRIX [P] IS:
     .5000    .0000    .0000    .5000    .0000   -.0000
     .0000    .6000    .0000    .0000    .2829   -.2829
     .0000    .0000    .5001    .0000    .3536    .3536
     .0000   -.0080    .0000    .0000    .0057   -.0057
     .0100    .0000    .0000   -.0100    .0000    .0000

    (VARIANCE OF CG ACCELERATIONS)/(VARIANCE OF ACCELEROMETER READINGS)
 0.5
 0.5200483346
 0.5000755114
 1.2801933386-6
 2E-6
```

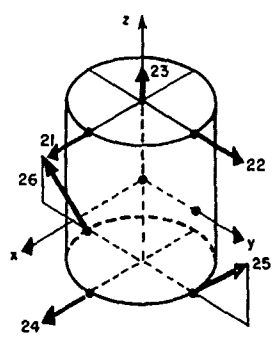

Figure 8. Sketch of and Quantitative Evaluation Results for Second Accelerometer Layout on a Rigid Body

```
    MSQSEA BEAMEQ1

THE ACCELEROMETER LOCATIONS AND DIRECTION COSINES ARE:
 GAGE-ID     X       Y       Z      COS-X   COS-Y   COS-Z
 -------   -----   -----   -----   -----   -----   -----
    11      2.00    0.00    0.00   0.000   0.000   1.000
    12      4.00    0.00    0.00   0.000   0.000   1.000
    13      6.00    0.00    0.00   0.000   0.000   1.000
    14      8.00    0.00    0.00   0.000   0.000   1.000
    15     10.00    0.00    0.00   0.000   0.000   1.000

  THE MODE SHAPES BEING CONSIDERED ARE:
   GAGE     MODE     MODE     MODE
    ID        1        2        3
   ----     ----     ----     ----
    11     0.500    0.866    1.000
    12     0.866    0.866    0.000
    13     1.000    0.000   -1.000
    14     0.866   -0.866    0.000
    15     0.500   -0.866    1.000

  THE LEAST SQUARES FILTERING MATRIX [U] x 1000 IS:
 667  394  167 -106  167
 394  500  289    0 -106
-167  289  667  289 -167
-106    0  289  500  394
 167 -106 -167  394  667

  THE PSEUDO INVERSE MATRIX [P] IS:
  .1667    .2887    .3333    .2887    .1667
  .2887    .2887    .0000   -.2887   -.2887
  .3333    .0000   -.3333    .0000    .3333

THE MODAL AMPLITUDE VARIANCE INDEXES (ROW SUMS OF SQUARES OF [P]) ARE:
  .3333
  .3334
  .3333
```

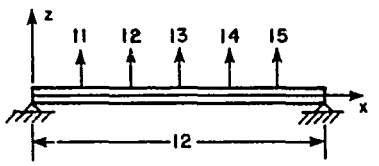

Figure 9. Equally Spaced Accelerometer Layout and Quantitative Results for Measurement of Modes 1,2 and 3 of a Simply Supported Beam

```
    MSQSEA BEAMEQ2

THE ACCELEROMETER LOCATIONS AND DIRECTION COSINES ARE:
 GAGE-ID     X       Y       Z      COS-X   COS-Y   COS-Z
 -------   -----   -----   -----   -----   -----   -----
    11      2.00    0.00    0.00   0.000   0.000   1.000
    12      4.00    0.00    0.00   0.000   0.000   1.000
    13      6.00    0.00    0.00   0.000   0.000   1.000
    14      8.00    0.00    0.00   0.000   0.000   1.000
    15     10.00    0.00    0.00   0.000   0.000   1.000

  THE MODE SHAPES BEING CONSIDERED ARE:
   GAGE     MODE     MODE     MODE
    ID        1        3        5
   ----     ----     ----     ----
    11     0.500    1.000    0.500
    12     0.866    0.000   -0.866
    13     1.000   -1.000    1.000
    14     0.866    0.000   -0.866
    15     0.500    1.000    0.500

  THE LEAST SQUARES FILTERING MATRIX [U] x 1000 IS:
 500    0    0    0  500
   0  500    0  500    0
   0    0 1000    0    0
   0  500    0  500    0
 500    0    0    0  500

  THE PSEUDO INVERSE MATRIX [P] IS:
  .1667    .2887    .3333    .2887    .1667
  .3333    .0000   -.3333    .0000    .3333
  .1667   -.2887    .3333   -.2887    .1667

THE MODAL AMPLITUDE VARIANCE INDEXES (ROW SUMS OF SQUARES OF [P]) ARE:
  .3333
  .3333
  .3333
```

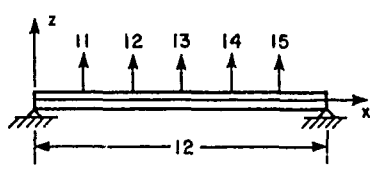

Figure 10. Equally Spaced Accelerometer Layout and Quantitative Results for Measurement of Modes 1,3 and 5 of a Simply Supported Beam

```
    MSQSEA BEAMNE3

 THE ACCELEROMETER LOCATIONS AND DIRECTION COSINES ARE:
  GAGE-ID     X       Y       Z      COS-X   COS-Y   COS-Z
  -------   -----   -----   -----   -----   -----   -----
     21      1.20    0.00    0.00   0.000   0.000   1.000
     22      2.40    0.00    0.00   0.000   0.000   1.000
     23      3.60    0.00    0.00   0.000   0.000   1.000
     24      4.80    0.00    0.00   0.000   0.000   1.000
     25      6.00    0.00    0.00   0.000   0.000   1.000

  THE MODE SHAPES BEING CONSIDERED ARE:
   GAGE     MODE    MODE    MODE    MODE    MODE
    ID        1       3       5       7       9
   ----    ----    ----    ----    ----    ----
     21    0.309   0.809   1.000   0.809   0.309
     22    0.588   0.951   0.000  -0.951  -0.588
     23    0.809   0.309  -1.000   0.309   0.809
     24    0.951  -0.588   0.000   0.588  -0.951
     25    1.000  -1.000   1.000  -1.000   1.000

  THE LEAST SQUARES FILTERING MATRIX [U] x 1000 IS:
1000    0    0    0    0
   0 1000    0    0    0
   0    0 1000    0    0
   0    0    0 1000    0
   0    0    0    0 1000

  THE PSEUDO INVERSE MATRIX [P] IS:
  .1236   .2352   .3236   .3804   .2000
  .3236   .3804   .1236  -.2352  -.2000
  .4000   .0000  -.4000   .0000   .2000
  .3236  -.3804   .1236   .2352  -.2000
  .1236  -.2352   .3236  -.3804   .2000

 THE MODAL AMPLITUDE VARIANCE INDEXES (ROW SUMS OF SQUARES OF [P])  *:
  .3600
  .3600
  .3600
  .3600
  .3600
```

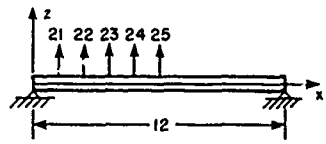

Figure 11. Left Side Accelerometer Layout and Quantitative Results for Measurement of the First Five Odd Modes of a Simply Supported Beam

```
    MSQSEA BEAMNE5

 THE ACCELEROMETER LOCATIONS AND DIRECTION COSINES ARE:
  GAGE-ID     X       Y       Z      COS-X   COS-Y   COS-Z
  -------   -----   -----   -----   -----   -----   -----
     31      2.18    0.00    0.00   0.000   0.000   1.000
     32      4.36    0.00    0.00   0.000   0.000   1.000
     33      6.55    0.00    0.00   0.000   0.000   1.000
     34      8.73    0.00    0.00   0.000   0.000   1.000
     35     10.91    0.00    0.00   0.000   0.000   1.000

  THE MODE SHAPES BEING CONSIDERED ARE:
   GAGE     MODE    MODE    MODE    MODE    MODE
    ID        1       3       5       7       9
   ----    ----    ----    ----    ----    ----
     31    0.541   0.990   0.282  -0.756  -0.910
     32    0.910  -0.282  -0.541   0.990  -0.756
     33    0.990  -0.910   0.756  -0.541   0.282
     34    0.756  -0.541  -0.910   0.282   0.990
     35    0.282   0.756   0.990   0.910   0.541

  THE LEAST SQUARES FILTERING MATRIX [U] x 1000 IS:
1000    0    0    0    0
   0 1000    0    0    0
   0    0 1000    0    0
   0    0    0 1000    0
   0    0    0    0 1000

  THE PSEUDO INVERSE MATRIX [P] IS:
  .1966   .3308   .3599   .2748   .1024
  .3599  -.1024  -.3308   .1966   .2748
  .1024  -.1966   .2748  -.3308   .3599
 -.2748   .3599  -.1966  -.1024   .3308
 -.3308  -.2748   .1024   .3599  -.1966

 THE MODAL AMPLITUDE VARIANCE INDEXES (ROW SUMS OF SQUARES OF [P]) ARE:
  .3636
  .3636
  .3636
  .3636
  .3636
```

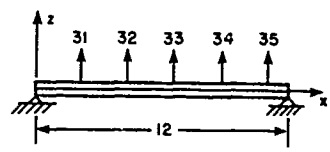

Figure 12. Layout With Accelerometers at Multiples of 2L/11 and Quantitative Results for Measurement of the First Five Modes of a Simply Supported Beam

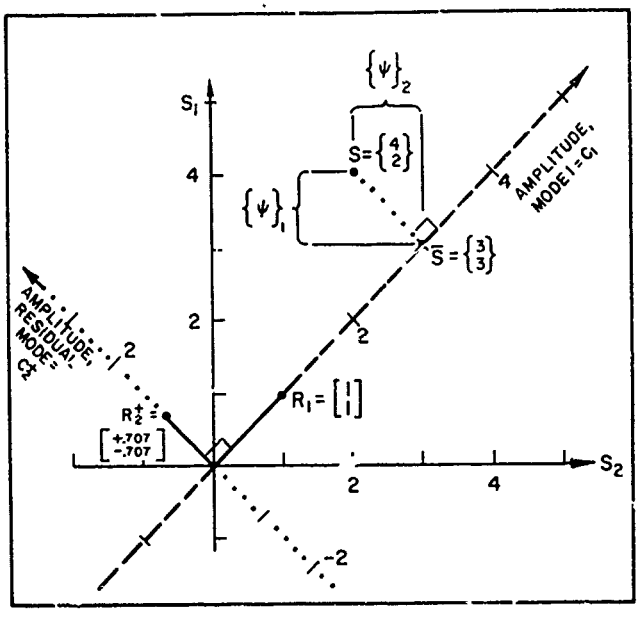

Figure A.1. Unweighted Fit of $\begin{Bmatrix}4\\2\end{Bmatrix}$ to $\begin{bmatrix}1\\1\end{bmatrix}$

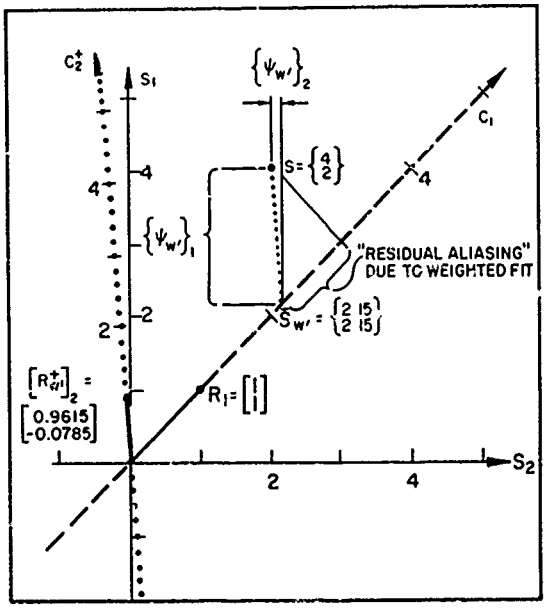

Figure A.2. Weighted Fit of $\begin{Bmatrix}4\\2\end{Bmatrix}$ to $\begin{bmatrix}1\\1\end{bmatrix}$ with $w' = \begin{bmatrix}1 & 0\\0 & 3.5\end{bmatrix}$

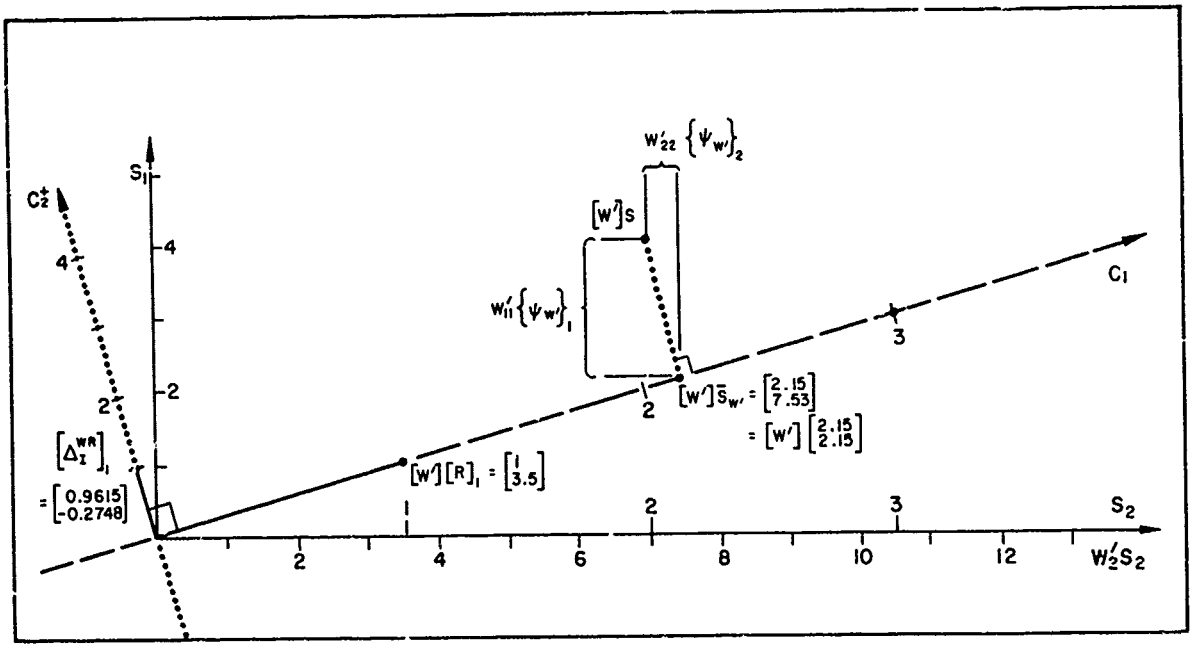

Figure A.3. Unweighted Fit of $[w']\begin{Bmatrix}4\\2\end{Bmatrix}$ to $[w'][R]$ with $[w'] = \begin{bmatrix}1 & 0\\0 & 3.5\end{bmatrix}$

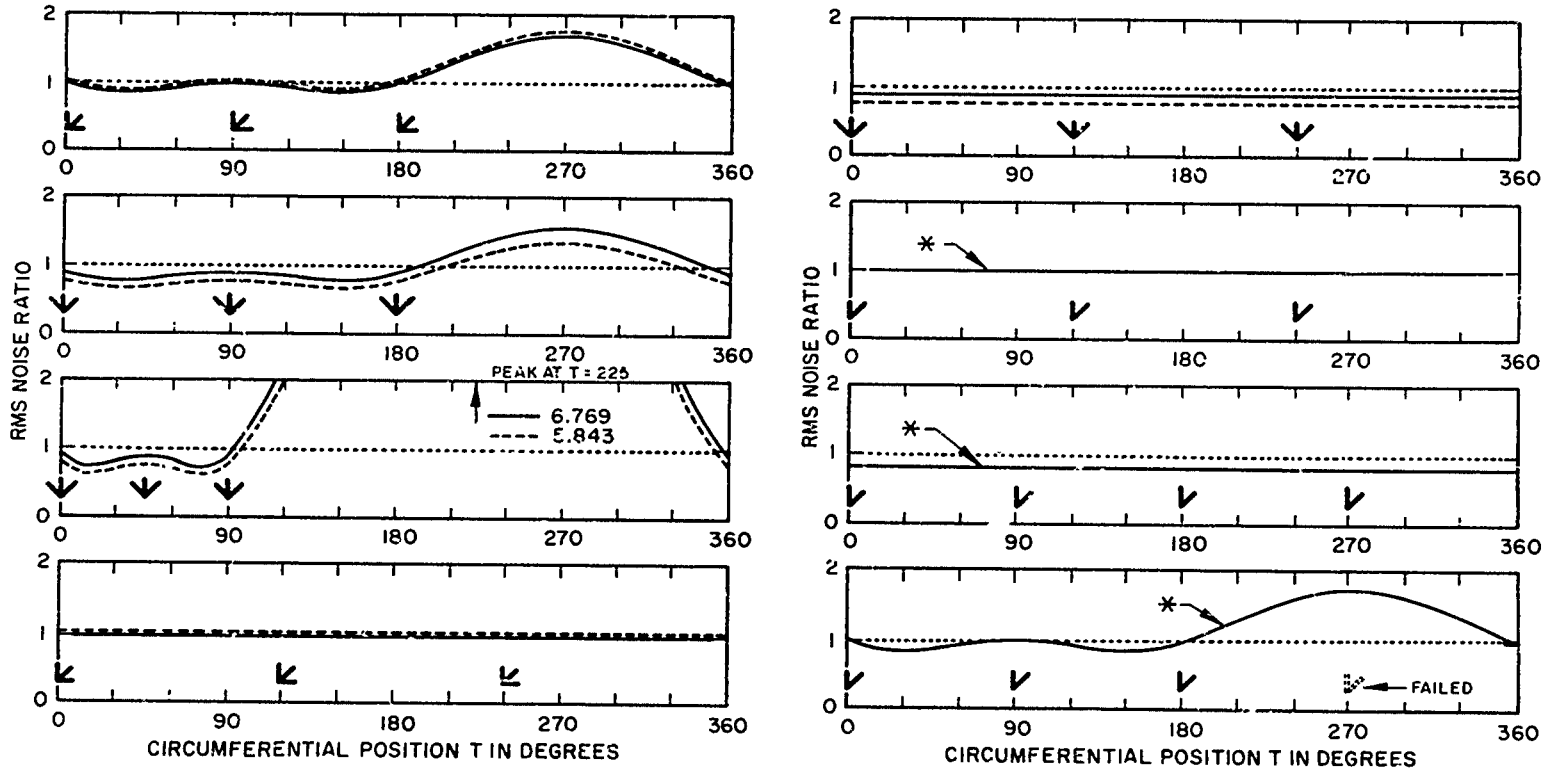

Figure A.4. RMS Noise Ratio of Calculated Axial Strain and Shear Strain Vs Position for Different Strain Gage Layouts on a Thin-Walled Cylinder

SHOCK ANALYSIS

A SUMMARY OF EXPERIMENTAL RESULTS ON SQUARE PLATES AND STIFFENED PANELS SUBJECTED TO AIR-BLAST LOADING

t. Houlston and J.E. Slater
Defence Research Establishment
Suffield, Ralston, Alberta, Canada

In combat operations, warships could be subjected to air blast and underwater shock loads capable of causing significant local damage. As part of a vulnerability and survivability study to improve Canadian warship design standards, square steel plates and stiffened panels were instrumented with pressure gauges, strain gauges, accelerometers, and displacement gauges, and then exposed to air-blast waves of various magnitudes and durations. This paper will summarize the experimental results obtained for the square plates and for the first stiffened panel tested.

1. INTRODUCTION

Metal plates or panels are fundamental elements in many military structures. Ships, in particular, are composed primarily of stiffened metal panels that make up the hull, decks, bulkheads and superstructure. In modern warfare, naval ships could be subjected to considerable air blast and underwater shock loads. Two distinctive types of response are induced by these loads. One is a local response of the panels and attached structure and equipment, while the other is a global response involving the whole ship in an overall flexural or whipping form of vibration. For effective warship design against air blast and underwater shock threats, a fundamental and detailed understanding of shock wave loading and the associated structural response is required. Knowledge in this area is also required for assessments of vulnerability and survivability of structures subjected to shock loading.

In recognition of these requirements, the Defence Research Establishment Suffield (DRES) is currently conducting research on shock wave-structure interaction to advance the state-of-art in structural response to air blast and underwater shock loading. A previous paper [1] outlined the testing facilities at DRES, and presented sample experimental and finite element results for the structural response of a square plate and a stiffened panel exposed to air-blast waves. The present paper will present a summary of the experimental results from these and other tests. In particular, Section 2 and 3 will present experimental results for the square plate tests and the stiffened panel tests, respectively, discussed in Reference 1. Section 3 will also present some preliminary experimental results from a stiffened panel subjected to a long duration blast wave from a ground burst at the U.S. Defence Nuclear Agency's event MINOR SCALE.

2. SQUARE PLATES

2.1 Introduction

The main objective of the square plate tests was to provide fundamental information on the structural response of a square plate with built in boundary conditions to spatially uniform air-blast loadings with various magnitudes and durations. Section 2.2 will briefly review the experimental procedure, equipment and instrumentation, and signal processing for the tests. Results are then presented and discussed in Section 2.3.

2.2 Experimental rocedure, Instrumentation and Tests

Reference 1 gives details regarding the experimental procedure, instrumentation and tests. This section will briefly review some of the details and present additional information as required.

The plates tested had effective dimensions of 508 mm x 508 mm and thicknesses of either 3.4 mm or 1.5 mm. Each test consisted of detonating a charge suspended directly above the centre of the plate at a known standoff distance. The plates were positioned on the plate mounting system illustrated in Figure 1. This system was designed to give fully clamped boundary conditions and to reduce the effects of reflected shock. Four pressure transducers (P1-P4) were mounted around the periphery of each plate with one or two under it. The tests were carried out at two experimental facilities at DRES: the Blast Chamber and Height-of-Burst Site (HOB site). Tables 1 and 2 summarize selected details from tests completed at each facility, respectively. Whilst several plates were tested, only one was fully instrumented with strain gauges and accelerometers. The

instrumentation layout is shown in Figure 2. All the tests listed in Table 1 were done on this plate as was test 4 in Table 2.

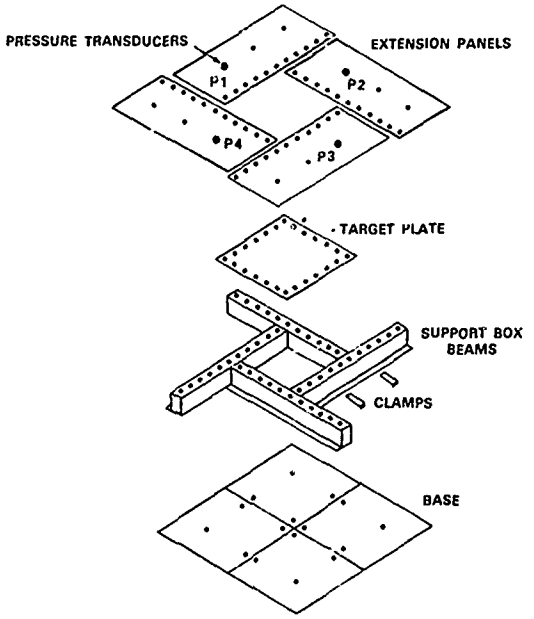

Figure 1. Exploded View of Plate Mounting System.

Table 1

SUMMARY OF THE BLAST CHAMBER TESTS WITH THE SQUARE PLATE

(Plate Thickness 3.4 mm)

TEST*	CHARGE MASS (g)	CHARGE STANDOFF (cm)	OVER PRESSURE (kPa)	PULSE DURATION (ms)
1	113	305	55.0	2.0
2	227	305	79.0	2.0
3	227	305	82.7	2.0
4	397	244	172	2.0
5	908	305	207	2.0
6	908	305	207	2.0
7	908	200	689	1.5

* All tests done on the same plate.

Table 2

SUMMARY OF THE HOB TESTS WITH THE SQUARE PLATES

TEST*	PLATE THICKNESS (mm)	STAND OFF (cm)	PEAK PRESSURE (kPa)	CENTRAL DEFLECTION (mm)
1	3.4	305	3720	38
2	1.5	305	3450	86
3	3.4	244	5520	52
4	3.4**	244	6890	47
5	1.5	244	6890	102

* All tests done with charge mass of 14.5 kg.

** Deformed plate from Blast Chamber tests.

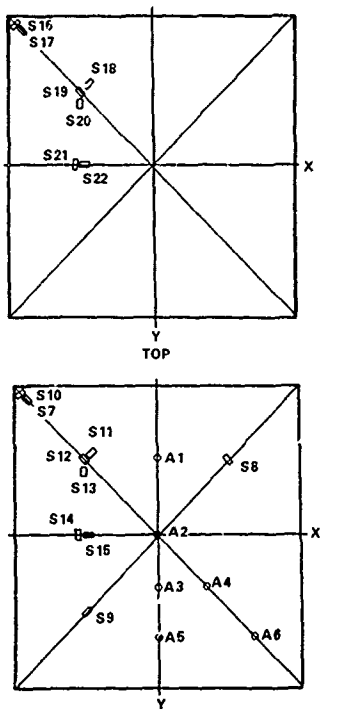

Figure 2. Strain Gauge (S) and Accelerometer (A) Positions for Test Series 1.

In addition to the tests listed in Tables 1 and 2, an additional plate of thickness 12.7 mm was instrumented with eight pressure transducers (P5 to P12) as shown in Figure 3 and tested at both the blast chamber and HOB facilities. The pressure transducers P1 to P4 shown in Figure 1 were also included. The purpose of these tests was to verify that the pressure distribution over the plate was spatially uniform. The first test on this plate consisted of suspending a 227 g charge 3.05 m above the panel in the blast chamber. The second test consisted of suspending a 3600 g charge 1.92 m above the plate at the HOB site.

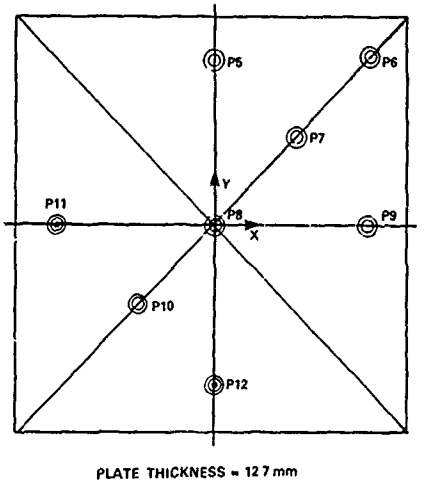

Figure 3. Location of Pressure Transducers P5 – P12 Used for Plate Loading Test.

2.3 Discussion of Results

Reference 1 gives a general discussion of the results and signal processing techniques applied for the square plate tests. The following sub-sections will summarize the experimental results obtained in the blast chamber and HOB tests. Whilst only a representative sampling of the data will be presented due to space limitations, a complete database of results has been created.

2.3.1 Blast Chamber Tests

Since spatial uniformity of the pressure loading on the plate surface was required, the result of the blast chamber test on the plate instrumented with pressure transducers was first examined. Figure 4 shows a plot of all the pressure transducer signals (P1-P12). Although there is some variation in the arrival times of the pressure wave for each transducer, it was concluded that the pressure distribution for each time point was spatially uniform to sufficient accuracy.

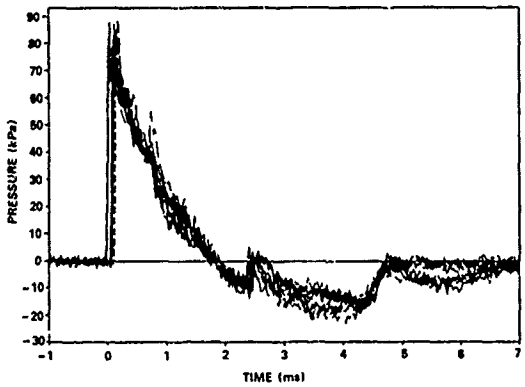

Figure 4. Summary Plots of Pressure Transducer Signals (P1 to P12) from the Blast Chamber Plate Loading Test.

In order to compare a low and high level loading case, summary results will now be presented for Tests 1 and 5 in Table 1. Figure 5(a) shows the pressure curves for Test 1 and Figure 5(b) those for Test 5. The loading

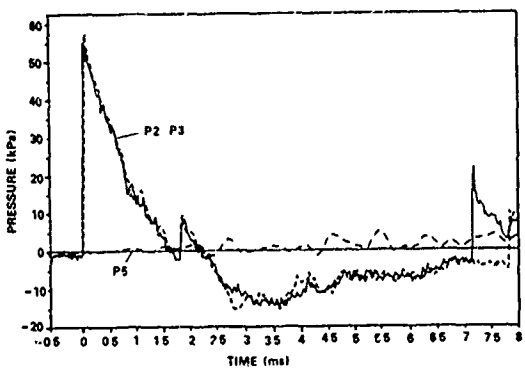

Figure 5(a). Plot of Pressure Against Time for Test 1 from the Transducers P2, P3 and P5.

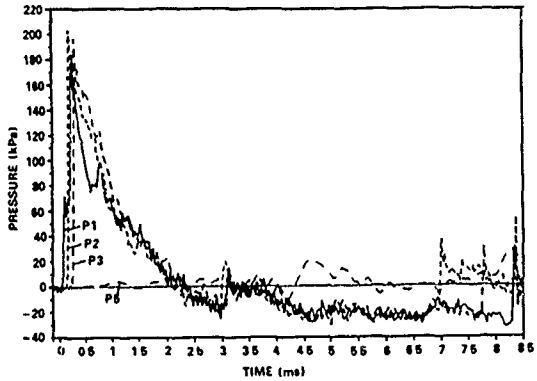

Figure 5(b). Plot of Pressure Against Time for Test 5 from the Transducers P1, P2, P3 and P5.

condition was considered to be satisfactory in each case since the pressure transducers around the plate periphery (Figure 1) gave similar pressure traces. The pressure transducers omitted from the plots (P1 and P4 in Figure 5(a) and P4 in Figure 5(b)) failed to remain fully operational during the tests. The positive duration is approximately 2 ms for both Test 1 Test 5. In each case the second shock can be seen at approximately 1.7 ms and 3 ms, respectively.

For the loading condition being investigated, the structural response of the plate should be symmetrical about the x and y axis shown in Figure 2. In order to check this, the response of strain gauge S8 was compared with that of S11. Similarly, the response of S9 was compared with S12. If the plate response is symmetrical then the strains should compare favourably. Figure 6 shows a plot of the strains for Test 5. The result indicates a satisfactory comparison of S8, S11 and S9, S12.

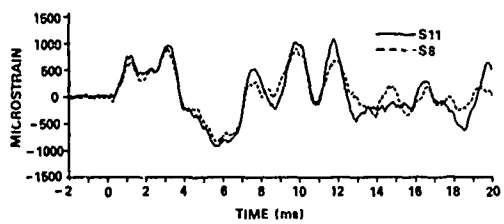

Figure 6(a). Plot of Strain for Test 5 from Strain Gauges S8 and S11.

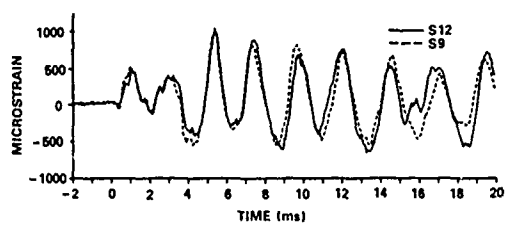

Figure 6(b). Plot of Strain for Test 5 from Strain Gauges S9 and S12.

Additional information on the structural response of the plate was found by calculating the Fourier transform of the signal from S18 and also that from S19 for Test 1. The results are shown in Figures 7(a) and 7(b). For comparison purposes the mode shapes and frequencies presented in Reference 1 are given as Figure 8. These results were determined from tests with a Modal Analyzer and by calculation with the computer program VAST [2]. The information in Figure 8 shows that mode shapes associated with the frequencies of 118 Hz and 407 Hz (435 Hz from VAST calculation) are those that are expected to be excited by a spatially constant pressure distribution. Figures 7(a) and 7(b) show that significant response does occur around these frequencies. In particular, S18 has significant response in the region of 118 Hz with minor peaks around 407 Hz. S19 has significant response in the region of 407 Hz with a minor peak around 118 Hz.

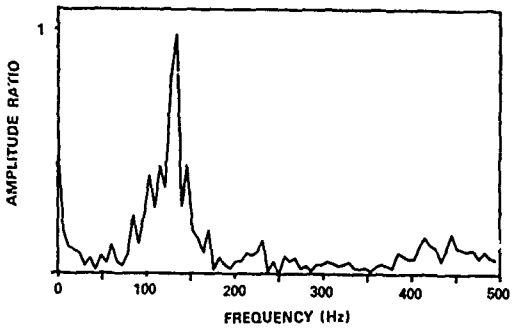

Figure 7(a). Frequency Spectrum for Strain Gauge S18 in Test 1.

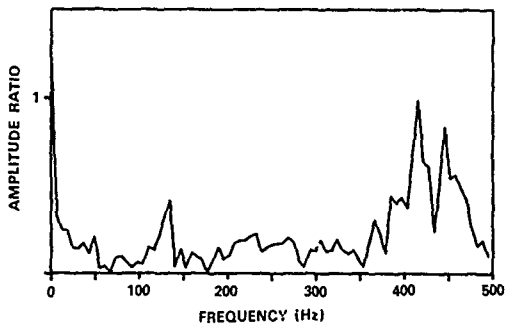

Figure 7(b) Frequency Spectrum for Strain Gauge S19 in Test 1.

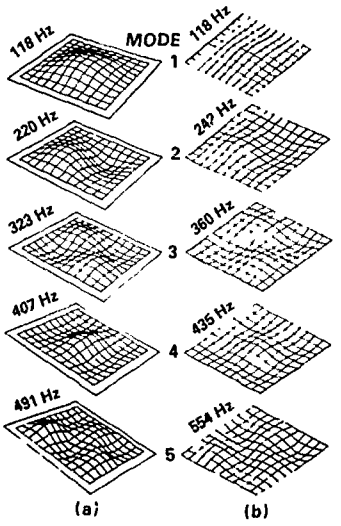

Figure 8. Mode Shape Patterns for Square Plate from (a) Modal Analyzer Tests and (b) VAST Program Predictions.

The displacement time histories will next be considered. Figures 9(a) and 9(b) show the displacements obtained by double integration of the accelerometer signals from accelerometers A1 to A6 shown in Figure 2. The peak displacements in Figure 9(a) are in reasonable agreement with the results of finite element calculations presented previously [1, Figure 23]. Comparing Figures 9(a) and 9(b) shows that the times of peak response decrease with amplitude. For example, in Figure 9(a) the first negative peak for A2 is reached at 2.5 ms, while in Figure 9(b) this peak is at 2.1 ms. Comparison of the displacement distributions to those obtained from linear and nonlinear finite element calculations [3] indicates that this effect is caused by significant membrane forces that develop when the displacements become large with respect to the plate thickness. The membrane forces cause the stiffness to increase and thus the period to decrease as displacement increases. Figure 10, which shows a summary plot of accelerometer A1 displacement for Tests 1 to 6, also shows the nonlinear effect of decrease of period with amplitude.

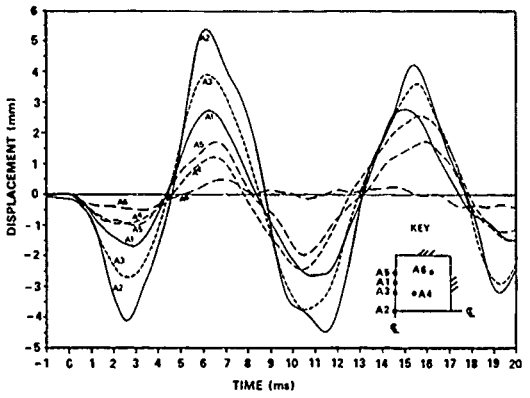

Figure 9(a). Displacement Time History Plots for Test 1: Accelerometers A1 – A6.

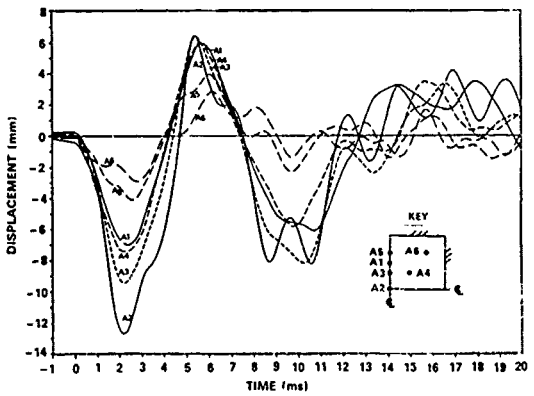

Figure 9(b). Displacement Time History Plots for Test 5: Accelerometers A1 – A6.

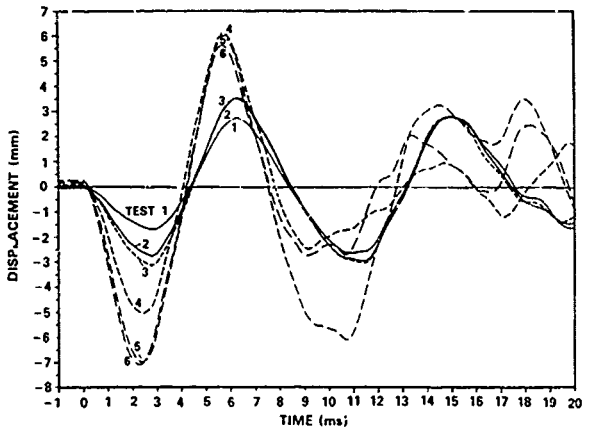

Figure 10. Displacement Time History Plots for Tests 1 to 6. Accelerometer A1.

Some representative strain time histories will next be examined. Figure 11(a) shows strain time histories for the surface pair of strain gauges S22 and S15. In order to explain these results, the significant features of the plate response are summarized as follows.

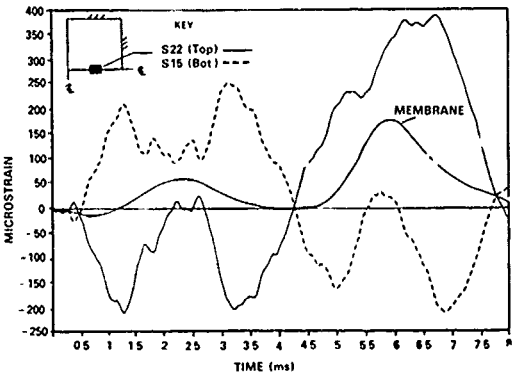

Figure 11(a). Strain Time History Plots for Test 1: Strain Gauges S15 (Bottom Surface) and S22 (Top Surface).

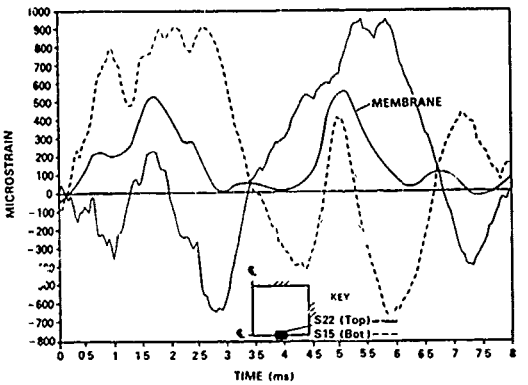

Figure 11(b) Strain Time History Plots: Strain Gauges S15 (Bottom Surface) and S22 (Top Surface).

Time 0.3 ms to 0.5 ms

The surface strains increase to a small local maximum at 0.4 ms due to a bending wave that moves from the plate edges toward the plate centre (Reference 1, Figure 23). As shown by a distinct peak in the plate centre acceleration time history plot shown in Figure 12(a), the bending wave reaches the plate centre at about 0.6 ms and causes the plate centre to be rapidly decelerated.

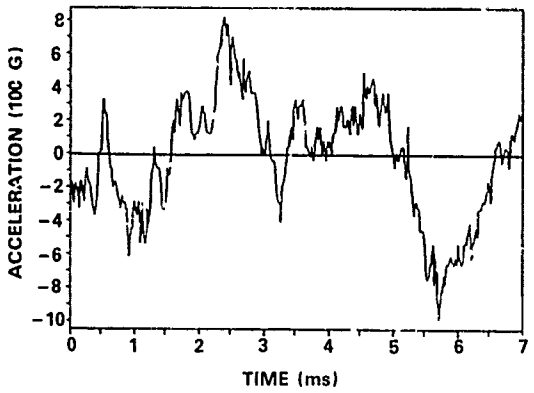

Figure 12(a) Acceleration Time History Plot for Test 1: Accelerometer A2.

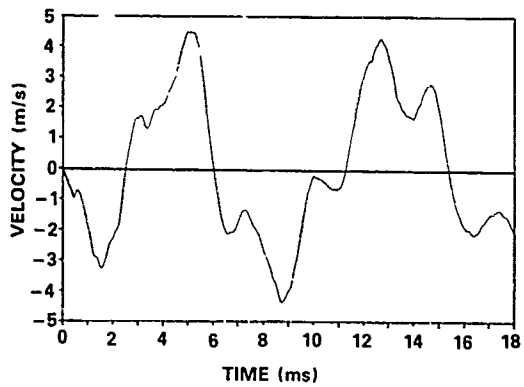

Figure 12(b) Velocity Time History Plot for Test 1: Accelerometer A2.

Time 0.5 ms to 1.25 ms

After the abrupt deceleration at 0.6 ms the plate centre continues to be increasingly accelerated downwards with a maximum value of acceleration occurring at approximately 1 ms. Since the plate surface becomes concave shaped during this time, the top surface strain (S22 in Figure 11(a)) becomes increasingly compressive and the bottom surface strain (S15) becomes increasingly tensile. At approximately 1.25 ms, a local minimum and maximum occurs in the top and bottom surface strains, respectively. Figure 11(a) shows that pure bending action has been dominant in the plate response to this point. Essentially no membrane strain has developed.

Time 1.25 ms to 2.5 ms

Between approximately 1 ms and 1.6 ms, the acceleration of the plate centre decreases from its maximum downward value to zero. Figure 11(a) indicates that between these times there is a reduction in bending strain and a small increase in membrane strain. At 1.6 ms the strain curves also show an inflection similar to that which occurred at 0.4 ms. This inflection occurs when the maximum plate displacement reaches the plate centre (Reference 1, Figure 23(b) and 23(c)). It is of interest to note that this is an effect that would not occur for a circular plate.

Between 1.6 ms and about 2.5 ms the acceleration of the plate centre increases from zero to its maximum upward value, and at 2.5 ms the centre plate displacement (Figure 9(a)) achieves its maximum downward value. Between these times there is also a significant decrease in bending strain and increase in membrane strain such that the two are approximately equal when the plate centre has reached its peak downward deflection at 2.5 ms (Figure 11(a)).

Time 2.5 ms to 4.5 ms

From 2.5 ms to 4.5 ms the plate centre rebounds from its maximum downward displacement to the zero position. Figure 11(a) shows that at 3.2 ms the bending strain has again become a maximum and the membrane strain has been significantly reduced. Also near this time the acceleration curve shows a localised negative peak. This observation makes it clear that the centre initially attains such a high velocity on rebound that its motion is suddenly arrested at 3.2 ms. A small inflection in the displacement curve at 3.2 ms for the plate centre (accelerometer A2) is also evident in Figure 9(a) and for the strain curves in Figure 11(a). At 4.2 ms the surface strains become zero, which indicates that the area of plate around strain gauges S22 and S15 has reached the zero position. This indication is also given by the displacements associated with accelerometers A1, A3 and A5 in Figure 9(a). At a slightly later time (4.5 ms approximately) the plate centre reaches the zero position.

Time 4.5 ms to 8.75 ms

Between 4.5 ms and 8.75 ms the plate centre achieves its maximum upward deflection and then returns to the zero position. From 4.2 ms to 5 ms the bending strain goes from zero to a local maximum with essentially no membrane strain being developed. Between 5 ms and approximately 6 ms the membrane strain builds up to a peak value and becomes equal to the bending strain, and the deflection of the plate centre achieves a maximum value which is about 29% higher than the magnitude of the minimum displacement that occurred at 2.5 ms. This increase in displacement is due to the negative phase in the pressure signal shown in Figure 5(a). The pressure curves show, in fact, that between 2 and about 3.5 ms the negative phase achieves a magnitude of approximately 27% the positive phase magnitude. This increased pressure increases the upward acceleration of the plate (see Figure 12(a)) and thus a greater magnitude of displacement is achieved (5.4 mm centre displacement at 6 ms compared with 4.2 mm at 2.5 ms). From 6 ms to about 6.8 ms the plate centre is rapidly accelerated downwards with an associated reduction in membrane strain and an increase in bending strain. As anticipated because of the negative phase loading, the velocity of the plate centre is greater at 6.8 ms (2 m/s in Figure 12(b)) than at the equivalent point of 3.2 ms (1.75 m/s) on the downward deflection. The deceleration after membrane recovery is thus greater and gives a more pronounced inflection on the displacement time graph as shown by the curve for A2 at approximately 7 ms in Figure 9(a). The centre of the plate returns to the zero position at about 8.75 ms. Figure 9(a) makes it clear that the deceleration at 6.8 ms has sufficiently reduced the centre velocity to make the centre the last point to go through the zero position.

Figure 11(b) for Test 5 indicates approximately the same pattern as Figure 11(a) for Test 1. The notable differences in Figure 11(b) due to an almost fourfold increase in overpressure are as follows:

1. In general the strain peaks are between 2.5 and 3.5 times greater.

2. The corresponding peaks occur several milliseconds earlier due to stiffening of the plate by membrane action.

3. Membrane strain is more pronounced and leads to more distinct inflection points at approximately 3 ms and 6.25 ms in the displacement time history for the plate centre (see Figure 9(b)).

2.3.2 HOB Tests

The purpose of the HOB tests was to examine the structural response of square plates under high load [1]. This section will present a summary of the results obtained.

As was done for the blast chamber tests, the panel shown in Figure 3 was used to check on uniformity of pressure loading over the plate surface for the HOB site test configuration. A charge of 3.6 kg was detonated at 1.92 m above the plate centre and the pressure transducer signals recorded. Figure 13 shows the result. Although there is some variation in the arrival times of the signals, the results were considered to be satisfactory.

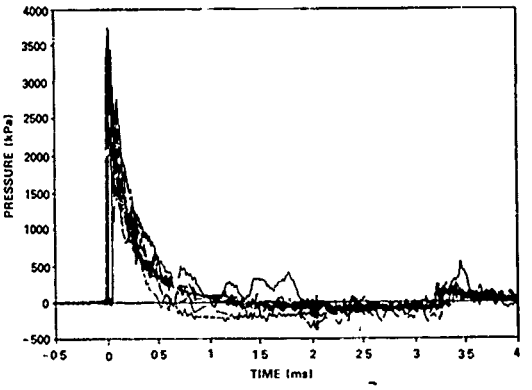

Figure 13. Summary Plots of Pressure Transducer Signals from the HOB Plate Loading Test.

Test 4 listed in Table 2 was done on the plate shown in Figure 2. Because of the predicted high accelerations, however, the accelerometers were removed from the plate before the test. Although several strain gauges failed during Test 4, reasonably satisfactory strain traces over a limited range were obtained for several gauges. Selected results from Test 4 will now be given.

Figure 14 shows the pressure time history signals. Pressure gauges P1 to P4 were mounted on the extension panels as shown in Figure 1, and pressure gauges P5 and P6 were mounted underneath the target plate. The results show that the top surface pressures are reasonably consistent both in amplitude and duration, and that the magnitude of the pressure under the plate is negligibly small in comparison with that on top. The average peak overpressure is 6890 kPa, which is an order of magnitude higher than the largest overpressure recorded in the blast chamber tests. The positive durations, however, are somewhat less well defined but are nominally less than half the positive durations encountered in the blast chamber tests.

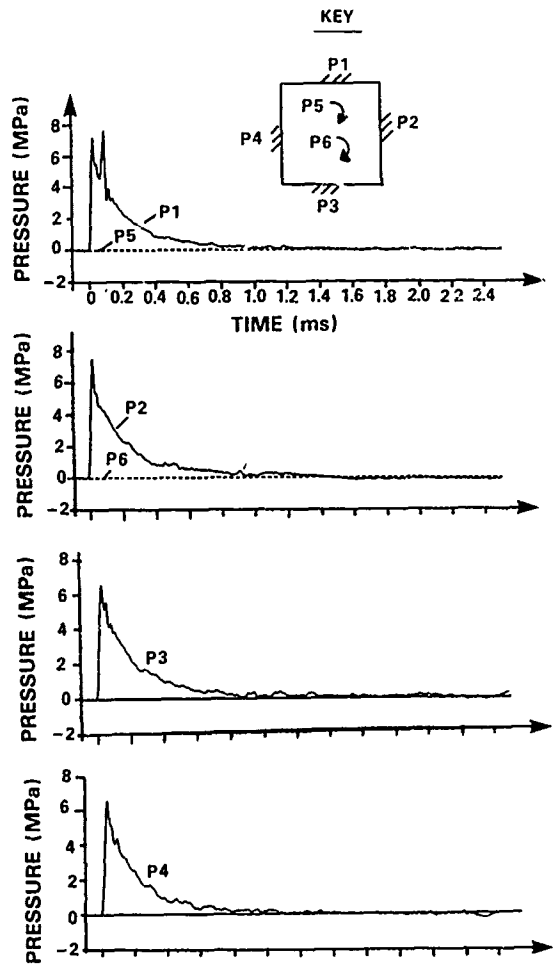

Figure 14. Plot of Pressure Against Time for HOB Test 4: Transducers P1 - P6.

In the case of pressure transducer P1, a spike occurs about 0.1 ms after the main pressure peak. It was felt that this anomaly was an effect caused by an inperfection in the charge that was detonated. Since only P1 detected this pressure spike, however, it was considered to be a localized effect that would not appreciably change the structural response of the target plate.

In order to check the symmetry of response, the strain time histories from strain gauges S8 and S11 are compared in Figure 15. The comparison is reasonably satisfactory.

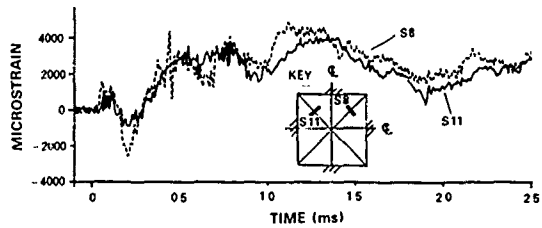

Figure 15. Plot of Strain for HOB Test 4: Strain Gauges S8 and S11.

As shown in Reference 4 and Reference 5 (Figures 11 and 15) the collapse mechanism for a square plate consists of essentially rigid triangular zones that rotate about hinges which form along the plate boundaries and from the plate corners. The response of the strain gauges that did not fail were consistent with this deformation pattern. To illustrate the results, Figures 16(a) and 16(b) show the strain gauge time histories, respectively, from surface strain gauges S19 and S12, which are oriented along a hinge, and strain gauges S18 and S11, which are oriented perpendicular to the hinge. In each case a high frequency response initially occured due to localized vibration of the individual strain gauges. After about 0.2 ms, however, this response had essentially been damped out and the strain response of the plate can be observed. The resulting strain histories are consistent with finite element calculations

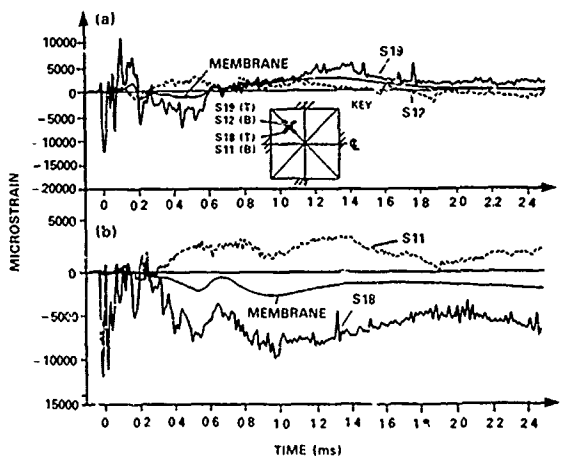

Figure 16. Strain Time History Plots for HOB Test 4 Strain Gauges S11, S12, S18, and S19

for the displacement patterns presented in Reference 5. The plate was shown to collapse to its final deformed shape in about 1.2 ms and then to recover elastically a small amount in about 0.5 ms. It then continued to vibrate elastically with small amplitude about the deformed shape. Figure 16(b) shows that the measured strains are consistent with this predicted dynamic response.

Strain gauges S19 and S12 in Figure 16(a) give further verification of the computed displacement time histories in Reference 5. At 0.5 ms a localized depression (caused by the plate corners) has moved to the position of strain gauges S19 and S12 and accounts for the surface strains observed at this time. At about 1.2 ms, when the plate has collapsed to its final shape, a tensile membrane strain has developed as anticipated. At about 2 ms this membrane strain has reduced due to elastic recovery after the initial collapse as predicted by finite element calculations.

3. STIFFENED PANELS

3.1 Introduction

The purpose of the air-blast loading tests on stiffened panels was to obtain displacement and strain data for comparison with computer code predictions. Since stiffened panels are used to construct the hull and superstructure of a modern warship, the experimental data in conjunction with numerical modelling results will be valuable in improving current Canadian design standards.

This paper will present results for two stiffened panels. The first panel was subjected to seven tests at the HOB site. The second stiffened panel was tested at the Defense Nuclear Agency's event MINOR SCALE at which a 4000-ton ANFO charge was detonated as a ground burst on White Sands Missile Range in June 1985.

3.2 Stiffened Panel Tested at the DRES HOB Site

3.2.1 Experimental Procedure, Instrumentation and Tests

Reference 1 gives details regarding the experimental procedure, instrumentation and tests for the panel tested at the HOB site on the DRES experimental range. The following discussion will briefly review the details.

The panel was 6.35 mm thick and had effective dimensions of 4.57 m x 2.44 m with 76 mm x 152 mm T beams at 0.914 m spacing. The panel was mounted flush with the ground in such a way as to achieve fully fixed boundary conditions and was instrumented with pressure gauges, accelerometers and strain gauges as shown in Figure 17. Each test consisted of detonating a charge suspended directly above the centre of the panel at a known standoff distance. Table 3 summarizes the tests. Since the pulse durations were typically less than half the fundamental period of the panel (25 ms), the loading was in the impulsive regime.

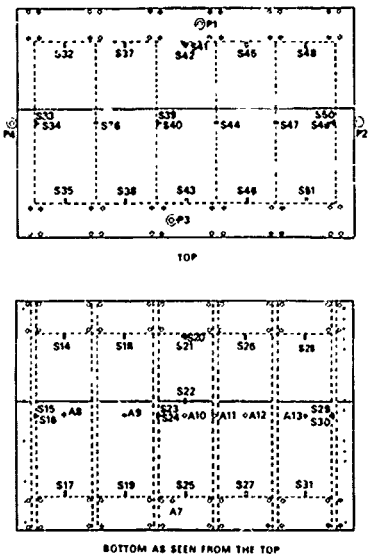

Figure 17. Transducer Locations on Panel
(P = Pressure, S = Strain, A = Acceleration)

3.2.2 Discussion of Results

Some preliminary results were presented in Reference 1. In particular, the deformed shape of the panel after Test 4 was shown. Severe deformation of the panel segments and beams were observed. The present paper will present a reasonably comprehensive set of results for Test 3, which is a moderately high level loading case.

Pressure Loading

As shown in Figure 17, four pressure transducers (P1-P4) were mounted around the panel. In addition, two pressure transducers (P5 and P6) were mounted underneath. Figure 18 shows a plot of the pressure signals for Test 3. These curves indicate a satisfactory spatially constant load. The difference in arrival times can be explained by considering the curvature of the shock front. The pressure under the panel is essentially zero compared to that on top over the region of interest. The positive duration of the pressure wave at the panel surface was approximately 8 ms. The magnitude of the negative phase (not shown in Figure 18) was essentially zero.

Table 3

SUMMARY OF THE HOB TESTS WITH THE STIFFENED PANEL

TEST	CHARGE MASS (kg)	STAND OFF (m)	PEAK PRESSURE (kPa)	DURATION (ms)	ACCELERATION* (g)	STRAIN** ($\mu\varepsilon$)	REMARKS
1	29.1	15.2	83	9.5	370	1300	Elastic
2	94.1	12.8	225	8.5	880	3000	Just Below Yield
3	94.1	10.1	476	8.0	1590	4000	Just Above Yield
4	188.1	7.3	6650	4.0	+	6400	Severe Plastic Deformation

* Average peak value for accelerometers located at panel centres.

** Average peak value for strain gauges located at panel edges.

\+ Accelerometers not mounted.

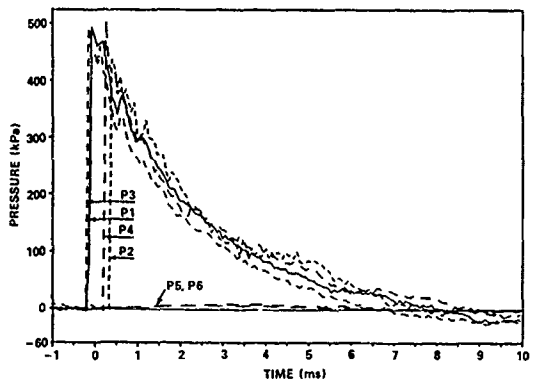

Figure 18 Plot of Pressure Against Time for Stiffened Panel Test 3: Transducers P1 - P6.

Motion Time History

As shown in Figure 17, accelerometers were mounted at the centre of each of the panel segments (A8-A10, A12, A13), on the "fixed" boundary (A7), and at the centre of one of the beams (A11). Figure 19 shows the displacement time histories found by double integration of the accelerations with drift correction. Although considerable drift in the displacement signals were observed after integration prior to drift correction, it is believed that the displacement signals presented are reasonably correct. The drift correction technique that was applied is discussed in Reference 1.

The following observations can be made on the basis of the results shown in Figure 19.

1. The displacement response of A9 and A12 are similar as required by symmetry. A8 and A13 are also similar except for a discrepancy in the peak displacements (due possibly to unknown factors such as residual stress).

2. Figures 19(d) and 19(e) show that the boundary of the panel was effectively fixed in comparison to the panel and beam displacements.

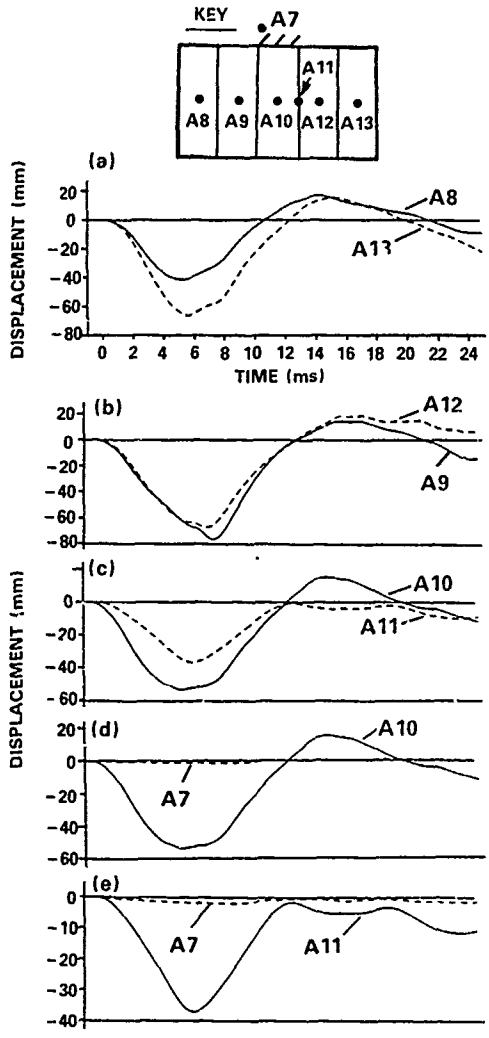

Figure 19. Displacement Time History Plots for Stiffened Panel Test 3. Accelerometers A8 - A13.

3. The average horizontal line through the peak displacements associated with the accelerometers at the panel segment centres is consistent with the approximate permanent deflections of 20 mm.

4. The period of response with respect to the average baseline is about 25 ms, which is the same as the value found from linear elastic analysis.

5. The centre displacements of the panel segments vary between 40 mm and 80 mm.

Observations 4 and 5 show that yield of the material has effectively cancelled out the membrane stiffness effects. This follows since the displacements would be smaller by at least an order of magnitude should yield of the material not have occurred.

Strain Time History

Some representative strain time histories are shown in Figure 20. Figures 20(a) and 20(b) indicate that significant membrane strain occurred during the downward motion of the panel (0-9 ms). There is also some similarity between Figures 20(a) and 20(b) for approximately the first seven milliseconds, but then some discrepancies occur. It is believed that this nonsymmetry is due mainly to construction details such as welds which affect the free vibration response of the panel after the initial loading phase. Figure 20(c) shows that significant strain has occurred parallel to the beam as well as perpendicular to it. The peak strains in Figure 20(c) occur at about 6.5 ms, which is also the time of peak displacement shown in Figure 19(c). The fact that the peak membrane strains in Figure 20(a) and 20(b) occur at about 3 ms suggests that higher modes other than the fundamental are significant (the mode shapes and frequencies are presented in Reference 5, Figure 19).

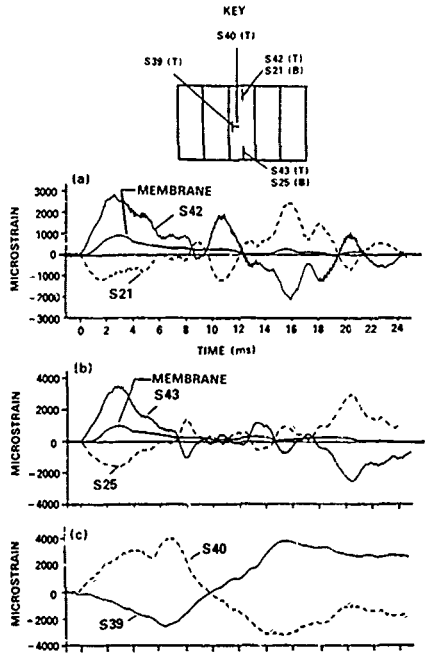

Figure 20. Strain Time History Plots for Stiffened Panel Test 3: Strain Gauges (S42,S21), (S43,S25) and (S39,S40).

3.3 Stiffened Panel Tested at MINOR SCALE

3.3.1 Experimental Procedure, Instrumentation and Tests

The stiffened panel tested was mounted flush with the ground surface at a radial location from the explosion for a peak side-on overpressure of 345 kPa. As for the HOB tests, the panel was embedded in a reinforced concrete foundation to simulate a clamped (built in) boundary condition.

The panel was instrumented with pressure gauges (Kulite Piezo-resistive strain type, model XT190), accelerometers (Endevco strain type, model 2264), electrical resistance strain gauges and displacement gauges (Schaevitz LVDT) as shown in Figure 21. The transducer analog signals were cabled to the DRES instrumentation

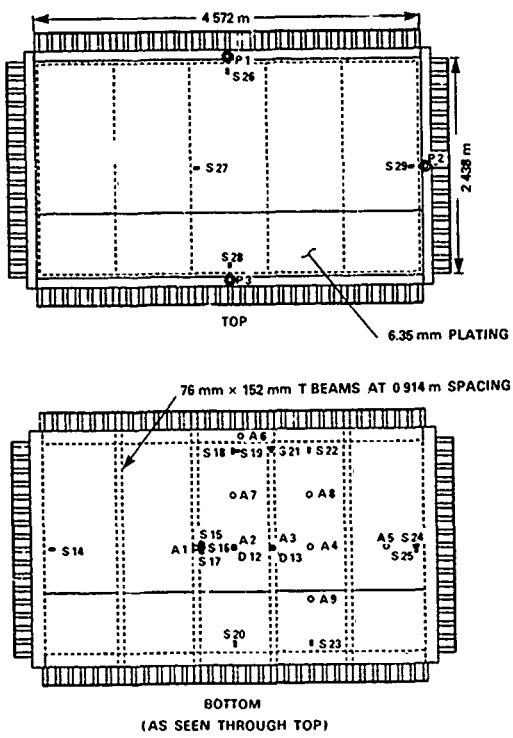

Figure 21. Transducer Locations on Stiffened Panel for Minor Scale Trial. (P = Pressure, A = Acceleration, D = Displacement, S = Strain)

bunker and recorded automatically on magnetic tape for later digitization and data processing. Following the blast, the panel was examined and surveyed to determine the shape of the permanently deformed surface and the extent of the damage.

3.3.2 Discussion of Results

Pressure Loading

Figure 22 shows the side-on pressure-time history for the transducer P2 located on the panel surface. The insert illustrates the perturbations in the initial wave form. These perturbations may be attributed to ground surface boundary layer effects, local anomalies in the shock front, ground/panel surface discontinuity or strain gauge cable obstruction near the pressure transducer. The peak overpressure of 350 kPa agreed closely with the predicted value. The positive duration was approximately 200 ms, which is about thirty times greater than the positive durations encountered at the DRES HOB site.

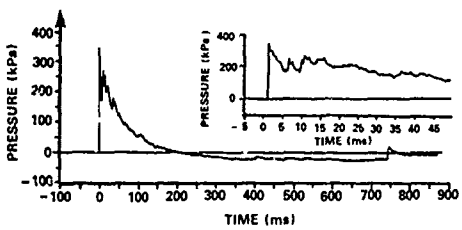

Figure 22. Plot of Pressure from Transducer P2 Against Time from the Miror Scale Test

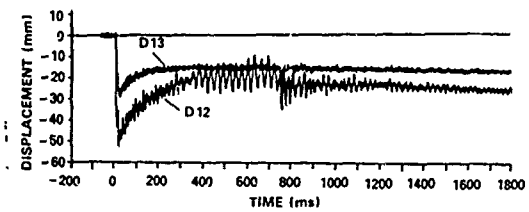

Figure 23. Displacement Time History Plots from Minor Scale Test: Displacement Transducers D12 and D13.

Motion Time History

Figures 23 and 24 shows the displacement time history recorded from displacement gauges D12 and D13 in Figure 21. The panel centre and beam were plastically deformed to their maximum displacement in only a few milliseconds. In particular, the centre of the panel essentially reached its first maximum displacement after 4 ms and the centre of the beam after about 7 ms. The panel then oscillated elastically about a mean displaced shape that recovered under a reducing load that varied slowly with respect to the natural period of the structure. When the external pressure became zero at 200 ms, the beam (D13) reached its recovery position with a permanent displacement of about 15 mm. It did not appreciably respond in the negative phase. The panel centre, however, did respond to the negative phase and also to the second shock that occurred at 750 ms (Figure 22). The centre of the panel then recovered to its final deformed displacement of about 25 mm after approximately 1500 ms.

It was also of interest to compare the measured displacements obtained with D12 and D13 with the doubly integrated accelerations with drift correction from accelerometers A2 and A3, respectively. The results are shown in Figure 24 for the first 50 ms. The displacements found by integration agree reasonably closely with the measured displacements.

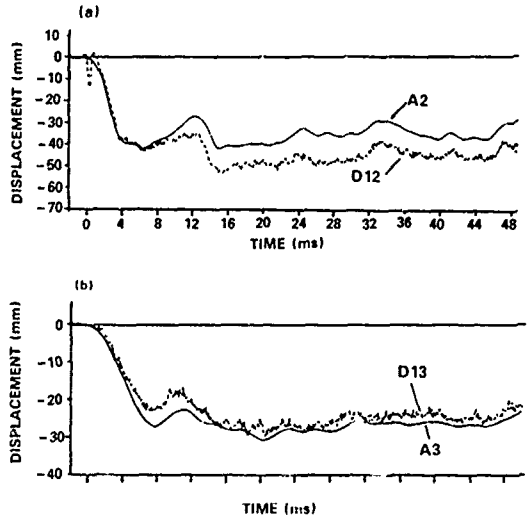

Figure 24. Comparison of Displacement Time Histories from Minor Scale Test. (a) Accelerometer A2 and Displacement Gauge D12, (b) Accelerometer A3 and Displacement Gauge D13.

Figure 25 shows the deformed shape of the panel at the end of the Minor Scale test. Moderate permanent distortion of the panel had occurred.

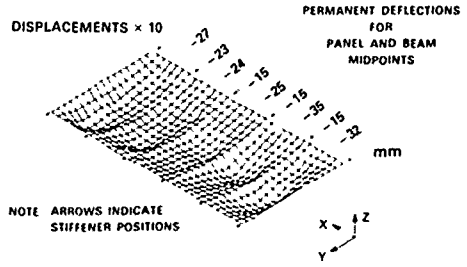

Figure 25 Final Displaced Shape of Panel after Minor Scale Test

4. CONCLUSIONS

The experimental results for the square plate tests enabled a reasonably good understanding of the plate response to be attained.

Even when plastic yielding of the material is not significant, it is clear that nonlinear effects such as membrane stiffening of the plates are important and must be included in analyses for accurate correlation with experiment.

The results for the HOB stiffened panel demonstrated that significant deflections of the beams occurred at overpressures sufficient to cause measurable permanent distortions. The loading in this case was in the impulsive regime. Since no cracking or weld failure was observed, however, the panel could still be classed as operational as far as structural integrity was concerned.

The Minor Scale test of the stiffened panel enabled the response in the dynamic, rather than the impulsive, loading regime to be determined. The excellent pressure and displacement measurements revealed the nature of the structural response. Plastic collapse and damage occurred in the first 6 ms of the 200 ms positive duration of the pressure load. Subsequent response consisted of elastic vibration about a mean deformed shape that recovered slowly during the rest of the positive duration to a final deformed shape. In fact, the only essential difference in the results from the impulsive loading case and the Minor Scale test was the rate of recovery.

5. ACKNOWLEDGMENT

The authors would like to thank Mr. D. Ritzel and Mr. G. Rude of the Shock and Blast Group at DRES for their assistance with the experimental work. We also thank the personnel of the Computer Group, the Field Operations Section, the Electronic Design and Instrumentation Group and the Photo Group at DRES for their assistance during the field trials.

The authors would also like to thank Miss C. Baumann for typing the manuscript and Miss S. Eaket for the artwork.

6. REFERENCES

1. R. Houlston and J.E. Slater, "Structural Response of Panels Subjected to Shock Loading", 55th Shock and Vibration Bulletin, Part 2, 149-163, June, 1985.

2. "Vibration And STrength Analysis Program (VAST): User's Manual, Version #02", MARTEC LTD., November, 1982.

3. R. Houlston and C.G. DesRochers, "Nonlinear Structural Response of Ship Panels Subjected to Air Blast Loading", to be published in Computers & Structures and presented at 6'th ADINA Conference, MIT, June 10-12, 1987.

4. W. Johnson, **Impact Strength of Materials**, Edward Arnold (Publishers) Ltd., 1972.

5. R. Houlston, J.E. Slater, N. Pegg and C.G. DesRochers, "On Analysis of Structural Response of Ship Panels Subjected to Air Blast Loading", Computers & Structures, Vol. 21, No. 1/2, pp. 273-289, 1985.

IN-STRUCTURE SHOCK IN A PROTOTYPE BLAST SHELTER

S. C. Woodson and S. A. Kiger
U.S. Army Engineer Waterways Experiment Station
Vicksburg, Mississippi

A full-scale, 100-man capacity reinforced-concrete blast shelter was tested in the high-explosive MINOR SCALE Event sponsored by the Defense Nuclear Agency (DNA). Approximately 4,800 tons of an ammonium nitrate fuel-oil mixture was detonated in June 1985 to simulate the airblast effects of an 8-kiloton nuclear weapon surface burst. The prototype shelter was constructed and backfilled to a depth of burial of 4 feet at the range corresponding to the predicted 0.50 MPa (75-psi) peak overpressure level. The U.S. Army Engineer Waterways Experiment Station (WES) and the U.S. Army Engineer Division, Huntsville (HND), cooperatively designed and fielded the prototype civil defense blast shelter in support of the Federal Emergency Management Agency (FEMA) Keyworker Blast Shelter Program. The test verified the structural design developed from a 3-year research program at WES. This paper compares the data from the prototype test with data from previous High-Explosive Simulation Technique (HEST) tests on 1/4-scale models. Specifically, in-structure shock is evaluated using shock spectra developed from acceleration data. Shock spectra developed from the prototype test are compared to the scaled shock spectra developed from the model tests. Also, a comparison is made with the in-structure shock environment measured in a full-scale, 18-man capacity corrugated steel blast shelter. Conclusions are drawn on the shock environment in civil defense blast shelters and its effects on personnel and typical blast shelter equipment. The validity of using small-scale model structures and HEST simulations in determining in-structure shock generated by nuclear weapons is discussed.

INTRODUCTION

WES has conducted several structural research studies in support of the FEMA Keyworker Blast Shelter Program. At the time this research program was initiated, civil defense planning called for the evacuation of nonessential personnel to safe (low-risk) areas (when a nuclear crisis is probable) and the construction of blast shelters to protect key workers remaining in the high-risk areas. FEMA tasked HND to develop keyworker shelter designs, and WES supported the HND effort with design calculations and experiments using 1/4-scale models and prototype structures. Both deliberate- and expedient-type shelters were studied. A deliberate shelter is a permanent structure with generally a capacity of 100 to 400 people. An expedient shelter consists of prefabricated components which can be installed within a time period of about 2 weeks and generally has a 20-man or less capacity.

Structural design parameters required that the shelters survive at a peak overpressure of 0.34 MPa (50 psi) from a 4,200-TJ (1-Mt) nuclear weapon. The structural design criteria and the levels of initial and residual radiation associated with the threat weapon dictated an earth-mounded or buried structure. Among the structures field tested under dynamic loadings were a full-scale corrugated-metal expedient-type shelter [1], six 1/4-scale reinforced concrete models of a deliberate-type shelter [2], and a full-scale reinforced concrete deliberate-type shelter [3]. In-structure shock determined from acceleration data recorded in the 1/4-scale model tests and the corrugated-metal shelter test are discussed by Slawson and others [4] and Woodson and others [5], respectively. This paper discusses the prototype reinforced-concrete shelter test and compares the in-structure shock environment with those discussed in References 4 and 5.

TEST DESCRIPTION

A full-scale, 100-man capacity reinforced-concrete blast shelter was tested in the high-explosive MINOR SCALE Event sponsored by DNA. Approximately 4,320 t (4,800 tons) of an ammonium nitrate fuel-oil mixture was detonated in June 1985 to simulate the airblast effects of a 33-TJ (8-kt) nuclear weapon surface burst. The prototype shelter was constructed and backfilled to a depth of burial of 1.2 m (4 ft) at the range corresponding to the predicted 0.50 MPa

(75 psi) peak overpressure level. In preparation for the prototype test, WES conducted a series of yield effects tests [6] to determine the overpressure required in the 33 TJ (8 kt) nuclear simulation to result in the same damage as the design threat (4,200 TJ at 0.34 MPa). The yield effects tests and analyses indicated that the prototype shelter should be placed near the 0.50 MPa (75 psi) peak overpressure level.

Figures 1 and 2, respectively, show plan and elevation views of the shelter. The shelter contained mechanical air-moving equipment (fans and ducts), a diesel generator, bunks, and three instrumented anthropomorphic mannequins. The mannequins were positioned in the standing, sitting, and supine positions, and their movement was documented using accelerometers and high-speed photography to investigate occupant survivability. The diesel generator and mechanical equipment were tested pre- and posttest to investigate equipment survivability. One hundred channels of instrumentation were recorded. Figures 3 and 4 show the instrumentation gage locations.

RESULTS

Damage to the shelter during the MINOR SCALE Event was light with structural reflections essentially within the elastic range. Maximum measured midspan deflections were approximately 2.0 cm (0.8 inch) with permanent roof deflections of 0.3 cm (0.13 inch) or less. Minor concrete cracking was noted on the roof slab as shown in Figure 5. Hairline cracks were visible on the walls as shown in Figure 6 and on the floor as shown in Figure 7. Figures 5 through 7 do not show all of the cracks in the structure but are representative of the types of cracks found throughout the shelter.

The mechanical equipment incurred no damage during the test, and the final positions of the mannequins were similar to the pretest settings. The feet of the standing mannequin moved forwarded approximately 1.3 cm (0.5 inch). Data recovery was very good for the airblast-pressure gages, soil-stress gages, accelerometers, interface-pressure gages, and deflection gages. The 100 channels of data will be published in a WES technical report [3].

The weapon simulation was determined by choosing the best fit, in a least-squares sense, of 100 msec of the airblast data to a 33-TJ (8 kt) nuclear weapon pressure-time history as defined by Speicher and Brode in Reference 7. The procedure used to select the best fit is described in some detail in Reference 8. The weapon simulations for each surface airblast data record are listed in Table 1.

Table 2 compares the average weapon simulation peak overpressure and yield values with those of the corrugated-metal shelter test and the 1/4-scale model test. Note that consistent with cube root scaling, the actual yield simulated in the 1/4-scale test has been multiplied by 16 for comparison to the full-scale tests. The peak overpressures simulated in the three tests were similar, but the weapon yields varied.

IN-STRUCTURE SHOCK

In-structure shock is typically represented in terms of shock spectra. Shock spectra are plots of the maximum responses, usually of relative displacement, pseudovelocity, and/or absolute acceleration of linear oscillators, with a specified amount of damping to a given input base acceleration-time history. The maximum response is plotted as a function of oscillator frequency.

Vertical shock spectra were generated from acceleration data recovered in the dynamic test using a computer code developed at WES. The experimentally determined shock spectra were calculated using a damping of 5 percent of critical, and smoothed versions are shown in Figures 8 through 13 for accelerometers AV-1 through AV-6, respectively. As shown in Figure 4, the accelerometers were located on the floor of the shelter.

Figure 14 compares shock spectra developed from accelerometer AV-1 with vertical floor shock spectra determined from data recorded in the corrugated-metal shelter test and the 1/4-scale model test (D-3B) discussed in References 4 and 5, respectively. For comparison with full-scale results, displacements and accelerations from the 1/4-scale test were multiplied and divided by 4, respectively. The spectra from the prototype shelter compare well with that of the metal shelter at all frequencies. However, scaled-up data from the 1/4-scale test indicate a much more severe shock environment than data from either of the full-scale tests. Note from Table 2 that yield is much higher in the 1/4-scale test than in the 2 full-scale tests, but yield was also higher in the metal shelter than in the 100-man shelter test with no corresponding increase in shock levels. No good explanation of the discrepancy between spectra generated from the 1/4-scale structure tests and the 2 prototype tests is apparent at this time. However, we note that the airblast generated by the MINOR SCALE Event was relatively smooth (no high-frequency oscillations) compared to the airblast generated in the simulators used for testing the 1/4-scale and expedient shelters, and that the metal expedient shelter may have effectively filtered out the high-frequency signals.

OCCUPANT SURVIVABILITY

Reference 8 discusses human shock tolerance. The effects of shock on personnel inside the structure depend on the magnitude, duration, frequency, and direction of motion. Also, the position of the man at the time of shock influences its effect.

Reference 8 recommends using a maximum design acceleration of 10 g's at frequencies at or below man's resonant frequency in the standing position (10 Hz). Figures 8 through 13 show that the floor acceleration was less than 5 g's at a frequency of 10 Hz. Since human shock tolerance is higher in the seated and supine positions than in the standing position, the probability of injury decreases.

Impact injuries occur at much lower accelerations than compressive bone fractures. Generally, impact injuries may occur at accelerations of 0.5 to 1 g for an unrestrained man in the standing or seated position. These injuries are the result of falling and hitting the floor or other objects. Impact injuries may be reduced by padding or restraining to prevent movement. The high-speed photography and posttest observations indicate that impact injuries are not probable. Maximum absolute values of velocity and displacement determined from evaluation of the high-speed movies are presented in Table 3.

MECHANICAL EQUIPMENT SURVIVABILITY

The vertical shock spectra in Figures 8 through 13 can be used to determine whether shock isolation is needed for a given piece of equipment, provided fragility curves for the equipment are known. Alternatively, these shock spectra can be used to write shock-resistance specifications that the equipment must be able to withstand. Figure 15 compares the experimentally determined shock spectra from accelerometer AV-1 with safe-response spectra fragility curves for typical floor-mounted equipment from Reference 9. Figure 9 shows that motor generators and communication equipment should be shock isolated to ensure survivability. The diesel engine generator inside the tested shelter was supported on mounting brackets on top of the fuel tank and incurred no damage.

CONCLUSIONS AND RECOMMENDATIONS

Based on results of the prototype shelter test in the MINOR SCALE Event, in-structure shock in the 100-man Keyworker Blast Shelter is within acceptable limits for occupants. It is recommended that typical blast-shelter equipment such as generators and communication equipment be shock isolated to ensure survivability. The shock spectra presented can be used to evaluate equipment survivability; or alternatively, they can be used to develop specifications for shock isolators.

ACKNOWLEDGEMENT

This work was sponsored by the Federal Emergency Management Agency (FEMA), Washington, D.C. Messrs. Tom Provenzano and Jim Jacobs, FEMA, were Program Monitors during this test and the preparation of this paper. Dr. S. A. Kiger, Structures Laboratory (SL), WES, was the Program Manager. The field test was supervised by Messrs. S. C. Woodson and T. R. Slawson, SL, WES. The structure was instrumented by Mr. Phil Parks, Instrumentation Services Division, WES.

REFERENCES

1. S. C. Woodson, et al., "Dynamic Test of a Corrugated Steel Keyworker Blast Shelter," Technical Report SL-86-6, May 1986, U. S. Army Engineer Waterways Experiment Station, Vicksburg, Mississippi.

2. T. R. Slawson, et al., "Structural Element Tests in Support of the Keyworker Blast Shelter Program," Technical Report SL-85-8, October 1985, U. S. Army Engineer Waterways Experiment Station, Vicksburg, Mississippi.

3. S. C. Woodson and T. R. Slawson, "Demonstration Test of a Prototype Keyworker Blast Shelter: MINOR SCALE," (in preparation), U. S. Army Engineer Waterways Experiment Station, Vicksburg, Mississippi.

4. T. R. Slawson, et al., "Shock Environment in a Civil Defense Blast Shelter," The Shock and Vibration Bulletin, Bulletin 55, Part 2, June 1985, The Shock and Vibration Information Center, Naval Research Laboratory, Washington, D.C.

5. S. C. Woodson, et al., "Shelter Response in a Simulated 1-Mt Nuclear Event," The Shock and Vibration Bulletin, Bulletin 56 (in preparation), The Shock and Vibration Information Center, Naval Research Laboratory, Washington, D.C.

6. T. R. Slawson, et al., "Yield Effects on the Response of a Buried Blast Shelter," The Shock and Vibration Bulletin, Bulletin 56 (in preparation), The Shock and Vibration Information Center, Naval Research Laboratory, Washington, D.C.

7. S. J. Speicher and H. L. Brode, "Airblast Overpressure Analytical Expression for Burst Height, Range, and Time Over and Ideal Surface," PSR Note 385, November 1981 (with updates through November 1982), Pacific-Sierra Research Corporation, Santa Monica, California.

8. P. F. Mlakar and R. E. Walker, "Statistical Estimation of Simulated Yield and Overpressure," The Shock and Vibration Bulletin, Bulletin 50, Part 2, September 1980, The Shock and Vibration Information Center, Naval Research Laboratory, Washington, D.C.

9. R. E. Crawford, et al., "The Air Force Design Manual for Design and Analysis of Hardened Structures," 1974, Air Force Weapons Laboratory, Kirtland Air Force Base, New Mexico.

10. U.S. Army Technical Manual TM-5-855-1, "Fundamentals of Protective Design for Conventional Weapons," 1984, U.S. Army, Washington, D.C.

Table 1. Nuclear Weapon Simulations

Gage	Weapon (kt)	Overpressure (psi)
AB-2	8	88
AB-3	8	74
AB-4	8	52
AB-5	8	63
AB-6	8	48
AB-7	8	53
AB-8	8	46
AB-9	8	59
AB-10	8	53
Average	8	58

Table 2. Comparison of Weapon Simulations

Test	Peak Overpressure (psi)	Weapon Yield (kt)
1/4-Scale Model Shelter	62	5,488
Expedient Metal Shelter (Prototype)	55	1,000
100-Man Prototype Shelter	58	8

Table 3. Mannequin Response

Mannequin	Maximum Displacement (inch)	Maximum Velocity (feet/sec)
supine	0.9	1.4
seated	3.2	2.9
standing	1.3	1.5

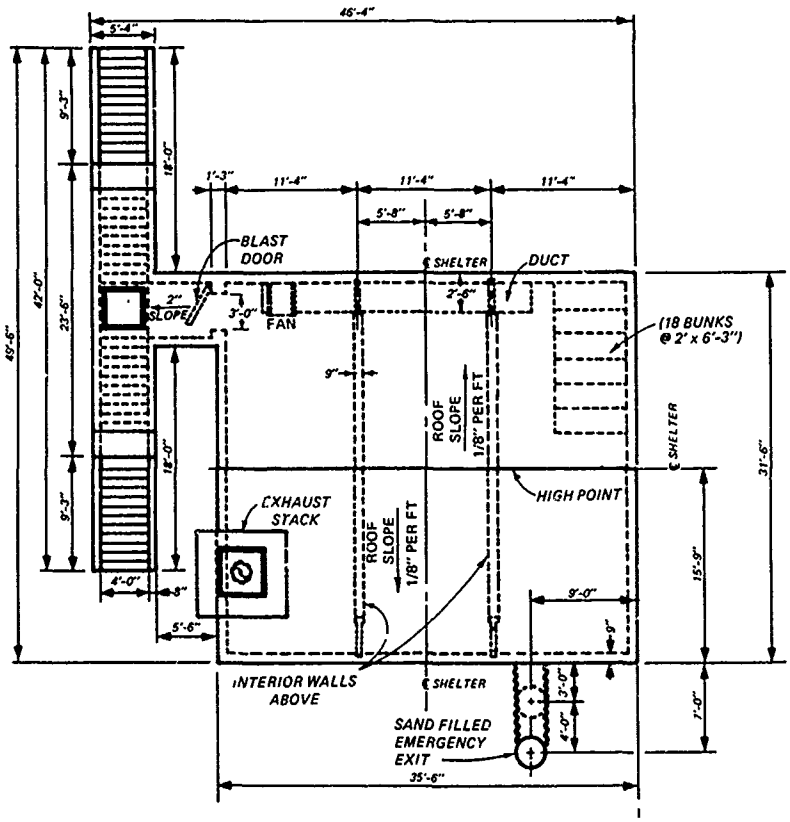

PLAN VIEW

Figure 1. Plan view.

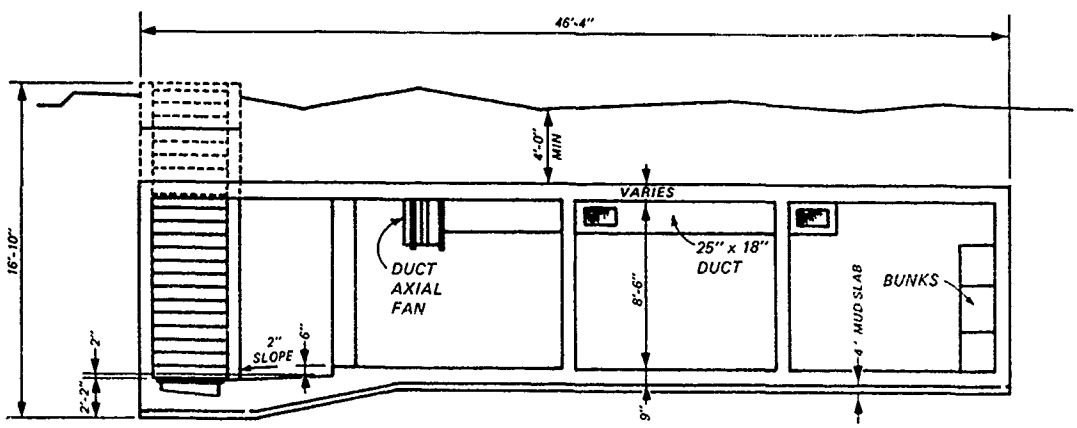

ELEVATION

Figure 2. Elevation view.

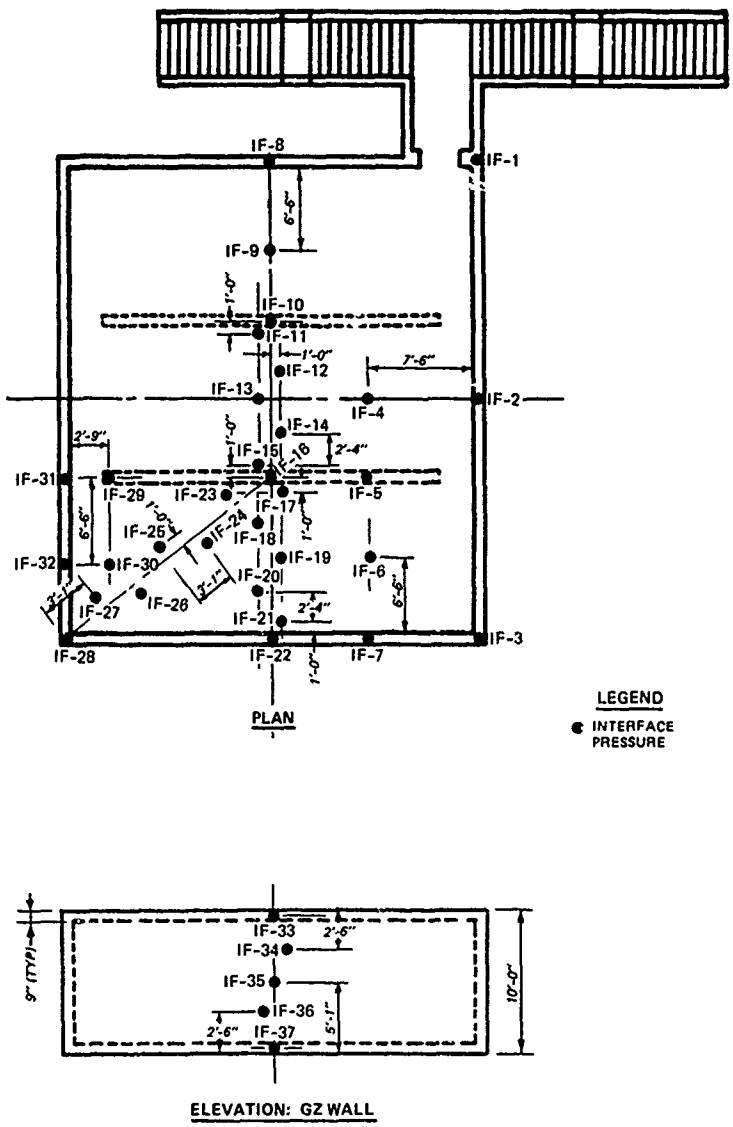

Figure 3. Interface pressure gage layout.

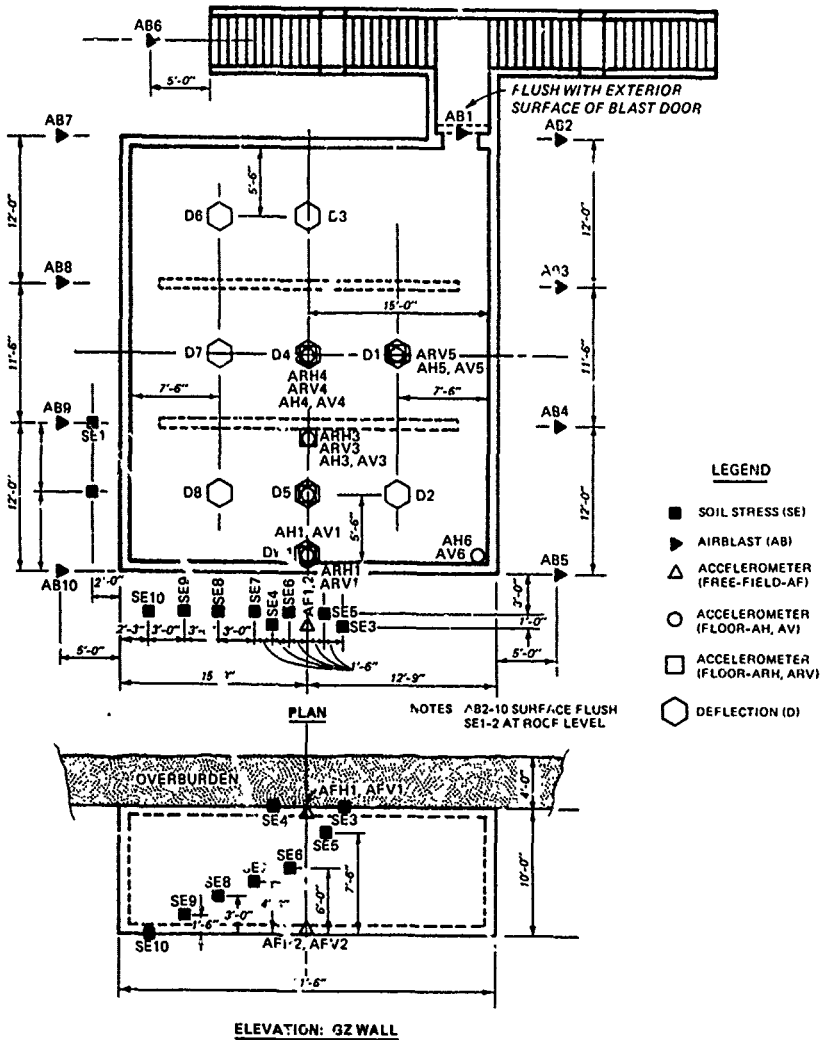

Figure 4.
Instrumentation layout excluding interface pressure gages.

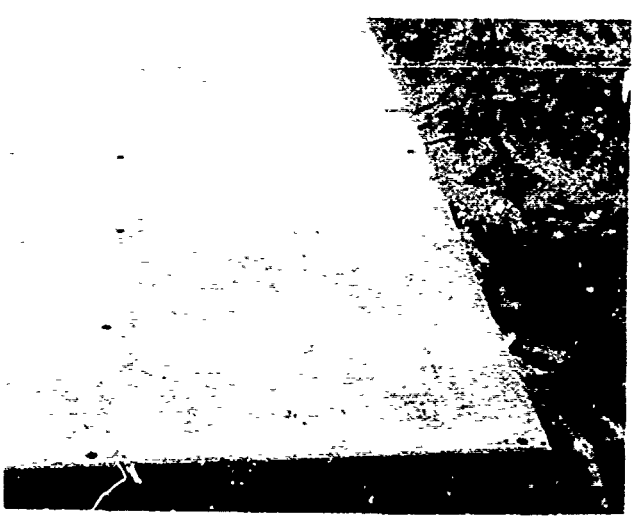

Figure 5.
Section of roof slab showing minor damage.

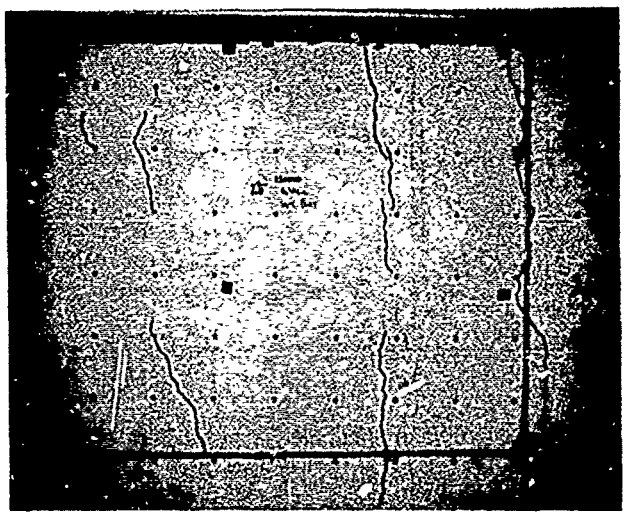

Figure 6. Hairline cracks on wall.

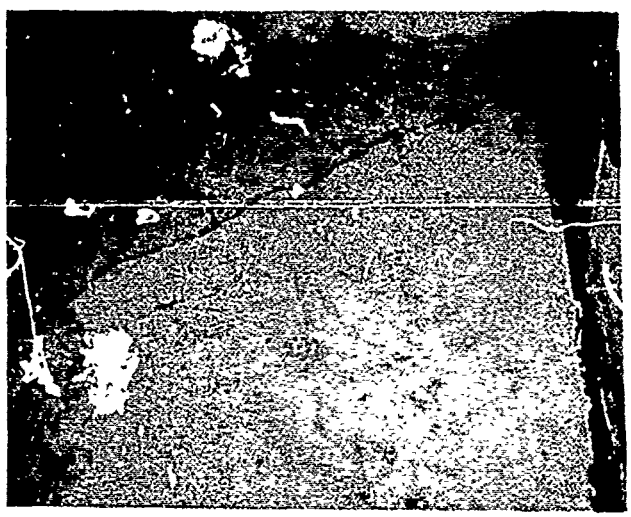

Figure 7. Hairline crack on floor.

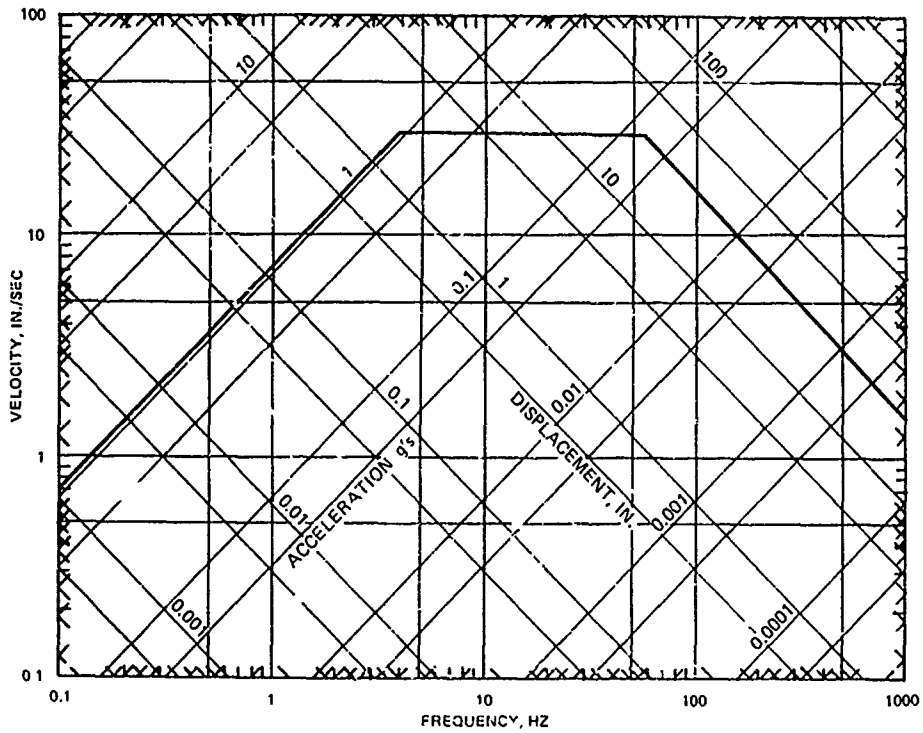

Figure 8. Vertical shock spectra from accelerometer AV-1.

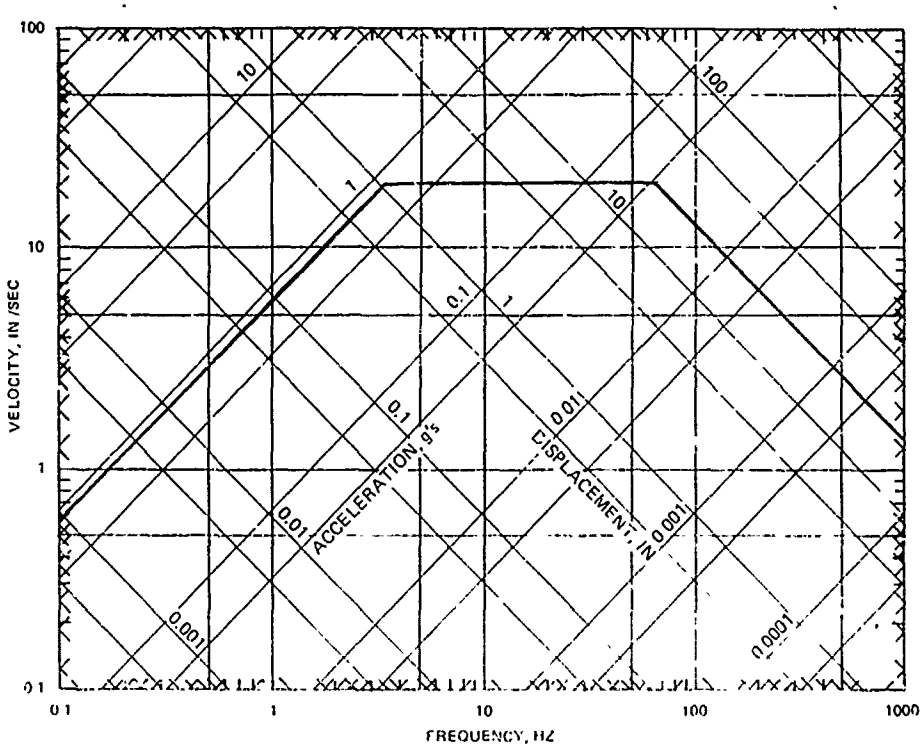

Figure 9. Vertical shock spectra from accelerometer AV-2.

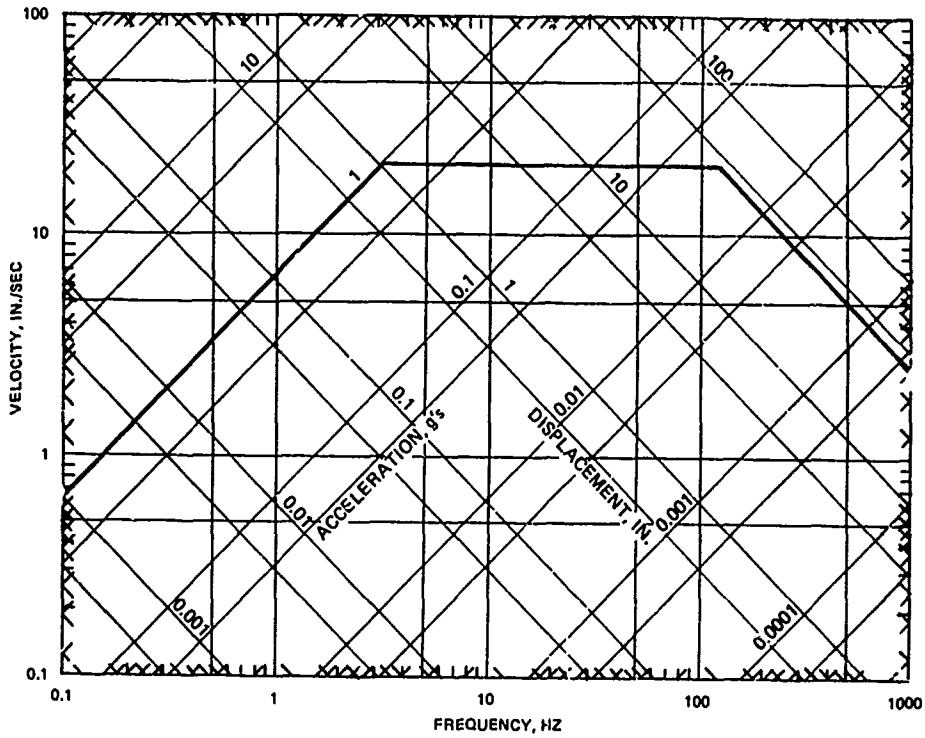

Figure 10. Vertical shock spectra from accelerometer AV-3.

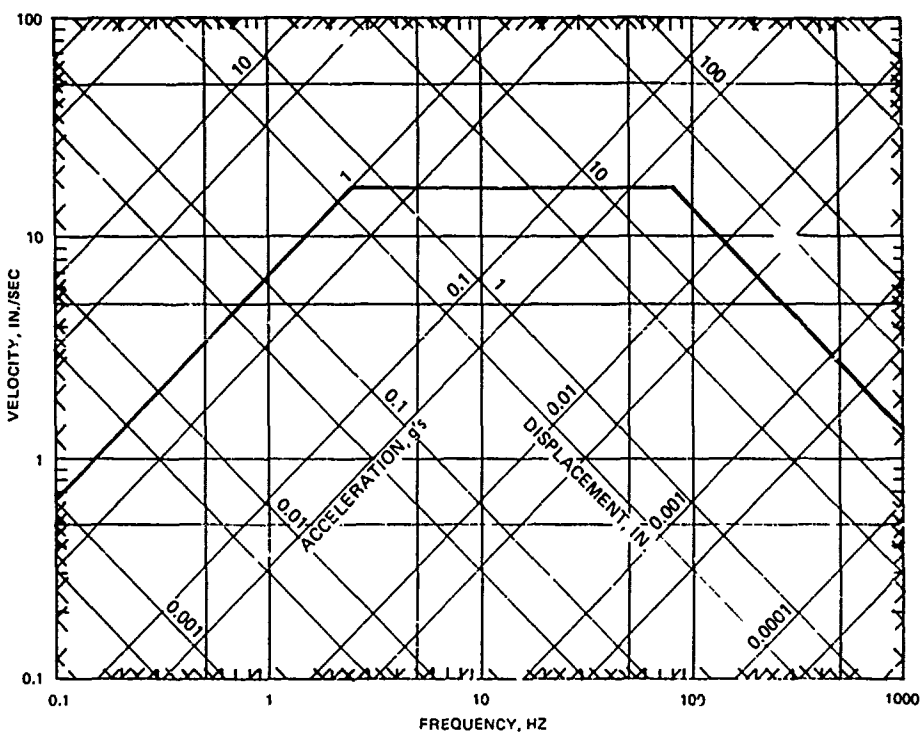

Figure 11. Vertical shock spectra from accelerometer AV-4.

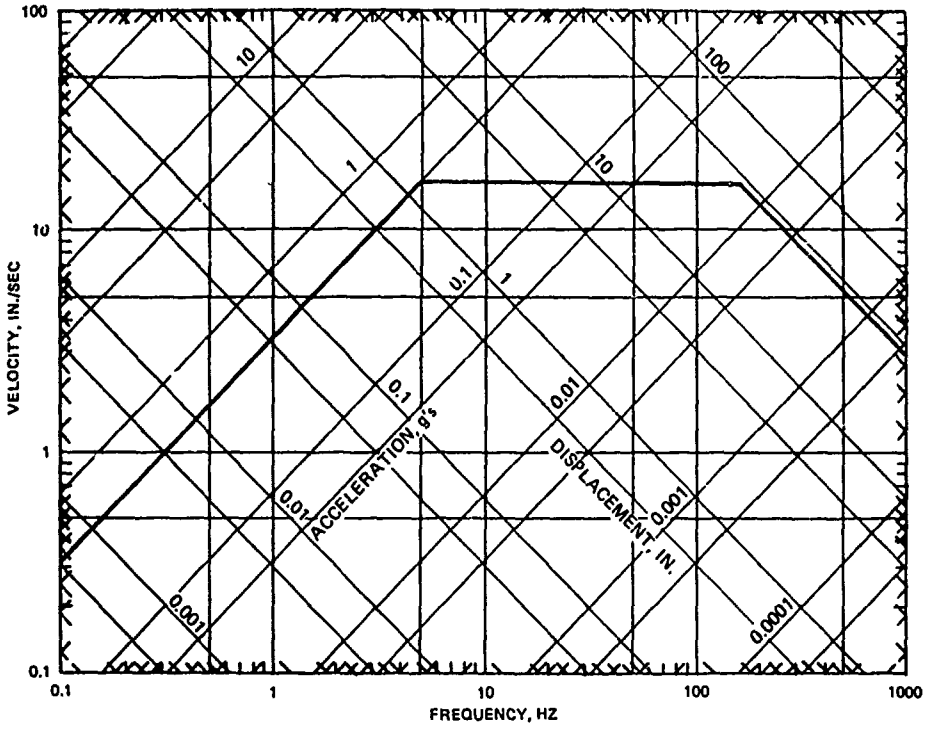

Figure 12. Vertical shock spectra from accelerometer \V-5.

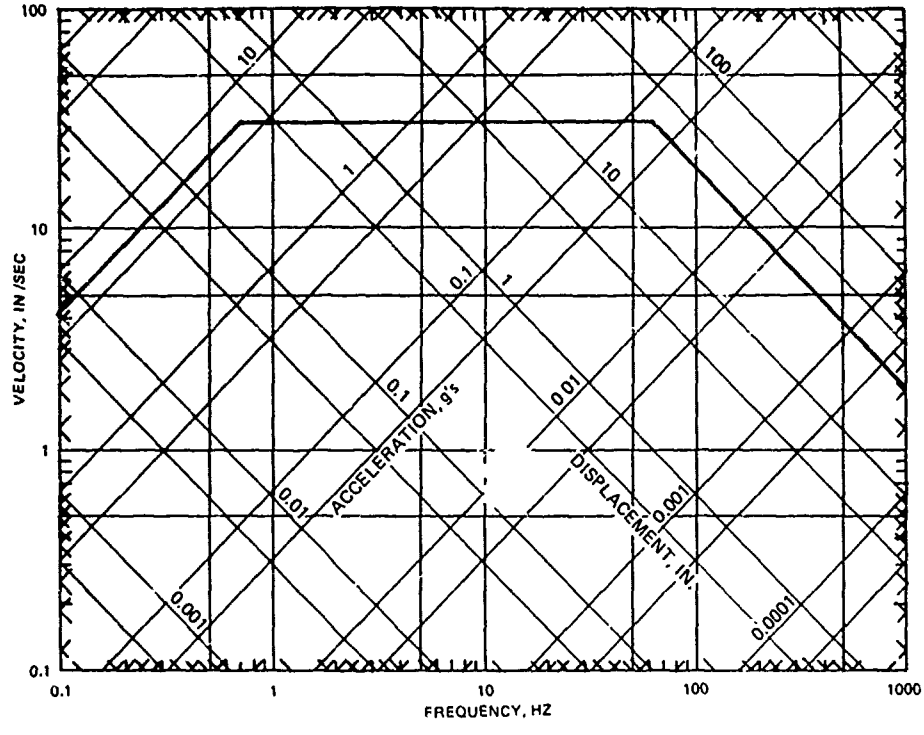

Figure 13. Vertical shock spectra from accelerometer AV-6.

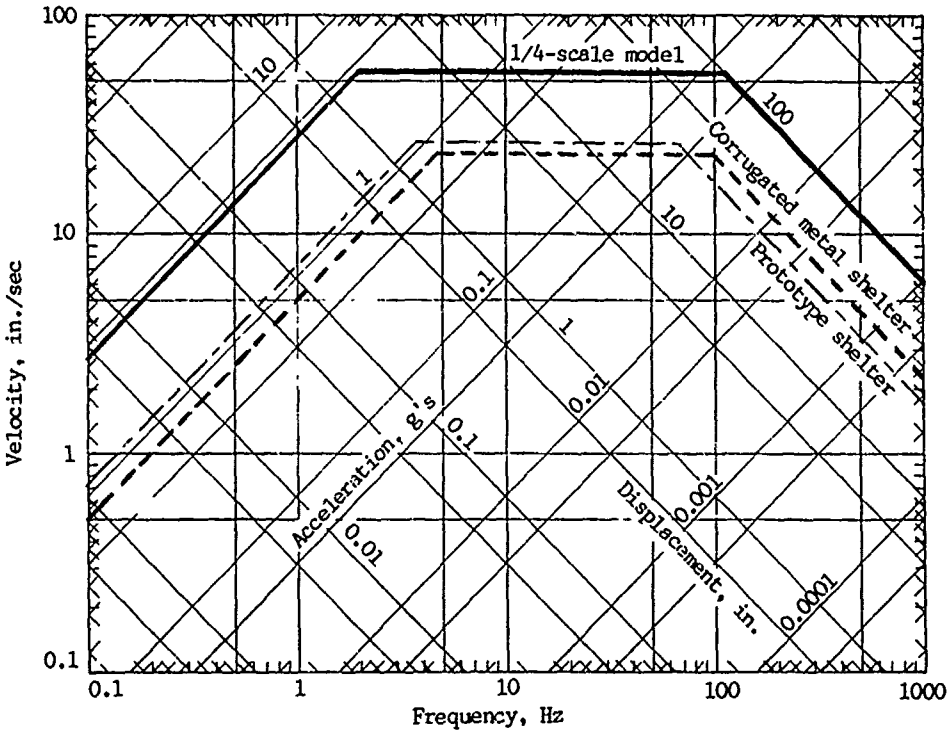

Figure 14. Comparison of shock spectra.

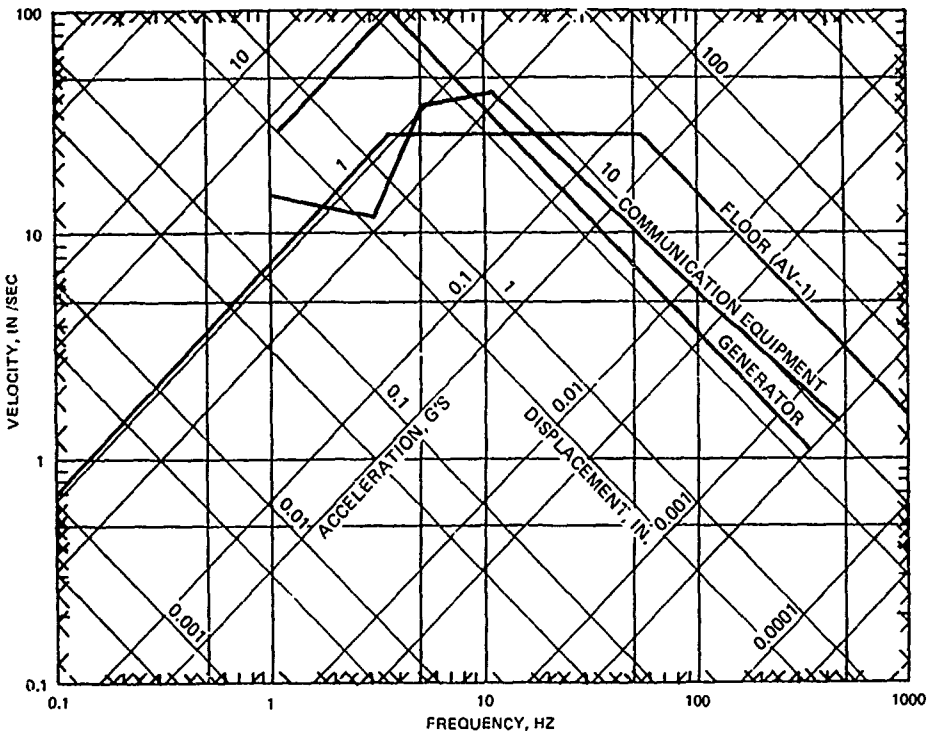

Figure 15. Comparison of experimental shock spectra with response spectra for typical floor-mounted equipment.

RESPONSE OF NONREINFORCED MASONRY WALLS TO CONVENTIONAL WEAPONS

James C. Ray, Robert E. Walker, and William L. Huff
U.S. Army Engineer Waterways Experiment Station
PO Box 631, Vicksburg, Mississippi 39180-0631

An existing computer code has been modified to analyze the vulnerability of nonreinforced masonry walls to airblast from conventional weapons. Two new subroutines were added to address the nonuniform loading and localized response associated with conventional weapons analysis. The predictions from the code have been compared to a limited amount of existing experimental data on masonry walls and have compared well in most cases.

INTRODUCTION

The dynamic response of structures to airblast has been studied extensively in the past. However, most of the analysis efforts have been directed toward materials (such as reinforced concrete) considered to be most suitable for construction of blast-resistant structures and toward structures in a nuclear airblast environment. Little effort has been made in the study of the dynamic response of masonry walls, especially when subjected to conventional weapons. Since many existing structures are of masonry-type construction and terrorist bombings have become a prevalent threat, the need to understand and predict the vulnerability of these structures to conventional weapons has escalated.

The response of structures to conventional weapons airblast is often very different from their response to nuclear weapons airblast. Nuclear airblast durations are generally in the hundreds of milliseconds range. Conventional weapons airblast is often much shorter in duration and can vary over several orders of magnitude depending upon weapon size and range.

The blast pressure distribution on walls from nuclear airblast can generally be closely approximated by assuming a uniform distribution over the entire wall surface. However, this is often not the case with conventional weapons. Not only does the blast pressure magnitude vary with time, but also its distribution over the structure's surface. If a conventional weapon is detonated at close range to a relatively large wall, the early-time loading will tend to be concentrated over a small area of the wall (see Figure 1a), and a local breaching (shear) of this area will be the likely failure mode. If the wall is not breached and if the blast wave is of long duration, the wave will begin to propagate outward from this area along the wall's surface as well as undergoing its normal time-dependent decay (see Figure 1b). When the wave reaches the wall edges, a refraction wave will be formed and will propagate back inward toward the center of the wall causing the reflected pressures to be relieved, leaving only the dynamic pressure on the wall surface. As the blast wave begins to clear from the wall surface, the pressures near the wall edges may possibly be greater than those nearest the point of detonation producing a distribution as seen in Figure 1c. Intuitively, it can be seen that as the weapon and/or range becomes larger with respect to the wall, the blast loading will become increasingly more uniform, and the above phenomena will become less prevalent.

In an attempt to predict the response of masonry walls to any size of conventional weapon, an existing computer code has been modified. The original code, named ARCHING, was developed by C. K. Wiehle and J. L. Buckholt [1] at the Stanford Research Institute to predict the response of nonreinforced masonry walls to airblast from nuclear weapons.

COMPUTER CODE

In the code, wall response is calculated through use of a single-degree-of-freedom (SDOF) analysis. The walls are assumed to rotate about their supports as two rigid bodies (see Figure 2). Resistance of the wall to lateral loads is assumed to be provided entirely from in-plane compressive forces caused by an arching effect at the wall's supports as demonstrated in Figure 3. Any wall resistance due to tensile strength of the mortar or bricks is assumed to be negligible compared to the resistance due to arching and is thus neglected. A typical resistance function as used in the code is shown in

Figure 4. The maximum resistance is taken to be the point at which the mortar between the masonry units (mortar assumed to be weaker in compression than the masonry units) begins to crush.

The failure criteria used in the code is wall instability. Instability is assumed to occur when the wall deflection becomes large enough to cause the moment arm between the wall and its supports to go to zero resulting in zero resisting moment and thus collapse. For a linearized elastic-plastic stress-strain assumption, instability will first occur at a deflection equal to the thickness of the wall.

The code is applicable to solid brick and hollow or filled concrete masonry unit (CMU) walls and can be used for response calculations of both one- and two-way action walls. It can be used to predict the response of a given wall to the airblast from a specified weapon yield, to solve for the incipient collapse pressure of a wall associated with a specified weapon yield, and/or to vary particular wall properties and compute the probabilistic incipient collapse overpressure for a given size wall [1].

COMPUTER-CODE MODIFICATIONS

Numerous minor modifications to the existing code were necessary in order to adopt it to conventional weapons analysis. However, only the three major changes associated with the previously mentioned conventional weapons phenomena will be discussed herein.

The integration time step sizes used in the SDOF analysis routine of the original code were the same regardless of weapon size and duration. This was not adequate for conventional weapons applications. Therefore, the time step sizes used for each particular analysis were made to be functions of the given weapon size, positive phase duration of the blast wave, and the current time with respect to the positive phase duration. Much smaller time steps are taken at early times in the computation when the pressure is decreasing very rapidly, and the time steps are increased in size as the computation continues and the pressure changes become less abrupt.

Since an assumption of a uniform wall loading (as in the original code) would be overly conservative in many cases with small conventional weapons, a subroutine TFORCE was added to the code to address the previously discussed nonuniform loading problem. In this routine, a cubic pressure distribution [2, 3] is assumed and is defined by the following equation (see Figure 5):

$$P(t,r) = P_o(t)\left(\frac{D}{r}\right)^3$$

where

$P(t,r)$ = pressure on wall at a distance r from weapon

$P_o(t)$ = pressure on wall nearest weapon

D = perpendicular distance from weapon to wall

r = slant distance from weapon

With this type of loading distribution, the loading on a given wall will approach uniform loading as the weapon range gets larger and/or the weapon size gets larger relative to the wall dimensions. Thus, the cubic equation automatically takes care of both localized and nonlocalized loading cases. The cubic distribution is assumed to occur immediately upon arrival of the blast wave and to remain in this form throughout the blast wave duration. Its magnitude is solely dependent upon the exponentially decaying pressure at the center of the wall. Future work in this area should be directed toward better defining and modeling the time-dependent variation of pressure distribution on walls.

The total force produced by this assumed pressure distribution is determined by integrating the volume under the portion of the distribution that covers the wall. The total force is defined by the following integral (see Figure 6):

$$F(t) = 2H \cdot \int_0^{\frac{H}{2}} P(r)dr$$

where

H = total height of the wall

$P(r)$ = pressure defined by the previous equation

$r<$ = 0.5 · wall width

The total force is then divided by the wall area in order to obtain a uniform pressure distribution. A uniform distribution is necessary for the code's existing SDOF analysis routine which uses load-mass factors developed for uniformly loaded beams. A subroutine is presently being added that will provide load-mass factors based on the cubic load distribution and the assumed deflected shape.

In order to check for the occurrence of a localized breaching of the wall, a subroutine SHEAR was added to the ARCHING code. Since very little information or data is available on the possible localized response mode of masonry walls, a very basic, conservative approach was necessary for a "first cut" at this type of analysis. Further refinement and improvement will be made to the analysis as more is learned in this area.

In this analysis, local breaching or shear failure is assumed to be initiated if the total applied force acting over a specific area at the time of arrival of the blast wave (cubicly distributed also) is greater than the total shear resistance of the mortar around the perimeter of that area (see Figure 7). This type of failure is assumed to occur very early in the response of the wall and to be caused by excessive material strains during the first propagation of the stress wave through the wall. If these initial stresses are greater than the allowable shear stress of the mortar (mortar assumed to be the "weak link"), shear failure is assumed to initiate.

At present, there is no available data on which to base any assumptions for the actual area over which shear failure for a given set of loading and wall parameters can be expected. Until further information is obtained, a shear diameter equal to 1.3 times the charge distance from wall has been assumed. This factor comes from TM 5-855-1 [2] where the figure is recommended for determining the area over which to apply load for close-in detonations. The total force acting over the specified area is determined by integration of that portion of the load distribution which is applied over that area (Figure 7). The integral for the total force is defined a follows:

$$F_t = 2\pi\int_0^R r \cdot P(t) \cdot dr$$

where

R = specified radius of shear area

The total resisting shear force is defined as:

$$R_t = 2\pi R t \sigma_u$$

where

t = wall thickness
σ = ultimate shear stress

The actual movement of the sheared-out section is not calculated, only the "initiation" of shearing. However, as more information is obtained, this would be a useful addition to the code.

As stated previously, many possible variables affecting the localized response of masonry walls are still unknown or had to be neglected in the present analysis due to lack of information on their effects. A major factor affecting this type of response is felt to be the increased shear resistance of the wall materials provided by in-plane arching forces developed within the wall panel and by increased material strengths due to the dynamic effects.

RESULTS

Maximum response calculations obtained from the revised code have been compared to a limited amount of experimental data on masonry wall response to conventional weapons. Table 1 shows a comparison between the actual and predicted response for four tests conducted by the Swedish National Defense Research Institute [4], two tests by researchers in the United Kingdom,* and four tests by WES.+ These results indicate that the code works well for predicting the response of walls which respond in a purely flexural mode, but that the predictions for shear failure were far too conservative.

Calculations using the code indicated that shear would just begin to initiate in the 30-cm-thick (12-in.) solid brick wall (WES test) with 6.2 kg (13.7 lbs) of TNT at a range of 56 cm (22 in.). However, no cracking in the expected shear area could be found. The charge weight was then doubled to 12.4 kg (27.4 lb) and still no indication of shearing could be found. In fact, little cracking other than minor vertical cracks at the wall edges were evident after either test. The actual and predicted flexural responses, neglecting shear, compare very closely for these walls.

CONCLUSIONS AND RECOMMENDATIONS

The revised ARCHING code appears to give good results for predicting the response of masonry walls when only a flexural mode is considered. However, as expected, much improvement is needed in the shear response analysis. At present, the shear analysis provides results that are far too conservative.

Basically, more research and experimentation is needed in all aspects of dynamic masonry wall response. Some primary areas of interest are the arching effect on masonry walls, the nonuniform time-dependent loading produced by small conventional weapons and the effects of this on the structural response, material strength and masonry bond pattern effects, and fragmentation effect on the structural response and failure mode. Also, the present code is not applicable to cavity-type masonry or reinforced masonry walls. Since these are very common types of construction, work should be performed to adapt the code to these types of walls. Pending these improvements, the present code should provide a means of obtaining a fairly reliable and conservative estimate of structural vulnerability to conventional weapons.

*Personal Communication, Mike Hedges, Property Services Agency, United Kingdom, 1986.

+Unpublished Data, David Coltharp, U.S. Army Engineer Waterways Experiment Station, Vicksburg, Mississippi, June 1986.

ACHNOWLEDGEMENT

This work was sponsored by the U.S. Army Belvoir Research and Development Center (BRDC), Fort Belvoir, Virginia. Mr. William Comeyne and Ms. Susan Adkins, BRDC, were Program Monitors during the time this work was performed. Messrs. Robert Walker and William Huff, Structures Laboratory (SL), WES, were the Program Managers. Mr. Jay Cheek, SL, WES, provided computer programming assistance. The Office, Chief of Engineers granted permission to publish this report.

REFERENCES

1. C. K. Wiehle and J. L. Buckholt, "Summary of Existing Structures Evaluation Part I: Walls," Technical Report, Stanford Research Institute (for the Office of Civil Defense), Menlo Park, California, November 1968.

2. Headquarters, Department of the Army, "Fundamentals of Protective Design for Conventional Weapons," Technical Manual 5-855-1, Washington, D. C., in preparation.

3. J. T. Baylot, S. A. Kiger, K. A. Marchand, and J. T. Painter, "Response of Buried Structures to Earth Penetrating Conventional Weapons," Technical Report ESL-TR-85-09, Air Force Engineering and Services Center, Tyndall Air Force Base, Florida, January 1985.

4. R. Forsen, "Airblast Loading of Wall Panels," FOA Report No. C 20586-D6, Swedish National Defense Research Institute, Stockholm, Sweden, October 1985.

Table 1. Actual Versus Predicted Results

Wall Description	Equivalent TNT Weight kg (lb)	Range m (ft)	Maximum Deflection mm (in.) Predicted	Measured
25.4 cm (10 in.) thick Swedish, solid yellow brick; 2.1 m x 1.2 m; one-way arching	8.4 (18.5)	5.0 (16.4)	13 (0.5)	13 (0.5)
Same as above	48.1 (106)	6.6 (21.7)	30 (1.2)	48 (1.9)
25.4 cm (10 in.) thick Swedish, solid red brick; 2.1 m x 1.2 m; one-way arching	8.4 (18.5)	5.0 (16.4)	13 (0.5)	10 (0.4)
Same as above	48.1 (106)	6.6 (21.7)	36 (1.4)	53 (2.1)
23 cm (9 in.) thick U.K., solid brick; 2.6 m x 2.7 m; Gap at top of wall	27.2 (60)	6.0 (19.7)	41 (1.6)	38-Perm. (1.5)
Same as above	27.2 (60)	9.0 (29.5)	15 (0.6)	3-rebound (.1)
10 cm (4 in.) thick U.K., solid brick; 2.6 m x 2.7 m; two-way arching	27.2 (60)	10.0 (32.8)	Collapse	Collapse
30.5 cm (12 in.) thick WES, solid brick; 3 m x 3.7 m; two-way arching	3.1 (6.9)	0.9 (2.9)	Shear fail. 9 (0.4)-flex.	No shear 8 (0.3) in flex.
Same as above	6.2 (13.7)	0.9 (2.9)	Shear fail. 15 (0.6)-flex.	No shear 17 (0.65) in flex
Same as above	12.4 (27.4)	0.9 (2.9)	Shear fail. 21 (0.85)-flex.	No shear 51 (2.0)-flex.
20.3 cm (8 in.) thick WES, solid brick; 2.7 m x 4.9 m; two-way arching	68.0 (150)	12.9 (42.4)	23 (0.9)	53 (2.1)
Same as above	6.2 (13.7)	0.9 (2.9)	26 (1.0)	57 (2.3)

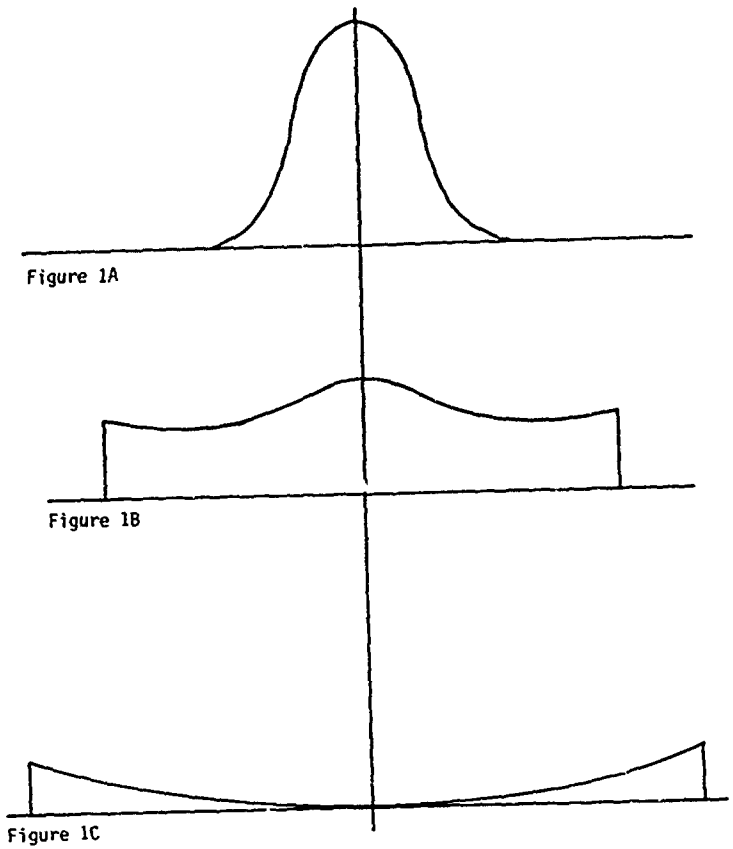

Figure 1. Variation of pressure distribution on walls

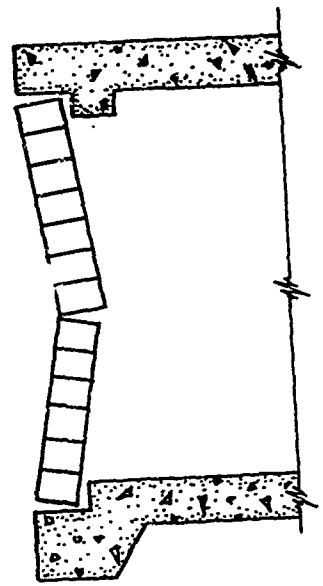

Figure 2. Assumed deflection mode of nonreinforced masonry wall

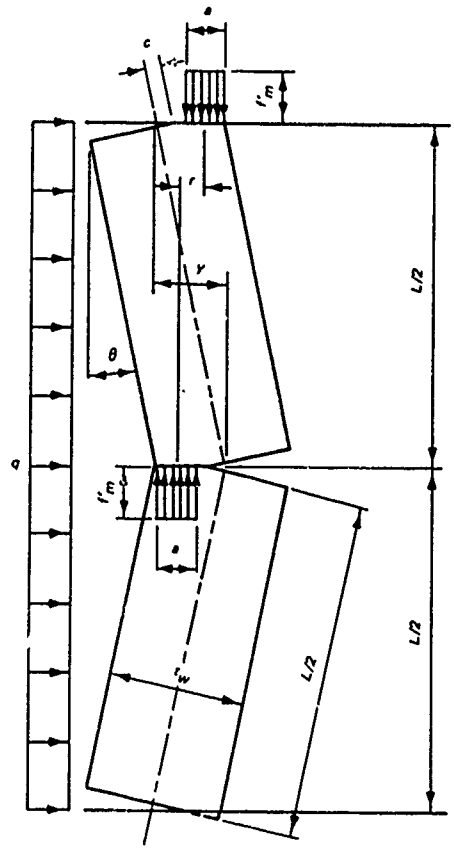

Figure 3. Assumed arching behavior of masonry wall (forces on bottom half not shown)

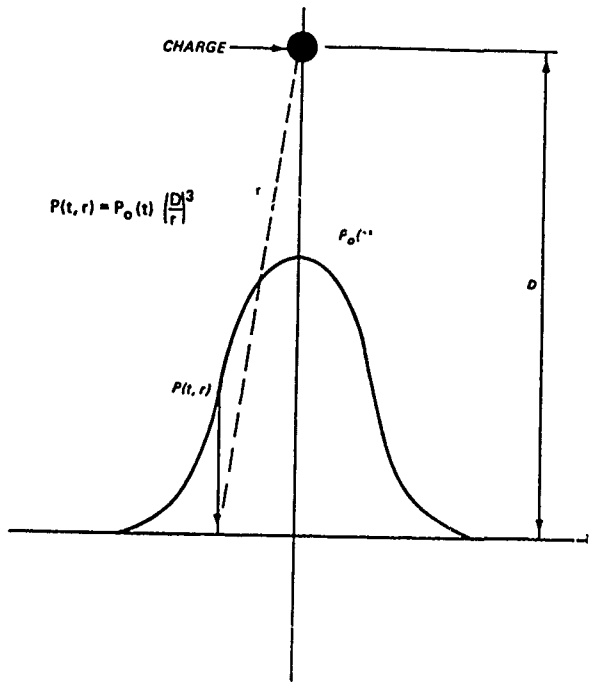

Figure 5. Assumed cubic pressure distribution on walls

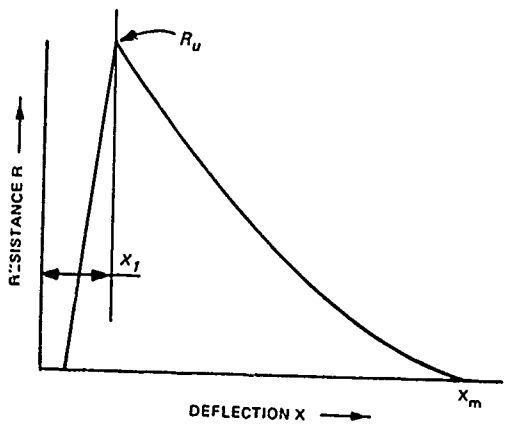

Figure 4. Resistance-deflection function

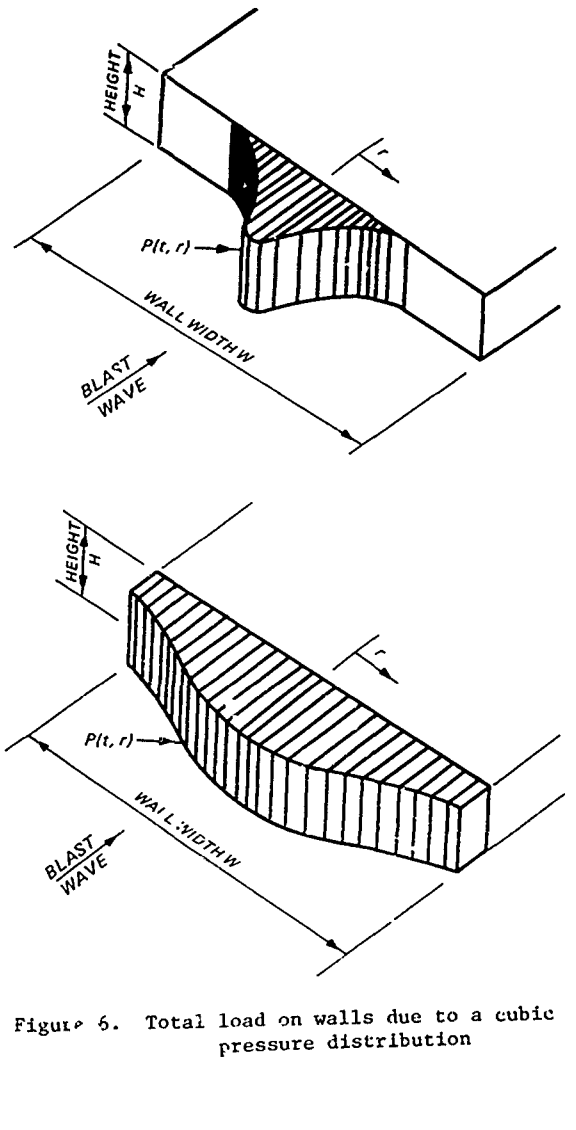

Figure 6. Total load on walls due to a cubic pressure distribution

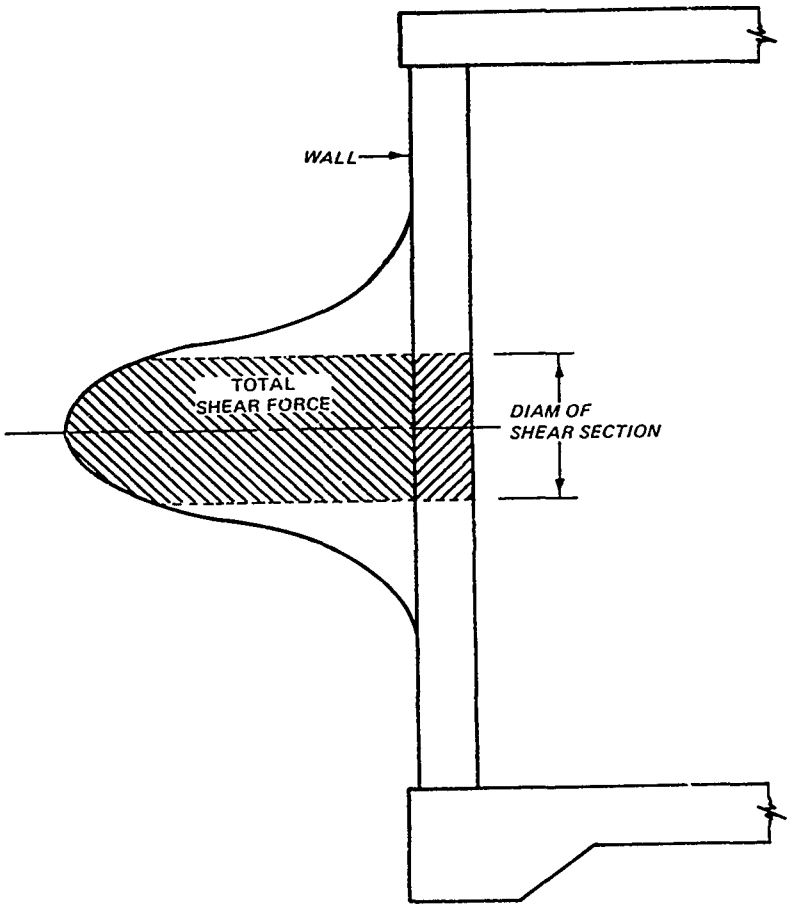

Figure 7. Portion of load distribution used for shear calculations

Retarded Potential Technique Applied for Shock Wave Loading of Doubly Symmetric Submerged Structures

W. W. Webbon
Martin Marietta Baltimore Aerospace
Baltimore, Maryland

M. Tamm
Naval Research Laboratory
Washington, D. C.

A three-dimensional application of the Kirchhoff retarded potential integral equation referred to as the Retarded Potential Technique is combined with the finite element structural analysis program ADINA. The combined method is used to predict the transient response of an elastic spherical shell immersed in fluid to an incident plane step pressure pulse. Predictions compare well with known series solutions for the response although divergence of the predicted responses occurs at later times. The method may be applied directly for non-spherical doubly symmetric structures with a continuous fluid-structure interface modeled with ADINA shell finite elements.

NOMENCLATURE

a	midsurface spherical shell radius
$\vec{r}$	vector from coordinate origin to observation point
t	observation time
t_0	$t - \frac{R}{c}$, retarded time
$\vec{r}_0$	$\vec{r}(x, y, z, t_0)$, vector from coordinate origin to integration point
R	$= \lvert\vec{r} - \vec{r}_0\rvert$, magnitude of vector from integration point to observation point
c	velocity of sound
$p(\vec{r}, t)$	total pressure
p_t	$= \frac{\partial p}{\partial t}$, time derivative of pressure
p^{inc}	prescribed incident pressure pulse
p^{rad}	radiated pressure due to non-rigid body
p^{sca}	scattered pressure of rigid body
p_0	magnitude of step pressure
S	surface of the body
$\vec{n}_0$	unit normal on S into the body
R_{max}	maximum distance between two points on S
t_{max}	$= \frac{R_{max}}{c}$, maximum retarded time
K	number of zones into which S is divided
S_k	k^{th} zone of S
$\vec{r}_k$	center of S_k
$\vec{r}_j$	observation point (the set of $\vec{r}_j$'s is the same as the set of $\vec{r}_k$'s)
τ	time step size
m	time step index
ρ	fluid density
$\tilde{\omega}$	structure inner directed normal acceleration
j	index of the observation point (zone) at which the pressure is calculated
k	index of the field point (zone) for the numerical integration for p_j^m
Γ_{jkl}	geometric coefficient defined by equation (4)
Ω_{jkl}	geometric coefficient defined by equation (5)
$\hat{t}_{jkl}$	$\frac{R_{jkl}}{c}$, time retardation corresponding to R_{jkl}
R_{jkl}	distance from zone j to subzone kl
n_{jkl}	largest integer in $\frac{\hat{t}_{jkl}}{\tau}$
γ_{jkl}	$\frac{\hat{t}_{jkl}}{\tau} - n_{jkl}$, fractional part of time retardation
C_q	numerical differentiation coefficient q
A_{ij}^k	influence coefficient relating the acceleration at zone k at time $(m-i)\tau$ to the pressure at zone j at time $m\tau$
B_{ij}^k	influence coefficient relating the pressure at zone k at time $(m-i)\tau$ to the pressure at zone j at time $m\tau$
(x, y, z)	cartesian coordinates with origin at center of sphere
θ	polar angle measured from z-axis
$\delta_z(\theta, t)$	x-directed deflection of sphere surface
$\dot{\delta}_z(\theta, t)$	z-directed velocity of sphere surface
δ	Newmark time integration parameter
α	second Newmark parameter given by $0.25(\delta + 0.50)^2$

INTRODUCTION

The Kirchhoff's retarded potential integral equation is appealing as a method for analysis of transient scattering and radiation from a submerged body because it provides a solution without inherent approximation. The equation reduces the volume integration over the entire fluid to an integration over the surface enclosing the body reducing the numerical computations required. The computation can be performed in the time domain permitting interface with direct integration structural analysis codes. Researchers have used exact solutions such as the retarded potential formulation for rigorous derivation of fluid-structure approximations such as the Doubly Asymptotic Approximation (DAA) [1,2]. The direct use of the Retarded Potential Technique (RPT) is investigated here to determine feasibility and accuracy.

The RPT method to be described was first implemented for scattering from a rigid sphere by K. M. Mitzner [3] who accurately calculated the scattering from the sphere due to a Gaussian incident pulse. This application was further extended by H. Huang [4] to include the radiated pressure component from an elastic sphere. The technique was applied to an axisymmetric NASTRAN spherical shell finite element model by applying the series solution for the rigid sphere scattered pressure and calculating the radiated pressure. Calculated pressures and velocities agreed with the series solutions. The present study extends this earlier work to solution of three-dimensional geometry performing rigid scattered and radiated pressure calculations concurrently. A quarter spherical model with double symmetry consisting of 34 shell finite elements is analyzed with a three-dimensional surface integration for the pressures. Concurrent solution for the structural dynamic response is accomplished by applying these pressures to the finite element model.

The ADINA [5] program is used and axisymmetric surfaces defined by the three-dimensional shell element form the RPT fluid-structure interface. The method is implemented in such a manner that non-spherical doubly symmetric surfaces may also be studied. The method, in principle, can be extended to fully three-dimensional geometries. Wave loading is described by specifying an incident waveform and its direction and location. The structural model may contain material non-linearities but not geometric non-linearities. Another task has been improvement of stability in the numerical solution. It was pointed out by Neilson, Lu, and Wang [6] that the numerical technique of Mitzner is most applicable for a pulse having a continuous envelope such as a Gaussian pulse. For a plane acoustic wave with discontinuous front, for example, a solution will "characteristically start out with reasonable values but degenerate rapidly into larger and larger oscillations" [6]. This convergence problem is reduced in the case of a plane step wave by utilizing continuous approximations of the step function.

FORMULATION

A discussion of the continuous and discrete retarded potential equations may be found in Refs. [3,4]. The equation for calculation of surface total pressures [4], $p(\vec{r},t)$, for a continuous closed surface in an infinite fluid subject to continuous wave loading is as follows:

$$p(\vec{r},t) = 2p^{inc}(\vec{r},t) - \frac{\rho}{2\pi}\int\int_S \frac{\ddot{\omega}(\vec{r}_0,t_0)}{R}dS + \frac{1}{2\pi}\int\int_S [p(\vec{r}_0,t_0) + \frac{R}{c}\frac{\partial p(\vec{r}_0,t_0)}{\partial t_0}]\frac{1}{R^2}(\frac{\partial R}{\partial \vec{n}_0})dS \quad (1)$$

The position vector, $\vec{r}$, refers to points on the surface as measured from the coordinate origin. The quantity, t_0 , is an earlier or "retarded" time which is determined for a specific integration point by subtraction from the current time, t , at the observation point of the transit time of sound between the points. The incident pressure, p^{inc} , is the surface pressure loading, ρ , is the fluid density, $\ddot{\omega}$ is the acceleration of the selected surface, $\vec{n}_0$ is the inner directed normal unit vector to the surface at an integration point. The equation is valid for continuous pressure waves which are solutions to the linear wave equation.

$$\nabla^2 p = \frac{1}{c^2}\frac{\partial^2 p}{\partial t^2} \quad (2)$$

Equation (1) may be shown to be the integral solution of equation (2) subject to the boundary condition $\nabla p \cdot \vec{n}_0 = -\rho\ddot{\omega}$ [4].

Application of equation (1) to solve problems involving structures in a (presumed) infinite fluid requires replacement, in effect, of the fluid within the selected surface by a structure whose boundary behaves exactly as the fluid boundary. This application may be described as follows. It is first noted that the total pressure, p, is the sum of the incident, scattered and radiated pressures.

$$p = p^{inc} + p^{sca} + p^{rad} \quad (3)$$

For convenience, the sum of the scattered plus incident pressures are denoted p^{rig} and equation (1) could be split into two equations for p^{rig} and p^{rad} [4], describing the problem of scattering of an incident pressure wave from

a rigid surface and the problem of radiation of pressure in a fluid due to imposed surface accelerations, respectively. The replacement, in effect, of the fluid inside the selected surface by a structure can be achieved by requiring that the imposed surface accelerations are the same as those experienced by a structure in response to the total pressure. The solution consists of the superposition of these two linear fluid dynamics problems with intermediate solution of the structural dynamics problem. In practice these two fluid problems may be solved concurrently. Note that there are no restrictions on the surface deformation although, for this study, the deformation is assumed to be small.

IMPLEMENTATION

For computation, the fluid dynamics problem defined by Equation (1) must be discretized and linked to the structural analysis code. The surface pressure field is approximated by subdividing the surface into K zones of constant pressure coinciding with individual finite element surfaces. The surface normal acceleration field is also approximated as constant on the surface of the finite element for calculation of the pressure. Pressures and accelerations are discretized in time to coincide with the time steps of the finite element program. Prior to conducting the time history computation of pressures and structural response, a matrix of influence coefficients must be calculated that expresses the dependence relations of current pressures on past pressures and past and present accelerations.

First the time derivative of pressure must be reduced to a finite difference scheme. A three point backward difference formula is used in this implementation [3,4]. Each zone is subdivided into a mesh of subzones so that the pressure and acceleration can be factored out of the integral expressions. This subdivision also permits accurate numerical integration of the geometric influence factors, as well as accurate determination of the time-delayed pressures and accelerations from each preceding time step. Fig. 1 illustrates the finite elements/zones (large numbered rectangles) and the subdivision into subzones. For the purpose of measuring the distance between source and observation points and thereby the time-retardation, the observation point is located at the center of the field zone and the source point is located at the center of the source subzone element. The source points will not fall at a whole number of time intervals from the field point, so an interpolation from adjacent whole time intervals is needed to determine the pressure at the source point as illustrated in Fig. 2. An important feature of the numerical integration technique is that the retarded time is allowed to vary over a zone thereby admitting much larger zones than could be permitted if a single retarded time were associated with each zone [3].

For the surface area immediately surrounding the observation point, a modified calculation must be used to compute the source influence, because of the close proximity of the observation point and the presence of a singularity at the observation point itself. The surface surrounding the observation point is approximated by an osculating paraboloid with principal curvatures matching those of the original defined surface and an exact integral, which takes into account the singularity, is evaluated over this surface. The curvatures are numerically evaluated at the center of each finite element surface. Further details of the surface integration technique are elaborated in Ref. [3]. The major points of the derivation are repeated here for continuity.

Each of the K zones are subdivided into L subzones, S_{jkl}, small enough that the pressure, pressure time derivative, and acceleration of equation (1) may be assumed constant. The remaining integrals,

$$\Gamma_{jkl} = \iint_{S_{jkl}} \frac{dS}{R_{jkl}} \tag{4}$$

and,

$$\Omega_{jkl} = -\iint_{S_{jkl}} \frac{1}{R_{jkl}^2} \frac{\partial R_{jkl}}{\partial \vec{n}_0} dS \tag{5}$$

are recognized as geometric coefficients, the latter being negative of the solid angle subtended by S_{jkl} at $\vec{r}_j$. The value of the retarded time, $\hat{t}_{jkl}$, will not in general be a multiple of $m\tau$ and may be expressed as

$$\hat{t}_{jkl} = (n_{jkl} + \gamma_{jkl})\tau \text{ ,n integer, } 0 \le \gamma < 1 \tag{6}$$

where, p_k, $p_{t,k}$, $\tilde{\omega}_k$ may now be interpolated

$$p_k(m\tau - \hat{t}) = (1-\gamma)p_k^{(m-n)} + \gamma p_k^{(m-n-1)} \tag{7}$$

The remaining step is to determine the time derivative of the pressure by the standard three point backward difference formula,

$$p_{t,k}^m = \frac{1}{\tau} \sum_{q=0}^{Q} C_q p_k^{(m-q)} \tag{8}$$

where, $Q = 2$, $C_0 = \frac{3}{2}$, $C_1 = -2$, $C_2 = \frac{1}{2}$. The discrete retarded potential formulation may now be expressed as [4]

$$p_j^m = +2(p^{inc})_j^m$$
$$-\frac{\rho}{2\pi}\sum_{k=1}^{K}\sum_{l=1}^{L}\Gamma_{jkl}[(1-\gamma_{jkl})\ddot{\omega}_k^{(m-n)} + \gamma_{jkl}\ddot{\omega}_k^{(m-n-1)}]$$
$$-\frac{1}{2\pi}\sum_{k=1}^{K}\sum_{l=1}^{L}\Omega_{jkl}\{(1-\gamma_{jkl})[p_k^{(m-n)} + \frac{\hat{t}_{jkl}}{\tau}\sum_{q=0}^{2}C_q p_k^{(m-n-q)}]$$
$$+\gamma_{jkl}[p_k^{(m-n-1)} + \frac{\hat{t}_{jkl}}{\tau}\sum_{q=0}^{2}C_q p_k^{(m-n-q-1)}]\} \quad (9)$$

Rearranging terms, the total pressure may be expressed in terms of two sets of time independent coefficients and the retarded accelerations and pressures.

$$p_j^m = 2(p^{inc})_j^m - \frac{\rho}{2\pi}\sum_{k=1}^{K}\sum_{i=0}^{I'}A_{ij}^k\ddot{\omega}_k^{(m-i)} - \frac{1}{2\pi}\sum_{k=1}^{K}\sum_{i=0}^{I}B_{ij}^k p_k^{(m-i)} \quad (10)$$

where,

$$I' = \frac{\max(R_{jkl})}{c\tau} + 1 \quad (11)$$

$$I = \frac{\max(R_{jkl})}{c\tau} + 3 \quad (12)$$

This rearrangement is carried out in machine computation. Since the pressures p_k^m on the R.H.S. are not yet known, the convergence criteria

$$\min\{R_{jkl}\}_{j\neq k} \geq c\tau \quad (13)$$

is imposed implying that a disturbance from one zone cannot affect any other zones in less than one time increment and therefore,

$$B_{0j}^k = 0 \text{ for all } j \neq k \quad (14)$$

Hence equation (10) becomes,

$$p_j^m = +4\pi(p^{inc})_j^m/(2\pi + B_{0j}^j) \quad (15)$$
$$+\frac{-\rho\sum_{k=1}^{K}\sum_{i=0}^{I'}A_{ij}^k\ddot{\omega}_k^{(m-i)} - \sum_{k=1}^{K}\sum_{i=1}^{I}B_{ij}^k p_k^{(m-i)}}{(2\pi + B_{0j}^j)}$$

Solution of equation (14) requires simultaneous knowledge of $\ddot{\omega}_j^{(m-i)}$ and $p_j^{(m-i)}$. The finite element code, however, calculates $\ddot{\omega}_j^{m+1}$ from the total pressure calculated at step m, p_j^m. Hence, the accelerations used in the pressure calculations lag one time step behind. Presumably, τ may be chosen small enough that this discrepancy is insignificant. The solution algorithm is based on the following steps.

1. Apply $(p^{inc})_j^0$ at $m = 0$, time step 1
2. Calculate zone accelerations, $\ddot{\omega}_j^1$ (Note $\ddot{\omega}_j^0 = 0$)
3. $m = m + 1$
4. Calculate p_j^m
5. Apply p_j^m to finite element model
6. Calculate zone accelerations, $\ddot{\omega}_j^{m+1}$ by averaging nodal accelerations from finite element solution
7. If maximum time step reached, stop solution
8. Go to step 3

STRUCTURAL RESPONSE

The finite element structural model which is utilized in the study consists of 34 finite elements as shown in Fig. 3. The spherical shell model has mid-surface radius, $a = 254cm$; Young's modulus, 2.0684 x $10^{11}Pa$; thickness, $5.08cm$; Poisson's ratio, 0.3, mass density, $7784.5kg/m^3$. The fluid density and sound velocity are $999.6kg/m^3$ and $1461.2m/s$, respectively. A consistent mass formulation is used in the finite element model. The incident wave approximation utilized for loading the model is shown in Fig. 4. This is the Fourier integral of the step function evaluated from 0 to 1500 hertz in steps of 1 hertz. Direction of the incident wave travel is $(0, 0, -1)$. Several other functions were tried including a linear ramp and a step function smoothed by a sin^2 function. The Fourier integral gives the best results over the entire time interval. The non-dimensional time increment used in this study is $c\tau/a = 0.04$.

The displacements of the sphere surface perpendicular to the direction of the incident wave and the velocities parallel to the direction of the incident wave are plotted in Figs. 5 to 7. Dashed curves in these figures indicate the predicted calculations and the solid curves the known responses from Ref. [7]. The calculated results agree very well with the known series solutions. The phase of the prediction is in good agreement but there appears to be amplitude decay of the numerical solutions. The numerical solution is seen to characteristically oscillate at later times, particularly the velocities. This oscillating behavior is physically a high frequency ringing which is superimposed upon the overall structural response. It is sensitive to the degree of numerical damping imposed by the numerical integration technique in the structural finite element model. The values of the Newmark parameters, δ and α, for the structural response shown in the figures are 0.75 and 0.39, respectively, corresponding to

a high degree of numerical damping. Good results were also obtained for Newmark parameters corresponding to no structural damping (0.50,0.25) by introducing algorithms to stabilize pressure oscillations. However, the stabilization also tends to overdamp the response.

The oscillating behavior of the solution is also affected by the smoothness of start of the incident pressure. Stability is improved by increasing the length of incident wave occurring before zero. The starting time for the curves shown is -10.0 although good responses are also obtained for starting values of -2.0 and -1.0 nondimensional times.

The RPT technique applied for the spherical shell appears to accurately model the fluid-structure interaction in spite of the relatively coarse finite element model. The initial inaccuracy in the transverse deflections at 18 degrees is due to the incident pressure being applied to all the nodes of the finite element containing node 1. This deficiency can be corrected by zoning the surface so that zone centers correspond with finite element nodes. The method may also be adjusted by time increment and frequency content of the incident wave to give more accurate responses at either early or late times for a given problem.

CONCLUSION

Although noted difficulties have been encountered in this approach; in particular, the oscillatory divergence at later times, the method has been demonstrated to be quite effective. It is clear that the next step in the implementation of this technique requires a stability study of the numerical integration. However the technique presents the capability to study the structural response of non-spherical three-dimensional submerged bodies which can easily be accomplished by removing double symmetry constraints in the current program. The feasibility for small test problems is clearly demonstrated. An advantage of the technique is that the pressure and acceleration coefficients need only be calculated once for a given surface geometry. Problems may be rerun by retrieving stored coefficients for a variety of incident wave loading and may include structural changes not affecting the surface geometry. For larger problems the machine storage requirement for the acceleration and pressure coefficients as shown by Huang [4] is dominated by the factor $(IK^2 + K)$ which can become limiting. For these problems the number of zones considered can be minimized by using larger zones in areas remote from the detailed area of most interest. The RPT can accurately be used for verification of approximate methods. The technique may itself be modified for approximate solution perhaps leading to improved solution accuracy.

ACKNOWLEDGEMENT

Gratitude is extended to Dr. Hanson Huang, NRL colleague, now at the U.S. Naval Surface Weapons Center for his encouragement and assistance in implementing the capability with the ADINA code. The portion of this work performed at NRL was supported through the Office of Naval Research under NRL problem number 58029204.

REFERENCES

1. T. L. Geers, "Residual Potential and Approximate Methods for Three- Dimensional Fluid-Structure Interaction Problems", Journal of the Acoustical Society of America, Vol. 49, 1971, pp. 1501-1510.
2. C. A. Felippa, "Top-down Derivation of Doubly Asymptotic Approximations for Structure-Fluid Interaction Analysis", Innovative Numerical Analysis for the Applied Engineering Sciences, The University Press of Virginia, 1980.
3. K. M. Mitzner, "Numerical Solution for Transient Scattering from a Hard Surface of Arbitrary Shape-Retarded Potential Technique", Journal of the Acoustical Society of America, Vol. 42, 1967, pp. 391-397.
4. H. Huang, G. C. Everstine, Y. F. Wang, "Retarded Potential Techniques for the Analysis of Submerged Structures Impinged by Weak Shock Waves", Computational Methods for Fluid-Structure Interation Problems AMD -Vol. 26, ASME, 1977.
5. "A Finite Element Program for Automatic Dynamic Incremental Nonlinear Analysis", Report AE 84-1, ADINA Engineering, Watertown, MA., Dec., 1984.
6. H. C. Neilson, Y. P. Lu, Y. F. Wang, "Transient Scattering by Arbitrary Axisymmetric Surfaces", Journal of the Acoustical Society of America, Vol. 63, 1978, pp. 1719-1726.
7. H. Huang, "Transient Interaction of Plane Acoustic Waves with a Spherical Elastic Shell", Journal of the Acoustical Society of America, Vol. 45, 1969, pp. 661-670.

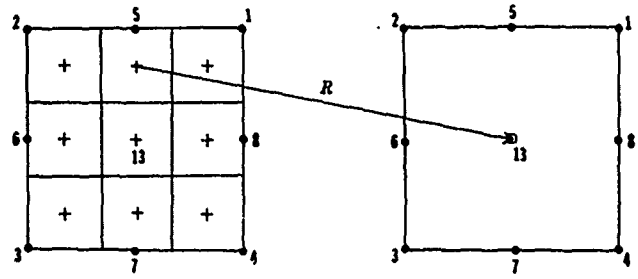

Radius between source point in subsone element and observation point of another sone

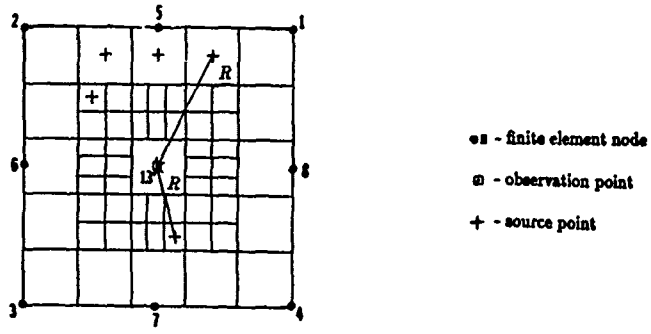

Radius between source points and observation point in same sone

Figure 1. Subzone mesh divisions showing observation points, source points, and finite elements node points

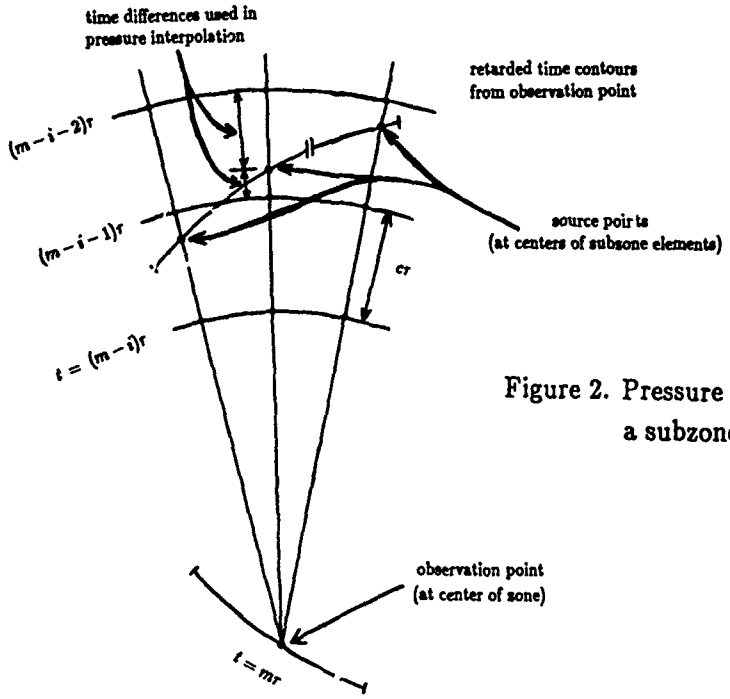

Figure 2. Pressure interpolation on a subzone in retarded time

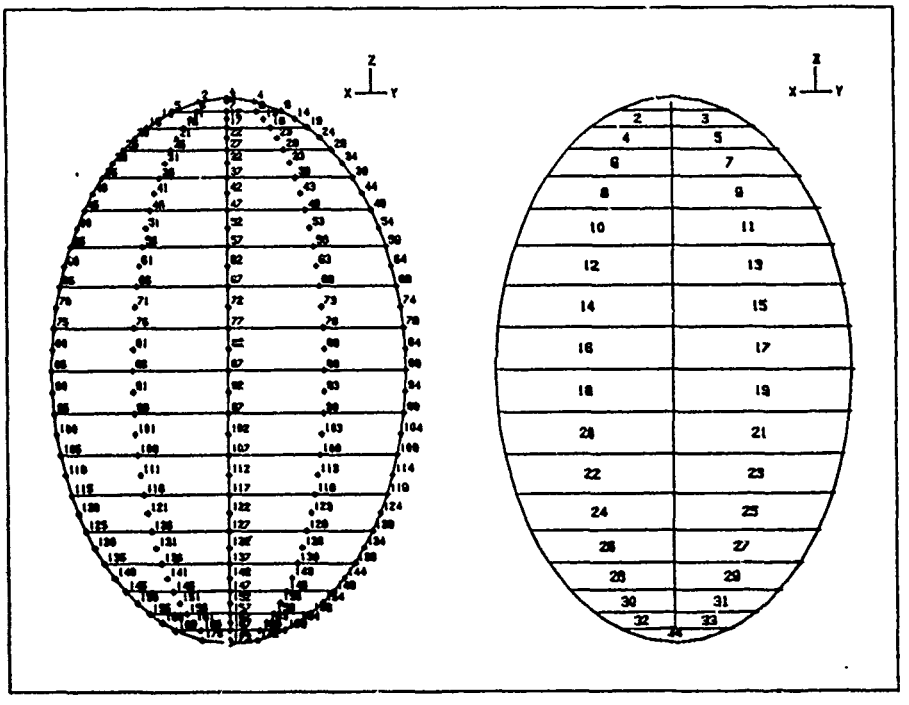

Figure 3. ADINA Finite Element Model

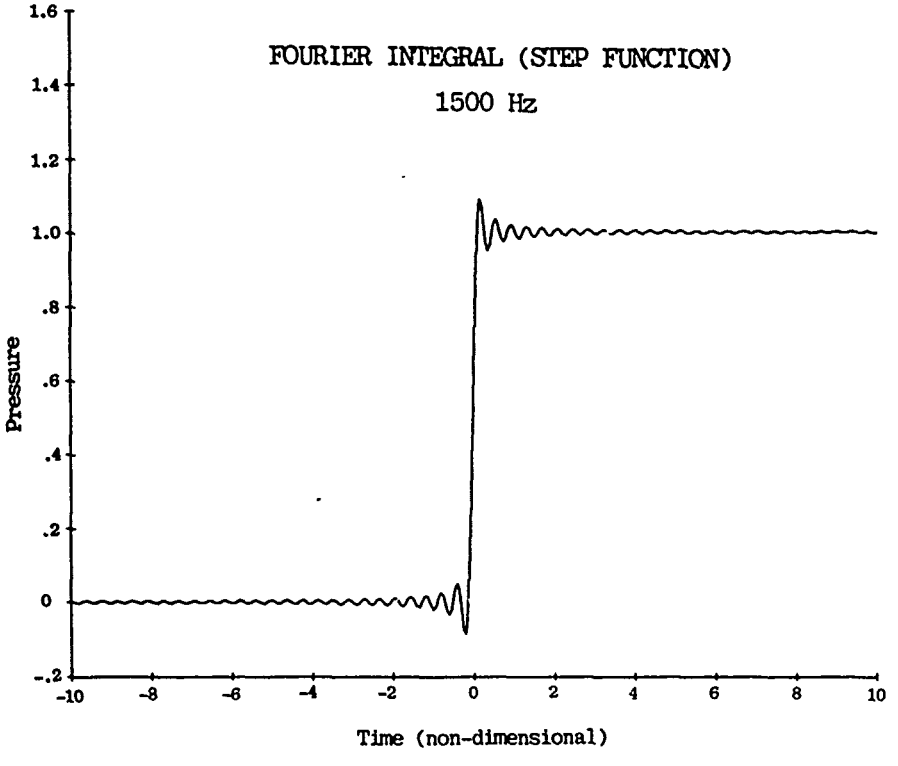

Figure 4. Incident Pressure Pulse

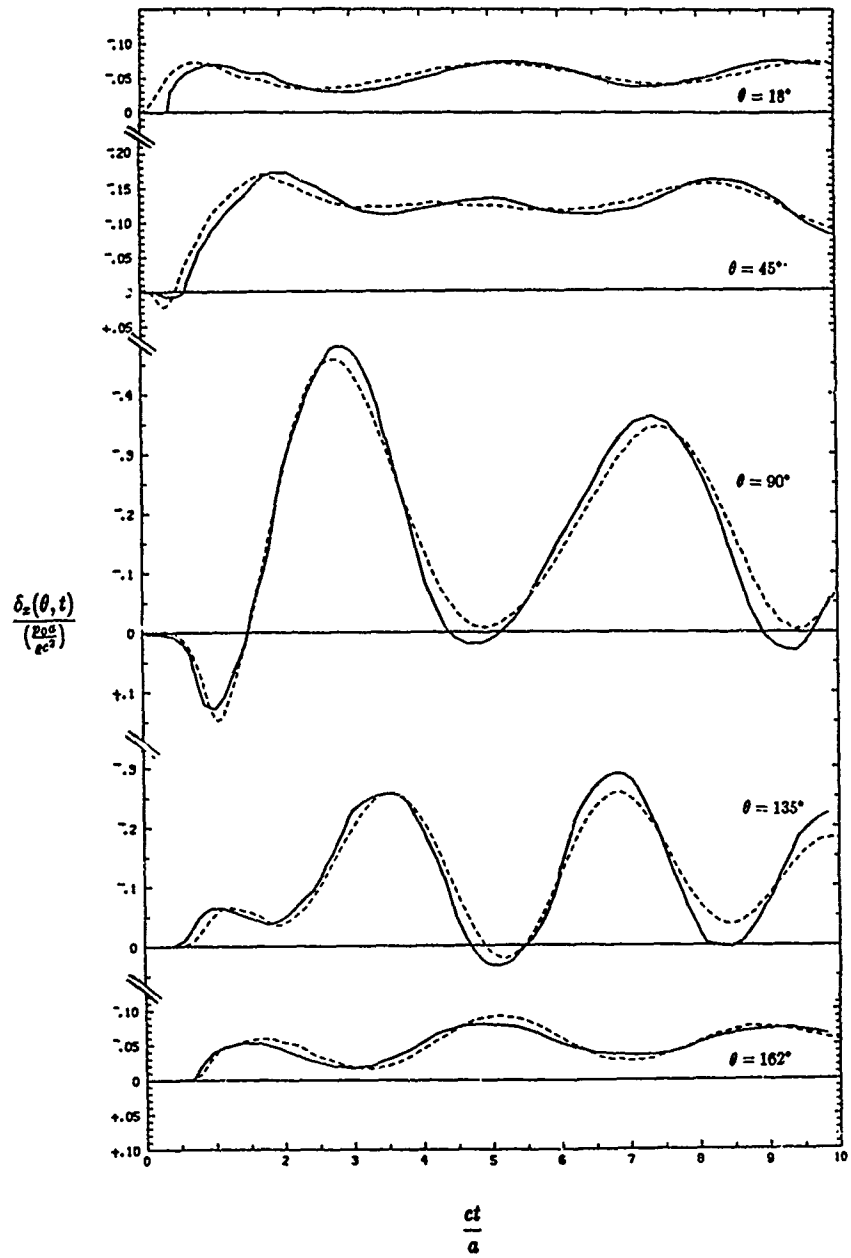

Figure 5. Time histories of shell deflection in the x-direction,
___classical solution, ...present results

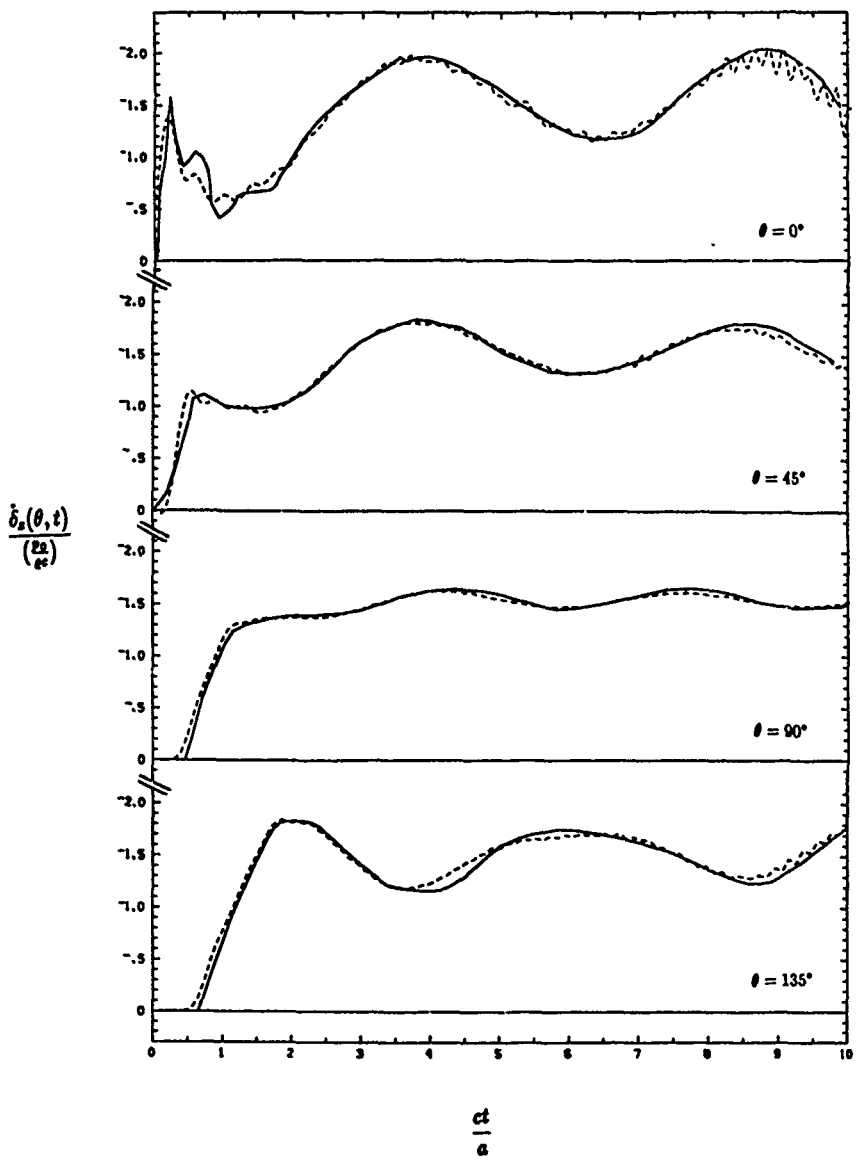

Figure 6. Time histories of shell velocity in the z-direction, ___classical solution, ...present results

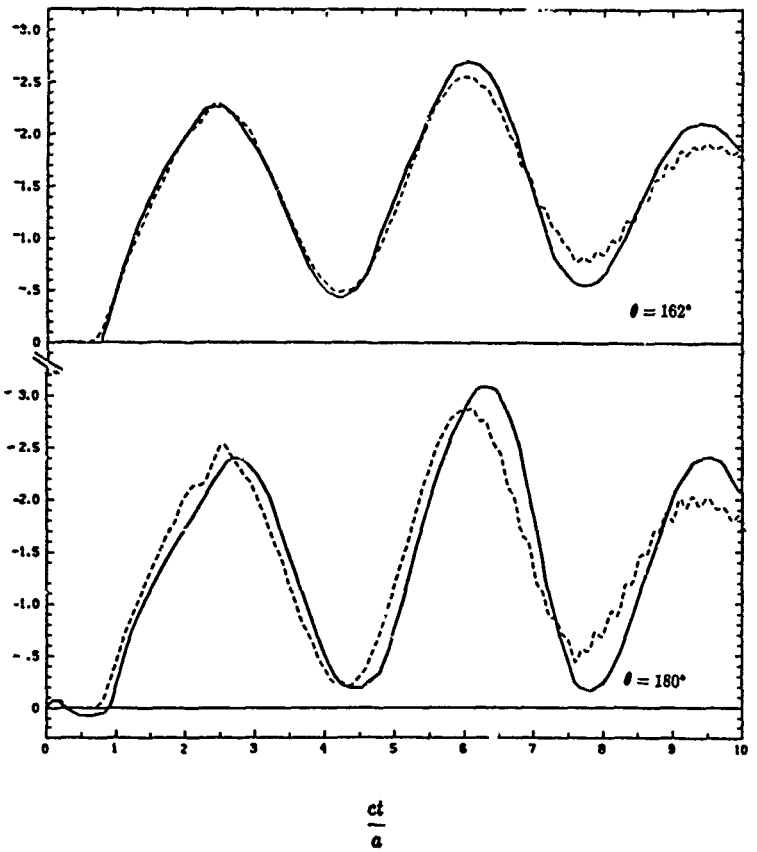

Figure 7. Time histories of shell velocity in the z-direction,
___classical solution, ...present results

HIGH-VELOCITY REVERSE BALLISTIC ROCKET SLED TESTING AT SANDIA NATIONAL LABORATORIES

R. D. M. Tachau
Sandia National Laboratories
Albuquerque, New Mexico

The design of an impact-fuzed weapon is dependent on accurate and predictable information about its behavior in an impact environment. Results from full-scale impact tests are essential in developing and verifying computer codes which model the crush-up of these weapons. This paper discusses the reverse ballistic impact test procedure and the advantages it offers over more conventional test methods for obtaining impact test results. Also described are recent developments by Sandia National Laboratories in the use of rocket sleds to push reverse ballistic impact targets faster than ever before.

INTRODUCTION

The 3,050 meter (10,000 foot) long rocket sled track at Sandia National Laboratories in Albuquerque, New Mexico, is a unique test facility. The track, along with its assortment of specially designed rocket sleds and laser tracking system, is the scene of a wide variety of tests. Over the course of many years, rocket sled testing at Sandia National Laboratories has ranged from nuclear waste transportation container crash tests to rain and dust erosion tests for high-velocity reentry vehicles. However, the most typical sled runs involve parachute deployment tests, component acceleration tests and impact tests.

Parachute deployment tests are essential in the development of air-delivered weapons or submunitions. For this type of test the unit is positioned on a rocket sled that ejects the test item vertically when the sled reaches a prescribed forward velocity. An onboard timer deploys the parachute at or near the test unit's apogee. From that point on, the trajectory replicates the free-fall trajectory from an aircraft bomb rack or munitions dispenser. Onboard telemetry and a motion picture camera, as well as ground-based photography and laser tracking, provide detailed and accurate information about the unit's performance.

The rocket sled facility is also ideally suited for testing the operation of components under high accelerations. For these tests the component is attached to a recoverable sled and run down the track on a predetermined acceleration profile. Onboard systems or telemetry monitor the performance of the component being evaluated.

Impact tests are the third type of test commonly conducted. These tests can be divided into two distinctly different groups. The setup for the first group involves attaching a test item to the front of a sled and propelling it into a fixed target at the end of the track. This is referred to as a direct impact test. The setup for the second group of impact-type tests involves fixing the test item at the end of the track, putting a target on a sled and then propelling that target into the stationary test item. This is referred to as a reverse ballistic impact test. This paper will discuss recent developments in the use of rocket sleds for reverse ballistic impact testing. The tests involve the high-velocity impact of reentry vehicles by 200 to 300 kilogram (440 to 660 pound) sled-mounted targets.

WEAPON SYSTEM DEVELOPMENT

It is necessary to have some background knowledge of weapon system development so that reverse ballistic impact testing can be fully appreciated. The design of an impact-fuzed weapon is dependent on accurate and predictable information about its behavior in an impact environment. Computer codes allow analysts to create detailed simulations of a weapon's crush-up and fuze timing during impact, but verification of these codes requires full-scale testing. Reverse ballistic testing offers significant advantages over the more conventional methods of field testing which require dropping or flying the test unit into a stationary ground target.

While the quantity and frequency of data that can be collected from a conventional test is limited by onboard telemetry systems, the

reverse ballistic procedure makes it possible to record large quantities of high-resolution test data via hardwire instrumentation. Reverse ballistic testing also allows precise control of target definition and impact geometry, information that is essential for computer modeling. The capability of identifying the precise impact point, before the test, makes it possible to include high-speed photography and flash x-rays as part of the reverse ballistic test diagnostics. In regard to the testing of reentry vehicles, another important advantage of a reverse ballistic rocket sled test is its relatively low cost compared to that of a missile flight test.

Results from high-velocity impact tests are essential in developing and verifying computer codes which model the crush-up of reentry vehicles. Reverse ballistic rocket sled testing provides one of the most practical means of collecting high-velocity, full-scale, crush-up data.

REVERSE BALLISTIC IMPACT TESTING AT SANDIA NATIONAL LABORATORIES

The Track and Cables Division at Sandia National Laboratories has conducted reverse ballistic rocket sled impact tests with target payloads ranging in weight from a few hundred to nearly 18,000 kilograms (500 to 39,600 pounds) at velocities from 100 to 1,844 m/s (330 to 6,050 ft/s). Naturally, for a given amount of propulsion, the relationship between payload weight and achievable velocity are inversely proportional. Until a few years ago, the velocity and weight requirements for most test scenarios could be met with available propulsion on the existing 1,525 meter (5,000 foot) long track facility. However, the trend for test requirements has been toward heavier targets and higher velocities. Tests with target payload weights of 200 to 300 kilograms (440 to 660 pounds) at impact velocities of 3,050 m/s (10,000 ft/s) have been suggested.

In October 1984 the existing technology at Sandia National Laboratories reached a practical upper limit when a 200 kilogram (440 pound) target was impacted into a reentry vehicle at about 1,500 m/s (4,920 ft/s). This was achieved with a two-stage sled propelled over the 1,525 meters (5,000 feet) of available track by 15 Zuni and 4 Javelin rocket motors. To achieve the test parameters for current reentry vehicle evaluation programs, Sandia National Laboratories has undertaken a development program which consists of facility upgrading, the acquisition of high-thrust, short-burn-time rocket motors and the development of new sled and testing technologies.

Even before the October 1984 sled test, the subjects of facility upgrading and the need for more potent propulsion had already been addressed. In the summer of 1984 ground was broken for the construction of a 1,525 meter (5,000 foot) long extension to the existing sled track. The search for a rocket motor with about 2,200,000 newton-seconds (500,000 pound-seconds) of impulse led to negotiations with the Army for acquisition of mothballed Sprint missiles. The Sprint missile propulsion and control assemblies had been in storage since deactivation of the Safeguard Anti-Ballistic Missile system. With its impulse of 4,400,000 newton-seconds (1,000,000 pound-seconds) and 1.65 second burn time, the Sprint first stage rocket motor offered an extremely cost-effective solution to the problem of adequate rocket sled propulsion. With the construction of the track extension underway and successful acquisition of the Sprint rocket motors, attention focused on development of a new sled.

THE FIRST SPRINT-POWERED REVERSE BALLISTIC IMPACT TEST

In early 1984, reverse ballistic impact test requirements for the Mk 21 reentry vehicle established the following performance and sled design parameters:

1. Minimum impact velocity: 1,830 m/s (6,000 ft/s)
2. Impact surface: elevated 20 degrees from horizontal
3. Target material: concrete

A new sled was to be built incorporating these design parameters and the newly acquired Sprint propulsion.

It was decided that the Sprint first stage rocket motor would be used as an integral part of the sled structure. Also, for aerodynamic and safety considerations, it was determined that the motor, with its 4 degree cone angle, should be positioned so that the axis of the cone would be inclined downward 4 degrees from the horizontal, thus making the lower surface of the motor parallel to the track structure.

The design of the forward payload section of the sled evolved into a modified horizontal cylinder with a 0.88 meter (34.6 inch) diameter to match the forward end of the rocket motor. The shape of the cylinder was modified to reduce aerodynamic drag by cutting the cylinder to form a vertical wedge with a 30 degree half-angle. The upper surface was cut to form the 20 degree impact surface. A drawing of the sled is shown in Figure 1.

The internal structure of the welded steel payload section created a cavity to support and contain a 235 kilogram (520 pound) cast-in-place concrete target and provided support to minimize aerodynamic-induced deflection of the steel plates forming the vertical wedge surfaces. The struts which attach the front of the sled to the rails were also integrated into the payload structure.

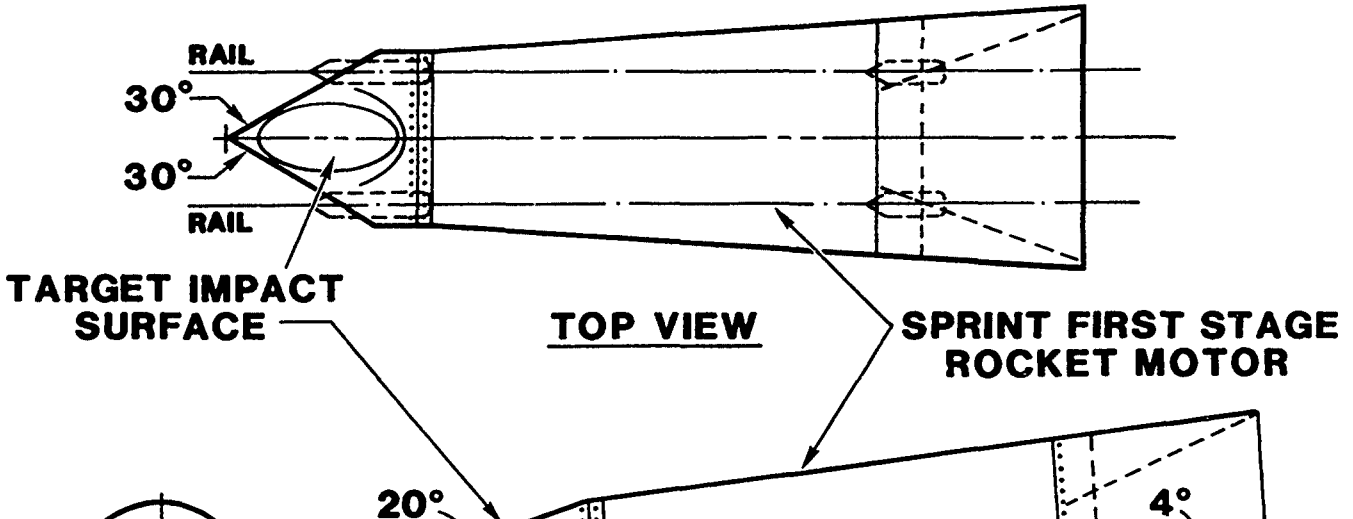

Figure 1. Sprint-powered rocket sled for reverse ballistic impact.

Finally, provisions were made to house the components of a 14-channel telemetry package. The package contained 4 strain gages, 3 accelerometers and 7 pressure transducers and was included to provide diagnostic data on the sled's performance. Fabrication of the sled was completed in March of 1985. While preliminary testing of the sled was being conducted, setup and instrumentation of the Mk 21 reentry vehicle were nearing completion.

On April 13, 1985, the reverse ballistic impact test was conducted. The Sprint-powered sled covered 1,503 meters (4,930 feet) in 1.55 seconds and impacted the test unit at 1,844 m/s (6,050 ft/s). The test yielded outstanding results and preparations began immediately for the next test which was desiginated HST-1.

THE HST-1 REVERSE BALLISTIC IMPACT TEST

The test parameters for HST-1 increased the impact velocity to 2,560 m/s (8,400 ft/s). The impact angle remained at 20 degrees from the horizontal so the external configuration of the payload structure was not changed. Internal modifications were made to create a cavity for a slightly larger concrete target.

Preliminary analysis for sled velocities over 1,700 m/s (5,580 ft/s) indicated that, in addition to severe vibrations, the sled would be subjected to significant aerodynamic loading and heating. In fact, the stagnation temperature on the leading edges of the sled would exceed the melting point of steel. Using a technique first employed at the Holloman Air Force Base rocket sled track, a system was to be developed which would enclose a portion of the track's length in a helium environment. With the reduced atmospheric density created by the helium, the effective Mach number of the sled would be greatly reduced, thereby reducing aerodynamic loads and heating.

To achieve the desired impact velocity the sled run would require 3,040 meters (9,970 feet) of track. The setup called for initially pushing the Sprint-powered reverse ballistic target sled with an additional Sprint first stage rocket motor. A drawing of the two-stage sled is shown in Figure 2. After pusher burnout the sled velocity would be 820 m/s (2,700 ft/s) at which time the target sled rocket motor would ignite and accelerate the sled to impact. The final 1,480 meters (4,850 feet) of the track were to be enveloped in a helium environment. The sled would enter the helium at 1,620 m/s (5,320 ft/s), accelerate and impact the instrumented test unit at 2,560 m/s (8,400 ft/s). The profile of the sled run is shown in Figure 3.

The track extension was completed in August 1985 while sled fabrication and development of the polyethylene sheet helium bag continued. For crosswind stability, the final bag configuration was semicircular in cross section with a 4.9 meter (16 foot) base. After preliminary helium bag and sled testing were complete, HST-1 was set for February 1986.

On the morning of February 15, 1986, the Mk 21 test unit was in place at the south end of the track. 3,040 meters (9,970 feet) to the north the two-stage sled was being readied for launch and the polyethylene bag was inflated with helium. Resembling a 1.5 kilometer (4,850 foot) long Quonset hut, the bag was purged to achieve a helium purity of 94 percent. With all systems "go" the two-stage 6,050 kilogram (13,360 pound) sled was launched.

Ignition, staging and bag entry occurred as planned, but after traveling 425 meters (1,400 feet) into the helium the rocket motor detonated. The sled velocity at the time of the explosion was determined to be 2,010 m/s (6,600 ft/s). Fortunately, the Mk 21 reentry vehicle at the impact end of the track was untouched by the sled debris and was recovered for future testing.

CONCLUSION

A thorough investigation of the incident did not lead to a conclusive explanation of what caused the rocket motor to explode. However, a long-recognized but little understood phenomenon, known as rail gouging, is thought to have been the major contributing factor. Rail gouging can be described as the localized scarring of the rail resulting from intermittent contact between the high-velocity sled shoe and the stationary rail. Experience has shown that the onset of gouging occurs as sleds accelerate through velocities of about 1,525 m/s (5,000 ft/s). Other contributing factors may have been structural loading of the sled and vibrational inputs from the sled/rail interface.

As a result of these findings research has intensified and is currently underway to develop and evaluate new sled shoe designs and materials. The sled structure is being modified to transfer loads away from critical motorcase joints and a new vibration damping mechanism is being substituted for the previous rigid sled-to-shoe connection. High-velocity reverse ballistic rocket sled impact testing will resume this fall with two scheduled rocket sled tests.

Pushing the reverse ballistic rocket sled technology forward to achieve higher velocity impacts with heavier targets is proving to be a very challenging task. Despite the difficulties, reverse ballistic rocket sleds still offer one of the most practical means of conducting an impact test under precisely controlled conditions. The large quantities of high-resolution data obtained from these tests are instrumental in the evaluation and development of fuze and reentry vehicle design.

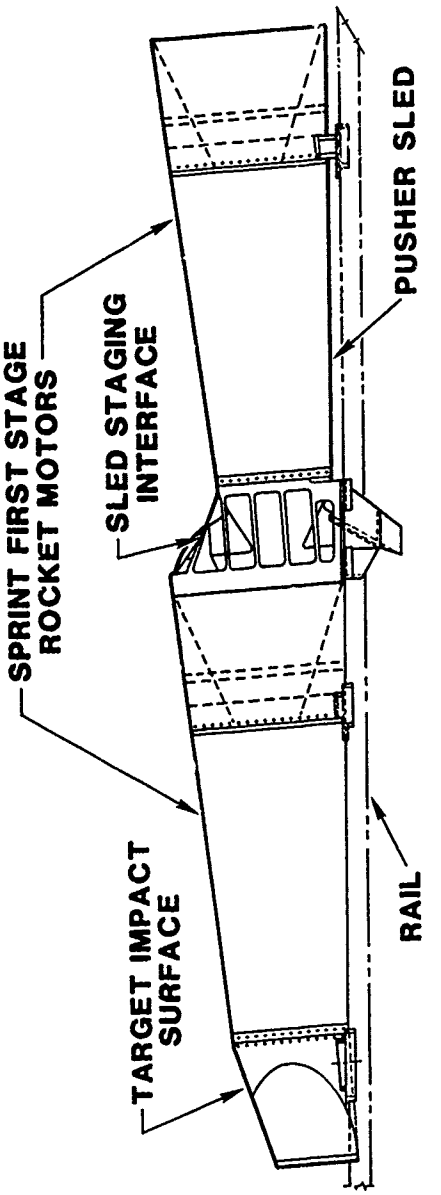

Figure 2. Two-stage, sprint-powered reverse ballistic rocket sled.

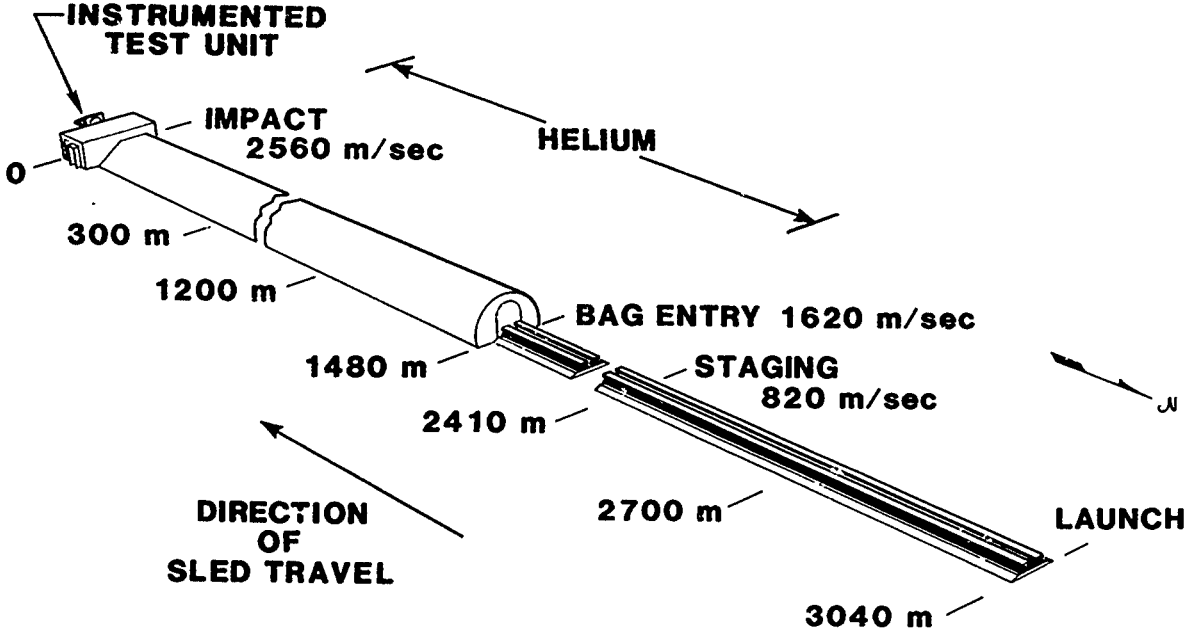

Figure 3. Test profile for two-stage, sprint-powered reverse ballistic rocket sled.

MECHANICAL IMPACT: THEORETICAL SIMULATION AND CORRELATION

G. L. Ferguson[1]
Sandia National Laboratories
Albuquerque, New Mexico

L. C. Mixon and F. W. Shearer
6585 Test Group/Test Track
Holloman Air Force Base, New Mexico

The response of structural systems subjected to dynamic impact conditions has long been of concern to the system designers. More designers are faced with the response problem as mechanical impact testing becomes a more prevalent method of simulating pyrotechnic shock. This paper discusses the development that led to a simple one-dimensional impact code for up to five colliding bodies. The results of the theoretical model were correlated with measured data taken on three and six percent scale models of a rocket sled system for impact duration, maximum acceleration during impact, and departing velocity.

1.0 INTRODUCTION

The drawback to simulating pyrotechnic shock by mechanical impact is in the adequate definition of the parameters describing the impact; i.e., impacting velocity, projectile size, and/or buffering material(s) used to obtain the desired shock profile. Traditionally, this has been resolved by a sequence of trial and error impacts until the right combination has been achieved. This technique does not lend itself to changing system parameters in a time or cost effective manner.

A development effort conducted by the Holloman Air Force Base High Speed Test Track was to simulate a pyrotechnic shock on a hardened missile silo to determine the response and structural stability of the missile suspension system. The pyrotechnic shock was simulated by impacting a large mass and accelerating it to predetermined velocities within given time and displacement constraints. Each proposed suspension system required separate masses, impact velocities, and displacements to approximate the appropriate shock response. The number of varying system parameters necessitated a numeric approach to defining the trajectory of the "impacted", or payload, body. Further constraints required that the "impacting", or hammer, body (bodies) only make contact once. Therefore, it is necessary to track all bodies during their trajectories.

Section 2 briefly presents the theory used to develop the equations of motion of a one-dimensional, general n-body system under impact. The third section deals with the correlation of theoretical and measured data for scaled model impacts. The final section describes the application of this technique to full scale testing.

2.0 IMPACT THEORY

2.1 EQUATIONS OF MOTION

When considering a general n-body system (Figure 1), the equation of motion for mass$_i$ of

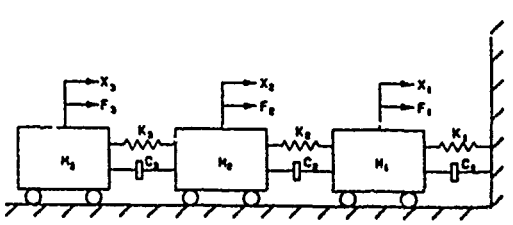

THREE DEGREE OF FREEDOM

FIGURE 1

1 formerly of 6585 Test Group/Test Track
Holloman Air Force Base, New Mexico

that system of bodies can be given as:

$$M_i\ddot{X}_i+C_i(\dot{X}_i-\dot{X}_{i-1})-C_{i+1}(\dot{X}_{i+1}-\dot{X}_i)+K_i(X_i-X_{i-1})-$$

$$K_{i+1}(X_{i+1}-X_i)=F_i \quad (1)$$

It is assumed that the mass, damping, and stiffness terms describing the motion are known, and are time invariant. Furthermore, the displacement X, its derivatives, and the forcing function are considered time dependent relations. Based on these assumptions, equation 1 can be integrated in the time domain to generate the displacement history of each body. One of the most easily applied methods of approximating time integration is the method of finite differences. A three-point central finite difference would yield the following acceleration and velocity relations:

$$\ddot{X}_{i,t} = (X_{i,t+1} - 2X_{i,t} + X_{i,t-1})/\Delta t^2$$

and (2)

$$\dot{X}_{i,t} = (X_{i,t+1} - X_{i,t-1})/2\Delta t$$

where the subscript t+1 and t-1 indicate plus or minus one time step, Δt, respectively.

Substituting these definitions for acceleration and velocity into equation 1, and rearranging allows the displacement quantities at the next time step to be expressed in terms of present and past displacements. This is given by:

$$\left(\frac{M_i}{\Delta t^2} + \frac{C_i + C_{i+1}}{2\Delta t}\right)X_{i,t-1} - \frac{C_i}{2\Delta t}X_{i-1,t+1} -$$

$$\frac{C_{i+1}}{2\Delta t}X_{i+1,t+1} = F_{i,t} + \left(\frac{2M_i}{\Delta t^2} - K_i - K_{i+1}\right)X_{i,t} +$$

$$\left(\frac{C_i + C_{i+1}}{2\Delta t} - \frac{M_i}{\Delta t^2}\right)X_{i,t-1} - \frac{C_i}{2\Delta t}X_{i-1,t-1} -$$

$$\frac{C_{i+1}}{2\Delta t}X_{i+1,t-1} + K_iX_{i-1,t} + K_{i+1,t} \quad (3)$$

Equation 3 can be used to establish the equation of motion at each point of the body. These equations can be solved simultaneously to give the nodal locations at the next instant of time. Iteration on this concept allows the time-history response of the n-body system to be determined analytically, provided that all initial conditions and the forcing function are known.

2.2 DERIVATION OF IMPACT FORCES

The general derivation of the equations of motion just described assumed the forcing function was well defined in its time dependence. However, if highly transient forces, such as impact forces, excite the system, it becomes quite difficult to characterize these as a function of time. This section will deal with one method of defining a force transient and its effect on the system.

Wu [1] presented two methods of describing the dynamic impact behavior of colliding collinear cylinders. The two methods were the collision force method and the collision induced velocity method. The collision velocity procedure tries to conserve energy and momentum throughout the collision.

The collision force method assumes the force due to an impact over a small time interval is directly related to the displacement undergone by the contact area within that time interval. The problem is further simplified to an equivalent static force by assuming that the impacted surface can be described by an equivalent spring stiffness that relates a "local indentation rigidity" to the "local indentation". Expressed mathematically, this is:

$$F_i = K_i\delta_i^{\alpha} \quad (4)$$

where δ_i^{α} represents the relative indentation at the center of the impact area. The power α is added to relate geometry and material properties. Wu stated that it had been shown for normal elastic behavior, α is one, and it had been determined empirically that for Hertzian contact, α is 1.5. The problem at hand is not Hertzian, therefore, α will be given the value of unity. Figure 2 shows the associated qualitative behavior of a system operating under these assumptions.

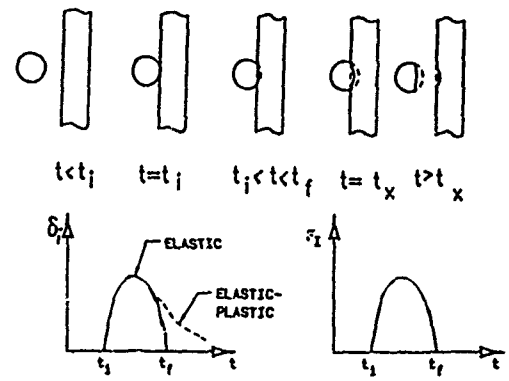

FIGURE 2

The equations as derived assume only elastic behavior, hence there is no energy dissipated throughout the contact period, except for the included damping terms. Noting this, equation 3 lets an n-body system, where each body has been discretized into M_i elastic members, be analyzed for total body response to an impact. It also allows for determining the internal member reactions to the impact, or transient, force input. This latter feature is extremely important for defining a transient forcing function that can be used in a transient dynamic response analysis to be performed on the system.

2.3 DEFINITION OF IMPACT

The derivation of the equations of motion have been based on impact having already started. This need not be the general situation. The development can be handled such that initial conditions can be defined so that collision has not yet occurred. This requires a definition for impact. The impact event is defined to start at that instant in time when two or more distinct bodies first come into contact with each other. Similarly, the impact ceases when these bodies are no longer touching. This means that prior to and after contact, the general equations of motion derived in Section 2.1 apply. During the time of contact the specialized equations of Section 2.2 apply; however, only for the bodies in contact.

Consider Figure 3 to allow for the conditions of contact to be defined, where $K_{i,j}$ and $C_{i,j}$ represents the internal elastic structural parameters and $N_{i,j}$ is the node number associated with the lumping of masses within the body. The first subscript i refers to the sled, or body, of interest, and the second subscript j represents the location within the body where the elastic element resides. The spring/damper assemblies shown outside of the bodies represent the impact stiffness characteristics for each body.

It is apparent from the figure that contact occurs the instant D_{12} is equal to zero and is maintained as long as D_{12} is less than or equal to zero. Similarly, once D_{12} becomes larger than zero, the impact stops. It is inherent in the argument that contact will never occur unless V_2 is greater that V_1, or D_{12} can never be reduced. Therefore, D_{ij} is defined, in general, as:

$$D_{ij} = X_{j,1} - X_{i,n} \qquad (5)$$

3.0 PHYSICAL CORRELATION

It is apparent from the discussion in Section 2 that the success of theoretically predicting the time histories of the collision are entirely dependent on the definition of the localized indentation rigidity term, K_i. The plan for physically verifying the computer code was to perform several controlled impacts and empirically determine the impact stiffness. Once this term had been evaluated, it would be possible to predict future impacts occurring under the same contact conditions. The control experiment planned consisted of impacting a hammer mass into an identical payload mass (i.e., a two body system), and again through a transfer mass into the payload mass (i.e., a three body system). These are shown schematically in Figures 4a and 4b, respectively.

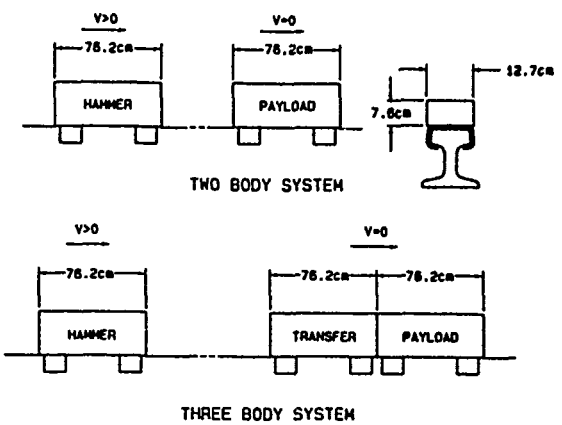

FIGURE 4

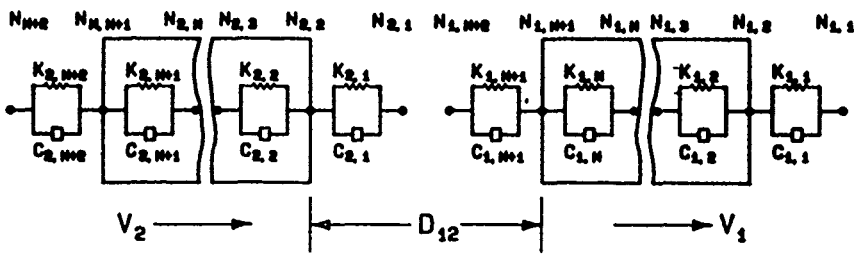

DEFINITION OF IMPACT

FIGURE 3

The developmental program was designed in three phases as follows:

a) Miniature sled systems: Monorail sleds weighing 56.7 kG (125 pounds).

b) Upscale sled systems: Inexpensive narrow gage sleds weighing 158.8 kG (350 pounds).

c) Full scale systems: Large expensive narrow gage sleds weighing 2268 to 3085 kG (5000 to 6800 pounds).

3.1 MINIATURE SLED SYSTEMS

A series of experimental data runs were accomplished at varying impact velocities under the control setup discussed. The preliminary data measurement method consisted of shock accelerometers mounted near the front end of the payload sled. The accelerometers were either directly mounted through a stud, epoxied, or mechanically attached to an intermediate block-usually phenolic. Secondary data measurement was performed by a velocity harp. A velocity harp is a device consisting of break wires set at predetermined distances apart, and as a knife cuts the wires, a time history is recorded. Finally high speed cameras recorded the collision at the contacting points.

One of the more successful miniature sled systems run was the only test where excess steel-on-steel contact was not exhibited in the accelerometer data. This impact was shaped with a material having the trade name Fabreeka. This is shown schematically in Figure 5.

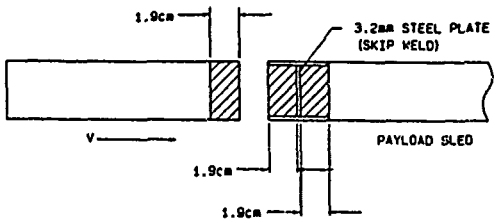

FABREEKA CONFIGURATION

FIGURE 5

Figure 6 shows the accelerometer trace for the A-18 run, and was filtered at a 4 kilohertz rate.

The envelope marked pulse time in Figure 6 is the actual time spent during the impact, and is two milliseconds in duration. The first spike is thought to be the start of the Fabreeka collapse. The large spike near the end of the contact window is the total collapse of the pad

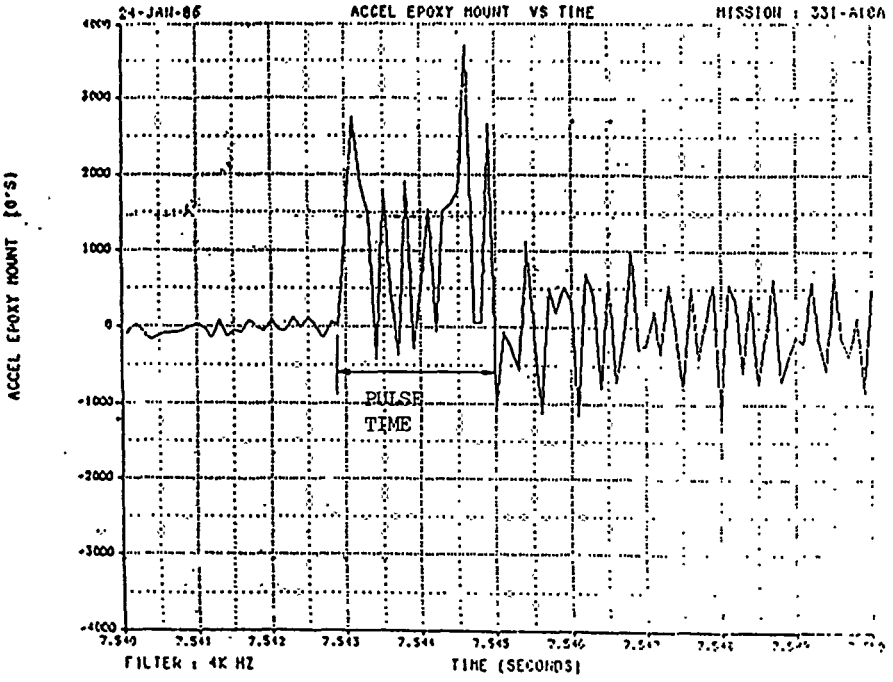

FIGURE 6

and steel-on-steel contact resulting. Each of the spikes in the pulse envelope are occurring at a frequency of approximately 3300 hertz. After the conclusion of the impact, the acceleration pulses are occurring at about 3700 hertz, the longitudinal natural frequency of the sled. Table I summarizes the payload sled frequency content. The maximum acceleration level measured was 3650 G's using a 4 kilohertz filter, or 2400 G's using a 2 khz filter.

TABLE I: A-SERIES LONGITUDINAL PAYLOAD FREQUENCY

SOURCE	CONFIGURATION	INTERFACE	FREQUENCY
A-10	3 SLEDS	STEEL	3,000 Hz.*
A-17	2 SLEDS	FABREEKA	3,750 Hz.+
A-18	2 SLEDS	FABREEKA	3,750 Hz.+
A-19	2 SLEDS	FABREEKA	3,670 Hz.+
DISTRIBUTED MODEL			3,774 Hz.
FINITE ELEMENT MODEL (NISA)			3,687 Hz.

* Mounted on a Phenolic Block
\+ Epoxied to Payload Block

3.1.1 SIMULATION DATA

It became apparent at the outset of the simulation sequence that modeling technique would play an important part in the results. It was decided that the two block system of A-18 could be modeled one of three ways, but which was best was unknown. The first model method was to be a three body system with the Fabreeka acting as the transfer block. The second method was to use a two body simulation containing no padding, but the impact terms were to be those of the cushioning material. The last method was to be a two body system with the Fabreeka modeled as an element in the proper bodies and the appropriate impact stiffness for the contacting materials to be used. Figure 7 shows the three configurations.

Since no criteria existed for defining the impact stiffness parameter, a series of simulations were performed to determine the effect of varying the stiffness. The trend of these results were for shorter pulse times and larger acceleration peaks as the effective stiffness of the system increased. Shown in Figure 8 are the results of this series of simulations where the effective impact stiffness is plotted as a function of pulse width and peak G's. As can be seen, there is essentially no difference in the two or three body cases until the effective stiffness approaches 5.25×10^8 N/M (3×10^6 lb_f/in). This effective stiffness value is when the impact terms approach the body stiffness, which is included in the simulations.

Using Figure 6, a simulation of the A-18 run was attempted. Knowing the pulse time of 2 milliseconds, the effective stiffness was found to be 7.01×10^7 N/M (0.4×10^6 lb_f/in). Setting the impact term for steel (model method 1) to be 1.23×10^9 N/M (7×10^6 lb_f/in, or one-half of the actual body stiffness), the Fabreeka

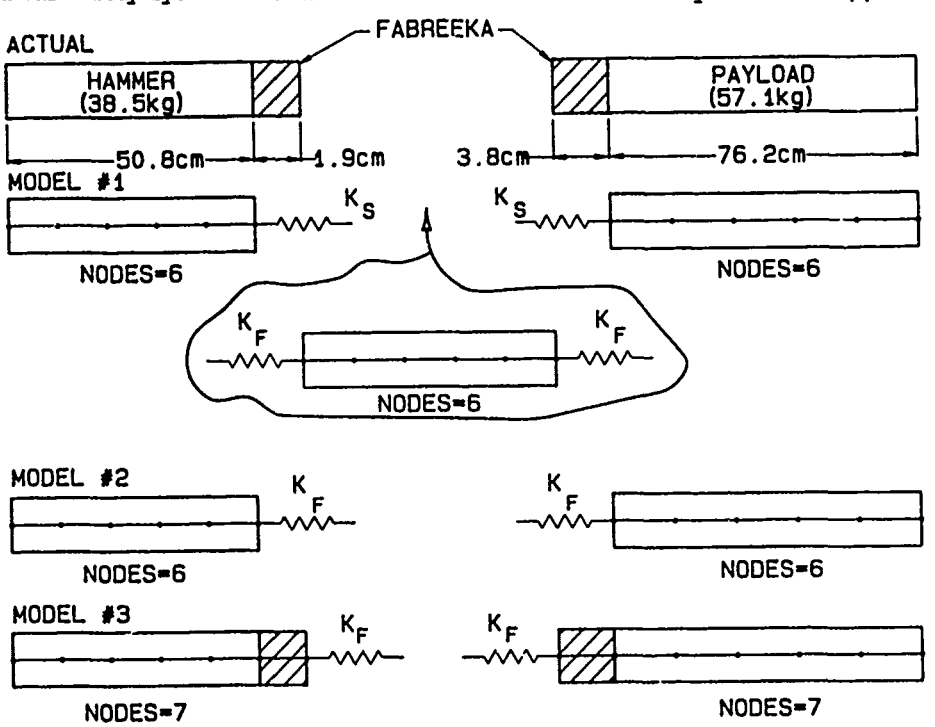

THREE MODELING METHODS

FIGURE 7

stiffness was found to be 1.58×10^8 N/M (0.9×10^6 lb_f/in). The first modeling technique was simulated using these values. Results for the acceleration spike was 250 percent of that measured, the departing payload block velocity was 200 percent of actual, and the pulse time was shorter-1.8 milliseconds versus 2. It is apparent that the actual system is dissipating energy the math model does not account for and secondly, the physical parameters of the body must be related to the reference bodies if Figure 8 is to be used for relating pulse width to impact stiffness.

3.1.2 ENERGY DISSIPATION

Investigation of the literature revealed that Roark [2] had developed an empirical relationship for kinetic energy loss during impact. For axial impact, with the payload mass fixed (Figure 9), the kinetic energy loss factor could be related by the mass ratio of the stationary bodies to that of the moving body, and is expressed in equation 6.

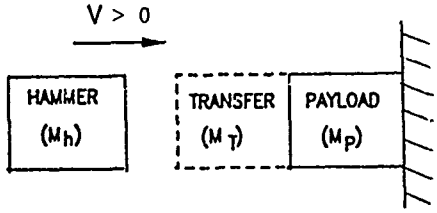

FIGURE 9

$$K_{LI} = \frac{1 + \frac{(M_p + M_t)}{3M_h}}{\left[1 + \frac{(M_p + M_t)}{2M_h}\right]^2} \qquad (6)$$

Using this relationship, a departing velocity envelope was calculated assuming that the hammer block velocity after impact ranged between zero and the payload block departing velocity. This examination revealed that sufficient kinetic energy still was not being removed to represent the Fabreeka crushing. Using information from the Fabreeka Products Company [3], an energy loss relationship for the Fabreeka crushing was derived assuming an initial crush-up value. Simulations were performed and the crush-up value was modified until acceptable acceleration and velocity levels were attained. The Fabreeka crush-up value was determined to be one-eighth of the original thickness instead of one-half as originally assumed. This resulted in the Fabreeka energy loss being:

$$K_{LF} = 0.02097 \frac{\Sigma_i (A_i t_i)}{KE} \qquad (7)$$

where KE is the system kinetic energy at time of impact, and A_i and t_i are Fabreeka area and thickness, respectively.

Using the modified crush-up relationship, the simulations relating the three modeling

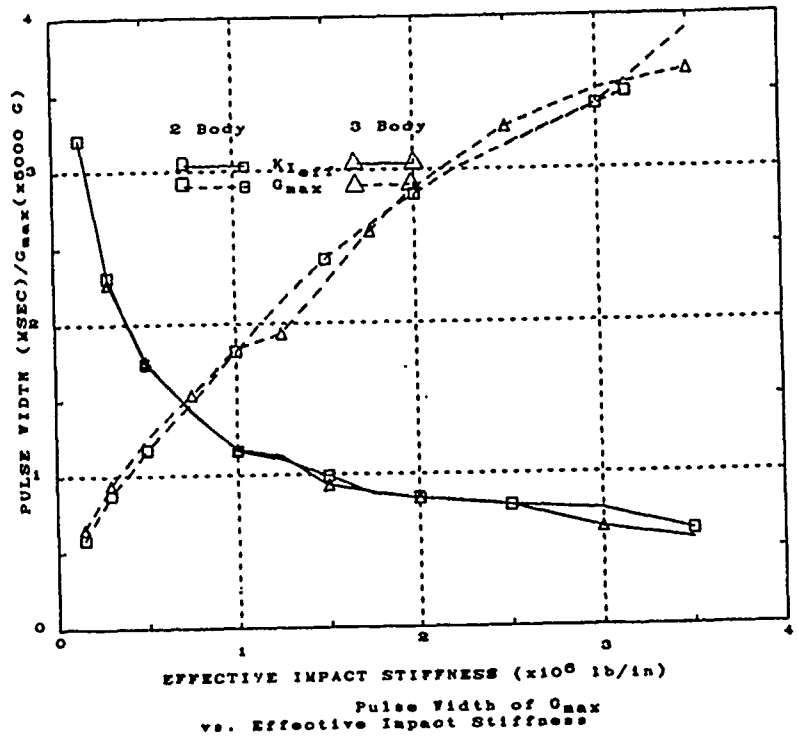

Pulse Width of G_{max} vs. Effective Impact Stiffness

FIGURE 8

techniques were redone. In all cases the pulse times were too short; however, the acceleration peaks and payload departing velocity were good. It was found that the best modeling method was technique three where the Fabreeka was modeled as an internal body member. Under this situation, the additional energy loss of equation 7 was not needed. Model method two was almost as good; however, the energy loss had to be adjusted by equation 7.

3.1.3 IMPACT STIFFNESS

The impact stiffness used in the computer simulation is linear; however, the actual characteristics of the Fabreeka are non-linear. A non-linear study is in process at the present time and will be reported at a later date. As previously discussed, the purpose of the mini-scale and up-scale testing was to provide scaling for the much larger full scale test. In this context, the use of linear stiffness was appropriate. Essentially, some effective linear modulus of elasticity, E, was assumed for matching down scaled data. Once this effective linear modulus was established, the same value was used for scaling up to the 2268 kG to 3085 kG (5000 to 6800 pound) sled systems. This approach was successful. The more aesthetical non-linear approach should allow more reliance on the static load data and theoretical predictions without the need for down scale testing in the future.

From the earlier discussions, Figure 8 can not be used directly to relate pulse width to impact stiffness because of the physical differences in geometry between the simulation and reference cases. It was hypothesized that the actual effective stiffness could be modified by relating the actual system geometry to the reference system geometry, and Figure 8 could then be used. Mathematically this relationship would look like:

$$K_E = \frac{1}{\Sigma_i \frac{1}{KI_i} + \frac{1}{KS_R} + \Sigma_j \frac{1}{k_j}} \qquad (8)$$

where KS_R is a reference stiffness relating the stiffness of the bodies of Figure 8, k_j is the actual physical geometry stiffness being used, and KI_i is the impact stiffness terms.

The physical geometry of the system is easy to calculate, it is the sum of the reciprocals of the individual stiffnesses comprising the system. For longitudinal stiffness, the individual terms are given by the relationship of k=AE/L.

After empirically determining KS_R, the appropriate KI's can be found using Figure 8 and equation 8. For the A-18 run, $K_E = 7.01 \times 10^7$ N/M (0.4×10^6 lb_f/in) and assuming that KI for steel is 1.23×10^9 N/M (7×10^6 lb_f/in), then KI for Fabreeka can be found. Shown in Figure 10 is the best modeling technique, using the modified impact stiffness terms. Examining the figure indicates the simulation can be done relatively well by the two body configuration, when Fabreeka is used as an internal element and is denoted by K_L=0.495 in the figure.

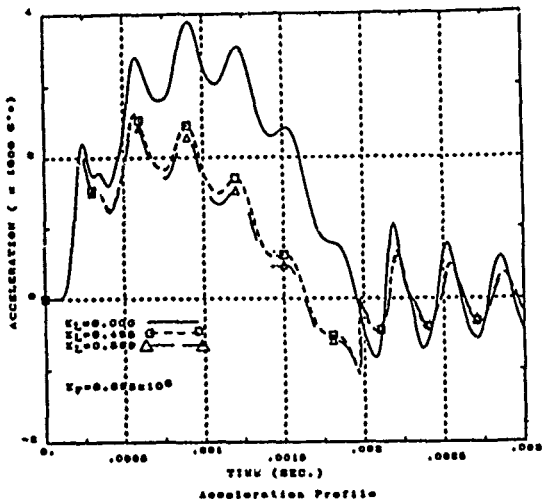

FIGURE 10

3.2 UPSCALE SLED SYSTEM

The upscale sled system was comprised of three sleds, each weighing approximately 158.8 kG (350 pounds). Photographs of this sled system are shown in Figures 11 and 12. The first photograph shows the hammer sled in front of the rocket sled pusher used to attain the required test velocity. The pusher sled is then stopped short of the event (impact) track location.

A schematic of the 158.8 kG (350 pound) upscale sled system in shown in Figure 13.

Although individual test parameters were varied from test to test, the nominal inside diameter of the containment cylinder was 0.203M (8 inches), and the outside diameter of the Fabreeka was 0.187M (7.38 inches), leaving a nominal radial relief of 0.008M (0.31 inches). This radial relief will be discussed later. In addition, an inner circular relief hole was provided. Table II summarizes seven of the upscale tests. Other upscale tests were either preliminary or used uncontained Fabreeka. Uncontained Fabreeka was found to be less repeatable and actually a different failure mechanism is associated with the uncontained mitigating material.

Two separate acceleration pulses were required, i.e., Pulse 1A and Pulse 1B. The first five test listed in Table II were designed to establish data for the design of 2268 to 3085 kG (5000 to 6800 pound) Pulse 1B tests. The last two tests, D-15 and D-16, were used to design the less difficult acceleration pulses for the same weight range for the Pulse 1A criteria.

Essentially, two basic parameters were varied in these series. First, the internal Fabreeka relief hole diameter was varied from 0.00 to 0.102 M (0.00 to 4.00 inches), and secondly, the hammer sled entrance velocity varied from 58.522 to 90.526 meters per second (192 to 297 feet per second) for the Pulse 1B series. The change in the two Pulse 1A tests were radial relief and the hammer entrance velocities. In the final analysis, D-13 was selected for upsizing to the large sled for Pulse 1B, and D-16 test results were used for large sled Pulse 1A designs. Consequently, these two tests will be used as examples for comparing theoretical and measured data.

3.2.1 SIMULATIONS

3.2.1.1 D-13 TESTS

The theoretical and measured data for the D-13 test is given in Figure 14. As shown, the correlation is quite satisfactory both for amplitude and pulse duration. Note that in the original D-13 data, a 0.95 millisecond lesser magnitude pulse preceded the presented data.

FIGURE 11

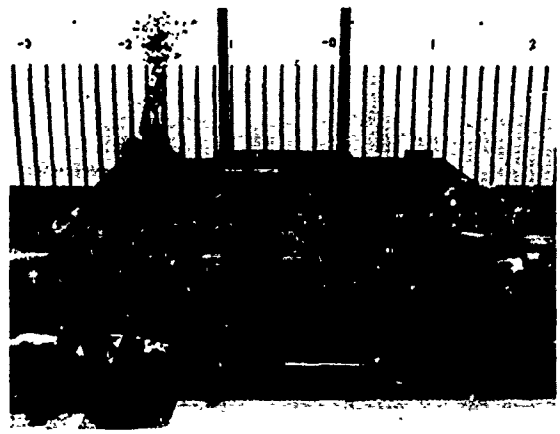

FIGURE 12

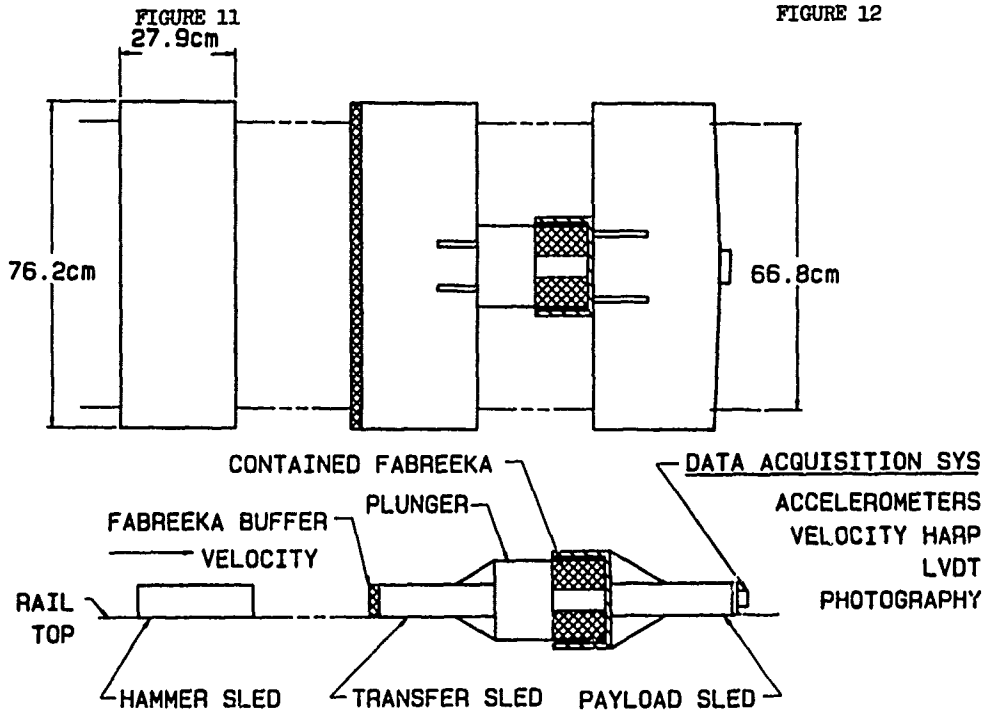

SCHEMATIC 159 kg UPSCALE SLED SYSTEM

FIGURE 13

TABLE II SUMMARY OF CONTAINED UPSCALE TESTS

PARAMETER	D-8	D-11	D-12	D-13	D-14	D-15	D-16
Fabreeka Thickness, cm	13.335	13.487	13.487	13.487	13.487	21.590	21.590
in	5.25	5.31	5.31	5.31	5.31	8.50	8.50
Fabreeka O.D., cm	15.240	18.745	18.745	18.745	18.745	12.700	12.700
in	6.00	7.38	7.38	7.38	7.38	5.00	5.00
Fabreeka I.D., cm	5.080	0.000	5.080	10.160	6.350	6.985	6.985
in	2.00	0.00	2.00	4.00	2.50	2.75	2.75
Fabreeka Radial Relief, cm	0.000	0.787	0.787	0.787	0.787	0.483	1.346
in	0.00	0.31	0.31	0.31	0.31	0.19	0.53
Fabreeka Area, cm^2	162.064	275.483	255.225	194.451	243.806	88.322	88.322
in^2	25.12	42.70	39.56	30.14	37.79	13.69	13.69
Velocity In, MPS	58.522	85.344	90.526	89.002	82.296	65.837	73.152
FPS	192.00	280.00	297.00	292.00	270.00	216.00	240.00
Velocity Out, MPS	20.726	29.566	31.090	35.357	32.614	24.689	30.785
FPS	68.00	97.00	102.00	116.00	107.00	81.00	101.00
Velocity Out/Velocity In	0.35	0.35	0.34	0.40	0.40	0.38	0.42
Kinetic Energy In, M/N	11,765	25,025	26,935	26,035	22,260	18,215	23,720
Ft/lbs.	171,700	365,200	393,110	379,980	324,880	265,800	346,140
Kinetic Energy Out, M/N	1,575	3,195	3,920	5,070	4,310	2,450	3,845
Ft/lbs	23,000	46,600	57,190	73,970	62,930	35,790	56,080
KE Out/KE In	0.13	0.13	0.15	0.19	0.19	0.13	0.16
Pulse Width, Milliseconds	2.85	1.60	2.30	0.95,3.00	0.95,3.00	2.00,5.20	1.90,4.10
G's Mean Peak	1,430	5,000	1,800	2,100	2,100	625	1,130
Peak Mean Pressure, kPascal	125,620	258,345	111,075	170,095	135,620	111,420	201,465
PSI	18,220	37,470	16,110	24,670	19,670	16,160	29,220

This pulse is associated with the one inch of Fabreeka placed on the back of the transfer sled. This material acts as a buffer to stop previously experienced surface-to-surface deformations between the hammer sled and the transfer sled. This pulse also provides some velocity which accounts for the enhanced velocity out/velocity in ratio shown in Table II. The computer code was not modified to include modeling of this aft Fabreeka pad. This relatively thin pad is extruded radially nearly immediately as the two flat surfaces meet. Velocity of the small Fabreeka particles from this rear buffer pad have been measured at speeds greater than Mach 1. The down-track velocity component introduced by this pad is accounted for by using a smaller energy dissipation factor, K_L.

One peculiarity exists in the comparison of the upscale sled system predicted and measured data. As shown in Figure 14, the ringing that takes place after the acceleration pulse is at two different frequencies, i.e., the prediction versus measured data. The measured data is oscillating at approximately 2,000 hertz, while the predicted data is vibrating at approximately 8,000 hertz. The reason for the difference is the type of model being used in the computer code. The structural model is lumped masses connected by linear springs; consequently, the first mode is the longitudinal frequency. The computer code used to predict the acceleration is correct. A separate finite element code was used to predict the first longitudinal mode, and had a computed result of 8,175 hertz. However, the first actual mode is not longitudinal motion, but a bending mode in the yaw plane. This mode is shown in Figure 15. A simple free floating beam computation yields a frequency of 2,330 hertz, which is close to the measured 2,000 hertz. It is interesting to note this large difference in frequency did not significantly affect correlation of data during the acceleration pulse.

Shown in Figure 15 are the various locations used to measure accelerations on the upscale tests. Initially, the down-track accelerations were measured at the front of the sled. Then slots were milled in the two sides and accelerations measured at these locations.

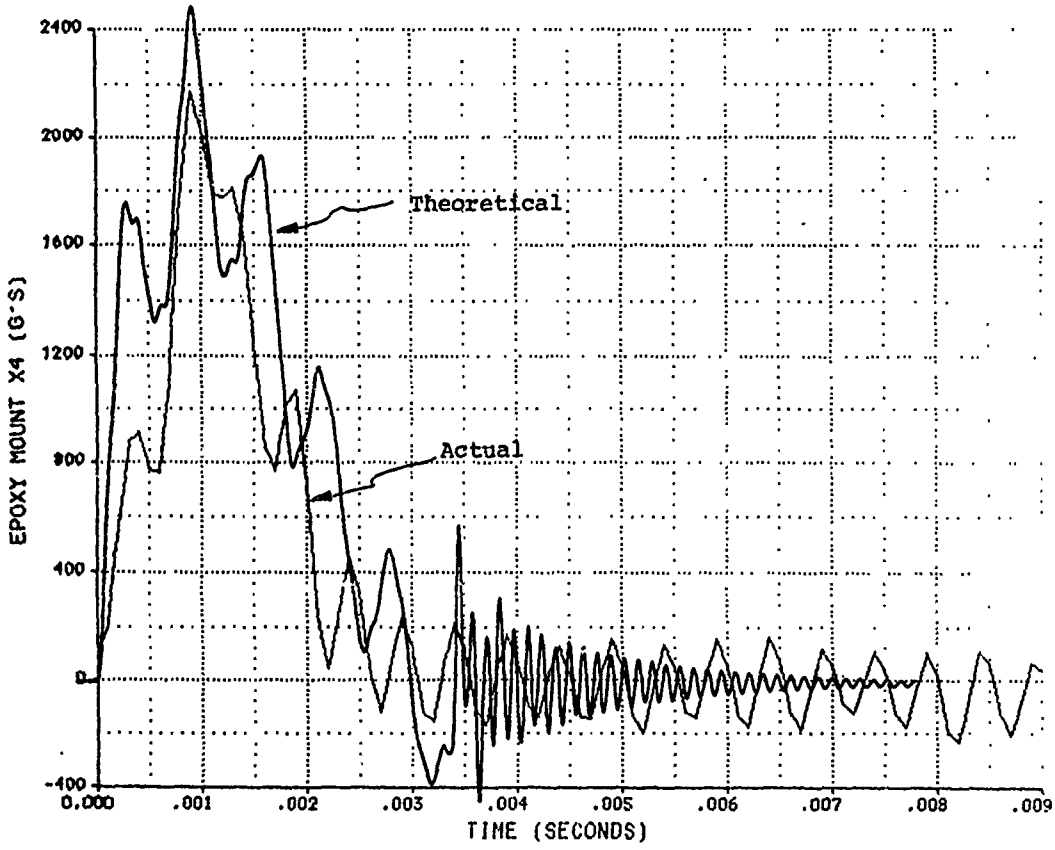

FIGURE 14

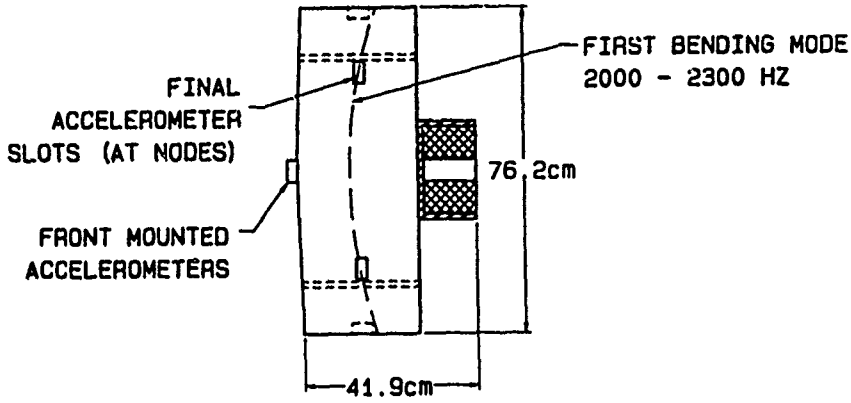

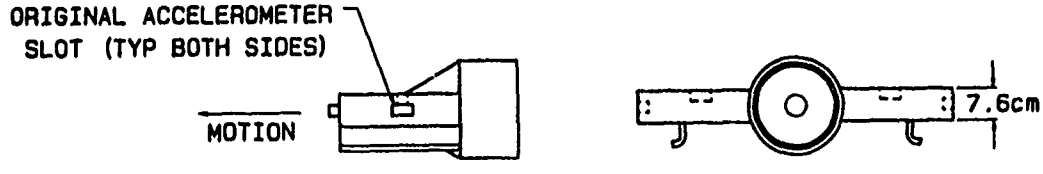

UPSCALE SLED ACCELEROMETER LOCATIONS

FIGURE 15

Both locations were amplifying positions as the sled vibrated in yaw bending. After the mode was discovered, the accelerometers were moved to milled slots located approximately at the node points. The vibration levels were reduced significantly. Both the D-13 and D-16 data are shown at these new locations.

3.2.1.2 D-16 TESTS

The comparison of theoretical and experimental data is shown in Figure 16 for this test. Again, the predicted and measured acceleration pulses agree. Just as in the previous test, the measured pulse shown was preceeded by a 1.90 millisecond pulse associated with the Fabreeka pad between the hammer and transfer sleds. Note the time duration of this preliminary pulse is longer than D-13 because of the lower entrance velocity.

3.2.2 ENERGY LOSSES

As shown in Table II, a significant amount of energy is lost in the impact process. For the seven tests listed, the kinetic energy out divided by the kinetic energy in provides ratios of 0.13 to 0.19. This energy loss results in permanent deformation of the structures, velocities imparted to other system elements-such as the decelerators, and Fabreeka flying radially from the aft of the transfer sled, and, of course, heat. Fire balls were photographed on at least one test.

The energy loss equation of Roark was originally programmed into the computer simulation. Later, this equation was dropped and an energy loss factor, K_L, was directly applied to remove the necessary kinetic energy from the system. A more interesting problem is in the method of extraction of this energy from the sled system simulations. Initially, the loss was assumed to be linear during the pulse duration (in the miniature sled simulations). The velocity was reduced for each node in each body over microsecond time intervals. This approach required the simulation be computed first without energy dissipation to establish the pulse width, and then a repeat computation was run where energy was dissipated to obtain final acceleration amplitudes and velocity out.

Later in the program (the upscale series), the energy loss was assumed to occur as a half sine wave such that more energy was lost in the middle of the pulse where the stresses are highest. Again, a preliminary simulation was conducted to establish the pulse width and then the appropriate energy subtracted for each microsecond during the simulation. The total energy loss is the same as in the linear case, except the method does not introduce irregularities observed in the prior method. Also, the pulse width is not as critical. This is the approach used in the upscale test series and the full scale tests.

3.3 FULL SCALE TESTS

Results from these and other upscale tests were used to design two large scale systems. This order of magnitude scaling was accomplished by holding the relief area (internal and radial) ratios constant, holding pressure (g's mean peak), and use of appropriate hammer sled entrance velocity. The 2268 kG (5000 pound)

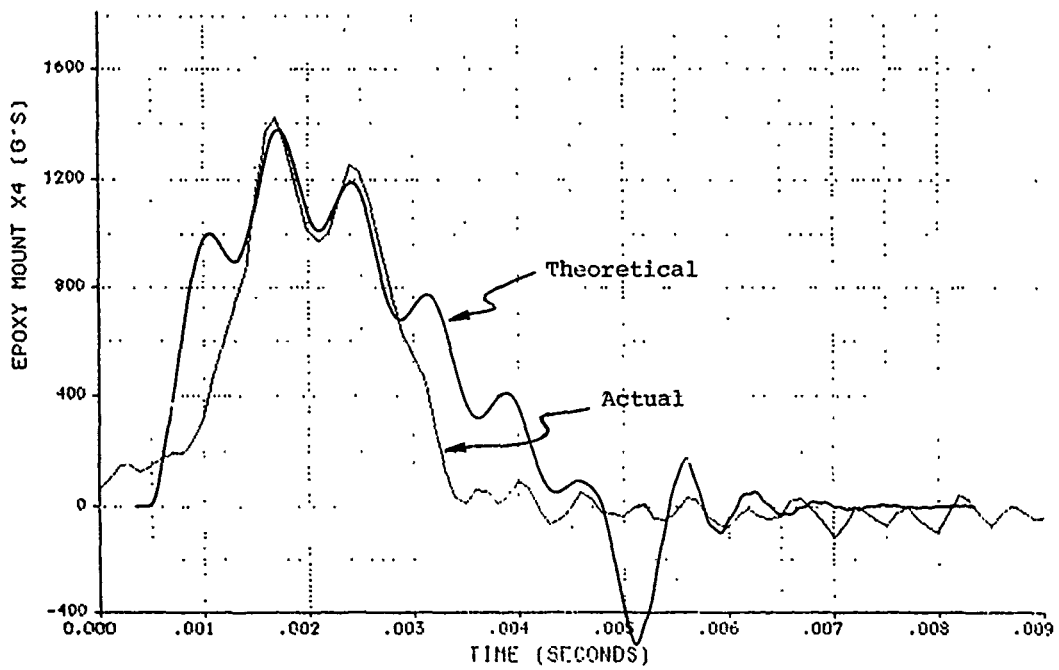

FIGURE 16

sled systems (3 sleds each weighing 5000 pounds) has been used to test three candidate suspension systems to two pulses each to date with good success. Details from these full scale tests will be given at a later date when final analyses has been completed.

3.3.1 STRUCTURAL SYSTEM

The basic structural elements of the full scale tests are:

a) Pusher sled with momentum exchange water brake

b) Hammer sled

c) Transfer sled with thin Fabreeka buffer on aft end

d) Payload, or carriage, sled with pulse shaping Fabreeka

e) Two large hydraulic decelerators

f) Two arrestors, either collapsible tubes or honeycomb aluminum

g) Test suspension system

h) Two large towers to support the test suspension cable

i) Hydraulic servo controlled preload for test suspension cable

j) Payload or carriage sled explosive deactivating hold back mechanism

k) Explosive bolts for hydraulic decelerator.

These systems are shown schematically in Figure 17. Also, photographs of actual hardware are shown in Figures 18 through 21.

The test scenario is to first position the payload sled at a specified track station and engage the bridle from the two hydraulic decelerators. The test cable is then used to pull the payload forward until the hold back mechanism can be engaged. This hold back is explosively released at the test event time. Next, 169kN (38,000 pounds) of tension is applied to the test cable using the hydraulic preload cylinder which simulates the proportional share of the missile weight assigned to each suspension cable. The transfer sled is then aligned behind the payload sled just in contact. Next, the arrestors are attached to the transfer sled. The last structural preparation is substitution of explosive bolts for safety bolts in the decelerator(s) load links.

Several thousand feet down track a pusher sled is positioned behind the hammer sled at a station which will provide the required impact velocity of the hammer sled with the transfer sled.

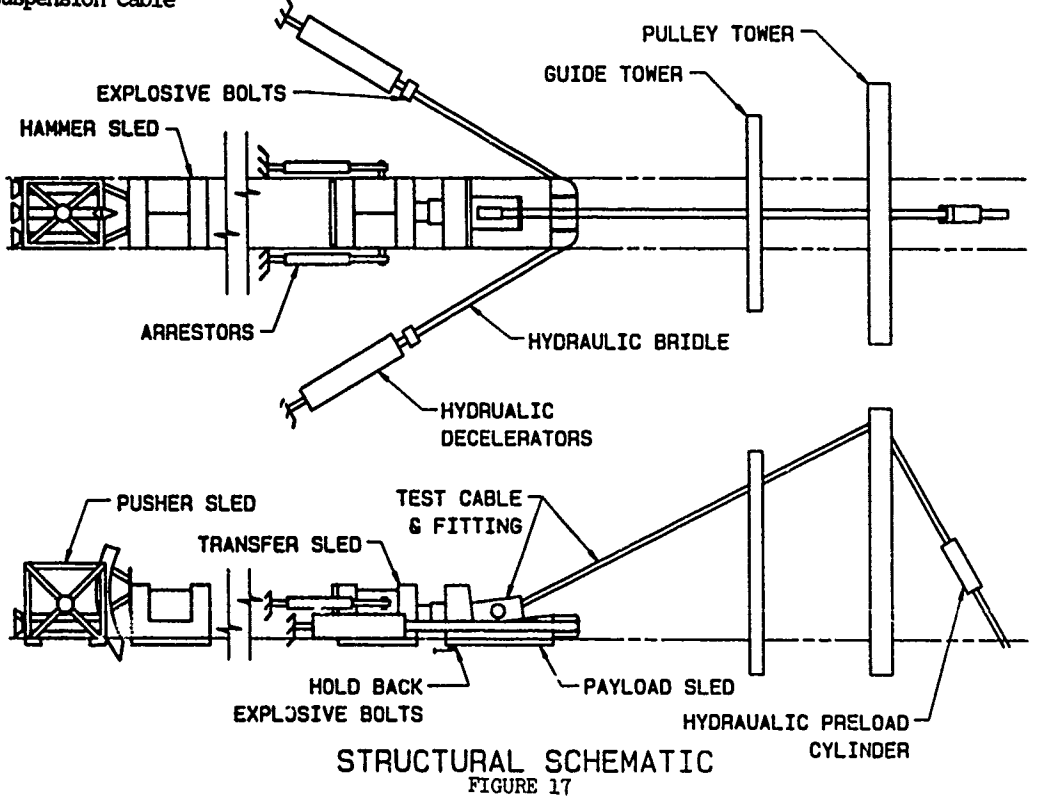

STRUCTURAL SCHEMATIC
FIGURE 17

After all safety and arming functions are complete and a "GO" instrumentation status is received, the pusher sled rocket motors are ignited and the pusher sled and hammer sled are accelerated to some velocity greater than the required impact velocity. The pusher sled then separates from the hammer sled and is stopped short of the test event station using water momentum exchange braking. Just before the hammer sled impacts the transfer sled, a trackside break wire is used to explode the two hold back bolts and the two decelerator bolts simultaneously. The required shape pulse is provided by the mitigating material (Fabreeka) and the required deceleration g's provided by the pre-programmed decelerators. The payload sled must be stopped in a controlled manner in 4.877M (16 feet). As soon as the acceleration pulse is achieved, the two arrestors are engaged on the transfer sled and the transfer sled and hammer sled brought to a stop in 1.828M (6 feet).

3.3.2 INSTRUMENTATION SYSTEM

The instrumentation system is comprised of the following elements:

a) Accelerometers

b) Velocity harp

c) Linear Variable Differential Transformer (LVDT)

d) Load cells

e) Pressure transducers

f) Load bolts

g) Spot velocity sensors

h) Photography.

FIGURE 18

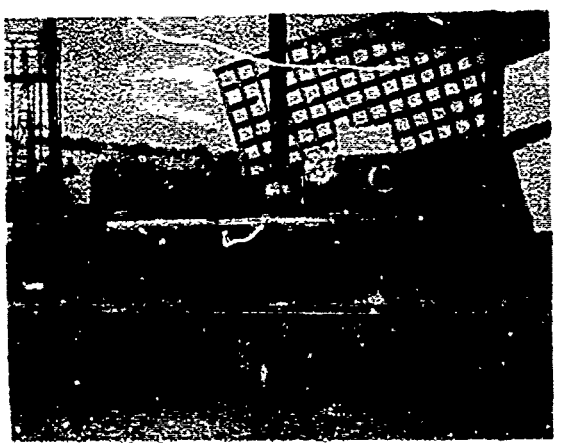

FIGURE 19

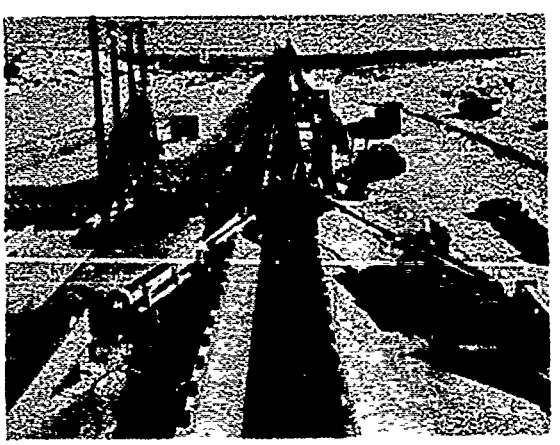

FIGURE 20

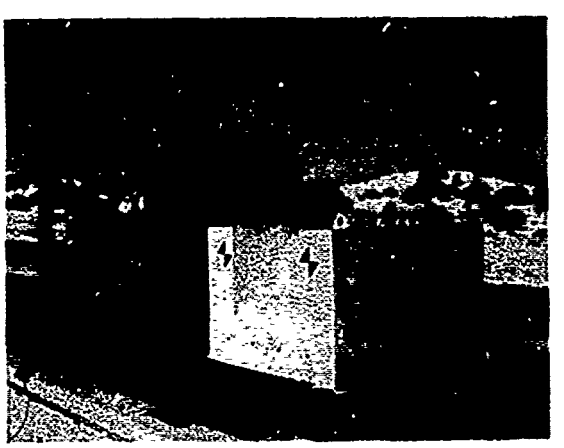

FIGURE 21

A description of the instrumentation is as follows.

a) Accelerometers are mounted on polysulfide rubber which provides a flat frequency response to 4500 hertz. Two downtrack accelerometers are mounted on the carriage sled in milled slots and two downtrack accelerometers are mounted on the test fitting. Vertical and cross-track accelerations were measured during the developmental phase of the program and found to be of significantly lesser magnitude than the down-track acceleration pulse. The measured impact acceleration pulses were integrated, compared to other velocity data, and found to provide reasonably good velocity data.

b) Velocity harp is a locally manufactured velocity measuring device made from a 4.267M (14 foot) long phenolic block. A slot is milled the length of the block and pins spaced along the block so wires can be stretched individually between sets of pins. A knife blade is attached to the carriage sled which breaks these wires as the sled passes. The spacing of the wires starts at 1.27cm (0.5 inches) and is stepped up to 15.24cm (6 inches) at the end of the harp. The displacement time data is then used to provide velocity versus time.

c) Linear Velocity Differential Transformer (LVDT) is another transducer which provides distance versus time data. The stroke of the LVDT's used is 25.4cm (10 inches), which covers the acceleration pulse phase. The slope of this curve (velocity) again agreed well with other data.

d) Load cells were designed and fabricated in-house. The loads on both sides of the decelerators and the loads on the arrestors are measured for a total of six load measurements. These data were invaluable in developing both the decelerators and associated computer code, and in the design of the arrestors.

e) Pressure transducers are used to measure pressures at four locations in one of the decelerators. These data were of significant importance during the development of the decelerators and associated computer code.

f) Load bolts are used in some tests to measure the pin loads on the bolts restraining the cable to its fitting. These devices were commercial transducers.

g) Spot Velocity are magnetic sensors located every 31.699M (104 feet) along the narrow gage facility and are used to monitor the velocity of the approaching hammer sled. In addition, special velocity sensors are spaced close to the impact area to precisely establish the hammer sled entrance velocity.

h) Photography is the last data source. Typically, 9 high speed cameras and one video camera were used for each test. Two 16mm cameras are run at 200 frames per second to provide overall sequencing and documentation. The video camera provides quick-look documentation. Three 16mm cameras are run at 5000 frames per second and four 16mm cameras at 1000 frames per second for detail event study. Photography was used to provide velocities of all three sleds. Also, the penetration of the transfer sled plunger into the payload Fabreeka was established using photography as well as crushing times for the arrestors. In addition photographs provided outstanding documentation of the test cable "bird caging" and the dynamic wave propagation of the acceleration pulse up the cable.

The use of these multi-data sources has been invaluable in developing overall test concept and has allowed for successful tests even when one source of data might have been lost.

3.3.3 RESULTS

This test series is still in process and only data from the first four tests are available. Results have been good. As shown in Figure 22 the total requirements was for an acceleration phase represented by the half-sine shown at the top of the figure. The matrix shows minimal, maximum, and nominal g-levels, pulse durations, and the resulting velocity. The bottom curves show the same data given as velocity versus time. As shown, the test results are exactly in the middle of the specified tolerance. More detailed data will be presented later.

4.0 CONCLUSIONS

This paper developed a simple one-dimensional approach to modeling the phenomenon of mechanical impact. The derivation assumes the system maintains purely elastic behavior, which it is realized is not always the situation. As the velocity of impact increases, a point is reached where plasticity occurs within the system, and many of the actual data runs exhibited plastic deformation of the sleds. Modeling of this plasticity would require a very sophisticated code that would examine the collision on a microscopic level, to study the effect of the crystalline structure, and quantify the associated energy loss. The simplistic approach taken in this paper was to require the entire response to be elastic in nature, with the plasticity and energy loss accounted for in a continuous manner throughout the impact.

A series of modeling tips were developed through the course of this paper. When these tips were used and the simulations compared to the actual runs, the largest error in acceleration and velocity for the down scaled tests were about 6 percent, and about 9 percent for the pulse width. Based on this investigation, it appears this simplified approach to modeling the complex behavior of mechanical impact is entirely adequate.

However, there are limitations to this work. First, only Fabreeka was used as a cushioning material and specific guidelines for its use was developed. Additional work must be done to determine if these guidelines are specific to Fabreeka, or can they be extended to other cushioning materials. Since the Fabreeka used has a non-linear stiffness associated with it the simulations need to be corrected to account for this non-linearity. Secondly, more studies must be done on the materials used for the blocks. Steel is a homogenous material and consistent impact relations were developed. It remains to be seen if these relationships are applicable as derived for other materials.

The results presented here only highlight the actual work done. A final, and more detailed, report is planned that will address the issues introduced here. The final report will also discuss the full scale test results. This final paper will be available as a Technical Report through the Air Force's Armament Division.

REFERENCES

1. Wu, R. W., Approximate Numerical Predictions of Impact Induced Structural Response, The Shock and Vibration Bulletin, Part 2, May, 1983.

2. Roark, R. J., Formulas for Stress and Strain, McGraw-Hill Book Company, New York, New York, 1965.

3. Fabreeka-Sections 1 and 2, Fabreeka Products Company.

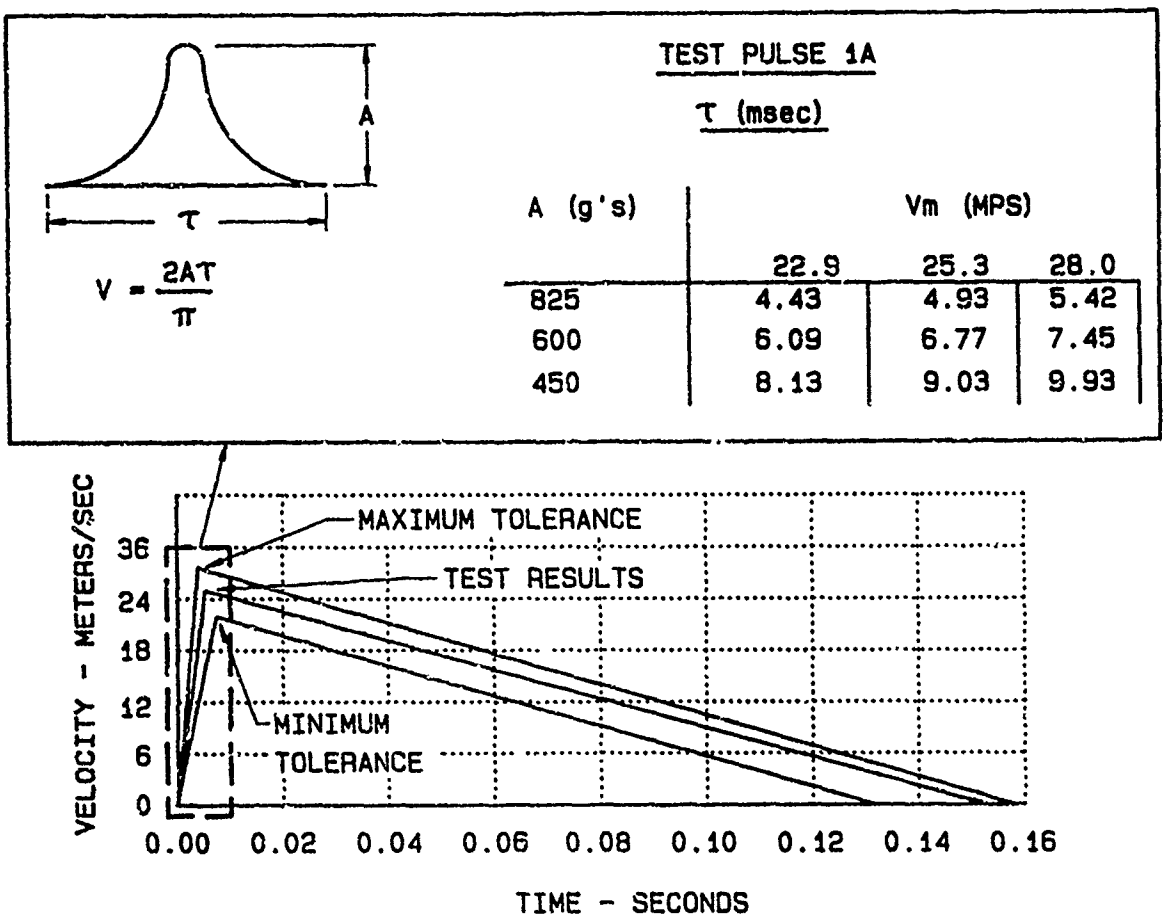

TEST REQUIREMENTS

FIGURE 22

MEASUREMENT, DATA ANALYSIS, AND PREDICTION OF PYROTECHNIC SHOCK FROM PIN-PULLERS AND SEPARATION JOINTS

Maria J. Evans, Vernon H. Neubert
The Pennsylvania State University
University Park, PA 16802

Laurence J. Bement
NASA Langley Research Center
Hampton, VA 23665

To evaluate the potential for spacecraft damage caused by activation of pyrotechnic mechanisms, pyrotechnic shock tests were conducted on three configurations: pin-pullers on an orthogonal double Hopkinson Bar arrangement, pin-pullers on a mock-up of the HALOE structure, and a section of separation joint on a single Hopkinson bar. Strains and accelerations were measured. The strains were converted to output stresses, forces and moments. Acceleration shock response spectra are presented for both acceleration- and force-time signals. The devices were attached to the Hopkinson bars with adaptors, which are typical of attachments used in practice. In order to predict the effect of the adaptors, finite element models of the adaptor-bar combinations were analyzed and results are presented with regard to grid size, time interval, and frequency range required to predict the response to pulses of 10 and 100 microsecond duration. This paper summarizes a more detailed report [1] and thesis [2]. The goals are to better understand, measure, and predict transmission of pyrotechnic shock in structures.

INTRODUCTION

The structural shock waves created on activation of pyrotechnic devices have the potential to damage electronic or other low-mass equipment or to activate motion-sensitive equipment. For example, a pyrotechnic-induced failure led to the loss of two solid rocket booster cases for the space shuttle in 1982. The parachute release system for the booster parachute system was prematurely activated from a non-separation system, rather than on water impact. Olsen, et al, [3], mentioned in 1968 that there were several examples of equipment items that had failed or malfunctioned during mechanical shock from pyrotechnic devices, even though the devices had successfully passed conventional shock and vibration tests. Many proof tests are done on the ground, but there is a lack of information on pyrotechnic-produced loads which can be used by designers. This lack of information is caused by the complexity of the pulses generated and the difficulty experienced in measurement and analysis. The pulses are extremely dynamic with high amplitudes and short durations, containing frequencies up to 50 or 100 kHz. These frequencies are near the limit of much instrumentation and require very fine meshes on analytical models of structures.

Progress is being made in measuring the outputs from pyrotechnic devices. In 1971, careful measurements of force-time outputs of simulated separation joints and explosive bolts were made by Parker and Neubert using a Hopkinson bar arrangement [4,5,6]. Output stresses with magnitudes as high as 34,700 psi and with durations of twelve microseconds were measured from a 1/4 inch diameter explosive bolt attached directly to the end of the Hopkinson bar. In 1973, similar tests were carried out by Bement and Neubert [7,8] to evaluate the output forces and accelerations of several standard explosive nuts compared to some special low-shock nuts. Recently, the shocks generated by several pyrotechnic pin-pullers were compared with the output of a mechanical pin-puller in the NASA Langley Pyrotechnics Laboratory. These pin-pullers were then mounted on the Halogen Occultation Experiment (HALOE) structure and strains and accelerations compared with those measured on the Hopkinson bar. The results of these tests are presented for the first time in this paper. Strain-time measurements, both on the bar and on the

HALOE structure, were converted to force-time and moment-time outputs of the devices. These, along with measured accelerations, were used to calculate acceleration response shock spectra for both the acceleration and force timewise records. A section of spacecraft separation joint was also tested on a single Hopkinson bar and the results are presented here for the first time.

Existing analytical methods were expanded to predict the response of the apparatus to pyrotechnic pulses. Results of some of this analysis using finite element models of the adaptors on the Hopkinson bars are also presented herein, from the more detailed thesis of Evans [2]. The ultimate goals of this analysis are: (1) to predict the effect of the adaptors on the pulse shapes, (2) to attempt to deduce the true output of the pyrotechnic device at the attachment point, (3) to determine the frequency content by ascertaining the number of modes needed to represent the response, and (4) to determine the fineness of the finite element mesh needed to predict the response to these inputs.

RELATED WORK

The idea of using a long, thin, cylindrical bar for measuring severe, transient pulses was presented by Hopkinson [9] in 1914, and consisted of applying an unknown pressure to the one end of a bar and monitoring the response of the bar. The magnitude of the applied pressure was deduced from measurement of momentum of detachable end-pieces at the other end of the bar. In 1946, Davies [10] improved the method by measuring electrically the variation of either the longitudinal displacement at the output end of the bar or the radial expansion of the cylindrical surface of the bar. Davies also concluded that if the pressure end of a 1/2 inch diameter bar could be submitted to a force which changed instantaneously from zero to a finite value, the observed rise time in the bar would be about 2 μs, due to the time for the stress wave to develop in the bar. Neubert [11] found that the strain gauges must be located at least five bar diameters from the excitation end, since that is the minimum distance required for a relatively long pulse to settle down to a plane wave in the bar.

A desirable goal is to have the bar as thin as possible, so the pulse will not disperse, or change shape, as it travels down the bar. A bar is thin if $\lambda/d \geq 5$, where λ is the half-wave length of the shortest wave, which is associated with the highest frequency component to have a small diameter d, but large enough so the bar will not yield or buckle. For a thick bar, with $\lambda/d < 5$, the stress wave will disperse as it travels down the bar. Parker [5,6] predicted the behavior of 10 and 100 μs pulses using both the elementary thin bar theory and the more exact, but still approximate, thick bar theory of Love [12]. The exact differential equations for a thick, cylindrical bar were presented by Pochhammer [13] and Chree [14] and have not been solved exactly. Neubert [11] used the Hopkinson bar as an impactor against beams having various end conditions, and measured the applied forces using strain gauges attached to the bar. He predicted the response of the beams to this mechanical excitation using Bernoulli-Euler and Timoshenko uniform beam theory as well as lumped-parameter representation of the beams. Parker [6,15] predicted the response of Timoshenko beams to pyrotechnic shock.

Recently, Smith [16] summarized some of the work being done with regard to measurement of pyrotechnic shock and included some references. He pointed out the importance of developing high frequency shock spectra, to 100 kHz, and emphasized the related difficulties in producing dependable acceleration measurements.

Results of a significant, careful, effort were reported by Powers [17], who performed a series of design optimization tests on subscale and full-scale vehicle interstage separation systems, finding shock response spectra useful to 80 kHz or more. He measured strains at locations very close to the high-energy separation joints. Many other investigators have measured response and processed data only up to 10 or 20 kHz, although there is an increasing awareness that such results are insufficient to accurately represent pyrotechnic shock effects on components and structures.

Shock spectra, as originally presented by Biot [18] and used by White [19], were useful because they could be readily measured during an earthquake and then used in a modal analysis of a building to predict the structural response to the earthquake. To date, the main use of shock spectra from pyrotechnic events has been to compare outputs and decide which device produces the smallest output in a certain frequency range. However, the analysis shows that it is possible to predict the response of simple structures at the design stage using finite element solutions.

ANALYTICAL APPROACH

Finite Element Analysis for Hopkinson Bar

To predict the response of a thick bar, with $\lambda/d < 5$, the Love equation has been used, which accounts for the radial inertial effects, and is

$$c^2 \frac{\partial^2 u}{\partial^2 x} = \frac{\partial^2 u}{\partial t^2} - (\nu r_g)^2 \frac{\partial^4 u}{\partial x^2 \partial t^2}$$

Table 1

Pulse and wave lengths for 10 and 100 μs pulses

	Pulse Duration 10 μs	100 μs
Pulse length on bar, ℓ_p, inches	2	20
Mesh spacing needed at $\ell_p/20$, inches	0.1	1
Highest modal freq. for strain	200 kHz	20 kHz
Mode half wave length, λ	0.5 in	5 in
Mode half period	2.5 μs	25 μs
Highest modal freq. for acceleration	500 kHz	50 kHz
Mode half wave length, λ	0.2 in	2 in
Mode half period	1.0 μs	10 μs

where
c = sonic velocity of the stress wave in the bar
u = particle displacement
x = coordinate location of particle
t = time
ν = Poisson's ratio
r_g = radius of gyration of bar cross-sectional area

If the bar is assumed thin, the radius r_g is taken as zero and the equation reduces to the simpler one-dimensional wave equation. Parker found, for the short 10 μs pulse, that 100 modes of vibration were needed to predict the strain magnitude to within 5% and about 250 were needed to predict the acceleration to the same accuracy. The associated natural frequencies of the bar for the 100th and 250th modes are 200 and 500 kHz. This was used as a guide for the present study to help determine the fineness of the space and time meshes needed in a finite element analysis. Because the wave velocity c = 200,000 in/sec in a steel or aluminum bar, the length of the 10 μs pulse on the bar is 2 inches. Thus, if one divided this into 20 space intervals, a space mesh of 0.1 inches would result. Timewise, 1/20th of pulse length of 10 μs is 0.5 μs. The half-period for the 500 kHz bar mode is 1 μs. The timewise mesh size should be about 1/20th of this half-period. These results are summarized in Table 1.

For a one inch diameter bar, the thin bar theory is supposed to be adequate for λ/d > 5, or for λ > 5 inches. The above table shows then that the thick bar theory should be used for the 10 μs pulse. Parker did this using the Love equation, and showed that it predicted the dispersion measured on the short pulses emanating from the explosive bolts.

The present finite element analysis was carried out in SAP IV computer program [20] for the Hopkinson bar with and without the end adaptors. The beam element was used to represent the stretching and bending motion

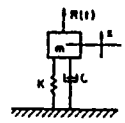

Figure 1. Base-driven mass-spring-dashpot filter.

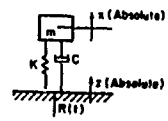

Figure 2. Force-driven mass-spring-dashpot filter.

of the bar. Although only axial motion was excited in the experiments, the low frequency bending modes were calculated at first to ascertain that a proper connection had been made in the analytical model between the bar and the adaptor. The two-dimensional plane stress plate element was used to represent the tapered plate adaptor, which allows two displacements at each of the four corners, but does not explicitly include rotations, while the beam element is one-dimensional and includes rotations explicitly. Timewise integration is done by the Wilson-θ Method, which is unconditionally stable.

SHOCK SPECTRA CALCULATIONS

The shock spectrum in general is the maximum response versus natural frequency of a mass-spring-dashpot filter to a specified input. Most often the input is a measured acceleration applied as a ground motion z(t) to the system as shown in Figure 1 and the response is the absolute acceleration x(t) of the mass of the filter. For the present work, the spectra were also calculated for force inputs, applied as R(t) as shown in Figure 2. The differential equation to be solved for the base motion-driven system is, after dividing through by the mass m

$$\ddot{x}_r + 2\zeta\omega_n\dot{x}_r + \omega_n^2 x_r = -\ddot{z}$$

$$\text{for } 0 \leq t \leq T_o$$

For the force-driven filter, the corresponding equation is

$$\ddot{x} + 2\zeta\omega_n\dot{x}_r + \omega_n^2 x = \frac{R(t)}{m}$$

$$0 \leq t \leq T_o$$

where
x = absolute displacement of m
x_r = x-z = relative displacement
z = base motion
ζ = ratio of damping to critical damping
k = spring stiffness
m = mass
$\omega_n^2 = k/m$
T_o = the length of the input pulse.

It is assumed the input is zero for $t \geq T_o$. The maximum response calculated for $0 \leq t \leq T_c$ is plotted on the initial shock spectrum and that occurring for $t \geq T_o$ is plotted on the residual spectrum. Note that the mass m remains in the equation for the force-driven system and it was taken as one for the present calculations. The digitizing interval for the pin-puller data was $\Delta t = 3.0625 \times 10^{-6}$s.

INSTRUMENTATION

The present tests were done in the Pyrotechnics Laboratory at NASA Langley. There were seven accelerometers used, one B&K Type 8309 and six Endevco 2225M5. The B&K accelerometer was installed where the frequency content was expected to be highest and had a capacity of 100,000g peak acceleration with an ideal mounted resonant frequency of 180 kHz. The Endevco accelerometers are supposed to be linear to 100,000g and have a mounted resonance of 80 kHz. Thus we expect the B&K and Endevco accelerometers to be flat within 5% to 36 kHz and 16 kHz, respectively. The accelerometers were attached using a threaded stud in a hole made by drilling and tapping into the structure.

The strain gauges were Model No. CEA-06-187-UW-350 and were 3/16 inch long, had 350 ohms resistance, and gauge factor of 2.08. Each strain gauge was monitored separately through a Vishay BAM-1 Bridge Amplifier, which had capacity to 100 kHz.

The data was recorded in analogue form on a Sangamo 3612 wide-band 1, frequency modulated configuration tape recorder, flat from zero to 80 kHz. The data was then played back on a visicorder and was digitized semiautomatically in the Pennsylvania State University computer laboratory.

APPARATUS AND TEST PROCEDURE FOR PIN-PULLER TESTS ON HOPKINSON BAR

The experimental apparatus for the pin-puller tests on the Hopkinson bar consisted of the monitoring system and six pin-pullers: Viking I (single initiator and opposed dual initiators), Viking V (dual), Polaris (dual), RCA BI.V (Hi Shear dual), ICI ATLAS pin retractor, and a mechanical pin-puller. A steel sphere on a ballistic pendulum was also used as an impactor for initial calibration. A sketch of the single Hopkinson bar and ballistic pendulum is shown in Figure 3.

Pyrotechnic pin-pullers are piston-cylinder devices with a high burn-rate propellant, which produces approximately 25,000 psi, to drive the piston to withdraw the pin. Pyrotechnic shock is produced on pressurization, release of load, and impact of the piston on completion of the stroke. A mechanical pin-puller has a spring-loaded piston with a meltwire release mechanism.

The main elements of the pin-puller monitoring system [Figure 4] were two cold-rolled steel bars 10 feet long and 3/4 inch in diameter. They were oriented at right angles to each other in order to measure the axial and transverse output forces from the pin-pullers, which were mounted on a special machined adaptor connected to the input ends of the bars. This adaptor was about 2-3/4" x 3-11/32" x 1-1/4" overall as shown in Figure 4.

The output end of each bar was fitted with a machined steel end cap 1-1/4" dia x 1-1/2" long [Figure 3] which was centrally drilled and tapped to accommodate the accelerometers.

The strain gauges were oriented longitudinally 17.82 inches from the input ends of the bars. They were located successively 90 degrees apart around the circumference of the bar. With this location, a pulse about 1000 μsec long could be observed before there was any interference from reflections from the free end of the bar.

The test procedure was as follows:

1. The axial bar was first tested by itself, with end caps as described above on each end. The input end was then impacted with a steel sphere 1-1/4" diameter on a pendulum 60 inches long. The B&K accelerometer was on the output end of the bar.
2. The double Hopkinson bar arrangement shown in Figure 4 was assembled and impacted with the steel sphere. The B&K accelerometer was on the output end of the axial bar and an Endevco accelerometer on the output end of the transverse bar.
3. The pin-pullers were attached to the adaptor, one by one, and activated.

APPARATUS AND TEST PROCEDURE FOR THE HALOE STRUCTURE

The apparatus was a full-scale model of the HALOE structure as shown in Figure 5. Five of the pin-pullers were tested, the

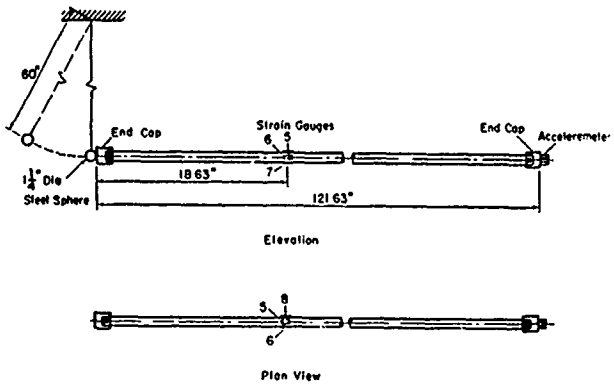

Figure 3. Single Hopkinson bar with ballistic pendulum.

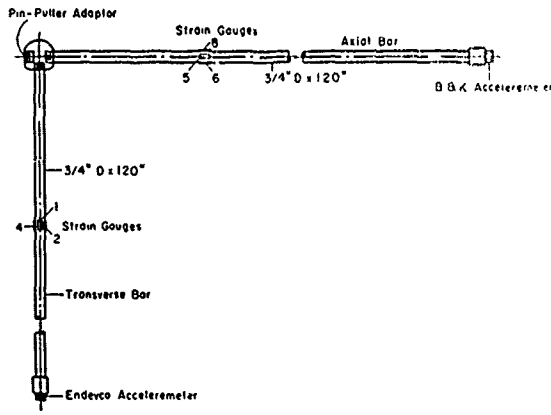

Figure 4. Plan view of Orthogonal Hopkinson bars for pin-puller tests.

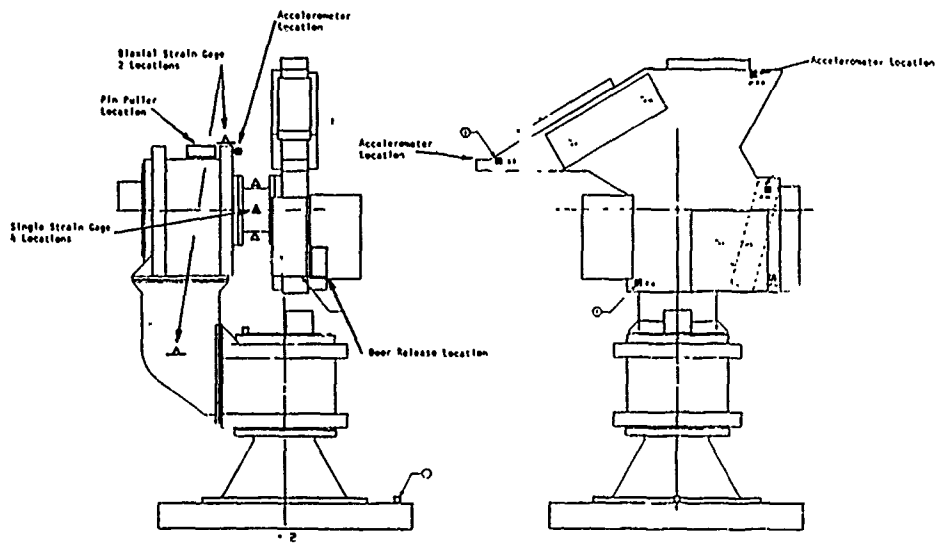

Figure 5. Location of strain gauges and accelerometers on HALOE structure.

Polaris being omitted.

The monitoring system consisted of eight strain gauges and five accelerometers. Four of the strain gauges were located parallel to the axis of a hollow aluminum cylindrical section between the main frame and the outboard elevation gimbal. This cylinder was 2.875" long and 3.25" in diameter. The gauges were located successively 90 degrees apart around the circumference, in the same pattern used on the Hopkinson bar. Two other gauges were orthogonal and mounted on the heavy ring on the outboard gimbal at a point about 3/4" from the pin-puller attachment. The last two gauges were orthogonal and located at a point on the hollow rectangular cross-section between the two gimbals.

The B&K accelerometer was located on the ring of the outboard gimbal adaptor, close to the pin-puller. Two Endevco accelerometers were orthogonal and near the tip of the frame on the tapered end. The other two Endevco accelerometers used were orthogonal and located on the other upper corner of the frame. No accelerations were measured perpendicular to the plane of the main frame. The back-up instrumentation was exactly the same as that used in the Hopkinson bar tests of the pin-pullers, described above.

The test procedure consisted of attaching and activating the pin-pullers, one by one.

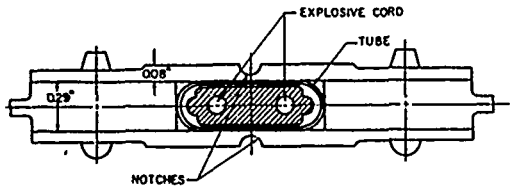

Figure 6. Cross-section of spacecraft separation joint.

APPARATUS AND TEST PROCEDURE FOR SPACECRAFT SEPARATION JOINT TESTS

The source of excitation was a twelve inch long section of the spacecraft separation joint and a monitoring system, which consisted of an aluminum tapered plate adaptor and a single Hopkinson Bar. This separation joint has a high explosive (approximately 1 x 10^6 psi) to expand a tube, which fractures a pre-notched surrounding structure as shown in Figure 6. The dimensions of the tapered plate are shown in Figure 7. The 1-1/4" diameter steel sphere impactor on the ballistic pendulum was also used during initial calibrations.

The Hopkinson bar was the axial bar used in the Pin-puller tests, as described above. The four strain gauges were monitored and the B&K accelerometer was mounted at the output end of the bar.

The steps in the test procedure were as follows.

1. Use the steel sphere on the ballistic pendulum with and without the tapered plate adaptor, to determine the effect of the adaptor on the transmitted pulse.
2. Install various separation joint configurations and measure their outputs. Seven variations were tested.

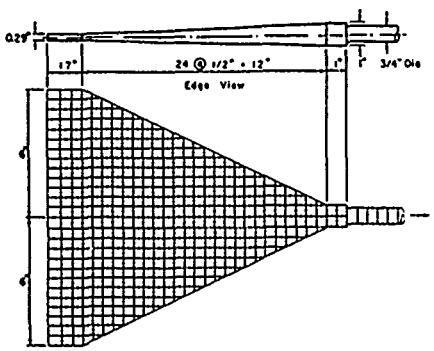

Figure 7. Separation joint tapered plate adaptor with 1/2" finite element mesh.

RESULTS FROM PIN-PULLER TESTS ON HOPKINSON BAR

In Figure 8, the axial and transverse forces are shown for the Viking I pin-puller for two initiators fired simultaneously. The solid line is for the axial bar and the dashed line for the transverse bar. Here a positive force is tensile. Thus, the axial force is compressive for the first 0.53 milliseconds, with -500. pounds maximum force; this is followed by a tensile region for 0.41 ms with 1075 pounds maximum force. Here, the first end reflection was subtracted numerically to extend the useful range of the record to about 0.00115 s. The maximum transverse force was about one-third the maximum axial force.

In Figure 9, the moments calculated from the strain signals in the axial and transverse bars are shown. The signals are only significant for the first 0.001 seconds. Besides reflections of the axial pulses, the moments induced in the orthogonal bars due to their interconnection must be considered. The magnitude of the maximum moment was 70 inch-pounds for this pin-puller.

The axial force-time outputs of the Viking I, Viking V and mechanical pin-pullers are compared in Figures 10(a) and 10(b). All of the pyrotechnic pin-pullers produced first a compression and then a tension. However, the initial portion of the force-time output of the mechanical pin-puller was tensile, as shown in the solid line in Figure 10(a), where the force-time output of the mechanical pin-puller is compared with that of the Viking I pin-puller. In Figure 10(b) it is seen that the initial compressive pulse from the Viking V pin-puller is higher in magnitude and shorter in duration than that from the Viking I.

An example of the acceleration response shock spectra of the force-time signal for the Viking I pin-puller in the axial direction is shown in Figure 11. The initial shock spectrum is solid and the residual is dotted. In most cases it was found that the residual spectrum fell below the initial shock spectrum. Note that the residual spectrum displays troughs which are always present for a signal of finite length. The troughs should go to zero if a fine enough frequency interval is taken to show them in detail.

The initial shock spectra for the transverse direction are compared in Figure 12 for the mechanical pin-puller, Hi-Shear, Viking V, and Viking I pin-pullers with one and two initiators fired. The spectrum of the mechanical pin puller is slightly below that of the others over most of the frequency range. The deep dip in the spectrum at 40 kHz appears to be due to the digitizing interval used.

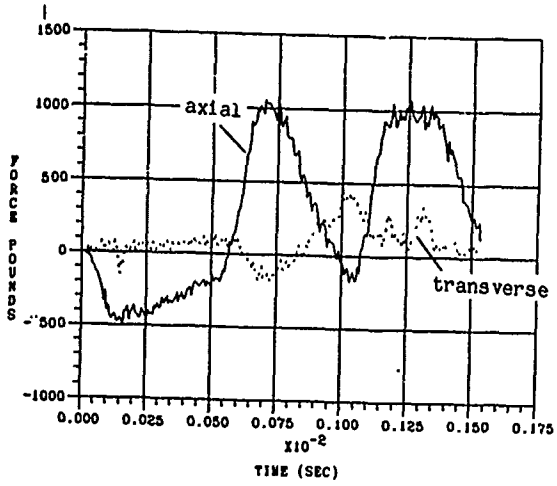

Figure 8. Experimental axial and transverse force, Viking I pin-puller.

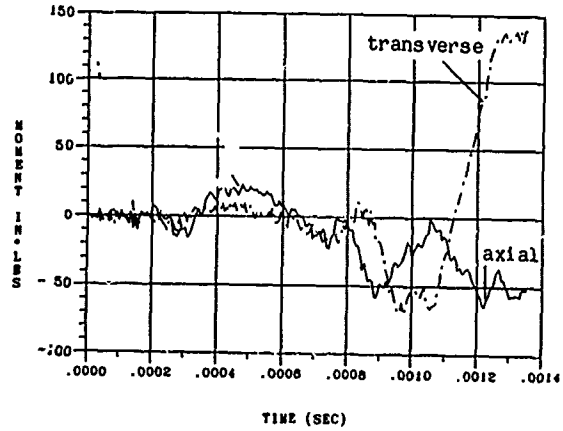

Figure 9. Experimental axial and transverse moment, Viking I pin-puller.

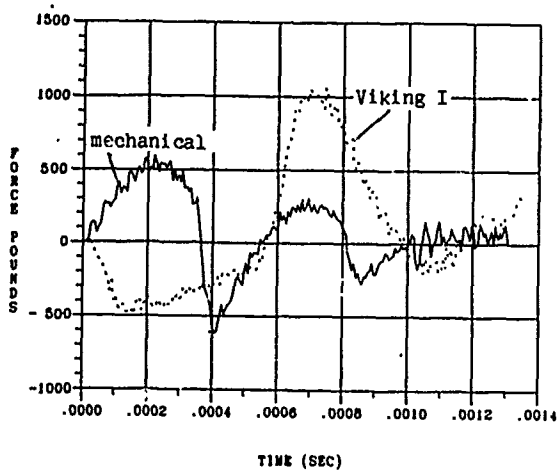

Figure 10(a). Experimental force, mechanical and Viking I pin-pullers.

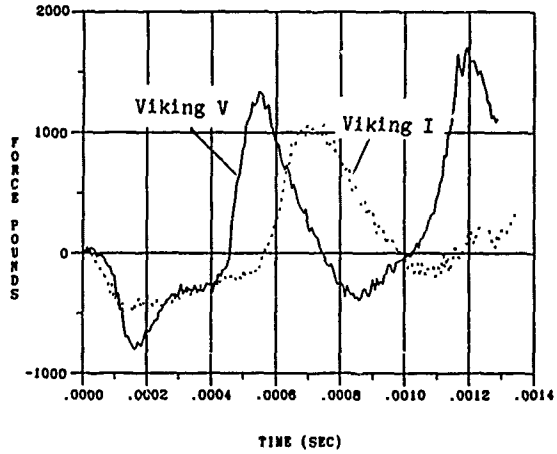

Figure 10(b). Experimental force, Viking V and Viking I pin-pullers.

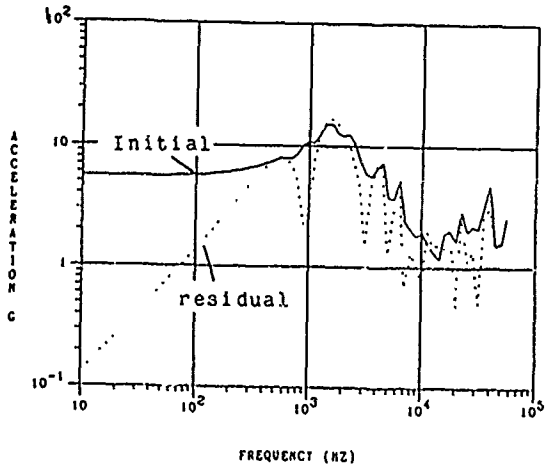

Figure 11. Initial and residual shock spectrum for force from Viking I pin-puller.

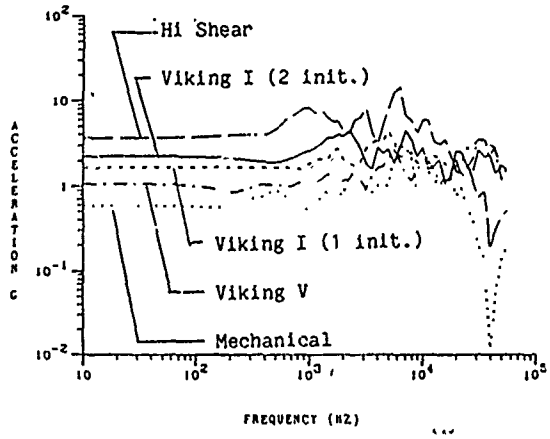

Figure 12. Initial shock spectra for forces from five pin-pullers.

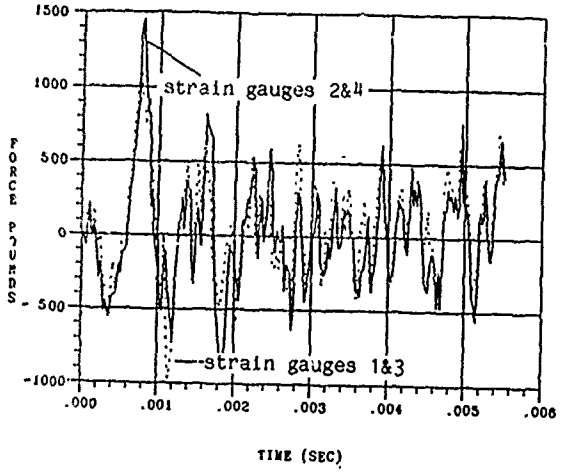

Figure 13(a). Force from strain gauges 1&3 and 2&4, Viking I pin-puller on HALOE structure.

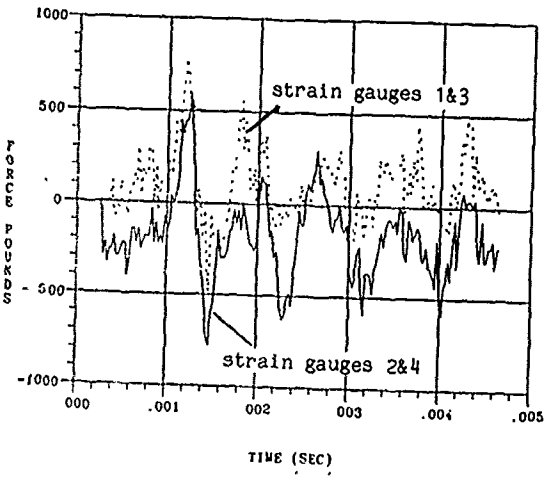

Figure 13(b). Force from strain gauges 1&3 and 2&4, Viking V pin-puller on HALOE structure.

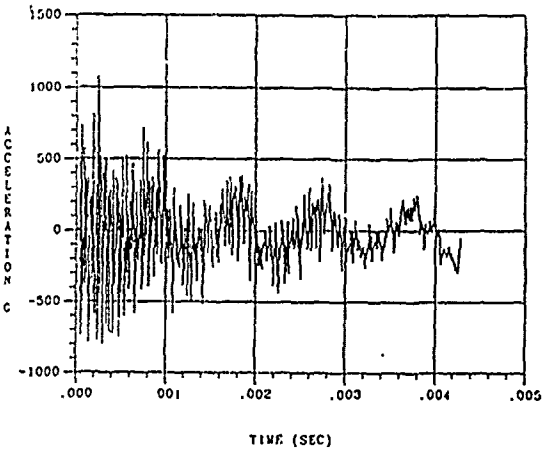

Figure 14. Acceleration vs. time, Viking V pin-puller on HALOE, B&K acc.

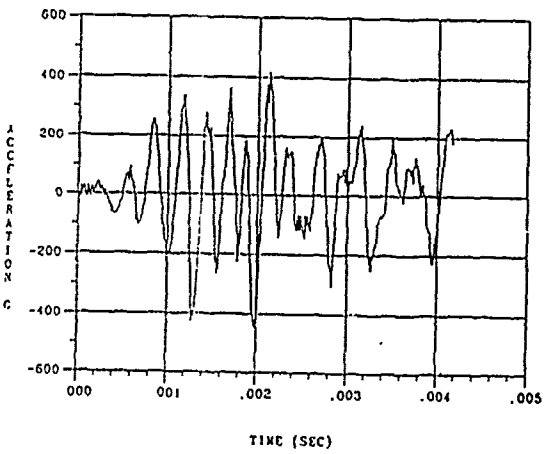

Figure 15. Acceleration vs. time, Viking V pin-puller on HALOE, Acc. 3.

RESULTS FROM HALOE STRUCTURE TESTS

For the pin-puller on the HALOE structure, the strain gauge data was converted to stress versus time. The Viking V pin-puller seemed to generate the most severe outputs overall, and caused stresses as high as 4450 psi in the cylinder which was monitored.

The forces and moments were calculated from opposite pairs of strain gauges on this same cylinder, even though it does not qualify as a long, thin beam because the length to depth ratio was only about 0.88. The measured forces for the Viking I and Viking V pin-pullers calculated from two separate pairs of gauges 90 degrees apart on the circumference of the cylinder are shown in Figure 13 (a) and 13 (b). The initial shape of the signals are amazingly the same, indicating that the short cylinder is almost acting like a bar with a plane dilational wave. Even more amazing is the similarity to the force-time pulse measured in the Hopkinson bar, in both shape and magnitude, in Figure 10 (a) and 10 (b).

The acceleration versus time for the Viking V pin-puller, measured on the B&K accelerometer, beside the pin-puller attachment, is shown in Figure 14. There is significant high frequency content and peaks rise to 1200g. This should be compared with the record from accelerometer 3 in Figure 15, where the very high frequency content is missing and the peaks were about 440g. The associated shock spectra from these two acceleration-time signals are shown in Figures 16 and 17. The spectral levels beside the pin-puller are higher than on the frame, as expected, except in the frequency

Table 2 Separation Joint Tests with Maximum Forces and Accelerations

No.	Plate Thkns	Charge (gr/ft)	Location	Max. Force Tens	Max. Force Comp.	Max. Moment (in lb)		Force Sh Sp at 100 Hz	Acc. Sh Sp at 100 Hz
11	Var.	8.7	Off-ctr	2500	-3500	+225	-175	8.8	---
12	Var.	8.7	Center	4000	-1500	+200	-110	10.2	20
13	Var.	8.7	Off-ctr	1750	-1750	+275	-275	6.5	52
14	Cnst.	8.7	Center	3000	-1000	+300	-275	10.2	30
15	Cnst.	8.7	Center	2150	-1500	+115	-100	5.5	9
16	Cnst.	11.0	Center	3000	-1150	+200	-200	7.5	---
17	Cnst.	11.0	Center	4500	-1250	+325	-350	11.8	---

range from 1500 to 10,000 Hz, where the level for Accelerometer 3 is about three times that of the B&K accelerometer. This says that the level a foot or more from the pyrotechnic is higher than the level beside the pyrotechnic in that frequency range. In addition, it demonstrates that it is dangerous to judge acceleration levels entirely from peaks on the time-wise signals. Because the mounted frequency of Accelerometer 3 should be 80 kHz, the accuracy of the associated shock spectrum is questionable above 16 kHz, but is shown nevertheless.

RESULTS FROM SPACECRAFT SEPARATION JOINT TESTS

The seven separation joint tests were numbered 11 through 17. A single string of explosive was used in each test, but the charge and position varied as summarized in Table 2. The charges were either 8.7 or 11 grains per foot and the position was either center or off-center. In addition, the thickness of the material torn in the notched joint varied, from one end of the joint section to the other, during the first three tests but was constant for the last four tests. The varying thicknesses had been used previously to determine, on a single test, how thickness of material torn was related to charge strength. In the table "Var." means varying thickness and "Cnst." means constant thickness material in the separation joint itself.

The strain gauges operated satisfactorily throughout the tests, with no indication of permanent set. The maximum stress at the strain gauges on the Hopkinson bar occurred on Test 17 with a peak of 10,200 psi, which is well below the static yield stress of the steel bar. The accelerometer loosened during Test 15, yielding inaccurate signals on Tests 16 and 17.

The force-time curve for Test 17 is shown in Figure 18. There is an initial compressive region having a maximum of -1250 pounds and a duration of 130 μs, followed by a severe tension having a maximum of 4500 pounds. Since it is thought, from

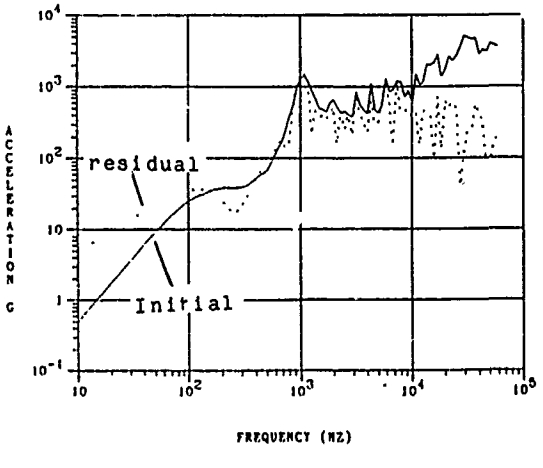

Figure 16. Initial and residual shock spectra for Viking V pin-puller on HALOE, B&K acc.

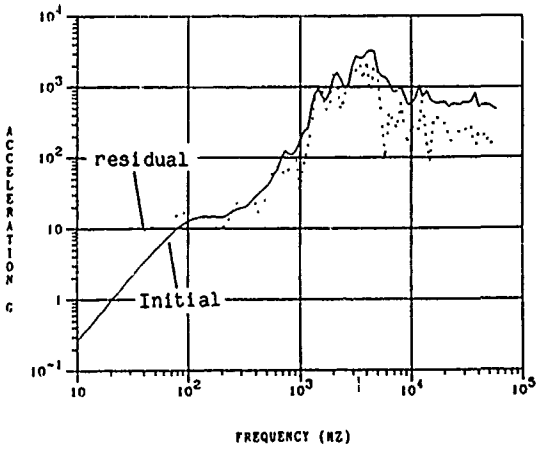

Figure 17. Inital and residual shock spectra for Viking V pin-puller on HALOE, B&K acc.

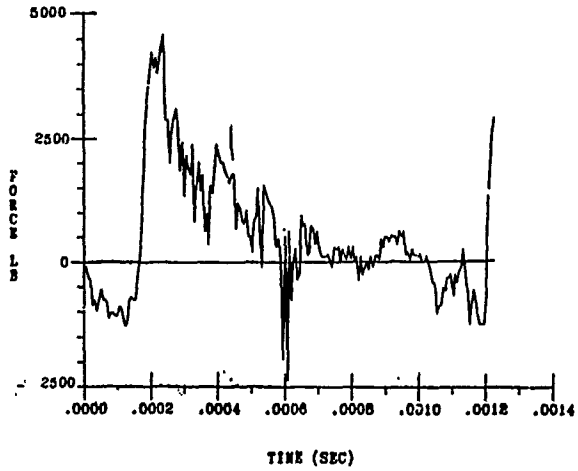

Figure 18. Force vs. time, separation joint test 17.

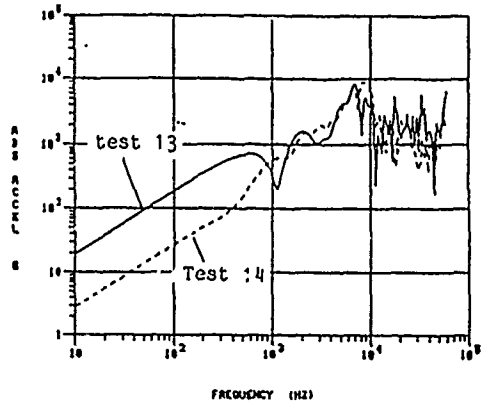

Figure 19. Initial shock spectra for acceleration, separation joint test 13 and test 14.

photographs, that the separation joint separates within 10 μs after detonation, it is expected that the duration of the excitation should be of that order-of-magnitude. This is seen in the high frequencies superimposed on the force-time signal. The lengthening of the pulse as seen in the Hopkinson bar is apparently due to dispersion and reflection of the stress wave as it travels through the separation joint itself, the tapered plate adaptor, and the adaptor-bar interface.

In Figure 19, acceleration shock spectra are shown from acceleration signals from the end of the Hopkinson bar for Tests 13 and 14. Below 1000 Hz, test 13 levels were the most severe, being about six times the level for Test 14. Above 1000 Hz, the spectra showed relatively little difference on the average. It should be noted that g-levels in the shock spectra calculated from accelerations are higher than those calculated from forces, partly because of the mass-spring-dashpot model used and partly because the accelerations on the Hopkinson bar can be predicted by taking the derivative of the strains or forces.

RESULTS OF ANALYTICAL PREDICTIONS USING FINITE ELEMENT ANALYSIS

Convergence of the finite element solution was studied by varying four parameters:

1. the duration of the input pulse length, using 10, 100, and 500 μs pulses.
2. the element grid size, or the number of elements.
3. the number of modes used in the solution.
4. the time increment used in the solution.

In Figure 20, the force versus time predicted at the strain gauge locations is shown for a haversine pulse 10 μs long and 10,000 pounds peak force, applied to the bar with no end caps or adaptors. Since the equivalent of thin bar theory is being used, then the exact solution is known and the force versus time in the bar should be exactly the same as the input. It is seen that a time increment of 1/60 μs is needed with a mesh spacing of 0.05 inches to predict the force. The solutions for mesh spacings of 0.25" and 1" are also shown.

The pulse length was changed to 100 μs for the forces shown in Figure 21. Here a time increment of 1 μs was used and the 1 inch mesh spacing was sufficiently accurate, since the change to 0.5 inch spacing resulted in little difference in the predicted force. The solution for 2" grid spacing is also shown.

The convergence with number of modes used is demonstrated in Figure 22. The SAP IV program has two options with regard to timewise solutions for transient inputs: (1) a direct integration of all the simultaneous equations, which should give the same answer as using all the modes or (2) a modal solution in which the number of modes calculated and summed may be specified. The curves show the force versus time in the bar obtained by including three, five, ten and thirty modes in the solution. The convergence is less rapid after the first ten modes are used, the thirty mode solution being only slightly different from the ten mode solution, but still about 11% deficient in predicting the peak force. The natural frequency for the 30th mode is 36,370 Hz.

The prediction of the experimental strain response of the system with the tapered plate adaptor for the spherical impactor excitation is shown in Figure 23. The work with the finite element analysis of the tapered plate adaptor shows that smaller

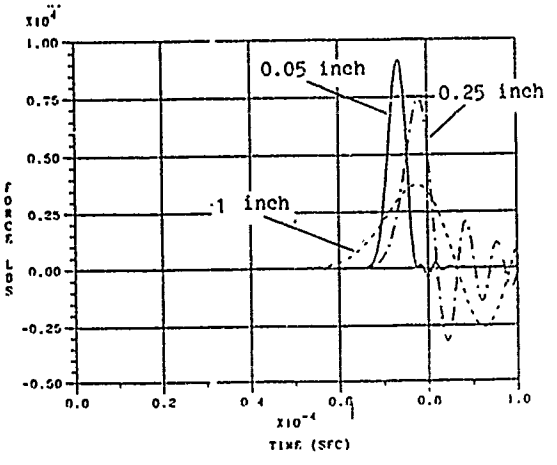

Figure 20. Theoretical force vs. time, Hopkinson bar, 10,000 pound, 10 μs pulse.

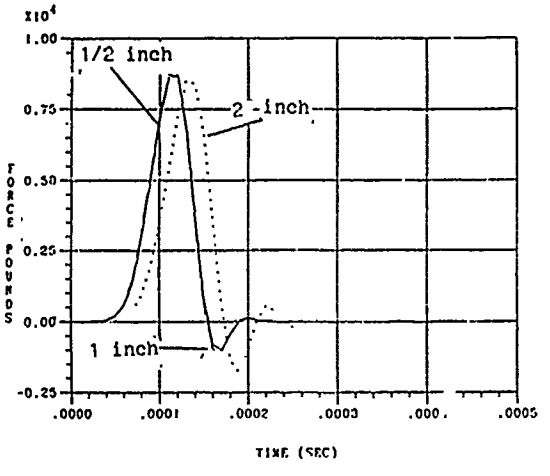

Figure 21. Theoretical force vs. time, Hopkinson bar, 10,000 pound, 100 μs pulse.

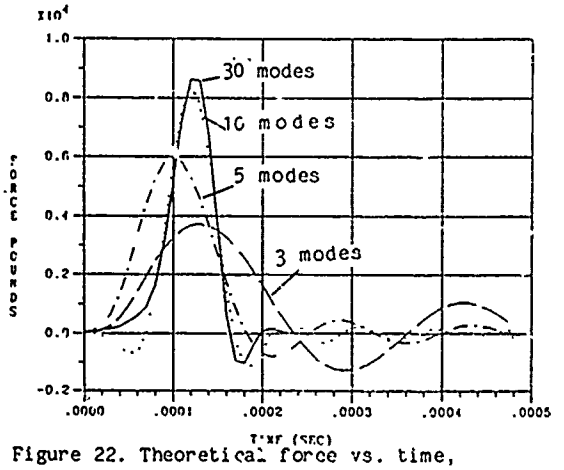

Figure 22. Theoretical force vs. time, Hopkinson bar, 10,000 pound, 100 μs pulse.

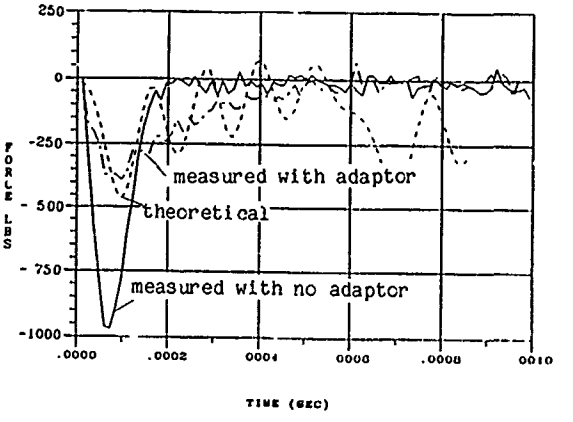

Figure 23. Force vs. time, Hopkinson bar with tapered plate adaptor for separation joint.

space intervals are needed for the shorter 10 μs pulse. While this is possible, it is not being pursued because of cost. Instead, a smaller adaptor is being tried on future tests.

SUMMARY

To evaluate the potential for spacecraft damage caused by activation of pyrotechnic mechanisms, pyrotechnic shock tests were conducted on three configurations: pin-pullers on an orthogonal double Hopkinson bar arrangement, pin-pullers on a prototype of the HALOE structure, and a section of separation joint on a single Hopkinson bar. Strains and accelerations were measured. The strains were converted to output stresses, forces, and moments. Acceleration shock response spectra are presented for both acceleration- and force-time signals. The devices were attached to the Hopkinson bars with adapters, which are typical of attachments used in practice. In order to predict the effect of the adaptors, finite element models of the adaptor-bar combinations were analyzed and results are presented with regard to grid size, time interval, and frequency range required to predict response to pulses of 10 and 100 microsecond duration. Some particular points to be made in summary follow.

1. Output forces as well as accelerations versus time were measured on Hopkinson bars for explosive bolts, explosive nuts, pin-pullers and separation joints. This represents a wide range of excitations, with regard to magnitude and length of pulse. The shortest pulse was about 12 μs long, from the explosive bolt attached directly to the bar. The fracture of the separation joint appears to happen in less than 10 μs, but the force signal received on the Hopkinson bar was much

longer, because of the filtering effect of the intervening adaptor. Considering the frequency limitations of the Hopkinson bar, the strain gauges, the amplifiers, and the recording system, the strain, stress, force and moment results presented should be reliable to 80 kHz. As noted above the two different types of accelerometers were flat to 36 kHz and 16 kHz.

2. The shock spectra were processed to 40 kHz from force signals and from acceleration signals. There is the question as to whether the high frequency signals can damage spacecraft components. In steel or aluminum, a frequency of 40 kHz corresponds to a half-wave length of 5 inches, so it is obvious that equipment pieces with dimensions in that range are vulnerable to high frequency inputs.

3. Force shock spectra were computed, apparently for the first time for pyrotechnic shock, where the input to the mass-spring-dashpot filter was force per unit mass.

4. Unique Hopkinson bar arrangements were used. In addition to the usual single bar, a split bar was used for the explosive nut tests. Two orthogonal bars were used successfully for the first time to measure the output forces, moments, and accelerations of the pin-pullers.

5. Force-time and acceleration-time outputs and their associated shock spectra were compared for four different pin-pullers. Overall, the mechanical pin-puller produced the least severe output. These results have not been previously available anywhere.

6. The same types of pin-pullers that were tested on the Hopkinson bars were also tested on the full-scale HALOE structure. The timewise force outputs compared favorably with those measured on the Hopkinson bar, giving credence to the use of the bar to compare devices. A Hopkinson bar set-up is much less expensive than a spacecraft structure mock-up.

7. The attenuation of acceleration with distance from the pyrotechnic as measured on the HALOE structure is especially noteworthy. Usually, one expects the acceleration signal to be attenuated with distance, which was the case below 1.5 kHz and above 10 kHz. However, between 1.5 and 10 kHz the spectra were higher on the frame than beside the pin-puller. These results also demonstrate that it is dangerous to judge acceleration levels simply by looking at acceleration-time curves.

8. Force-time and acceleration-time outputs were obtained from seven variations of an explosively expanded tube separation joint.

9. The behavior of the thin Hopkinson bar was represented analytically using finite elements. The fineness of the element gridwork, the time interval, and the number of modes needed to trace pulses of 10 and 100 μs, required a time interval of 1/60 μs and a mesh spacing of 0.05 inches.

Thus, the understanding of the pyrotechnic phenomenon has been considerably increased by measuring the outputs from a variety of pyrotechnic devices on Hopkinson bars and on a prototype structure. This provides the necessary information, not only for comparing various devices but for predicting the structural response and evaluating the potential for damage. The capability to predict structural response has been demonstrated using finite element models. The entire procedure, using the Hopkinson bars and associated measurements and analysis, should be useful to spacecraft designers to make comparison and evaluation tests before committing to costly spacecraft hardware.

ACKNOWLEDGMENTS

The assistance of N. A. Roy in checking the shock spectrum computer program and of Milind Saraph with the digitizing of data is gratefully acknowledged.

REFERENCES

1. Neubert, V. H., Evans, Maria J., and Bement, Laurence J., "Measurement, Data Analysis, and Prediction of Pyrotechnic Shock," Final Report, NASA Grant NAG 1-543 #4, August, 1986.

2. Evans, Maria J., "Analysis and Prediction of Pyrotechnic Shock Using a Hopkinson Bar," M.S. Thesis, The Pennsylvania State University, in process.

3. Olsen, J. R., et al, "Mechanical Shock of Honeycomb Structure from Pyrotechnic Separation," The Shock and Vibration Bulletin, No. 37, Part 4, pp 15-42, 1968.

4. Neubert, V. H. and Parker, R. P., "High Frequency Shock of Spacecraft Systems," Final Report, NASA Contract NGR 39-009046, Nov. 24, 1971.

5. Neubert, V. H. and Parker, R. P., "Timewise Output of Pyrotechnic Bolts," Proc. of the 44th Shock and Vibration Symposium, Shock and Vibration Information Center, Washington, DC 20375, 1975.

6. Parker, Robert Paul, "High Frequency Response of Bars and Beams," Doctoral Thesis, The Pennsylvania State University, 1973.

7. Neubert, V. H., "Measurement and Analysis of Force-time Outputs of Pyrotechnic Nuts," Final Report, NASA Contract No. NAS 1-12045, November, 1973.

8. Bement, L. J. and Neubert, V. H., "Performance of Low-Shock Pyrotechnic Separation Nuts," 8th Aerospace and Mechanisms Conference, NASA Langley, Oct. 18, 1973.

9. Hopkinson, B., Philosophical Transactions of the Royal Society of London, Series A, Vol. 213, 1914, p. 437.

10. Davies, R. M., "A Critical Study of the Hopkinson Pressure Bar," Phil. Trans. Royal Society, Series A, Vol. 240, 1948.

11. Neubert, V. H. Response of a Beam to Transverse Impact, Doctoral Dissertation, Yale University, 1957.

12. Love, A. E. H., The Mathematical Theory of Elasticity, Cambridge, 1927.

13. Pochhammer, L., "Uber Fortplanzungsgeschwindigkeiten Kleiner Schwingungen in einem unbegrenzten isotropan Kreiszylinder," J. F. reine u. angw. Math. (Crelle), Vo. 81, 1876.

14. Chree, G., "The Equations of an Isotropic Elastic Solid in Polar and Cylindrical Coordinates, Their Solution and Application," Trans. Camb. Phil. Soc., vol. 14, 1889.

15. Parker, R. P. and Neubert, V. H., "High Frequency Response of Beams," Journal of Applied Mechanics, Vol. 42, pp. 805-808, December, 1975.

16. Smith, James Lee, "Effects of Variables Upon Pyrotechnically Induced Shock Response Spectra," NASA Technical Paper 2603, Marshall Space Flight Center, May 1986.

17. Powers, D. R., "Strain Histories Associated with Stage Separation Systems Using Linear Shaped Charge," The Shock and Vibration Bulletin No. 53. Part I, pp. 89-96, May 1983.

18. Biot, Maurice A., "Transient Oscillations of Elastic Systems," Thesis No. 259, Aeronautics Department, California Institute of Technology, 1932.

19. White, Merit P., "Formulation of Shock Problems," in Neubert, V. H. (Ed.), Shock Analysis of Lumped Parameter Systems, Proceedings of Short course, The Pennsylvania State University, 1964.

20. Bathe, K., Wilson, E. L., and Peterson, F. E., SAP IV, Report No. EERC 73-11, University of California, Berkeley, California, June 1973, Revised April 1974.

FACILITIES FOR SHOCK TESTING OF NUCLEAR SHELTER EQUIPMENT IN SWITZERLAND

P. Hunziker
Defense Technology and Procurement Group. NC-Laboratory Spiez
Spiez, Switzerland

All kind of equipment installed in Swiss civil defense shelters and military fortifications is systematically shocktested according to the Technical Directives for the Shock Resistance of Equipment, where test procedures and test criteria are described. A set of three so-called shock parameters (test table acceleration a_{max}, velocity v_{max} and displacement d_{max}) are used as test criteria and are simulated on shock testing machines. More than 1000 different objects have been shocktested in the past 20 years. The NC-Laboratory disposes of two shock testing machines of the mechanical type. One for test objects up to three tons, where shocktests can be performed in the horizontal as well as in the vertical axis, and the other for test objects up to twelve tons, where shocktests only in the horizontal axes are possible. A new fully hydraulically driven vertical shock testing machine for objects up to twelve tons will be set in operation this year.

PREFACE

The protection of the civil population against the effects resulting from the possible use of nuclear, chemical and biological weapons in addition to those due to conventional weapons is the main and ambitious objective of the Swiss Federal Office of Civil Defense (FOCD).

Since 1964 corresponding federal legislation [2] has led to the construction of a large number of collective protection facilities such as private shelters incorporated in almost every newer dwellinghouse, command- and intelligence complexes as well as sheltered hospitals and dispensaries at a rate of about 1000 shelterplaces every day. These shelter places provide protection against a 1 bar peak overpressure blast and the related effects of a nuclear explosion in the MT-range. Although some civil defense shelters and, of course, military fortifications have a higher degree of protection, they are based on the same design criteria.

One important aspect within this context is the adequacy, reliability and durability of vital shelter equipment that is, equipment which is essential for the survivability of the occupants. The NC-Laboratory in Spiez of the Defense Technology and Procurement Group of the Swiss Military Department has been officially appointed to perform all the relevant tests and to evaluate equipment and materials according to established requirements and criteria [9,10] by order of the FOCD or the army (no commercial operations).

This paper deals only with one of all the necessary tests carried out in this Laboratory: The shocktesting and its facilities used for that purpose.

INTRODUCTION

All kinds of shelter equipment, ranging from a simple ventilating system of a private shelter to an operating theatre of a medical station have to withstand the severe ground shock loading induced by nuclear explosions (Fig. 1).

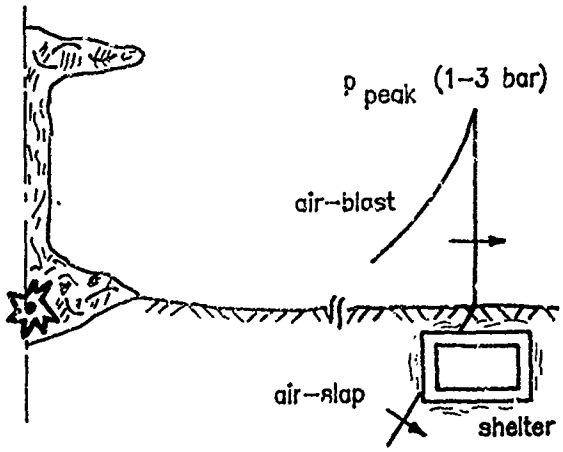

Fig. 1: Nuclear loading of a buried shelter

Therefore, equipment of Swiss civil defense shelters and military fortifications is systematically shocktested.

In the following paper the shocktesting method and the shock test facilities used in Switzerland are presented.

SHOCKTESTING METHOD

The transient loadings caused by the ground shock induced by a nuclear explosion produce strong shock motions of the shelter. As the interaction between the ground shock and the structure is a difficult and hardly investigated problem, in a first theoretical approach the structure is assumed to follow the same shock motion as the surrounding soil. This assumption seems reasonable as the majority of the shelters are usually of small dimensions and simple geometry and therefore relatively rigid. The resulting transient motions of the structure are transmitted to the supports of all installed shelter equipment.

In Switzerland up to now only the rigid body motion due to the so-called air-slap ground shock, the motion directly induced by the air-blast as it propagates over the shelter, has been considered for shock testing purposes.

Based on standard values for the soil parameters and for the structure, the following test criteria have been defined:

displacement	$d_{max} = 0.25$ m
velocity	$v_{max} = 1.6$ m/s
acceleration	$a_{max} = 160$ m/s^2

(the jerk has to be at least $40 \cdot 10^3$ m/s^3)

The test procedures, prescribed in the Technical Directives for the Shock Resistance of Equipment for Civil Defense Shelters [11], are still based on a "conventional" deterministic approach and will be improved in the near future with a new probabilistic shock testing concept [3,4].

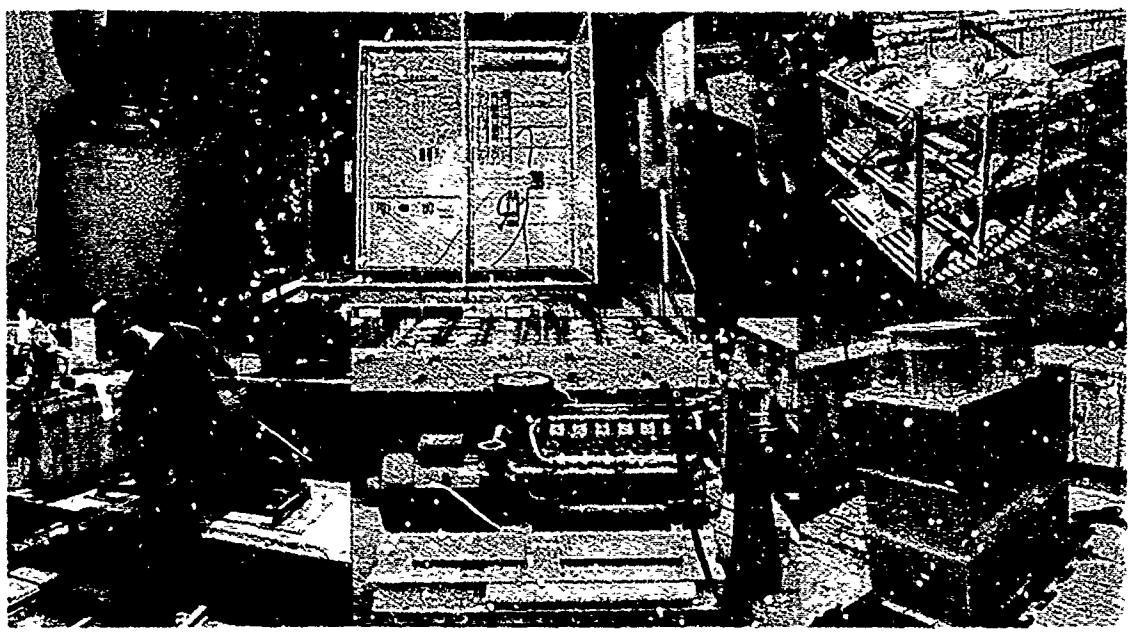

Fig. 2: Examples of shocktested equipment: gas filter, electric panel, bunks, ventilator, emergency generator set, air-conditioning unit

TEST PROCEDURE

More than 1000 different objects, e.g. gas filters, ventilating units, pumps, emergency generator sets, installations for communication, medical service installations etc. (Fig. 2), have been shocktested in the past 20 years [7,8].

The test objects are submitted to a shock according to the criteria defined above in each of the three main axes in the positive as well as in the negative sense. The resulting six shocks have to be within a tolerance field of ± 20 % of the nominal value (a_{max}, v_{max}, d_{max}). Whenever possible, test objects are subjected to the shock in running or operating conditions. Usually a visual inspection of the test object after each shock and a more detailed inspection at the end of the test series provide enough insight into the response of the object. Structural failures and damages which have a negative effect on the function of the test object are not tolerated. Slight deformations without consequence for the function are usually accepted.

SHOCKTESTING FACILITIES

The NC-Laboratory disposes of two shocktesting machines, a third one will be set in operation in about two months.
The shocktesting machine shown in Fig. 3 is constructed for test objects up to 3 tons. The shocks can be carried out in two directions.

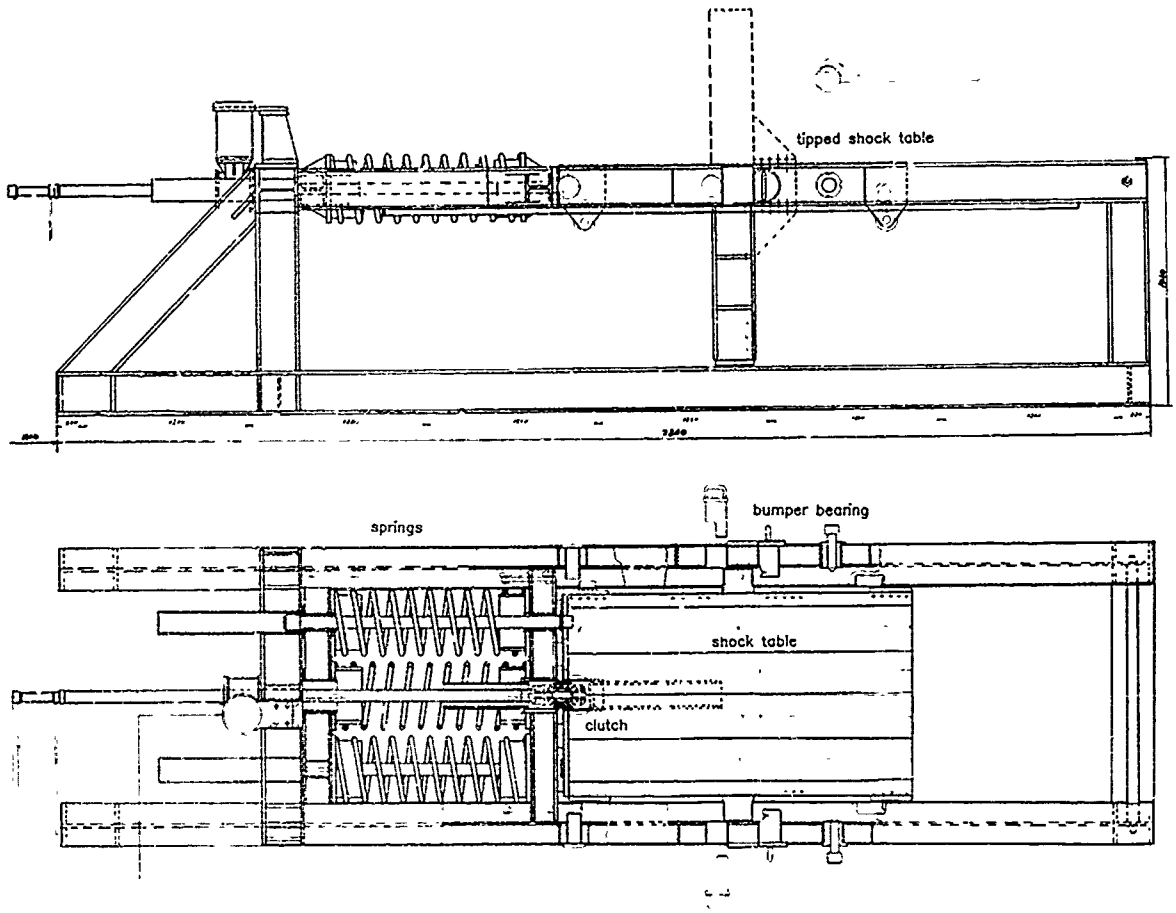

Technical data

dimensions of the shock table	:	1.25 x 2.50 m
maximum mass of test object	:	3000 kg
acceleration range	:	5 - 30 kg
maximum velocity of the table	:	without test object: 6.3 m/s with 3t-test object: 3.5 m/s
spring force	:	80 kN

Fig. 3: 3t-shocktesting machine

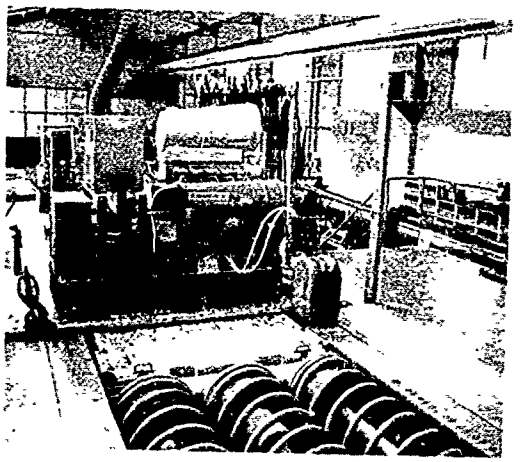

Fig. 4: 3t-shocktesting machine with an emergency generator set as test object

Fig. 5: 3t-shocktesting machine with tipped table

With this impact type device, which is used since 1968, the natural shock process is inverted, i.e. the shock table is decelerated instead of accelerated.

The test objects are usually robust, rigid and solidly fixed to the shock table. Considering futhermore that their response to the shock loading should remain in the elastic range, it can be assumed that this inversion does not falsify the test results.

The wheel mounted shock table travelling at the velocity according to the prescribed shocktesting criteria is abruptly decelerated by impacting on two copper bolts fixed to the two bumper bearings at the left and the right side of the machine. The plastic deformation of the copper bolts gives the desired acceleration time function of the shock table whereon the test object is fixed with regular steel bolts.
The necessary energy for the motion of the shock table is produced by releasing compressed tension springs.
The shape and the amplitude of the applied acceleration time function on the shock table are influenced by the dimensions of the copper bolts and by the compression of the springs.
The 2.5 x 1.25 m shock table can be turned about 90 ° for the tests in a "pseudo" vertical axis (Figs. 4, 5).

For large and heavy equipment up to 12 tons the shocktesting machine shown in Fig. 6 is used. It consists of an inclined ramp with a length of 28 m and a width of 7 m. Therein a concrete shock table (5 x 5 m, 18 tons) and a concrete bump truck (6 x 3 m, 40 tons) are placed.

Both shock table and bump truck are seated on eight special rollers (Fig. 8), which move on rails fixed to the ramp. Another four rollers, two on the left and two on the right side, are mounted on the shock table and on the bump truck to secure the side-guidance.
Futhermore, the shock table and the bump truck are equipped with two special brake elements (Fig. 8). These brake elements are opened hydraulically and closed by spring tension.

The shocks can be carried out by the crashing of the free moving shock table against the bumper bearing at the end of the ramp, or by the crashing of the free rolling bump truck in the unbraked but stillstanding shock table. So the simulation of both the inverted and the natural shock loading is possible. The end of the ramp as well as the bump truck are equipped with special steel tubes which are plastically deformed by the process of impaction (Fig. 9).

The control of the correct opening and closing of the brake elements is made electronically.
For the positioning of the shock table and the bump truck a winch is at disposal.
Because shocktesting on this testing machine is only possible in the horizontal axes, the shocks of heavy equipment in the vertical axis have to be simulated by fall tests which are again inverted shocks because in reality the air-slap loading would induce a transient downmotion of the shelter.

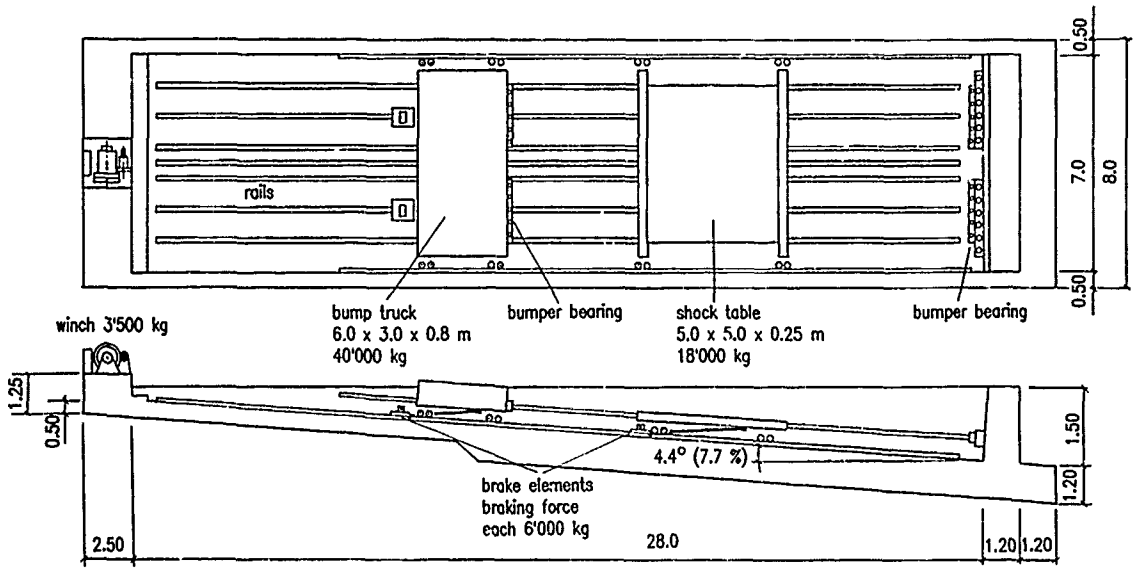

Technical data

dimensions of the ramp	:	28 x 7 m, incline 4.4 ° (7.7 %)
dimensions of the shock table	:	5 x 5 x 0.2 m, 18'000 kg
dimensions of the bump truck	:	6 x 3 x 0.8 m, 40'000 kg
maximum mass of test object	:	12'000 kg
acceleration range	:	5 - 30 g

Fig. 6: 12t-shocktesting machine, horizontal

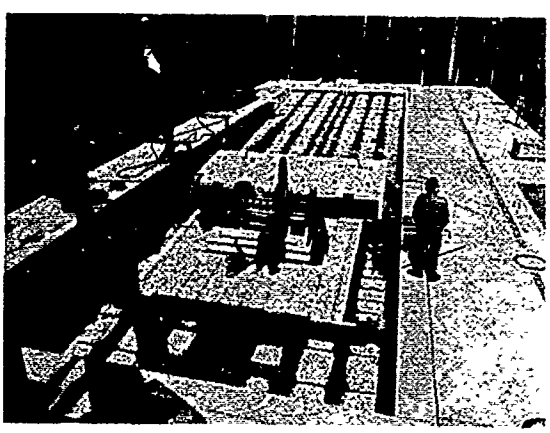

Fig. 7: 12t-shocktesting machine with test object

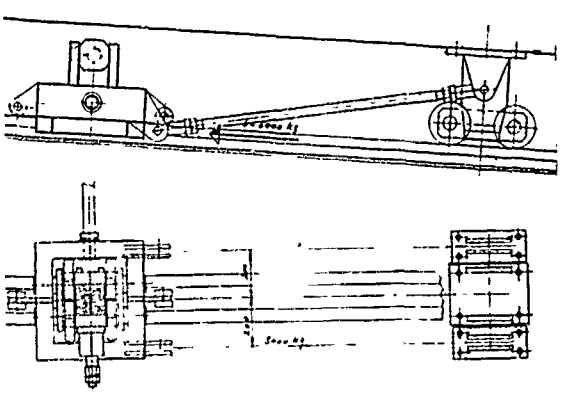

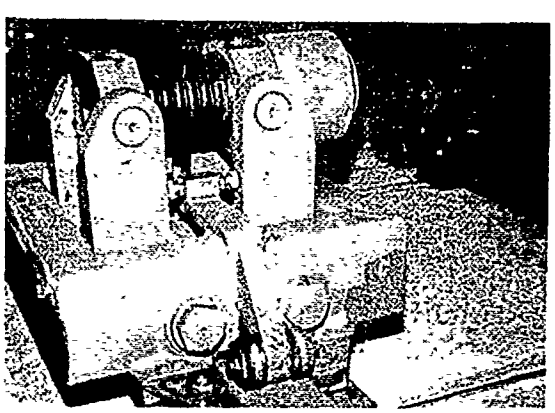

Fig. 8: Roller and brake element of the 12t-shocktesting machine

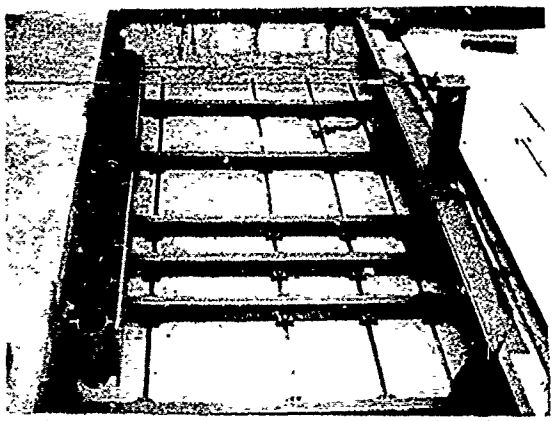

Fig. 9: Steel tubes used as bumper bearing

At the end of this year, a new vertical shocktesting machine for objects up to 12 tons will be set in operation. This fully hydraulically driven shock machine shown in Fig. 10 signifies a real and tremendous improvement in the shock testing facilities at the NC-Laboratory Spiez.
The new machine will not only allow us to simulate air-slap but also such other components of the nuclear ground shock as the long duration but low levelled earthquake-like ground roll motion.
With full control of the shockmotion it will be further possible to realize the test conditions for a new probabilistic shocktesting concept developed at our Laboratory, too [3,4,5,6].
For each test the test object will be exposed to a different stochastically generated representative shock motion and the final test result being then a concrete statement for the probability of failure for any kind of nuclear shock loading.
The simulation of strong earthquake motion will also be possible. This shock machine consists of a steel shock table (6 x 4 m), a special guiding construction and a hydraulic cylinder which is equipped with two specially designed servovalves (nominal flowrate 300 l/s) and pressure reservoirs, four for the high pressure (100 l, 330 bar) and four for the low pressure (100 l, 300 bar).

A possible eccentric loading of the shock table is taken over by a built-in torsional tube. With the slanting ($\approx 5^\circ$ from vertical) installation of the hydraulic cylinder the radial forces in the bearings of the piston rod can be reduced. The piston with a diameter of 480 mm has a stroke of 475 mm. The shocks according to the test criteria mentionned earlier can be carried out in both the positive and the negative senses of the vertical axes.

MEASURING EQUIPMENT

In "routine" tests only the motion of the shock table is measured with piezoelectric acceleration transducers, this mainly in order to control loading level and reproducibility. As Fig. 11 shows, the signal from the acceleration transducer is amplified, filtered and then recorded and analysed by a PDP 11/34 computer. If more information is needed, e.g. the response of some parts of the tested object, up to twelve acceleration transducers can be installed. At the end of this year, the PDP 11/34 computer will be extended to a 11/84, so that it will not only be able to record and analyse the measuring data but also to take the steering and the control of the new vertical shocktesting machine. For the calibration of the acceleration transducers a special device has been developed and is now on trial. With this calibration device the acceleration-time-function and independent of it also the displacement-time-function are recorded and compared, so it is not dependent on a reference transducer.

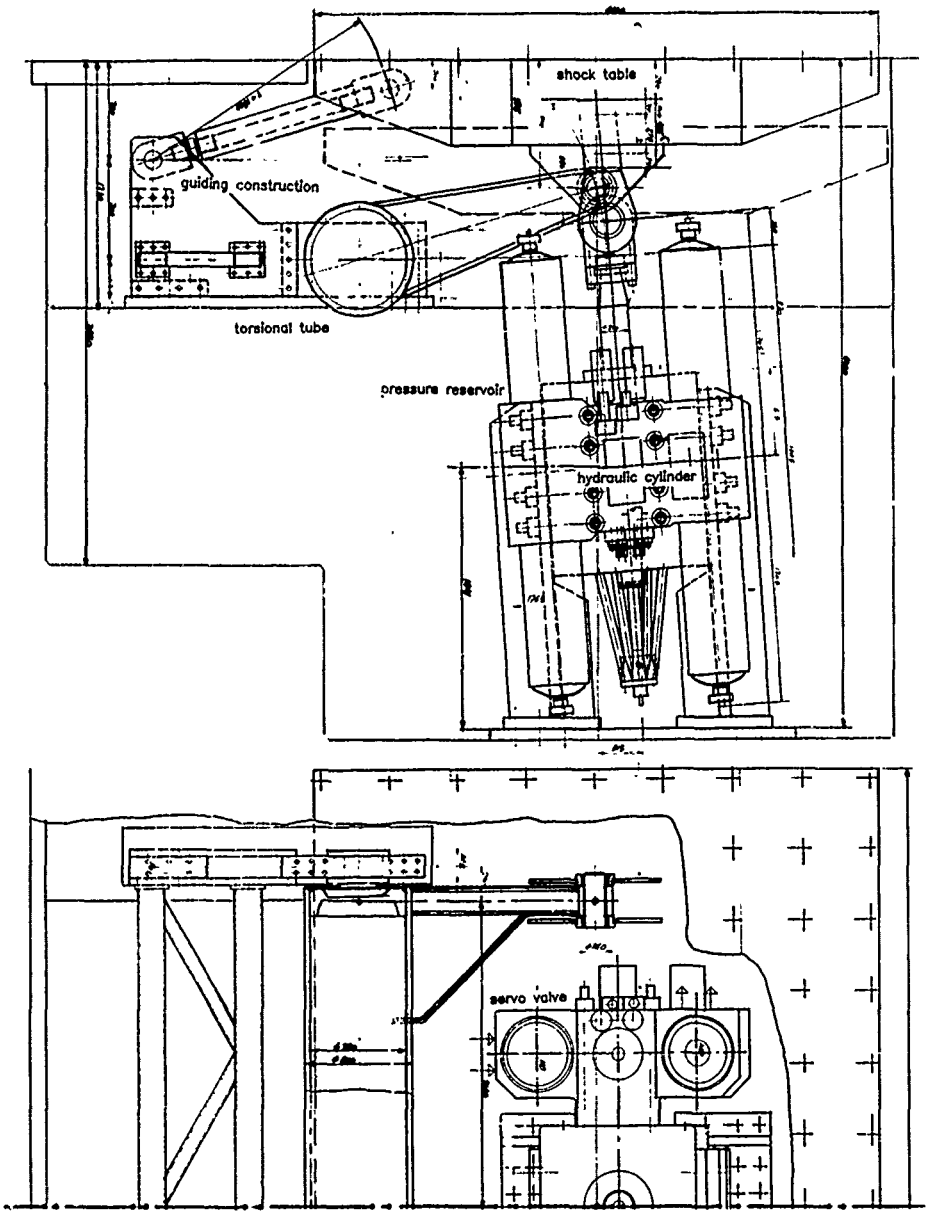

Technical data

dimensions of the shock table		:	6.1 x 4.1 m
maximum mass of test object		:	12'000 kg
maximum velocity of the table		:	± 2.0 m/s
acceleration range		:	± < 1 - 20 g
stroke		:	475 mm
servo valves:	nominal flow rate	:	300 l/s (p = 70 bar)
	nominal pressure	:	210 bar
pressure reservoirs:	high pressure	:	4 x 100 l, 330 bar
	low pressure	:	4 x 100 l, 300 bar

Fig. 10: 12t-shocktesting machine, vertical

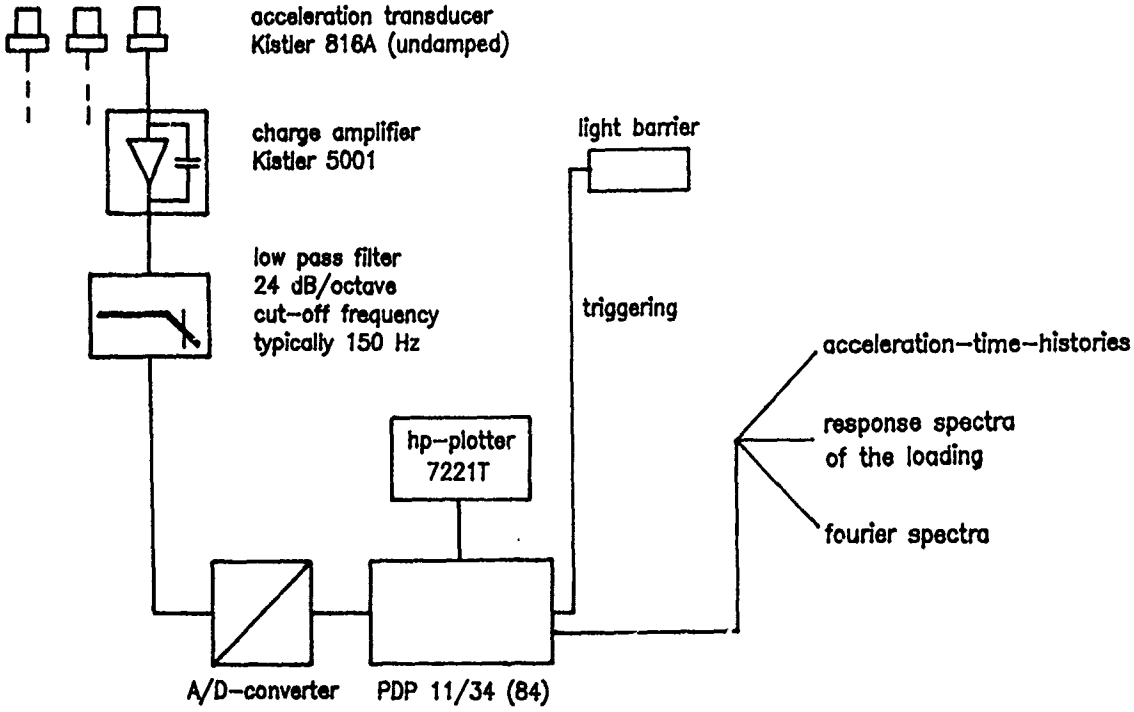

Fig. 11: Measuring equipment

CONCLUDING REMARKS

Among the full range of testing acitivites going on at the NC-Laboratory Spiez this paper has concentrated only on the practical part of shocktesting while others as well as the unavoidable paper work and administrative procedures have been left aside.
Successful implementation of shock tested equipment in Swiss civil defense shelters depends on well coordinated efforts by many institutions and bodies: Private manufacturers work closely together with our Laboratory and the Office of Civil Defense or military authorities, to place a variety of well suited equipment at the disposal of architects and civil engineers who in turn are responsible for the shelter design and construction according to regulations. Implementation by reliable contractors with their well trained craftsmen and final acceptance inspection are concluding steps in a long chain of events in order to provide a reliable protection against the ground shock loading induced by nuclear explosions.

ACKNOWLEDGEMENTS

The author would like to thank Bernard ANET, Erwin KESSLER and George McCALL for their valuable assistance by preparing this paper.

REFERENCES

[1] Bauer, R. and Binggeli, P.
Testing facilities for Civil and Military NBC-Shelter Equipment in Switzerland
NC-Laboratory, 3700 Spiez, Switzerland

[2] Schweizerischer Bundesrat
Bundesgesetz über die baulichen Massnahmen im Zivilschutz
15 May 1964, Bern, Switzerland

[3] Kessler, E.
Stochastische Simulation von Schutzraumerschütterungen infolge von Nuklearexplosionen
NC-Laboratory, 3700 Spiez, 1985

[4] Kessler, E.
Stochastic Simulation of Shelter Equipment Vibrations due to Nuclear Explosions
MABS 8, 1983

[5] Kessler, E.; Anet, B.; Hunziker, P.
Statistics of Stochastic Shelter Shock Motions induced by Nuclear Explosions
MABS 9, 1985

[6] Kessler, E.
Erschütterung von 3 bar und 1 bar Schutzbauten in Lockergestein infolge Nuklearexplosionen
Statistische Auswertung stochastisch generierter Erschütterungs-Zeit-Funktionen
NC-Laboratory, 3700 Spiez, 1984

[7] Anet, B.
Die Schockbelastung von Schutzbauten und deren Simulation für die Schockprüfung von Schutzbaueinrichtungen
NC-Laboratory, 3700 Spiez, 1982

[8] Anet, B.; Hunziker, P.
Schockprüfung von Schutzbaueinrichtungen für den Zivilschutz und für die Armee in der Schweiz
VDI Bericht Nr. 355, 1979

[9] TWP 1966
Technical Directives for the Construction of Private Air Raid Shelters
Swiss Federal Office of Civil Defense, 3000 Bern

[10] TWO 1977
Technische Weisungen für die Schutzanlagen der Organisation und des Sanitätsdienstes
Swiss Federal Office of Civil Defense, 3000 Bern

[11] TW Schocksicherheit 1980
Technical Directives for the Shock Resistance of Equipment for Swiss Civil Defense Shelters
Swiss Federal Office of Civil Defense, 3000 Bern

SHOCK TESTS OF CONCRETE ANCHOR BOLTS FOR SHOCK RESISTANT APPLICATIONS IN PROTECTIVE STRUCTURES

P. Hunziker
Defense Technology and Procurement Group. NC-Laboratory Spiez
Spiez, Switzerland

Since many pieces of equipment are fixed to concrete walls, ceilings and floors of the shelter by means of concrete anchor bolts, special investigations have been started to obtain more insight into the dynamic behaviour of such fixing elements, specially emphasizing their behaviour in cracked concrete and under shock loading. An anchor shock testing machine, in principle a "fall" machine, is used for testing such effects. The dynamic loading of the tested anchor and its slip are measured in each test. Nine of twenty different anchor products, tested in the past ten years, could be approved and are now allowed to be used as fastenings for shock resistant equipment in protective structures.

INTRODUCTION

The object of this paper is to give a survey of the techniques and testing methods used in Switzerland to investigate the shock behaviour of concrete anchor bolts used as mechanical fasteners for shelter equipment. According to the current design criteria all kind of equipment, installed in civil defense structures and military fortifications in Switzerland have among other things to withstand the ground shock loading induced by a nuclear explosion. Therefore this shelter equipment is systematically shocktested in a set of thorough examinations. However, the desired shock reliability of the equipment is only relevant if its attachments withstand the ground shock loading too.

Since many pieces of equipment are fixed to concrete walls, ceilings and floors of the shelter by means of concrete anchor bolts, special investigations have been started to obtain more insight into the dynamic behaviour of such fixing elements.
According to the Technical Directives of the Shock Resistance of Equipment in Civil Defense Structures the shelter will experience a shock loading mainly determined by the so-called airslap, the loading component directly induced by the air-blast. The resulting strong but relatively short motion of the shelter is transmitted to its equipment.

As at the designed load, corresponding to 1 resp. 3 bar peak overpressure of the blast at shelter location, the structure is supposed to show some degree of plastic deformation, say cracks, the behaviour of the fastening elements, once fixed to the uncracked concrete is of primary importance.
The significance of our efforts in the field of shock resistant fastenings becomes quite clear, if one takes into account that only in the field of civil defense every day about 1000 new shelter places are installed in our small country. These shelter places offer protection against a 1 bar peak overpressure blast and the related effects of a nuclear explosion in the MT-range in addition to a full C-protection.

The kind of shelter equipment considered in this paper ranges from a simple ventilating system of a private shelter to an operating theatre of a medical station.

ANCHOR WORKING PRINCIPLES

Anchors were already known as a means of fastenings in ancient times. In the famous ruins of the Roman Colosseum the holes for the anchors that held the marble cladding are unmistakable, even today.
Despite in fact that anchors have been in use

much longer than screws, only screws are accepted widely as an engineering fixing agent: the concrete anchor is even today in many cases derided and called an instrument for hobbyists. Nevertheless in recent years, anchor bolts have been developed in a way that meets many of the requirements of the fastening technology in engineering. [2]

According to the current level of technology, anchors can be differentiated according to their working principles. [1, 3, 4]

A. Metal anchors with automatic expansion by the controlled application of force.

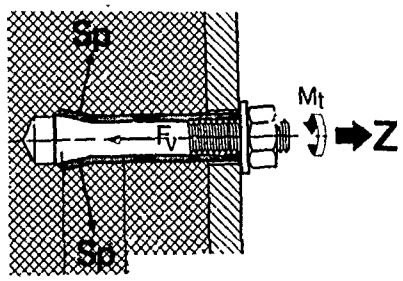

Fig. 1: Heavy-duty anchor

The torque (Mt) applied to tighten the nut produces a tensioning force (Fv) which presses the cone and expansion sleeve against the base material. On applying a tensile load (Z), the expansion pressure (sp) and thus also the holding power are increased (follow-up expansion principle) as soon as Z becomes larger than Fv.

B. Metal anchor with automatic expansion over a defined distance.

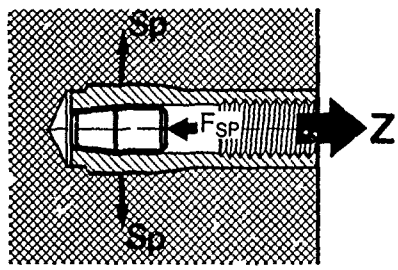

Fig. 2: Drive-in anchor

An expansion plug is driven into an anchor body with an impact force (Fsp).
The distance travelled by the plug is a good measure for controlling the amount of expansion.
An applied tensile load (Z) does not alter the degree of expansion of the anchor body.

C. Undercut anchor

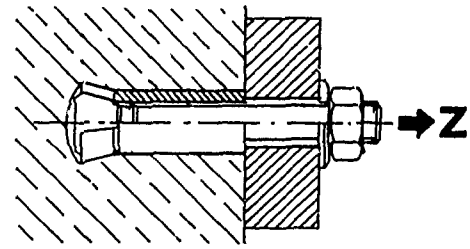

Fig. 3: Undercut anchor

This type of anchor usually requires a second drilling operation to create an undercut at or near the bottom of the drill-hole. It is anchored in the undercut of the drill-hole by hammering an expansion sleeve on to a cone-bolt.
An applied tensile load(Z) is transferred through direct bearing between the sleeve and the conical undercut in the concrete.

D. Plastic anchors

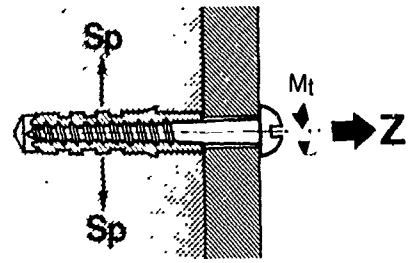

Fig. 4: Plastic anchor

On tapping in a drive screw, pin etc. or screwing in a woodscrew etc. the plastic anchor body is forced apart and pressed against the hole wall. In this way there is not only the expansion pressure (sp) but also a keying effect, and the two resist the applied tensile load (Z).

E. Adesive anchors

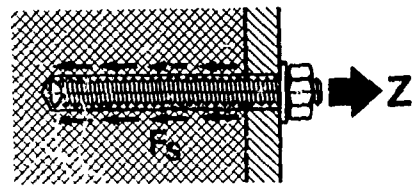

Fig. 5: Adhesive anchor

An anchor rod is driven into a hole filled with adhesive mortar (polyester resin or cement basis). The bond between the anchor rod and adhesive mortar, on the one hand, and between the adhesive mortar and the concrete, on the other, resists the applied tensile load (Z).

ANCHOR TESTING

Today the approval of the Institute of Building Technology Berlin (IfBT) is one of the most important certificates of quality for the static behaviour of concrete anchor bolts for loadbearing fastenings. [6]

In this certificate of approval (Fig. 6), the safe working loads (Psw), with a safety factor of 3, the depths of embedment (T), the distances between anchors (A) and from edges (R) are authoritatively fixed, while the constructive applications and the setting operations are clearly defined. This Berlin-approval represents the basis for the dynamic tests (shock loading) of the anchors carried out at our laboratory.

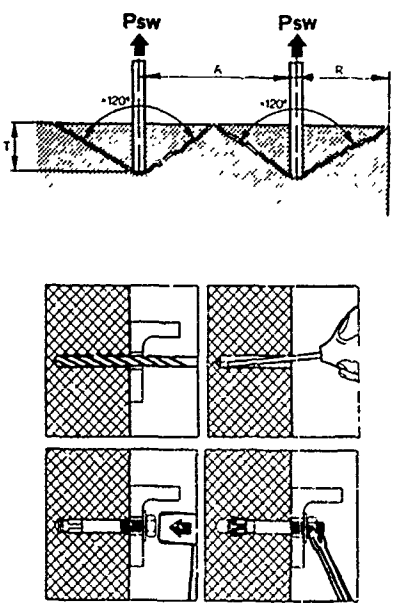

Fig. 6: Specifications of the Berlin-approval

For anchors which are approved by the IfBt or which are in possession of an equivalent certificate, the manufacturer can apply for approval from the Swiss Federal Office of Civil Defense (FOCD) if he intends to use his anchors in protective structures.

Here the FOCD arranges a suitability-trial based on additional tests to investigate the dynamic behaviour of the anchors in cracked concrete and under shock loading [5]. As already mentionned in the introduction these tests are carried out in cracked concrete as the Swiss design criteria for shelters allow for economical reason some degree of nonelastic loading, that means cracking, at the design load (1 resp. 3 bar peak overpressure of the blastwave at shelter location).

SHOCK TEST AND MEASURING EQUIPMENT

A simple fall machine is used to simulate the representative part, the air-slap, of the ground shock (Fig. 7).

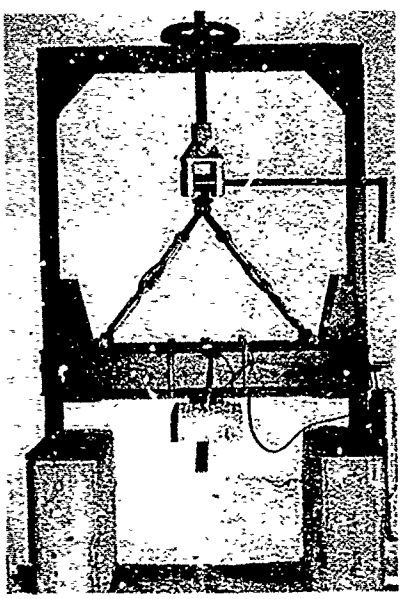

Fig. 7: Anchor shocktesting machine

In this anchor shocktesting machine a concrete body is fixed to the cross beam by means of the anchor which is to be tested. The cross beam hangs on a special release mechanism and its fall height is adjustable.
After releasing the cross beam falls down and is abruptly decelerated by impacting on two pieces of horizontally lying steel tubes, whose plastic deformation produces the desired acceleration-time function (Fig. 8), which has to be matched to the prescribed test criteria for Swiss civil defense shelter equipment (max. acceleration $a_{max} = 160\ m/s^2$; max. velocity $v_{max} = 1.6\ m/s$; max. displacement $d_{max} = 0.25\ m$).

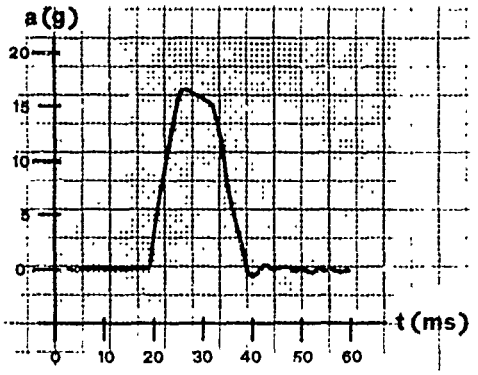

Fig. 8: Acceleration-time function

With the impact of the cross beam on the steel tubes the inertial force of the concrete body produces a dynamic tensile loading of the anchor. Thereby the mass of the concrete test body has to be chosen so that its multiplication with the max. acceleration (160 m/s^2) gives the safe working load of the tested anchor.

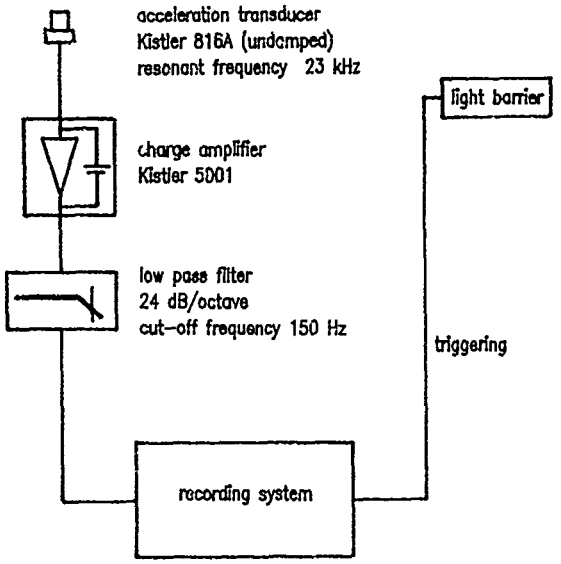

Fig. 9: Measuring equipment

In each test, the motion of the cross beam is measured with piezo-electric acceleration transducers. The measuring equipment is shown in Fig. 9. The slip (the amount of withdrawal from the cracked concrete) of the anchor is measured after each shock with a depth gauge.

TEST DESCRIPTION

At first the hole for the anchor which will be tested is drilled in the middle of the surface of the reinforced concrete body which is made of dense concrete with a characteristic strength of 30 N/mm^2. After cleaning the hole of bore dust, the anchor can be set and tightened to the necessary torque (Fig. 10).

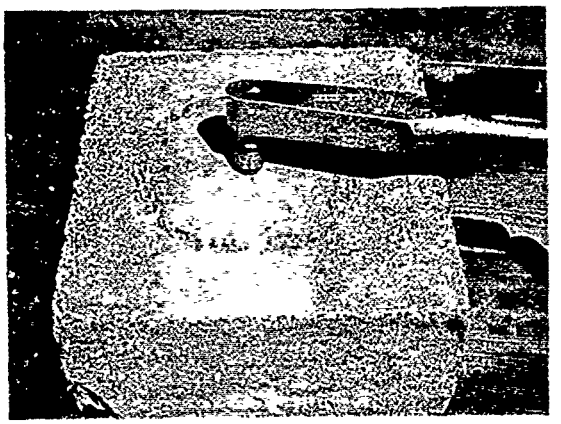

Fig. 10: Tightening of the concrete anchor bolt

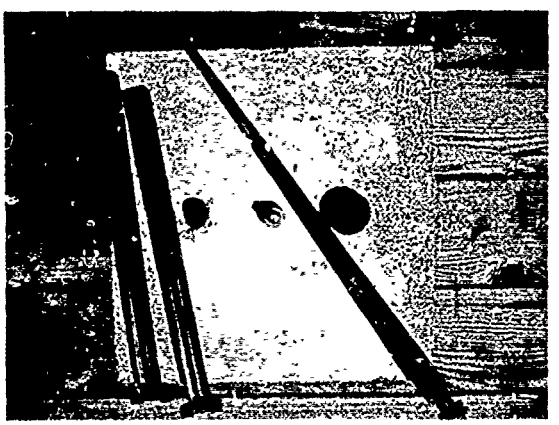

Fig. 11: Setting of the guiding sleeves for the wedges

After that, the holes (ø 25 mm) for the guiding sleeves of the wedges, used to produce the crack, are drilled besides the anchor. Afterwards the guiding sleeves are set in these holes and then special wedges are hammered into the sleeves (Fig. 11, 12). Thereby the concrete

test body cracks. Because of the special design of the wedges, the produced crack becomes parallel and leads through the anchor-hole. The crack will be opened until its width reaches 1.0 mm over the whole height of the test body (Fig. 13).

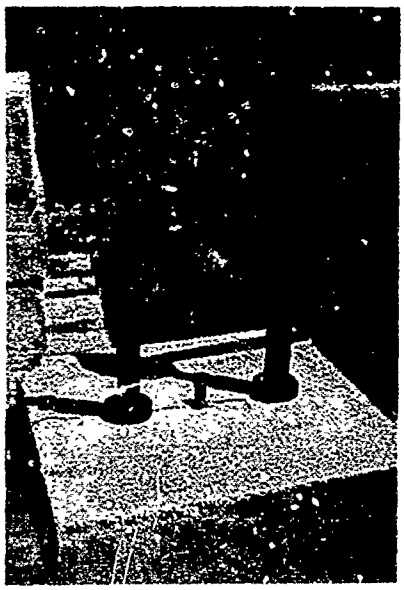

Fig. 12: The crack is produced by hammering the wedges into the guiding sleeves

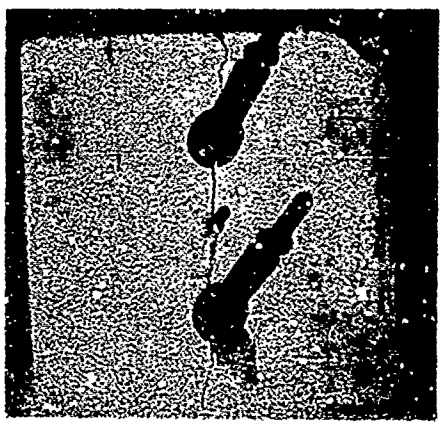

Fig. 13: The 1 mm crack leads through the anchor hole

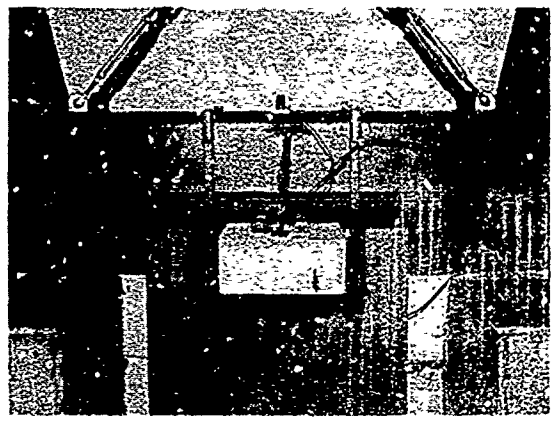

Fig. 14: The concrete body is fixed to the crossbeam of the test machine

The testbody is now fixed to cross beam of the shock machine by means of the anchor, without tightening the anchorscrew anymore (Fig. 14). This is to simulate the real condition, where the cracking of the concrete occurs after setting and tightening the anchor bolt.
Each tested anchor has to withstand two successive shocks with a dynamic tensile loading up to the static safe working load. The total slip ($slip_{1.\ shock} + slip_{2.\ shock}$) after the two shocks ought not to be more than 5.0 mm, whereby a probability of failure of about 20 percent is allowed, otherwise the anchor type cannot be approved by the FOCD.
Usually 15 to 25 anchors of the sizes M6 or M8 and M10 or M12 of each product are tested.

TEST RESULTS

In the last eight years, twenty different anchor products have been tested, whereby nine products could be approved by the FOCD. In this chapter the typical test results of some anchors are introduced.

Fig. 15 shows the test results of a heavy-duty anchor which is a typical representative of the metal anchors with automatic expansion by the controlled application of force (Fig. 1). As an example, the first and the second shock of each tested anchor are marked in this figure. On applying a tensile load, the expansion pressure and thus the holding power of this type of anchor increases (follow-up expansion principle). The safe working load of the tested heavy-duty anchor M8 was 4.3 kN. The applied dynamic load is scattered because it is difficult to obtain precisely the design load with this type of shock machine.

The test results show that 12 tests with a dynamic tensile loading in the range of the safe working load and 14 tests in the range of double the safe working load were carried out. The latter were carried out to investigate the sensitivity of the anchor to test conditions which deviate from the usual.

The test results show that the slip at the lower loading range lay after the first shock between 0.3 and 5.0 mm and after the second shock between 0.1 and 1.7 mm. In the test series at the upper loading range the slip lay after the first shock between 1.5 and 6.2 mm and after the second shock between 0.4 and 3.6 mm.
This heavy-duty anchor could be approved by the FOCD, whereby it is allowed to be used up to the safe working load. Its use up to the double safe working load could not be approved because the probability of failure was higher than 20 %.

These results demonstrate conspicuously the follow-up expansion principle of this type of anchor. The slip after the second shock is significantally smaller than after the first one.

So far all of the 7 tested heavy-duty anchor products have shown similar results as presented here and all of them could be approved by the FOCD.

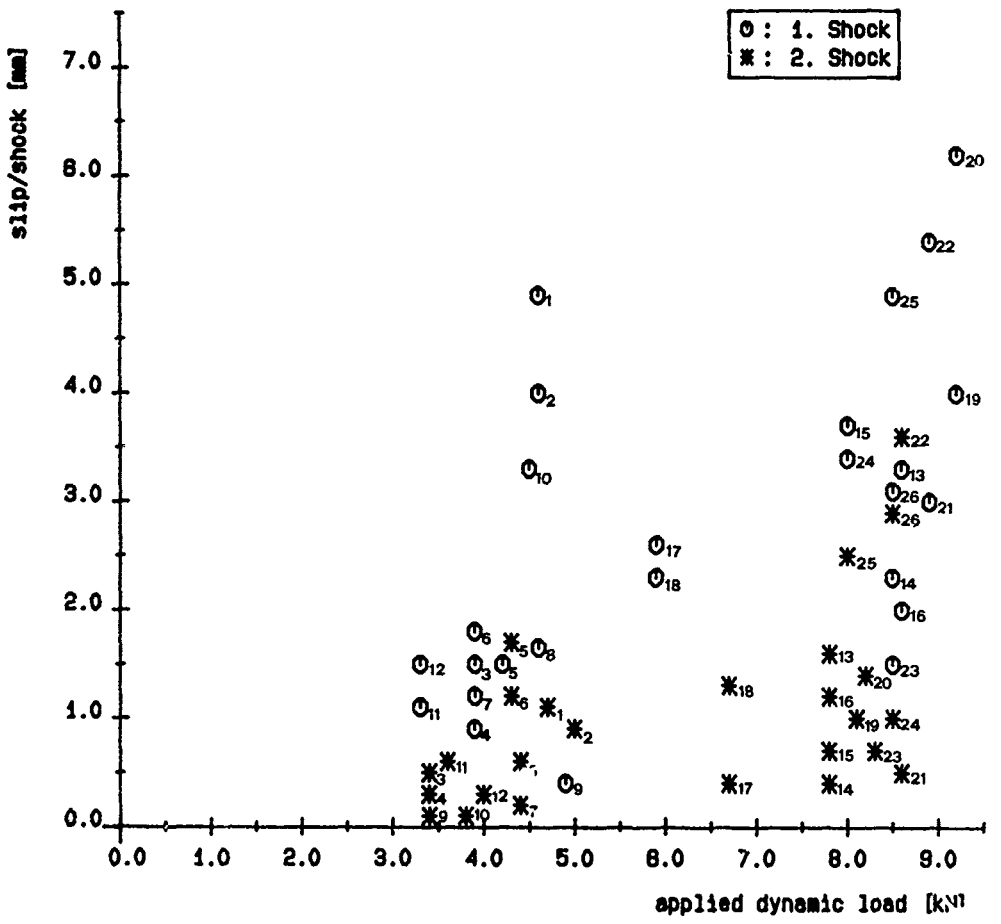

Fig. 15: Test results heavy-duty anchor M8

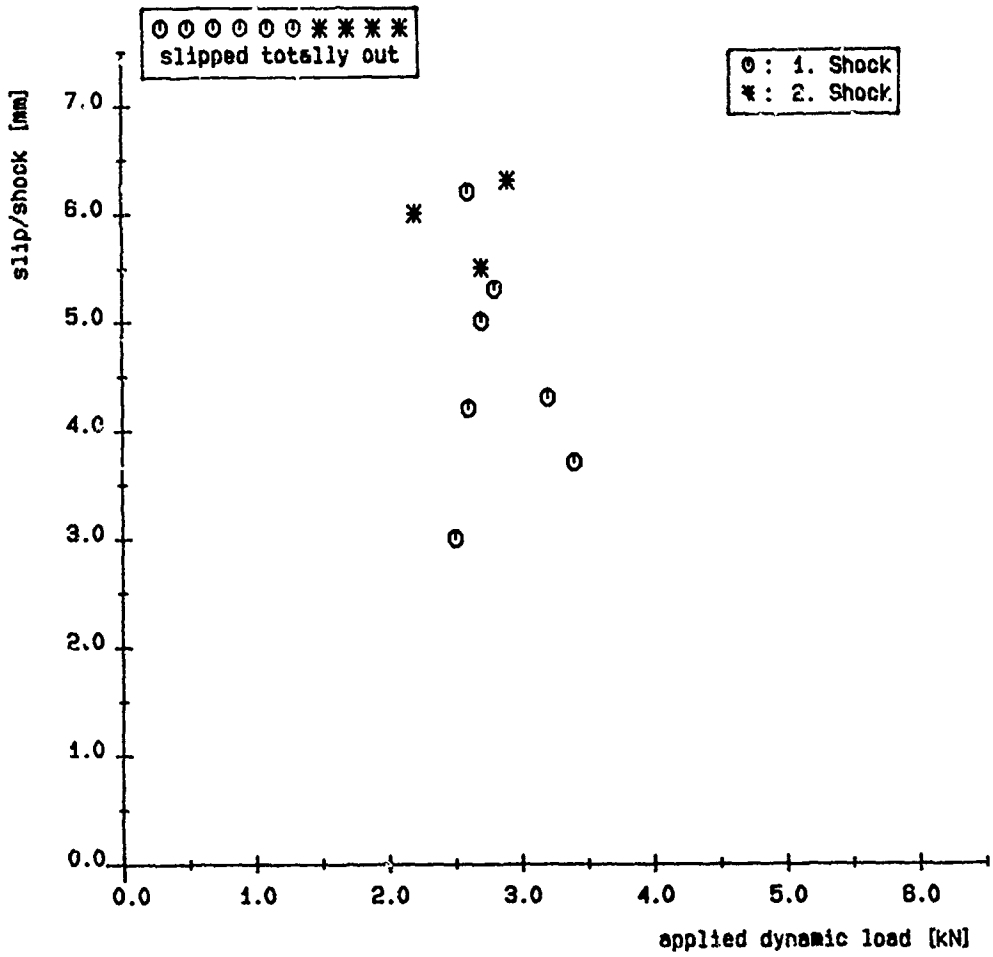

Fig. 16: Test results drive-in anchor M8

Fig. 16 shows the test results of a drive-in anchor, which is a metal anchor with automatic expansion over a defined distance (Fig. 2). The safe working load of the tested drive-in anchor M8 was 3.0 kN. The test results show that nearly 50 percent of the tested anchors slipped out totally of their holes during the first shock. The slip of the other 50 percent lay between 3.0 and 6.2 mm. During the second shock 60 percent of the rest slipped out totally and the remaining three anchors slipped between 5.5 and 6.3 mm. The drive-in anchor could not be approved by the FOCD.
The test results prove that an anchor without the follow-up expansion principle can hardly withstand shocktesting in cracked concrete.

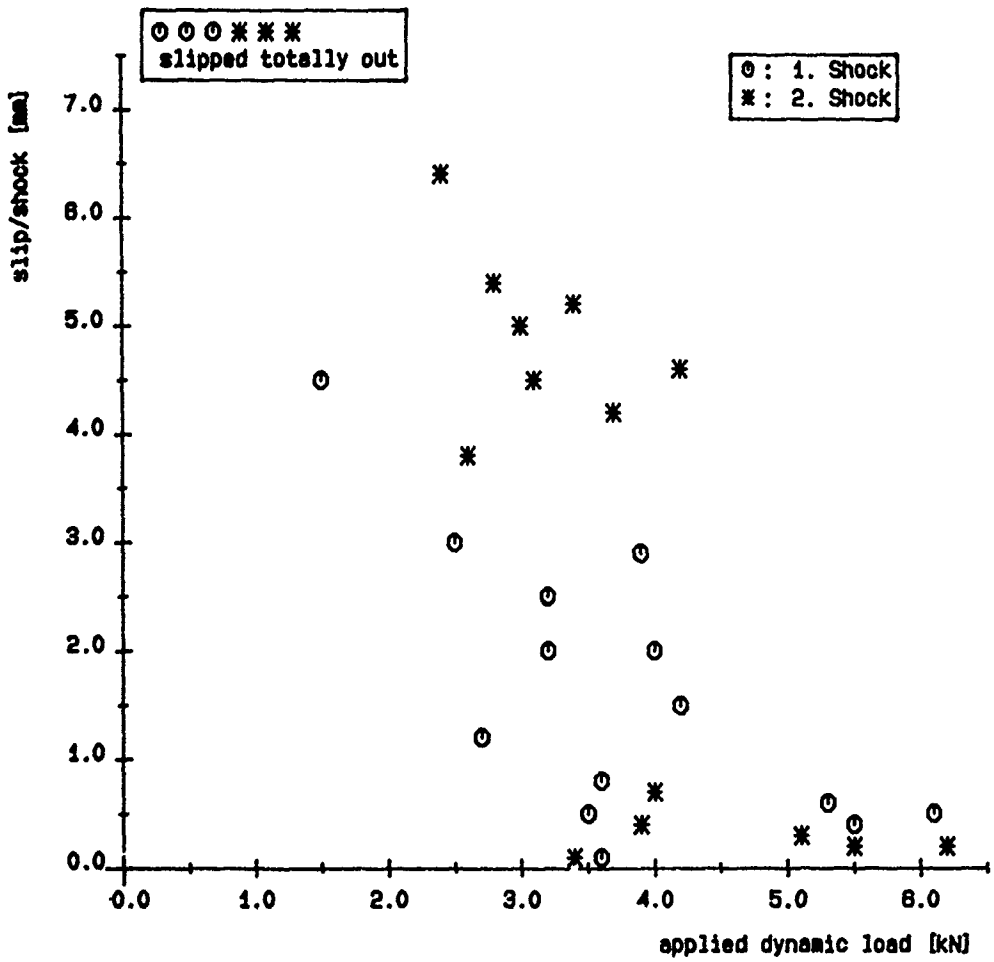

Fig. 17: Test results adhesive anchor M8

Fig. 17 shows the test results of an adhesive anchor (Fig. 3). The safe working load of the tested adhesive anchor M8 was 4.5 kN. The test results show that after the second shock the slip was mostly higher than after the first shock. It lay between 0.1 and 4.4 mm after the first and between 0.1 and 7.0 mm after the second shock. Three anchors during the first and another three during the second shock slipped out totally. Because of too much slip and because the slip was higher after the second shock (no follow-up expansion principle) than after the first, the adhesive anchor could not be approved by the FOCD.

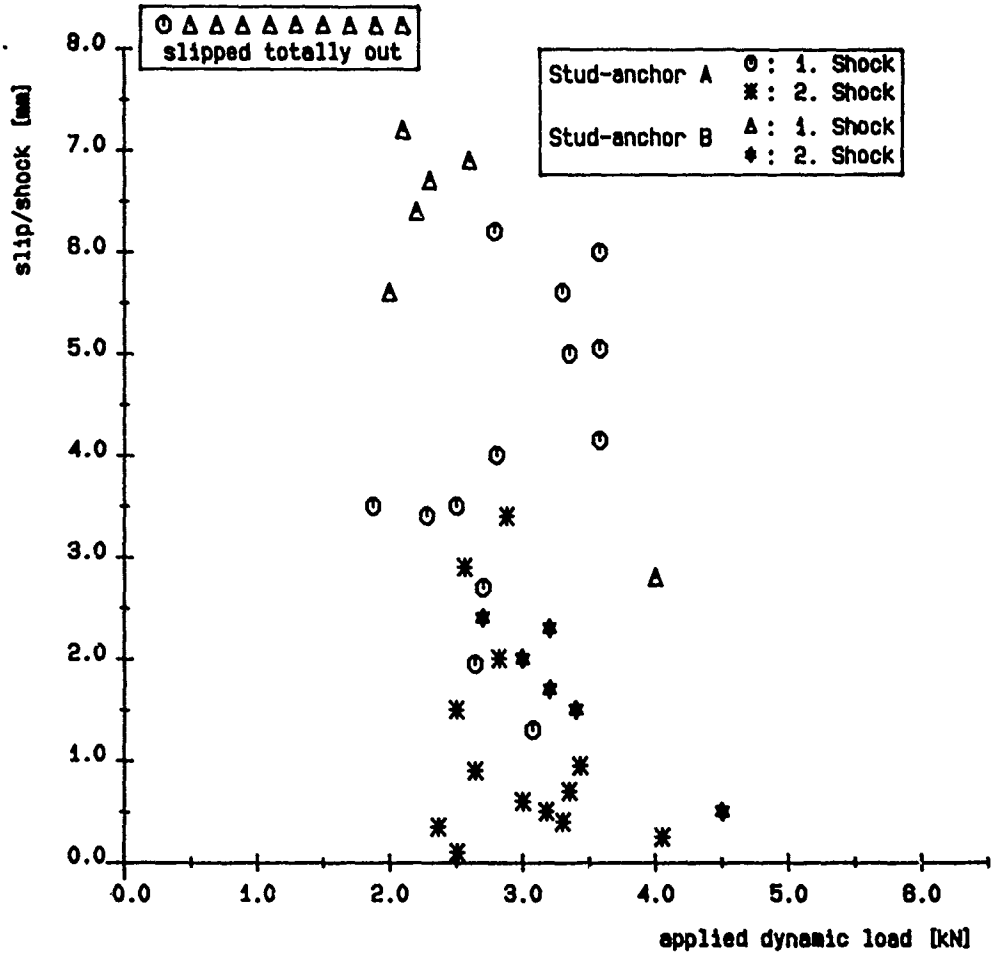

Fig. 18: Test results stud-anchor M8

Another type of metal anchor with automatic expansion by the controlled application of force is the stud-anchor.
Ten different stud-anchor products were tested in the last years and nevertheless the design distinguished only in details, the test results have differed in a broad range.

Fig. 18 shows the results of two of the tested stud-anchors M8 with the same safe working load of 2.8 kN.
The one slipped out during the first shock between 1.2 and 6.2 mm and during the second between 0.1 and 3.4 mm. One anchor slipped out totally. This product could be approved by the FOCD.

From the other product more than half of the tested anchors slipped out totally during the first shock. The slip of the rest lay between 2.8 and 7.3 mm after the first and between 0.5 and 2.4 mm after the second shock, so that this product could not be approved.
From all the tested stud-anchors only one product could be approved by the FOCD.

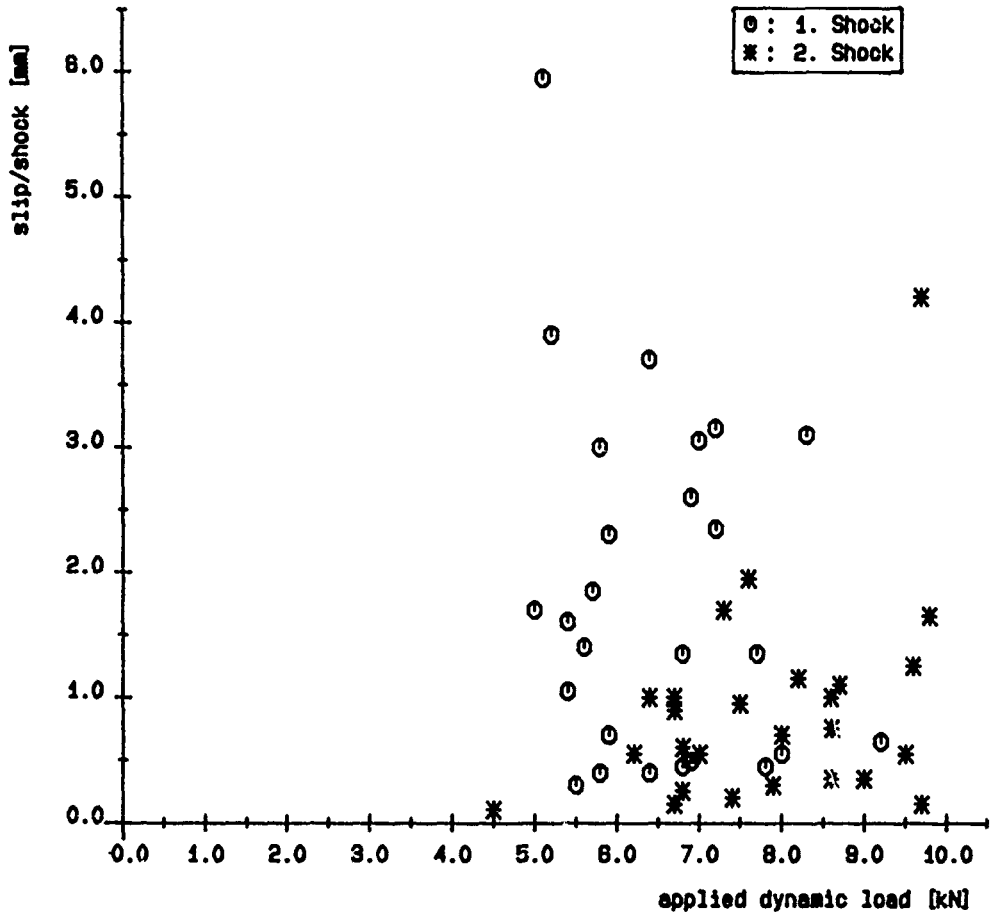

Fig. 19: Test results undercut anchor M6

Finally Fig. 19 shows the results of an undercut anchor. The safe working load of the tested undercut anchor M6 was 4.0 kN. The test results presented here show that this type of anchor can also withstand dynamic tensile loadings in the range of double the safe working load, whereby the slip after the first shock lay between 0.5 and 6.0 mm and after the second shock between 0 and 4.0 mm. This undercut anchor could be approved by the FOCD, whereby it is allowed to use it up to double the static safe working load.

ACUTAL PROBLEMS

TEST CRITERIONS

A decisive test criterion is the crack width in the concrete which has to be assumed for the anchor shocktesting.
There exist, to our knowledge, no investigations, neither about the maximum expected crack width nor about the crack frequency in protective strutures under the conditions of a nuclear ground shock as considered here and especially not for the particular design of the standardized Swiss shelters.
The crack width used in the current test criteria have been partly determinated by evaluating cracks in concrete buildings after a strong earthquake loading (e.g. Italy 1980).
Nevertheless anchor shocktestings carried out in the last years have shown that a more precise investigation of the crack width is urgent. So some further investigations have been started to get more insight into these problems.

PRACTICAL APPLICATIONS IN PROTECTIVE STRUCTURES

In the use of concrete anchors in protective structures some practical problems can occur. For example, reinforcement makes it difficult for the hole to be drilled if the bit strikes the steel. For that reason it is recommended to use diamond core bits which cut a cylindrical hole straight through the concrete and the metal.

Another important problem is the distance between anchors. These distances defined in the IfBT-approval are very large: for example for a heavy-duty anchor M12, a distance between anchors of 600 mm is prescribed. In practice these large distances often lead to problems. For that reason several types of anchors have been shock tested with a reduced distance between anchors.

In these cases two anchors were set in the same crack with a distance between them of 2 x depth of embedment. For a heavy-duty anchor M12 a distance between anchors of 160 mm was tested. The test results showed neither a worse slip behaviour nor a reduction of the safe working load compared to the tests carried out with a single anchor. Therefore all anchors approved by the FOCD are allowed to be used with a minimum distance between anchors of 2 x depth of embedment without reduction of the safe working load.

At present the necessary quantity of anchors and the anchor sizes for a shock resistant fastening of equipment are calculated in a simple manner.

At the present some specially designed dynamometers are set in operation in order to determine the actual shock loading forces. The new dynamometers will allow us to measure the forces of each fixture point during the shocktesting of a piece of equipment, these loads being then used for the determination of the anchor type and size.

CONCLUDING REMARKS

The anchor shocktestings carried out have shown that not every concrete anchor bolt may be used as a fastening of shock resistant equipment in shock loaded protective structures. Only a few anchors offered on the market can withstand the severe ground shock loading due to nuclear explosions and are able to hold equipment in cracked concrete with crack widths up to 1.0 mm.

Since 1981, in Switzerland, only concrete anchor bolts which are approved by the FOCD are allowed to be used as fastenings for shock resistant equipment in protective structures.

The additional costs for the shock resistant fastening of the equipment are usually low, not more than 5 percent of the price of the equipment itself.

ACKNOWLEDGEMENTS

The author would like to thank Bernard Anet, Erwin Kessler and George McCall for their valuable assistance by preparing this paper.

REFERENCES

[1] Hilti AG, Schaan
Drilling and Anchoring Manual
Edition 5/81

[2] Seghezzi, H. and Vollmer, H.
Modern Anchorage Systems for Concrete Paper presented at the ACI-Symposium "Anchorage to Concrete", Atlanta, January 1982 (not published)

[3] Eligehausen, R. and Pusill-Wachtsmuth, P.
Stand der Befestigungstechnik im Stahlbetonbau
IABSE SURVEYS S-19/82
IABSE Periodica 1/1982, February 1982

[4] Eligehausen, R.
Anchorage to Concrete by Metallic Expansion Anchors
Paper presented at the ACI-Symposium "Anchorage to Concrete", Los Angeles, March 1983 (not published)

[5] Swiss Department of Justice and Police
Federal Office of Civil Defense
Technical Directives for the Shock-Resistance of Equipment in Civil Defense Structures

[6] Irstitute of Building Technology Berlin
Approvals of Concrete Anchor Bolts

MICROCOMPUTERS IN SHOCK TESTING OF WATER SATURATED SANDS

W.A. Charlie[1], H. Hassen[1], and D.O. Doehring[2]
[1]Department of Civil Engineering, Colorado State University
[2]Department of Earth Resources, Colorado State University
Fort Collins, Colorado

and

M.E. Hubert
Applied Research Associates, Inc.
South Royalton, Vermont

This paper summarizes the use of state-of-the-art, commercial "off-the-shelf" products currently being used at Colorado State University for sponsored research on the behavior of water saturated sands subjected to explosively induced shock loadings. The paper discusses the microcomputers (personal computers), the smart high speed digital Transient Data Recorders, (TDR's), software for data acquisition and analysis, and data flow and extension of IEEE 488 communication lines. As our microcomputer and TDR system now stands, we have 20 channels of TDR's with 32k bits memory per channel (expandable to 128k bits memory per channel). Each channel has a sampling rate of up to 500,000 samples per second and can have up to 16 changes of sampling rates during data acquisition. Our total investment for this system, which includes the microcomputer, 20 channels of high speed TDR's with 32k bits of memory per channel, software, cables, extenders, plotter and printer, is approximately $2,700 per channel. For an additional $300 per channel, this system can be upgraded to 128k bits of memory per channel.

INTRODUCTION

The use of microcomputer-controlled instrumentation for data acquisition and analysis has become increasingly popular for research and experiments involving large numbers of measurements and critical timing requirements. This trend will undoubtedly continue as the cost of microcomputers and reliable add-ons continue to decrease and as more engineers and researchers become familiar with personal computers.

Integration of the microcomputer with data acquisition units and off-the-shelf software packages are described for data acquisition, control and analysis. Our system is being used to monitor acceleration, water pressure, soil stress and strains of water saturated sands under explosive loadings. The basic concept of the system is presented as well as the hardware configuration and software use. The system is centered around an IBM PC-XT personal computer and a smart high speed digital Transient Data Recorders, TDR's. Peripheral equipment consists of printers, digital plotter, digital oscilloscopes, data flow and extension of IEEE-488 communication lines and signal conditioners. Data conversion and analysis is carried out through the use of commercially available non-dedicated software packages.

HARDWARE

Compatibility with hardware and software is very important in choosing microcomputers. Several custom systems are available with data acquisition systems which can support specific systems and needs. As shown in Figure 1, we chose to integrate an IBM compatible personal computer (PC) with our data acquisition system. Our personal computer (IBM PC-XT) is configured with 640k of random access memory (RAM), a 360k floppy disk drive and a high speed 10 MB hard disk. In addition to the color display monitor, the PC-XT is equipped with 8087 math coprocessor for faster computations. Two serial and three parallel ports for physical interface with peripherals and an IEEE-488 (GPIB) for interface with the TDR's are also part of the set up. Another microcomputer (portable Compaq PC) configured similar but without a hard disk is available for back up and for field use. The total system is portable, weighs under 50 kg, and can be operated at remote sites using a

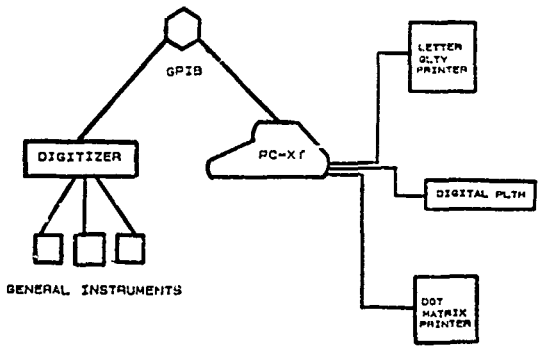

Figure 1. Hardware Arrangement

generator with the aid of an uninterruptible power supply equipped with power surge protectors and RMF/EMF noise filtering.

The Transient Data Recorder System (Pacific Instruments Model 9820) has 20 channels each consisting of a sample-and-hold amplifier, 12 bit analog-to-digital converter, control logic and 32k words of non-volatile complementary metal oxide silicon (CMOS) memory with battery back-up. The digitization of an incoming analog signal is done at a programmable sampling rate up to 500,000 samples per second and samples are stored in successive locations of memory. The sample rate may be programmed to change as memory is filled. Up to 15 rate changes are available. Either internal triggering, based on the level of the input analog signal or external triggering may be used. A calibration mode is available, which sets aside one segment of protected memory for calibration data. In pre-trigger operation the TDR continuously samples the analog input. Upon the receipt of a trigger command, the TDR takes a selected number of post-trigger samples. After acquisition of data is completed, the digital data may be transferred for processing at data transfer rates up to 500k bytes/second.

SOFTWARE

In developing software for a data acquisition system, one is faced with three major options. One can purchase a dedicated software package of defined scope with set but limited capabilities, develop a custom system which supports specific needs, or can integrate a series of the commercially available non-dedicated software packages into a flexible, user-defined tool. Custom programming, however, can be a very expensive option and the inflexibility of dedicated packages limits their utility. The combination of simplicity, power and flexibility of the non-dedicated package, makes them suitable and attractive application development tools. Without having to learn computer programming, the system user can quickly and easily acquire data; file data and manage the data base; manipulate, reduce, and analyze data; perform statistical analysis and curve-fitting operations; obtain and generate high quality technical reports with good quality plots integrated with the text.

Figure 2 shows our IBM compatible software set up. Currently a front end program, DEMOGPIB, (Pacific Instruments Inc.) is used to set up the TDR's and save the acquired data on the personal computer's hard disk. ASYST (MacMillan Software Company) is used for data management, analysis and plotting. Currently the ASYST version used with the system does not have some of the statistical functions and curve fitting that are needed for the research project and so it was decided to also use STATGRAPHICS (S.T.S.C., Inc.). The package has a large number of statistical and numerical functions and is used for nonlinear regression analysis and curve fitting. WORDMARC (MARC Software International, Inc.) is used for word processing. Note that several other IBM compatible software are also available with similar capabilities.

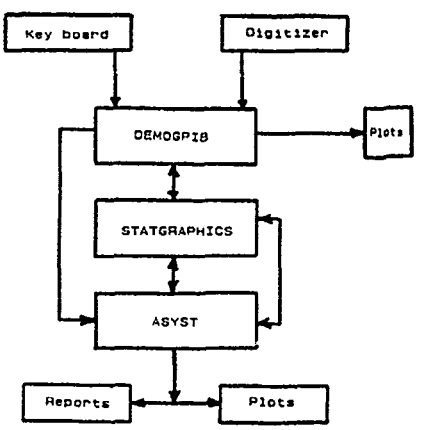

Figure 2. Typical Software Setup

SYSTEM CAPABILITIES, OPERATION AND APPLICATIONS

The system is adaptable to a wide range of experiments. However, the system is most suitable for dynamic, shock, and blast loadings tests. The main feature of this system is its capability of measuring the initial transient behavior as well as the late time response that is characteristic of some materials. This is true in the case of saturated sand being tested under shock and explosive loadings.

Figure 3 shows the menu the program uses for data acquisition. Up to 200 channels can be used simultaneously. The channels are programmed through the personal computer to acquire a certain number of data points at the specified sampling rate. The addressing scheme is flexible and allows programming by individual channel, rack or the whole system. For example, if all channels in a system were to be programmed to the same sample rate, the sample rate command and data would only be input once. In addition to interface control of data recording, a master ARM, master START and master TRIGGER provides means to initiate recording for all channels simultaneously and independent of the host computer. Data, then can either be plotted on the screen for any time interval desired, sent to a printer for a hard copy or saved on a disk for later use. After acquiring the data, the user may select one of the data reduction and data analysis options, then immediately begin working with the data. The user can integrate, differentiate or do fast fourier transforms of the data. The data can be displayed for revision, plotted on the screen or sent to the plotter for a permanent copy. Drafts of the final reports may be printed on the inexpensive dot-matrix printer. The final version then can be printed on a letter quality printer and pen plotter(Figure 4).

DISCUSSION AND CONCLUSIONS

The experience gained in the development and application of the system described above shows the commercially available, off-the-shelf software packages to be tools of tremendous potential for use in data acquisition and analysis. The programmability, flexibility and versatility provided by some packages, coupled with the programmable computational capabilities of a microcomputer opens a multitude of possibilities for this application.

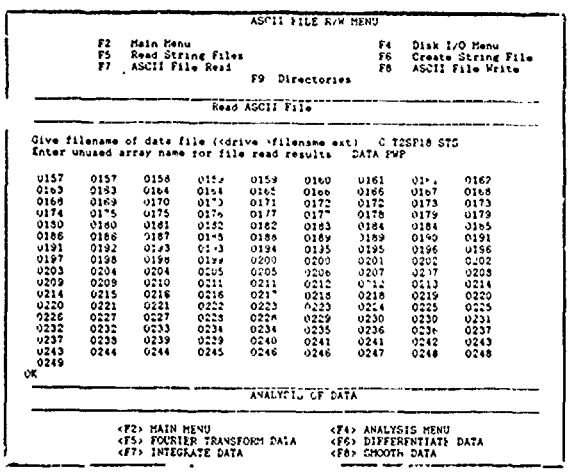

Figure 3. DEMOGPIB Menu for Data Acquisition and Analysis

A number of modifications in both software and hardware are available which will allow the system to provide more capabilities. This upgrading will provide the system with tremendous capabilities including real-time testing and control.

The system is easy to learn. A person who is familiar with the software (ASYST) will be ready to use the system efficiently in a few hours. However, this non-dedicated software package takes considerable time to learn. It is our intention to modify the system software in the near future so that all processes; data acquisition, reduction, analysis and plotting will be done with the non-dedicated software package. This will provide more memory in the computer which can be used to speed up testing, and the user will not have to switch between one program and another during analysis and data reduction.

ACKNOWLEDGEMENTS

We thank the U.S. Air Force, Office of Scientific Research for research funding which purchased the equipment described herein. The authors are grateful to Mr. Wes Boulton of Vic Meyers Associates of Denver, Colorado and Mr. Mike Rubinstein of Pacific Instruments, Inc., Concord, California for their persistence in developing and debugging the IBM-PC, IBM-XT, IBM-AT and compatible computer software described in this research. We also thank Mr. Suhaib Khan of Hewlett-Packard, Inc. of Fort Collins, Colorado for his computer help, Mrs. Teresa Tribelhorn for typing this paper, Ms. Lynn Schure, Messrs. Dave Allard, Wayne Lewis, Tom Bretz, and Bill Butler who helped with the research.

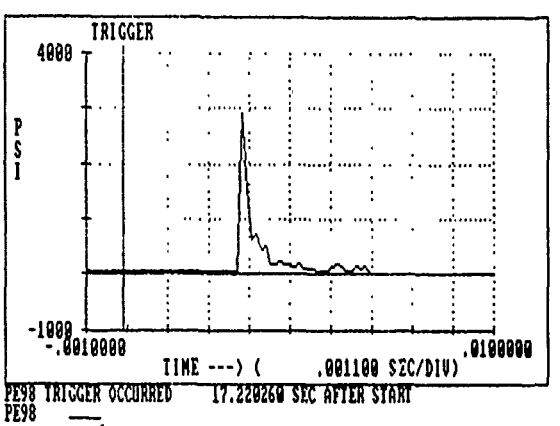

Figure 4. Porewater Pressure Ratio as a Function of Density and Effective Stress

SHOCK INDUCED POREWATER PRESSURE INCREASES IN WATER SATURATED SOILS

W.A. Charlie
Department of Civil Engineering
Colorado State University
Fort Collins, Colorado

G.E. Veyera
California Research and Technology, Inc.
Albuquerque, New Mexico

and

T.E. Bretz and D.J. Allard
Department of Civil Engineering
Colorado State University
Fort Collins, Colorado

Porewater pressure response was measured in water saturated quartz sands subjected to laboratory 1-D compressional shock loadings. The peak stress, peak strain and peak particle velocity levels required to increase the porewater pressure until liquefaction occurred were found to depend on the soil's relative density and initial integranular stress. For sands at low relative densities with an initial integranular stress of 172 kPa, the soil could be liquefied under a single shock loading if the peak strain or peak particle velocity exceeded 10^{-1}% or 1.5 m/sec, respectively. For sands at high relative densities with an initial stress of 690 kPa, the soil could be liquefied if the peak strain or peak particle velocity exceeded 1% or 15 m/sec, respectively. Above a threshold strain of $5x10^{-3}$%, which corresponds to a peak particle velocity of 0.075 m/sec, residual porewater pressure increases could be induced in all samples tested and liquefaction could be induced under multiple shocks. The actual number of shocks required for liquefaction depended on shock amplitude, soil density and initial integranular stress. Below a threshold strain of $5x10^{-3}$%, liquefaction could not be induced.

INTRODUCTION

Long term increases of porewater pressure in saturated cohesionless soils (such as sands, silts, and gravels) can result from shock loadings. This increase of pressure, which may last for seconds, minutes, or even hours, causes a reduction in the shear strength of soil, and if the pressure approaches the total stress in the soil, liquefaction may ensue. A liquefied soil behaves as a viscous fluid which has no shear strength, and thus bearing capacity is lost. Structures on liquefied soil are highly susceptible to foundation failure, and structures buried in the soil (fluid storage tanks, for example) are likely to become bouyant and "float" upwards.

A well programmed series of laboratory shock tests on water saturated cohesionless soils and analytical and empirical predictions of water pressure increase in these soils has been conducted at Colorado State University. The overall research goal was to establish if soil liquefaction of water saturated sands could be induced under transient compressional wave loading. As secondary objectives, the residual porewater pressure increase as a function of effective stress, soil density and peak strain were determined; finite difference and finite element codes were and are being developed to better understand the behavior and test results; and potential differences between cohesionless soils of differing grain shape, size and hardness are under investigation. The overall goal

has been completed. Water saturated cohesionless soils can be liquefied under transient compressional wave loadings. Shock testing of water saturated Monterey No. 0/30 beach sands obtained from Monterey, California have been completed. Testing of coral beach sands, river sands and gravels and fine beach sands and field explosive testing of river sands are currently under way. This paner focuses on the porewater pressure response of water saturated Monterey No. 0/30 sands shock tested under undrained conditions.

The objective of the above studies is to increase our understanding of the mechanisms that govern soil liquefaction. It is suggested that within a given soil, a threshold strain exists above which soil particle crushing or movement causes the porewater pressure to increase sufficiently to cause liquefaction. Above this threshold strain, the water pressure increases and remains at this increased level until sufficient time has passed to allow for drainage. The results of these studies and future planned efforts should lead to improved methods for identifying areas that may have potentially liquefiable soils.

TEST APPARATUS

Laboratory testing was accomplished using a gas powered cannon that fired a 6.80 cm diameter by 10.15 cm long stainless steel projectile into a 122 cm long cylinder containing water. As the projectile impacted a piston at that end of the cylinder, a compressive wave was generated and traveled through the water to the soil sample. The sample was separated from the water with a rubber membrane. The cylindrical sample container was constructed of stainless steel with an inner diameter of 8.90 cm and a length of 15.25 cm. The far end of the sample container was welded to a 2.54 cm thick end plate. In order to minimize reflections coming back through the soil, a momentum trap consisting of a solid polyvinylchloride (PVC) rod was placed against the sample container's end plate. Figures 1 and 2 show the shock system.

In order to measure incoming water pressures and porewater pressures in the soil sample, modified piezoresistive pressure transducers (Endevco Model 8511a-5kM1) were used. One transducer was exposed to the water through which the compressive wave traveled and another was placed in the soil sample. The responses in the transducers were amplified and sent to a digital waveform recorder (Gould/Biomation Model 2805). Both transient and residual porewater pressures were recorded by use of dual sampling rates. A microcomputer (HP-9835A) was used to analyze the data.

SOIL DESCRIPTION

Basic physical and index properties for Monterey No. 0/30 sand, evaluated according to accepted standard laboratory testing procedures set forth by the American Society for Testing and Materials [1] are given in Table 1. Details of the tests are given by Muzzy [3], Charlie, et al. [2] and Veyera [4]. The soil grains are uniform in size and are subangular to subrounded in shape (Figure 3). The predominate mineral constituent is quartz with several others existing in substantially smaller amounts.

Soils were placed in the sample container at various densities (relative densities of 0%, 20%, 40%, 60% and 80%). Table 2 lists the void ratio (e), total saturated mass density (ρ_t), and predicted compressional wave velocity (V_{mix}) at 100% saturation for each relative density. To ensure 100% saturation, the samples were flushed with CO_2 gas to remove air, flushed with deaired water and back pressured to 345 kPa. After saturation, the compressional wave velocity exceeded 1500 m/sec.

SHOCK TESTS

A total of 35 samples were tested. For each density (0%, 20%, 40%, 60% and 80%), seven samples were tested at four different effective stresses (86, 172, 345, and 690 kPa). The porewater pressures were recorded. From the peak porewater pressure the peak compressive strain was calculated. From the residual porewater pressure the porewater pressure ratio (PPR) was calculated for the first impact of each sample. The PPR is defined as:

$$PPR = \frac{\Delta u_{Res}}{\bar{\sigma}_o} \qquad \text{Eq. 1}$$

where Δu_{Res} is the residual porewater pressure increase after passage of the compression wave and $\bar{\sigma}_o$ is the initial effective stress. The ratio ranges from zero to 1, with zero being no increase in residual porewater pressure and one indicating liquefaction (zero effective stress). The PPR was found to increase with increasing peak compression strains and decrease with increased initial effective stress and relative density. The results of the 35 tests are reported in Table 3 and plotted on Figure 4.

The results of a multivariate regression analysis of the data given in Table 3 produced the following form:

$$PPR=(16.00)(\varepsilon_{pk})^{0.331}(\bar{\sigma}_o)^{-0.308}(Dr)^{-.179} \qquad \text{Eq. 2}$$

where relative density, (Dr), and peak compressive strain, (ε_{pk}), are both in percent and the initial effective stress, ($\bar{\sigma}_o$), is in kPa. The standard error estimated is 0.19 and the coefficient of determination (R^2) is 66%. Each sample

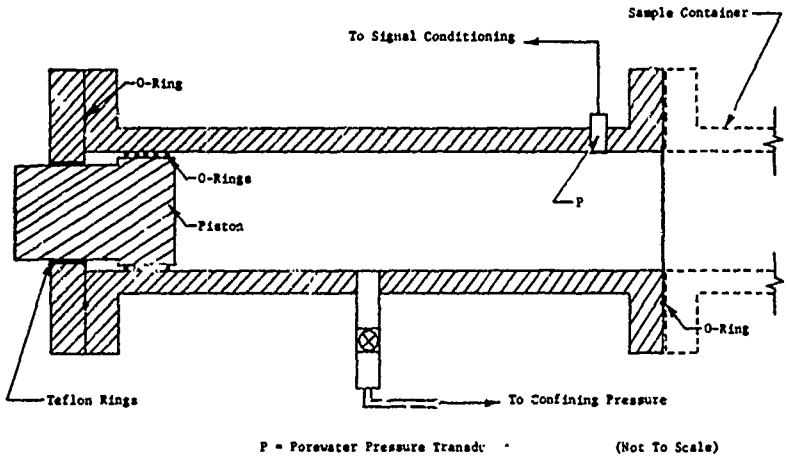

Figure 1. Cross-section of the confining pressure tube (Veyera, 1985)

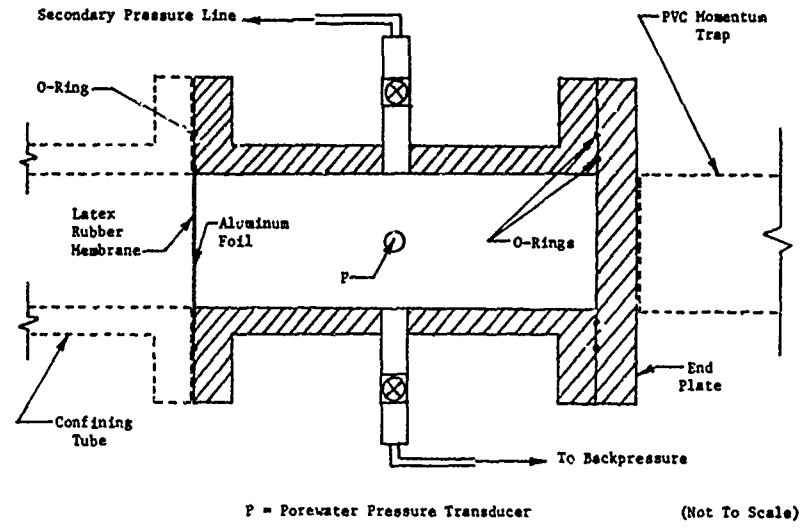

Figure 2. Cross-section of the sample container (Veyera, 1985)

Table 1. Physical Properties of Monterey No. 0/30 Sand

USCS Classification	SP
Specific Gravity	2.65
Particle Size Data	
D_{50}	0.45mm
D_{30}	0.38mm
D_{10}	0.29mm
% Passing #20 sieve	100%
% Passing #100 sieve	0.05%
Relative Density Test Data:	
Dry Unit Weight	
Maximum	1700 kg/m^3
Minimum	1470 kg/m^3

Table 2. Stress Wave Propagation Parameters for Monterey No. 0/30 Sand

DR (%)	Void Ratio (e)	ρ_t (kg/m³)	V_{mix} (m/sec)
0	0.803	1915	1519
20	0.755	1940	1532
40	0.707	1967	1546
60	0.659	1995	1563
80	0.611	2024	1582

Note: The compressive stress wave velocity in fresh water at 20°C is 1500 m/sec

Table 3. Peak Porewater Pressure, Peak Compressive Strain and Pore Pressure Ratio for Monterey No. 0/30 Sand (First Impacts)

Test ID	$\bar{\sigma}_o$ (kPa)	DR (%)	u_{pk} (1) (kPa)	ε_{pk} (2) (%)	PPR (1)
DR = "0%" Series					
	86	10.0	272	0.0061	0.33
	172	4.6	461	0.0103	0.77
	172	4.6	5711	0.1283	0.66
	345	7.5	1222	0.0273	0.56
	345	3.8	6585	0.1481	1.08
	690	7.5	81	0.0018	0.02
	690	5.8	2912	0.0653	1.01
DR = "20%" Series					
	86	29.2	353	0.0076	0.12
	172	27.9	524	0.0114	0.10
	172	23.8	3817	0.0833	1.01
	345	29.6	661	0.0143	0.23
	345	27.5	5400	0.1172	0.99
	690	28.8	380	0.0082	0.18
	690	22.1	5768	0.1262	1.03
DR = "40%" Series					
	86	46.7	517	0.0109	0.42
	172	47.1	1692	0.0355	0.61
	172	44.2	4524	0.0955	0.50
	345	45.9	543	0.0114	0.06
	345	46.7	4693	0.0987	0.83
	690	46.7	742	0.0152	0.35
	690	46.7	3845	0.0808	0.79
DR = "60%" Series					
	86	67.5	349	0.0077	0.46
	172	67.1	380	0.0077	0.16
	172	61.1	4156	0.0850	0.83
	345	66.3	290	0.0059	0.12
	345	64.2	6022	0.1226	0.66
	690	65.8	480	0.0097	0.18
	690	62.5	5994	0.1224	0.62
DR = "80%" Series					
	86	85.8	796	0.0155	0.64
	172	87.9	950	0.0184	0.53
	172	81.3	6867	0.1353	1.15
	345	85.4	697	0.0136	0.36
	345	83.3	8198	0.1607	0.33
	690	86.3	715	0.0139	0.33
	690	83.8	5966	0.1169	0.63

(1) Measured
(2) Calculated

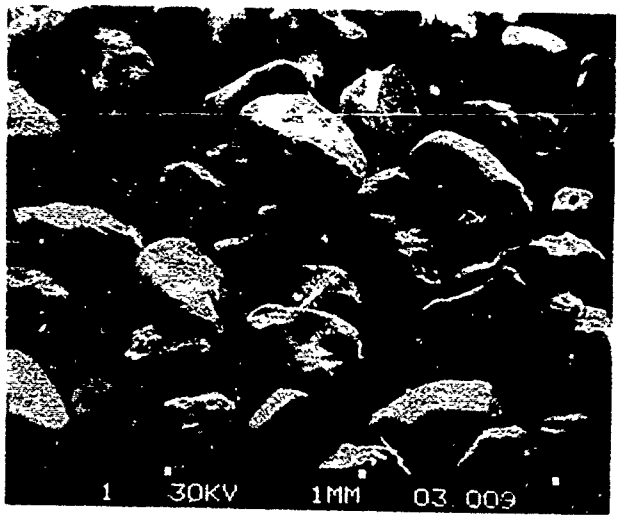

Figure 3. Photomicrograph of Monterey No. 0/30 Sand (Muzzy, 1983)

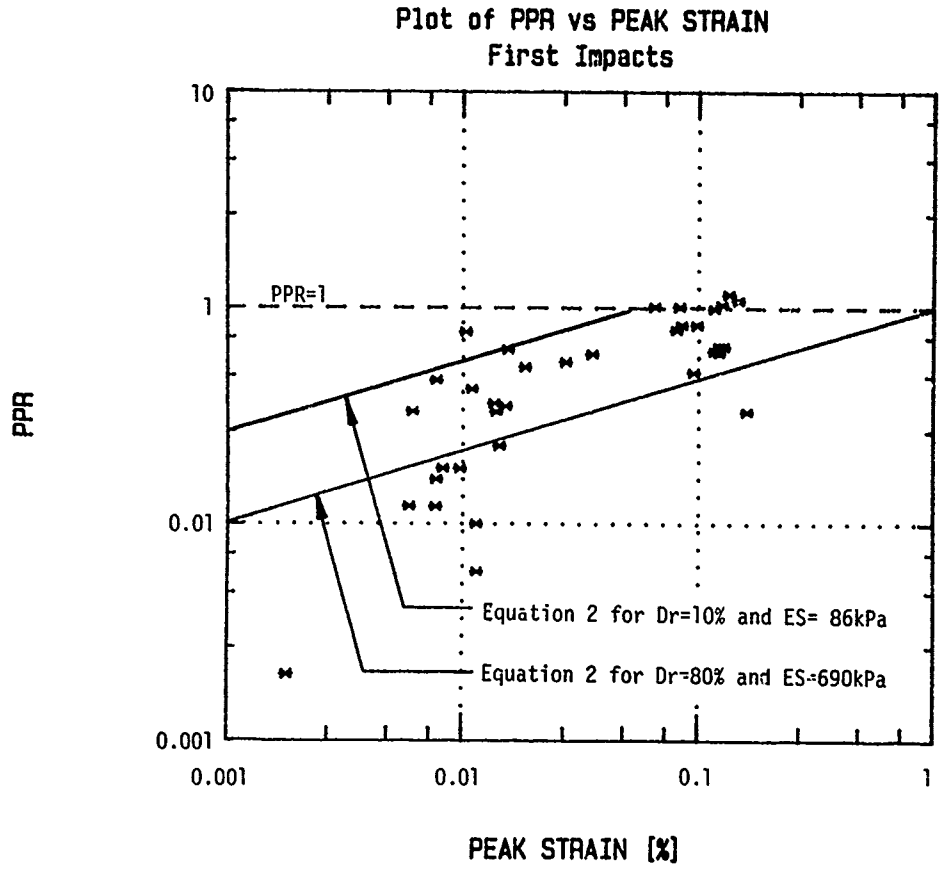

Figure 4. Porewater Pressure Ratio as a Function of Density and Effective Stress

was also subjected to additional multiple shocks and the results were similar to Eq. 2. A finite difference model utilizing quasi-static stress strain information obtained from drained one-dimensional loading tests on the soil also predicted PPR similar to Eq. 2 [4].

The next phase of the investigation is a field effort in which actual explosives are used to generate compression waves in saturated sand. The test setup consists of a 4.27m diameter steel tank located below the groundwater table and filled with saturated sand. The top of the tank is 3.66m below the surrounding ground surface in a pit 15m square. The pit is filled with water and explosives are detonated in this water, sending the compressional shock waves vertically downward through the sand. Instrumentation consists of piezoresistive porepressure transducers (ENDEVCO model 8511a-5km1), total stress gages (Kulite model UDP-393-160), inductive strain gages (locally manufactured), piezometers and transient data recorders (Pacific Instruments, Inc. model 9820). To date, 11 detonations have been made, and preliminary data indicate that liquefaction of the sand may be occurring during the larger shots and residual porewater pressure increases have been measured for several minutes after the blast.

ENGINEERING IMPLICATIONS

Since the shear strength and shear wave and Rayleigh wave velocity of saturated cohesionless soils depends on the soils' intergranular stress, increases in residual porewater pressure (decrease in intergranular stress), will result in a decrease in soil shear strength, decreased shear wave velocity and decreased Rayleigh wave velocity. If liquefaction occurs, the soils cannot transmit shear or Rayleigh waves and only compressional and gravity waves can exist. Current methods for determining ground shock do not incorporate this possibility. Accurate predictions of late time ground shock from single explosive shots and ground shock from multiple shots in saturated cohesionless soils require an accurate method to predict shear properties of soils. Liquefaction may explain the unexpected size of craters in the Pacific Proving Range and unexpected late-time low frequency motion observed in some explosive tests in saturated cohesionless soils.

CONCLUSIONS

Water saturated sands can be liquefied under transient compressional wave loadings. The peak strain necessary for liquefaction depends on the soils' density, the initial effective stress and to a much lesser extent, the particle size, shape and hardness. At strains greater than 1%, all samples tested under the first impact liquefied, and at strains less than 5×10^{-3}% liquefaction could not be induced ever under multiple impacts. Peak strains between these limits resulted in residual porewater pressure increases (partial liquefaction) and at these peak strains liquefaction could be induced under multiple impacts.

ACKNOWLEDGEMENTS

We thank the U.S. Air Force, Office of Scientific Research for the research funding which supported this research. The writers acknowledge and appreciate the technical assistance received from Jim Shinn and Scott Blouin of Applied Research, Inc. of South Royalton, Vermont and Eric Rinehart of California Research and Technology, Inc., Albuquerque, New Mexico. We also thank Teresa Tribelhorn for typing this paper and Matt Muzzy who helped with the research.

REFERENCES

1. American Society for Testing and Materials,Annual Book of ASTM Standards, "Soil and Rock: Building Stones", Vol. 04.08, Philadelphia, Penn., 734 p., 1983.

2. W.A. Charlie, G.E. Veyera, D.O. Doehring, and S.R. Abt, "Blast Induced Liquefaction Potential and Transient Porewater Pressure Response of Saturated Sands", Final Report to Air Force Office of Scientific Research, Grant No. AFOSR-80-0260, Colorado State University, Dept. Civil Engineering, Fort Collins, Colorado, Oct., 198 p., 1985.

3. M.W. Muzzy, "Cyclic Triaxial Behavior of Monterey No. 0 and No. 0/30 Sands", Master's Thesis, Dept. of Civil Engineering, Colorado State University, Fort Collins, Colorado, May, 138 p., 1983.

4. G.E. Veyera, "Transient Porewater Pressure Response and Liquefaction in a Saturated Sand", Doctoral Dissertation, Dept. of Civil Engineering, Colorado State University, Fort Collins, Colorado. Aug., 199 p., 1985.

U.S. GOVERNMENT PRINTING OFFICE:1987-181-588/40015